Enhanced kinetics and modeling of PAN-based carbon felt anodes in vanadium redox flow batteries

A Dissertation Presented for the

Doctor of Philosophy

Degree

The University of Tennessee, Knoxville

Michael Cyrus Daugherty

December 2020

Copyright © 2020, by Michael Cyrus Daugherty

All Rights Reserved

Dedication

Dedicated to my grandmother Ashlyn who passed away this year and to my family.

Acknowledgments

This will be an inexhaustive list of all the people who have helped me through my studies, and research work so to those who I do not have space here to mention, this acknowledgment is to you.

I would like to thank Dr. Mench, my advisor, for giving me the opportunity to work under his guidance. The lab culture, which he has facilitated is one of camaraderie and collaboration which was both enjoyable and helpful while going through graduate school. All my lab mates both past and present have been a pleasure to work with, and I am very grateful to have worked with each of them. I would also like to thank the other members of my committee, Dr. Kenneth Kihm, Dr. Feng-Yuan Zhang and Dr. Vasilios Alexiades.

I would like to especially thank Alan Pezeshki for giving me a great deal of guidance and advice early in my graduate career. Discussions and insights that I gained through those early conversations were extremely insightful and helped direct the path I chose to pursue. I would also like to express a great deal of gratitude to Dr. Chien Hsieh. His guidance, insights and assistance were extremely helpful.

I would like to thank the University of Tennessee for granting me the Chancellor's Fellowship, which funded me for the first four years of my studies. Finally, I would like to thank my family both immediate and extended for helping and supporting me through this process.

Abstract

All-vanadium redox flow batteries (VRFBs) are a promising technology for grid-level energy storage, however, there are still several limitations in the forms of durability, efficiency, and overall costs, which are barriers to its commercial viability. With both bulk electrolyte flowing through its porous matrix and species flux at the solid-electrolyte interface, electrodes are the component of VRFB systems which host electrochemical reactions and facilitate contact between the liquid phase electrolyte and the electronically conductive solid phase. While the more limiting electrode in VRFB systems is dependent on the material, for polyacrylonitrile (PAN)-based carbon felts, the anode constitutes a larger portion of the total overpotential than the cathode. In-situ characterization of modified felts can provide both a path towards understanding the source improvements to the anode but also their transient behavior, thereby creating a path to higher voltage and energy efficiencies and higher commercial viability.

The primary experimental components of this work are the symmetric cell configuration and electrochemical impedance spectroscopy (EIS). The symmetric cell is an in-situ experimental configuration, which utilizes a single electrolyte at both half-cells of a reactor. The symmetric cell allows an experiment to maintain a constant state of charge, incur no net-crossover and isolate a single redox couple. Electrochemical impedance spectroscopy is the focal experimental diagnostic technique in this work, owing to both its minimal perturbation of the state of a cell and to the insights into electrochemical interfaces it provides. The combination of these

two techniques is utilized in this work to both characterize several material modifications and to enhance the understanding of the sensitivity of this diagnostic for the purposes of model selection. A novel experimental configuration is also developed, which combines a cell-in-series approach with the symmetric cell in order to continuously characterize VRFB electrodes as a function of state of charge.

The outcomes of this work elucidate methodologies for in-situ characterization of anode modifications from an experimental perspective and also frameworks for characterizing porous electrochemical interfaces, investigating sensitivity, and elucidating systematic approaches to separate electrochemical phenomena occurring at a VRFB anode interface.

Table of Contents

1 Introduction **1**
- 1.1 Motivation . . . 2
- 1.2 Literature Review . . . 11
  - 1.2.1 Electrodes . . . 16
  - 1.2.2 Electrolyte . . . 18
  - 1.2.3 Bipolar Plates . . . 20
  - 1.2.4 Degradation / Durability . . . 21
  - 1.2.5 VRFB parameter estimation . . . 23
  - 1.2.6 VRFB modeling . . . 23
- 1.3 Objectives . . . 25

2 Impedance Model Specific Parameter Estimation of Treated Carbon Felt Electrodes in Vanadium Redox Flow Batteries **27**
- 2.1 Introduction . . . 29
- 2.2 Methods . . . 31
  - 2.2.1 Treatments . . . 31
  - 2.2.2 Experimental . . . 34
  - 2.2.3 EIS data . . . 36
  - 2.2.4 Monte Carlo Simulations . . . 41
- 2.3 Results and Discussion . . . 42
  - 2.3.1 Complex decay length . . . 42
  - 2.3.2 Monte Carlo Simulations . . . 44
- 2.4 Conclusions . . . 63

3 Contributions from graphitic plates to in-situ kinetics measurements in all vanadium redox flow batteries **65**
- 3.1 Introduction . . . 66
- 3.2 Methods . . . 69
  - 3.2.1 Experimental . . . 69
  - 3.2.2 Impedance . . . 71
  - 3.2.3 Mass transport at the channel electrode . . . 74
- 3.3 Results and discussion . . . 75
  - 3.3.1 Mass transport analysis . . . 75
  - 3.3.2 Frequency analysis . . . 78
  - 3.3.3 Anode Polarization Curves . . . 78
  - 3.3.4 Capacitance and exchange current density . . . 86
- 3.4 Conclusions . . . 91

4 Graphene and Graphitic Carbon Nitride Quantum Dot Decorated Carbon Electrodes for Energy Storage in Vanadium Redox Flow Batteries **92**
- 4.1 Introduction . . . 94
- 4.2 Experimental . . . 97

4.2.1 Synthesis of quantum dots by SPMA method 97
4.2.2 Materials characterization of quantum dots 97
4.2.3 VRFB cell architecture and GQD / GF composite electrode fabrication 98
4.2.4 Electrochemical performance of VRFBs using GQD/GF electrodes 99
4.2.5 Impedance modeling and parameter estimation 100
4.3 Results and discussion 103
4.4 Conclusions 121

5 Decorating Sulfur and Nitrogen Co-doped Graphene Quantum Dots on Graphite Felt as High-Performance Electrodes for Vanadium Redox Flow Batteries 122
5.1 Introduction 124
5.2 Experimental 127
5.2.1 IR-assisted synthesis of S/N co-doped GQDs 127
5.2.2 Materials characterization of S/N co-doped GQDs 128
5.2.3 Electrochemical characterization of VRFBs 128
5.3 Results and discussion 130
5.4 Conclusions 145

6 In-situ state-of-charge dependent parameter estimation for all vanadium redox flow battery 147
6.1 Introduction 148
6.2 Experimental Methods 148
6.2.1 Novel in-situ cell-in-series configuration 148
6.2.2 Electrochemical experiment procedure 149
6.2.3 Experiment Protocol 149
6.2.4 Electrochemical Impedance Modeling 151
6.2.5 Modeling the efficiency as a function of electrolyte composition 153
6.3 Results and discussion 155
6.3.1 Area Specific Resistance 155
6.3.2 Anode analysis 158
6.4 Conclusions 164

7 Improved rate capability and low internal resistance for vanadium redox flow batteries utilizing ultrafast laser structured graphite felt 165
7.1 Introduction 167
7.2 Methods 170
7.2.1 Laser treatment of GF electrodes 170
7.2.2 Assembly of VRFBs 171
7.2.3 Electrochemical characterization of VRFBs 173
7.3 Results and discussion 174
7.4 Conclusions 186

8 Lattice Boltzmann modeling of 2D element of all vanadium redox flow battery electrode: Part I **188**
8.1 Introduction . . . 189
8.2 Lattice Boltzmann Model . . . 190
8.2.1 Fluid Transport . . . 191
8.2.2 Species Transport . . . 193
8.2.3 Boundary Conditions . . . 195
8.3 Results and discussion . . . 197
8.3.1 Model validation: diffusion field . . . 197
8.3.2 Model validation: advection and diffusion . . . 198
8.3.3 Porous media . . . 200
8.4 Conclusions . . . 207

9 Power flexibility analysis for strip cell vanadium redox flow battery **208**
9.1 Introduction . . . 209
9.2 Methods . . . 210
9.3 Results and discussion . . . 212
9.4 Conclusions . . . 217

10 Conclusions and Recommendations **219**
10.1 Conclusions . . . 220
10.1.1 Electrode modifications . . . 220
10.1.2 Modeling . . . 221
10.2 Recommendations . . . 223

Bibliography **227**

Appendices **249**

Vita **307**

List of Tables

2.1 Electrode treatments 32

3.1 Characteristic frequency and complex decay length for different electrode configurations. The actual thickness of the porosity of the channel electrode has not been measured so the thickness of 1 Layer of felt was use (.18 cm) to give a lower bound for $\frac{\lambda}{b}$. 79

4.1 ASR magnitudes and fitted parameters for the spectra shown in Figure 4.4 111

A.1 MHPE Derivation Nomenclature 253
A.2 Chapter 2 Nomenclature 264
A.3 Model Parameters (95% confidence intervals) 265
A.4 Chapter 3 Nomenclature 266
A.5 Reynolds number and entry length for flow rates used in channel electrode experiments 269
A.6 Chapter 4 Nomenclature 273
A.7 Parameters used for Figure 8.2 284
A.8 Parameters used for Figure 8.2 285
A.9 Chapter 8 Nomenclature 286
A.10 Strip cell analysis data (from ref [231]) 287
A.11 Chapter 9 Nomenclature 288

List of Figures

1.1 Characteristics of energy storage technologies [6,9] 3
1.2 Examples of grid level energy storage for different time scales. 5
1.3 Comparison of grid-scale electrochemical storage technologies (pumped-hydro included for reference). The values shown are averages and the scale is log base 10. (Data from [11]). 6
1.4 Lab-scale redox flow battery with 5 cm^2 rectangular flow through flow field. 8
1.5 Schematic of a single cell VRFB (discharging): (1) Ion exchange membrane (2) anode (3) anolyte tank (4) cathode (5) catholyte tank (6) graphite flow fields (7) end plates (8) pumps (9) load (discharge) / source (charge), (10) current collectors 10
1.6 The Nernst equation (1.2) for the VRFB and its sensitivity with respect to SoC as a function of SoC. 13
1.7 Three variations of the Nernst equation for the VRFB 15

2.1 Rectangular flow-through flow-field (5 cm^2) schematic. The blue and red channels show the electrolyte inlet and outlet respectively. . 35
2.2 Impact of frequency on complex decay length (λ). The left figure shows $\gamma(\omega)$ with ω_1 labeled on each spectrum with a white circle. The right plot shows the ratio of λ to characteristic length b at the lowest measured frequency (ω_{min}) 43
2.3 SEM Images: (A) Untreated (Raw) GFD3 fiber; (B) Am4 electrode fiber; (C) Inset increased magnification of porosity on fiber surface (fiber diameter ≈ 8 μm; pore diameter ≤ 50 nm) 45
2.4 Monte Carlo Simulation for untreated (Raw) electrodes 47
2.5 Monte Carlo Simulation for nitric acid soaked (NAS) electrodes . . . 49
2.6 Monte Carlo Simulation for nitrogen heat treated (HtN) electrodes . . 50
2.7 Monte Carlo Simulation for 60 °C hydrothermally treated (HyB) electrodes 52
2.8 Monte Carlo Simulation for 80 °C hydrothermally treated (HyA) electrodes 54
2.9 Monte Carlo Simulation for oxygen heat treated (HtO) electrodes . . 56
2.10 Monte Carlo Simulation for mixed hydrothermal / heat treated (Hyt) electrodes 57
2.11 Nyquist plots for Am4 electrodes. A) shows the non-faradaic spectrum (measured in 4M H_2SO_4), fit with the MHPE model with $C_R \rightarrow 0$ and $C_O \rightarrow 0$. The inset shows the distributed resistance which is observed at high frequency. B) shows the spectrum measured in the presence of vanadium electrolyte. The characteristic frequency is labeled with the white circle in both figures. 59

3.1 IR corrected polarization curves for symmetric cell between 10 and 32.5 $mLmin^{-1}$. The left shows the catholyte as a function of flow rate where the onset of mass transport dominated polarization begins at low current. The right shows the anolyte as a function of flow rate where mass transport polarization is non-dominant up to $\approx$ 20 mA cm^{-2}. 76
3.2 Open circuit catholyte diffusion ASR and mean diffusion layer thickness as a function of $V_f^{-\frac{1}{3}}$. This relationship indicates onset of mass transport control is at OCV. 77
3.3 Impedance resolved anolyte channel polarization curves as a function of flow rate, the semi-transparent Overlay shows the convergence of the polarization curves to the potential where mass transport limitation starts. 80
3.4 Impedance resolved polarization curves for each electrode configuration (channel, 1 Layer, 2 Layers) with increasing flow rate. Cell voltage is shown in white circles to confirm the sum of the overpotential components. 82
3.5 Parallel combination of plates and one layer of electrode predicts polarization of two layers of electrode. The bottom figure shows the percentage of current that is supported by the plates as the overpotential goes to zero. This is for the instance of a volumetric flow rate of 10 mL min^{-1}. 84
3.6 Tafel plots for one and two layers of electrode thickness for estimation of the geometric exchange current density. 85
3.7 Effect of stacked electrodes on (A) charge transfer ASR and (B) finite diffusion ASR measured at open circuit. 87
3.8 Effect of stacked electrodes on (A) geometric exchange current density ($i_{0,geo}$), (B) effective surface area (A_{eff}), and (C) diffusion boundary layer thickness (δ_{eff}). The linear fits are the values projected to zero thickness using one and two layers. 88

4.1 (a) XRD patterns and (b) Raman spectra of QD-1,Qd-2, and QD-3 samples. XPS (c) 1s and (d) N 1s peaks of QD-1, QD-2 and QD-3 samples 104
4.2 HR-TEM micrographs of QD-1, QD-2 and QD-3 samples, where inset shows their corresponding lattice fringes. Particle size distributions are shown in the histograms on the right for the respective treatments 107
4.3 Schematic diagram illustrating (a) the procedure of GQD/GF composite electrode for VRFBs and reversible redox pairs at (b) positive and (c) negative electrodes, where GQDs serve as active sites for catalyzing the redox couples. 109

4.4 EIS Spectra and fits fo reach electrode treatment. The left column shows the initial spectrum and the right shows the initial (semi-transparent) and the final spectra 110
4.5 Evolution of open circuit charge transfer ASR, diffusion ASR, capacitance and exchange current density with respect to time. Each treatment is shown with 2 linear fits: 1) electroless degradation regime (first 5 points) and 2) electrochemical degradation regime (final 4 points). 112
4.6 Impedance resolved polarization curves with QD-1, QD-2, QD-3, untreated GF electrodes at 50% SOC. 115
4.7 Distributions of equivalent series area specific resistance components by diffusion, charge transfer, and ohmic components at open circuit of the VRFBs based on the EIS analysis. 116
4.8 (a) Variation of current density (blue circles) and equivalent series resistance (red diamonds) with fraction of C-O groups on GQD/GF electrodes. The operating conditions of the VRFBs were overpotential of 0.4 V, 50% SOC, ambient temperature, and the first polarization curve cycle. Schematic illustration regarding the distribution of active sites on highly O-/N-functionalized GQDs, i.e., basal plane: (i) dual phenolic groups and (ii) phenolic group and edge: (iii) carboxyl group. The lattice "N" atoms induces a smaller charge transfer resistance during the redox reactions of VO^{2+}/VO_2^+ and V^{2+}/V^{3+} pairs. 119
4.9 Charge-discharge curves of the VRFBs equipped with (a) QD-2 and (b) untreated GF at a constant current density of 100 mA cm^{-2}. Variation of capacity retention and Coulombic efficiency with cycle number shown in (c). 120

5.1 (a) FT-IR spectrum and (b) survey-scan XPS spectrum of N/S co-doped GQD sample. 131
5.2 High-resolution XPS spectra of (a) C 1s, (b) O 1s, (c) N 1s, and (d) S 2p peaks of N/S co-doped GQD sample, deconvoluted by a multiple Gaussian function. 133
5.3 (a) HR-TEM micrograph and (b) lattice fringes of N/S co-doped GQD sample. The inset of (b) shows selected area diffraction of individual N/S co-doped GQD. 135
5.4 Typical XRD patterns of untreated GF and N/S co-doped GQD/GF samples. The inset shows their corresponding FE-SEM images. 136
5.5 FE-SEM images of N/S co-doped GQD/GF composite with (a) low and (b) high magnification. The left shows elemental mapping of C, N, O, and S on the individual carbon fiber. 137

5.6 (a) Open circuit Nyquist plots of untreated and N/S co-doped GQD-coated GFs at 1st, 10th, and 40th cycle, where the inset shows an equivalent circuit. (b) Resistance analysis of untreated and N/S co-doped GQD-coated GFs at 1st, 10th, and 40th cycle, where ESR is the sum of ohmic, charge transfer, and diffusion resistance. 139
5.7 Discharge capacity, Coulombic efficiency, and energy efficiency as a function of cycle number. 143

6.1 Schematic of experimental configuration. 1) catholyte tank, 2) peristaltic pump (2 channels), 3) anolyte tank, 4) symmetric cell membrane (1 x Nafion 117), 5) end plate, 6) current collector, 7) flow field, 8) control cell cathode, 9) Control Cell Membrane (2 x Nafion 117), 10) control cell anode. Each cell is connected to a separate potentiostat channel 150
6.2 ASR magnitudes for the anode and cathode as a function of composition. 156
6.3 Overpotential at 50 mA cm^{-2} as a function of open circuit |ASR|, theoretical SoCs are annotated. Each row shows two instances with equivalent concentration of vanadium; the columns indicate the two separate experiments 157
6.4 ASR components for the anode as a function of SoC. 159
6.5 Exchange current density (j_0) and effective surface area ($Area_{effective}$) as functions of state of charge. 161
6.6 System efficiency predictions using 1.5 M V. The black and red dashed lines indicates 50 and 0% SoC references respectively. 163

7.1 FE-SEM images of L electrode with (a) low and (b) high magnification. The inset (a) shows tilted view of FE-SEM image of L electrode. 175
7.2 Typical XRD patterns of U and L electrodes. The inset shows cross-sectional view of optical microscopy image of L electrode. 176
7.3 (A) Nyquist plots of U and L electrodes at 1st and 10th cycle at open circuit volt- age, where the inset shows a Randles circuit. (b) Resistance analysis of U and L electrodes at 1st and 10th cycle, where ESR is the sum of ohmic, charge transfer, and diffusion resistance. 178
7.4 (A) Charge-discharge curves of U and L electrodes at a constant current density of 150 mA cm^{-2}, (b) specific capacity as a function of cycle number at different current density, (c) average capacity as a function of current density, and (d) both capacity retention and coulombic efficiency as a function of cycle number. 181
7.5 Variation of contact angle of water droplet and liquid volume with time for (a) U and (b) L electrodes. 184

8.1 The two lattices used in this work were D2Q9 (for solving the fluid flow) and D2Q5 (for solving species transport). 194

8.2 Analytic solution vs. D2Q5 LBM solution for Da = 3.0 and Da 30.0. The solid line is the LBM solution and the dashed line is the analytic. Parameters used in these simulations are shown in Table A.7. 199
8.3 Comparison of the LBM solution to the Levesque analytic solution. Parameters used for this simulation are shown in Table A.8 201
8.4 Boundaries for lattice Boltzmann simulations. The solid internal obstacles were bounce-back boundaries for solving Navier Stokes, and Kang boundary (Equations 8.17 and A.51) for species transport. . . . 203
8.5 Impact of $\bar{\eta}$ on concentration distribution. The three plots were scaled to a single normal distribution with a mean centered at zero and a standard deviation of 1. [Re = 0.211. Da = 0.141, inlet SoC = 50%]. 204
8.6 Percentage change in inlet concentration as a function of inlet SoC and dimensionless overpotential $\bar{\eta}$ 206

9.1 Cell power (P_{cell}) and pump power (P_{pump}) as functions of volumetric flow rate. 213
9.2 Ratio of cell power to pump power. 215
9.3 Sensitivities of P_{cell} to $\sqrt{P_{pump}}$ as a function of channel depth 216

A.1 Oxygen Heat Treated electrode fit to a lemniscate 251
A.2 CV profiles of N/S co-doped GQD/GF electrode in 1M H_2SO_4 under N_2 flow at 50 mV s^{-1}. 271
A.3 The atomic configurations of (a) QD-1, (b) QD-2, and (c) QD-3 samples, simulated by LAAMPS [45]. 275
A.4 Schematic of the VRFB. The components are (in clockwise order): (a) membrane, (b) gasket, (c) current collector, (d) end plate, (e) graphite plate, (f) electrode. The inset shows the GQD/GF electrode sheet. . . 276
A.5 Equivalent circuit proposed for describing the electrochemical impedance behavior of the symmetric cell VRFBs, where Rohmic, RCT, Zf, Zwarburg and Q components represent ohmic resistance, charge transfer resistance, faradaic impedance, Warburg impedance and constant phase element capacitance, respectively. 277
A.6 Two sets of possible surface reaction steps at (a) positive and (b) negative GQD/GF electrodes of VRFBs [32,36]. 278
A.7 Schematic of symmetric cell configuration. (1) and (2) are respectively the cathode and anode in this schematic [though these can be switched for the same operation] (3) is the point where the reference electrode contacts the cell, (4) is the electrolyte reservoir (50% SoC) and (5) is the pump. 279
A.8 Schematic of full cell configuration in discharge mode. (1) membrane/separator; (2) anode; (3) anolyte tank; (4) cathode; (5) catholyte tank; (6) graphite flow plates; (7) aluminum end plates; (8) pumps; (9) load (during discharge); (10) current collectors 280

A.9 Schematic of electrochemical boundary identification. Edges are shown in red, (1,2,3,4). The direction of unknown correspond with the directions from the D2Q5 lattice in Figure 8.1. Convex corners (5,6,7,8) are shown in blue. 282
A.10 SEM image of typical GFD3 fiber. 283
A.11 Cathode and anode impedance spectra at open circuit (90% So; 0.5 M V)) 291
A.12 Cathode and anode impedance spectra at open circuit (50% SoC; 0.5 M V) 292
A.13 ASR components for the cathode as a function of SoC. 293
A.14 Experimental profile with OCV and discharge steps labeled. Spectra shown in blue are the measured anode spectrum in the symmetric cell, while spectra in red are the cathode symmetric cell. 294
A.15 Schematic diagram of electrolyte wetting on (a) U and (b) L electrodes, where a, b, and c represent original penetration depth, height, and width of pore channel, respectively. The pore channels, created by the laser treatment, allow more electrolyte diffusion, creating more reactive sites and promoting chemical reaction kinetics in VRFBs. 295

Chapter 1
Introduction

1.1 Motivation

Grid-scale energy storage is a technology that has garnered an increase in attention in recent years as efforts to modernize power grids have become a goal of governments worldwide [1]. The U.S. Department of Energy announced, in January 2019, a $40 million budget for FY19 for Grid Modernization Initiative [2], and in its Grid Modernization Multi-Year Program Plan outlined the necessities of a modern grid, which, among others, included: improved reliability for optimal operation, superior flexibility to accommodate uncertainty and variability in power output responding to conditions at one or more timescales, and increased sustainability for incorporation of renewable energy sources [3]. Energy storage fits squarely into the set of technologies to enable these qualities for a modern grid.

Broadly, grid-level energy storage technologies can be separated into three groups all of which are utilized in commercial systems presently: kinetic energy (e.g. pumped hydro, flywheels), electrochemical (e.g. lead acid and redox flow batteries), and thermal storage (e.g. thermal salts) [4]. Presently pumped hydro comprises the majority of installed storage capacity in the United States (~94%) and globally (~99%) [5–7], however, its expansion is limited by specific geographical requirements and high capital costs [8]. Comparing different grid-level energy technologies can be challenging as there is no one technology that is perfect for every potential use. Figure 1.1 shows discharge times and system power ratings for a visual comparison grid-energy storage technologies.

While this is a very general comparison (many of these options have broader

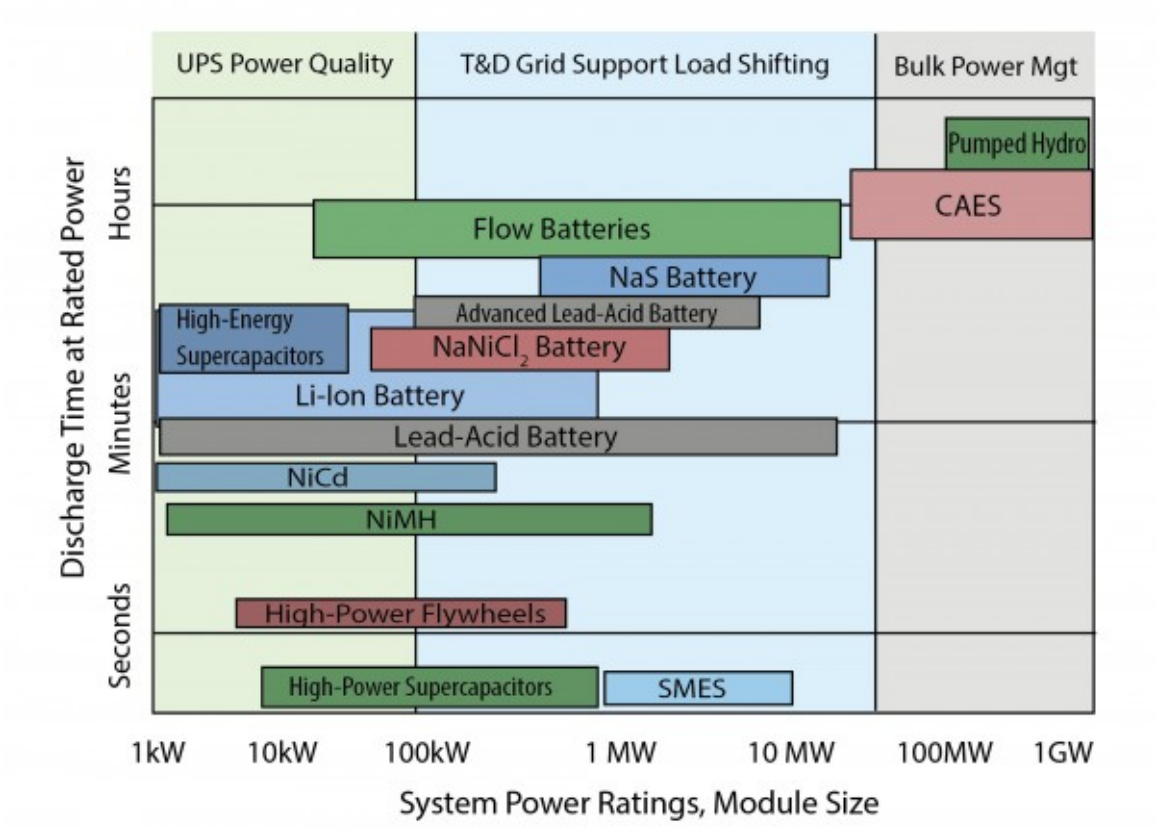

Figure 1.1: Characteristics of energy storage technologies [6,9]

power ranges than shown), it is helpful in understanding not only a comparison of the technologies, but also, classifying power-ranges in grid-management categories (power quality, load shifting and power management).

An important consideration in grid-scale energy technologies is the use-case as no current technology accommodates power, capacity and frequency demands [7,9]. These use-cases are typically organized by their respective time scales which range from sub-second up to days/months [10]. To elucidate the need for grid-scale energy at different time-scales two examples are illustrated. One use-case for grid-energy storage on the high frequency end of the spectrum is variable renewable energy (VRE). Grids must maintain inertia (the ability to resist changes in frequency) which necessitates near-instantaneous charging and discharging of a storage mechanism in order to output a constant frequency [7]. Figure 1.2a illustrates the application of smoothing VRE power so that it does not disrupt grid inertia.

On the lower end of the frequency spectrum, load-shifting (arbitrage) can utilize grid-scale storage by charging reserves when demand is low and discharging when demand is high. This process, temporally, can occur on the order of hours or days as illustrated in Figure 1.2b. Load-leveling allows the base-line power generation to be lowered and supplemented by a storage system. Taking a closer look at several electrochemical energy storage solutions, multi-dimensional comparison of grid-scale technologies is shown in Figure 1.3, which compares several key metrics of grid-scale energy storage and illustrates the multi-dimensional nature of these technologies (data are from [11]).

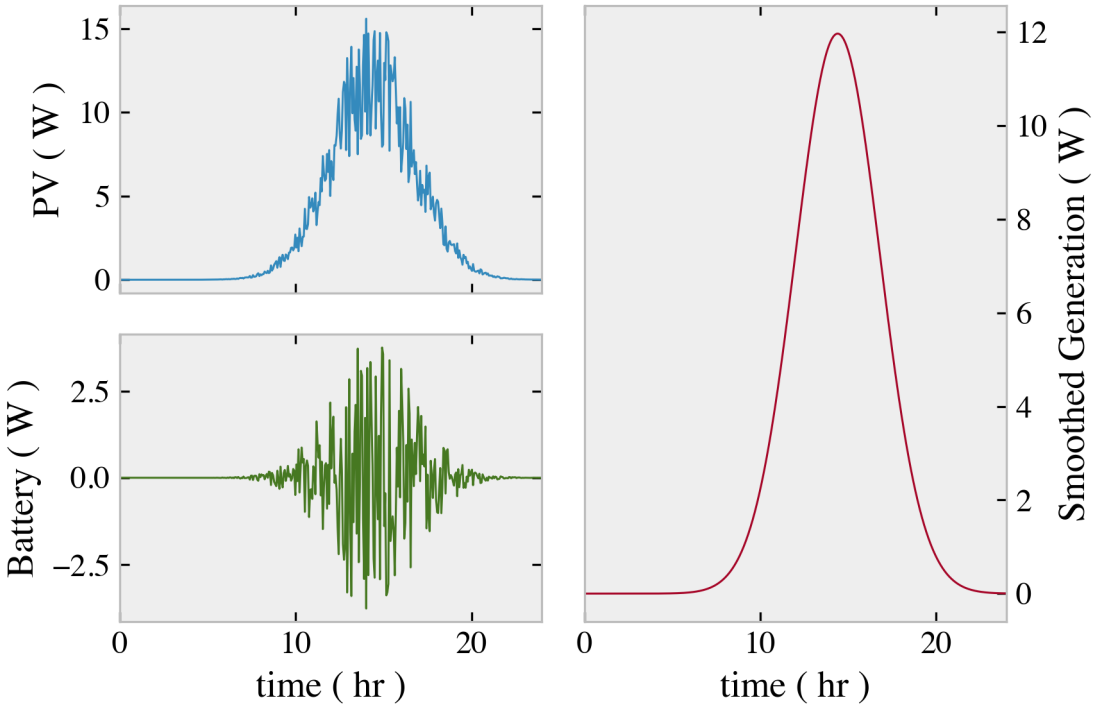

(a) Variable renewable energy smoothing for PV output.

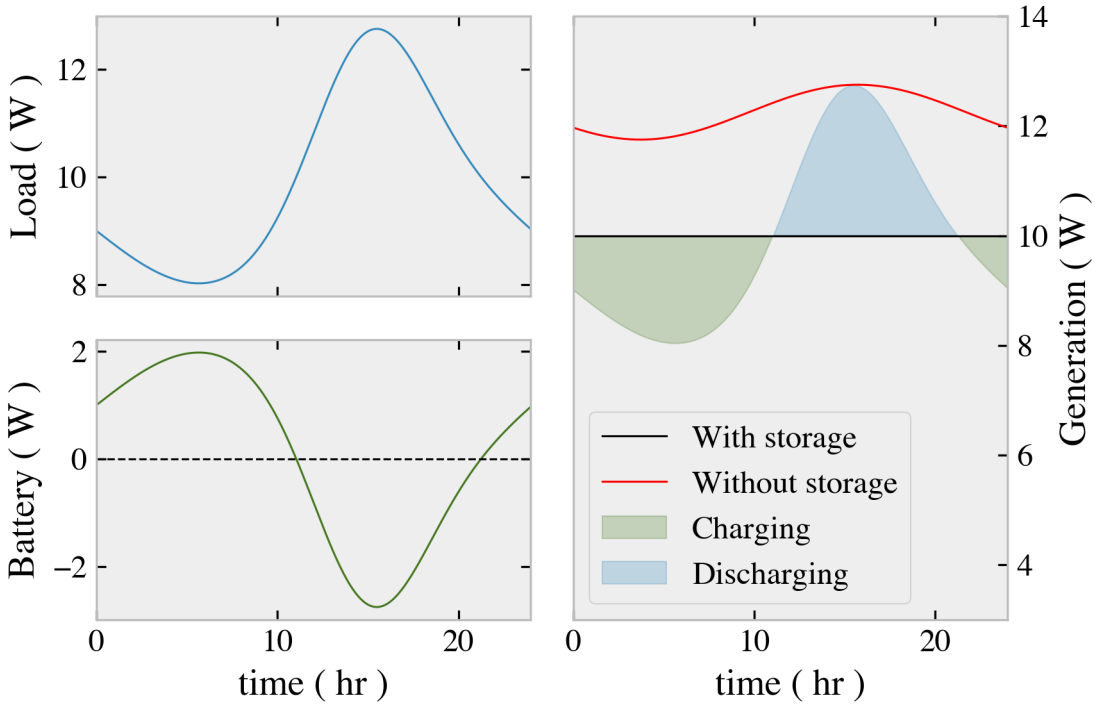

(b) Load-Leveling

Figure 1.2: Examples of grid level energy storage for different time scales.

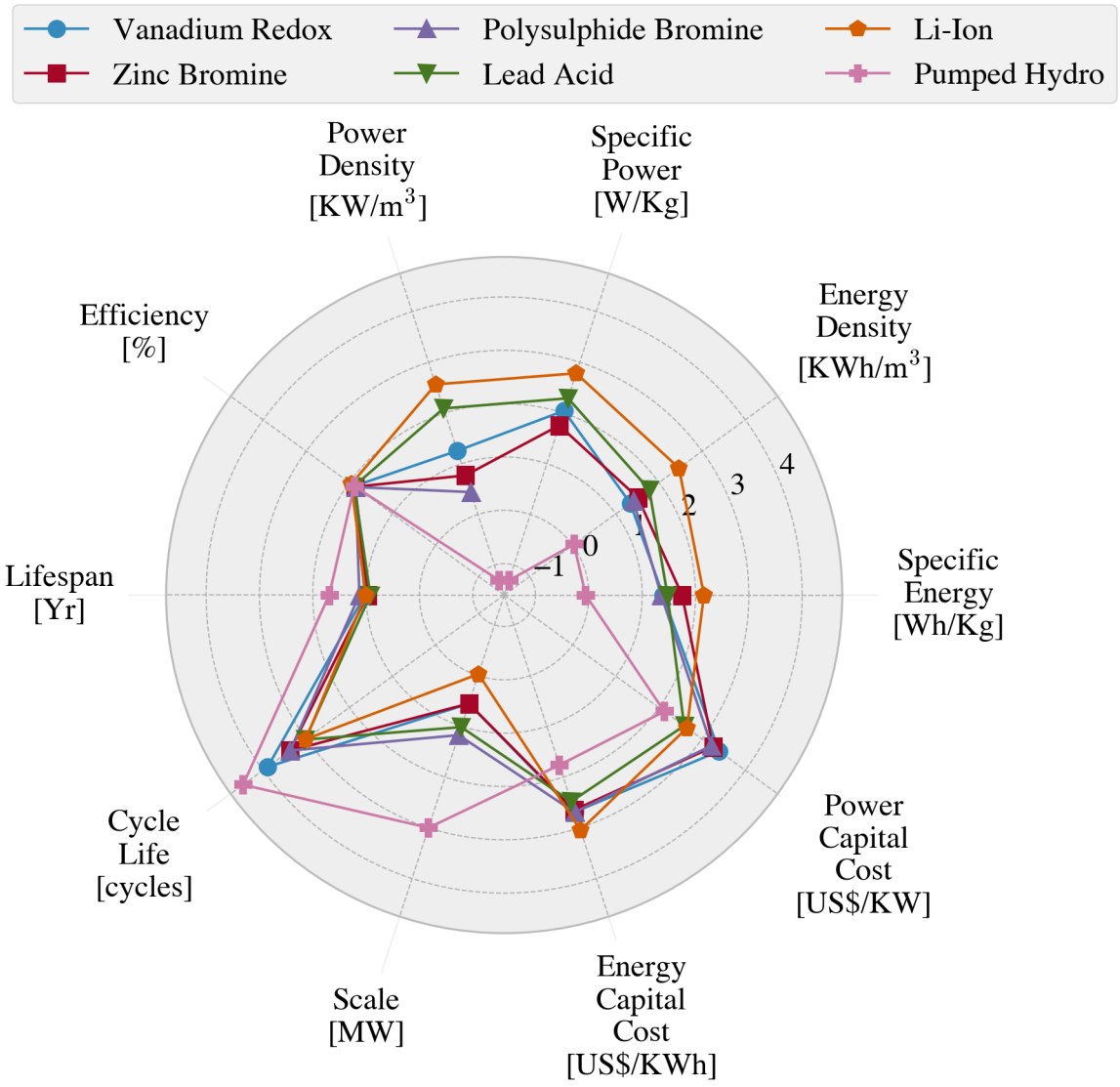

Figure 1.3: Comparison of grid-scale electrochemical storage technologies (pumped-hydro included for reference). The values shown are averages and the scale is log base 10. (Data from [11]).

Pumped hydro comprised ~94% of the installed power in the United States as of 2019 [6], and is included in Figure 1.3 as a reference point. While it is a mature and widely adopted technology (see the lifespan, cycles scale and cost metrics in 1.3), it has several significant limitations to universal adoption, primarily that it necessitates geographic features, which are not universally available and secondly it has both low power and energy densities and is not well suited for higher (and medium) frequency power quality management. Figures 1.1 and 1.3 elucidate both the challenges and potential for electrochemical energy storage solutions in the space of grid-scale energy storage.

Redox Flow Batteries

Redox flow batteries (RFBs) are a promising technology with the potential to both serve the DOE's stated goals for a modern grid and the flexibility in design and operation to satisfy any combination of the energy storage suitability characteristics. One of the primary benefits of RFBs is the decoupling of energy capacity and power generation capacity. The spatial independence of the reactor from the electroactive species allows for independent scaling of energy capacity (volume of electrolyte tanks) and power (geometry of reactor and number of cells in stack) [12]. This modularity allows for application-specific design and retrofitting/modifying of existing systems to accommodate shifting grid demand conditions [13].

RFBs are classified as secondary (rechargeable) batteries [14] and, in the context of grid-level energy storage, are expected to undergo thousands of charge/discharge cycles during their operational lifetime [15]. An RFB cell consists of two elec-

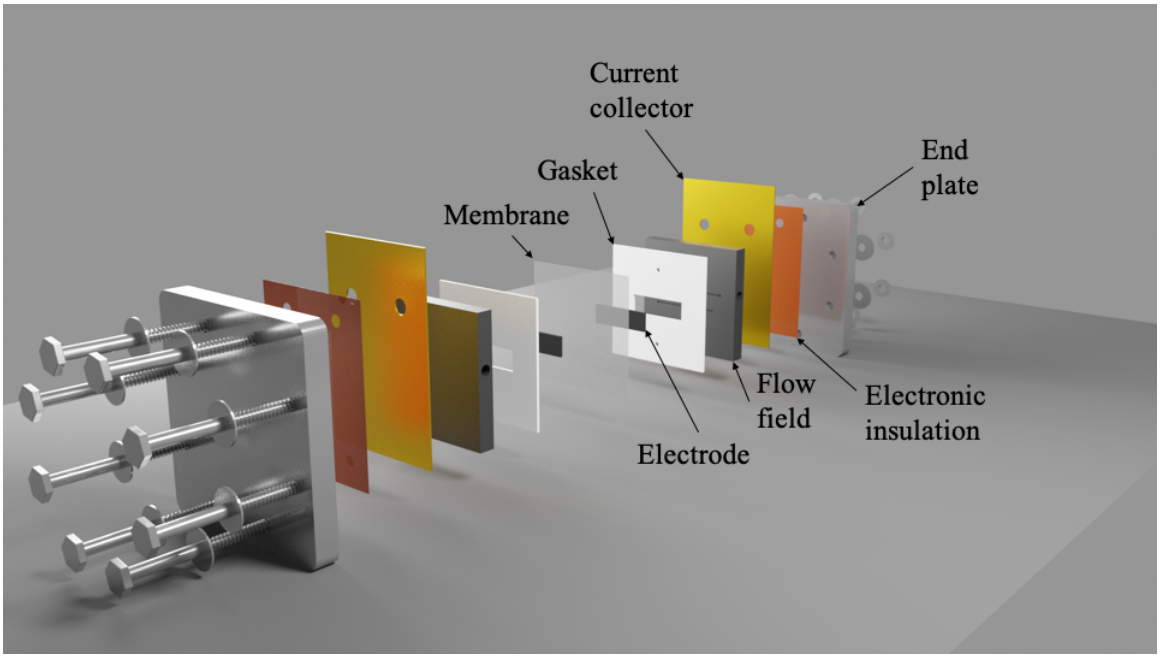

Figure 1.4: Lab-scale redox flow battery with 5 cm^2 rectangular flow through flow field.

trodes, isolated by a separator (typically an ion exchange membrane) disallowing crossover of active species and electronic current, but allowing ions to move between the two half-cells [16]. Negative and Positive electrolytes are stored in reservoirs external to the reactor and, during operation, are pumped into their respective half-cell where porous electrodes provide sites for redox reactions [17]. Upon leaving the reactor, the electrolytes are returned to their external reservoirs (see Figure (1.5)). Cells can be connected serially to form a stack in which the net voltage is the sum of each individual cell voltage, scaling the power density.

Although RFBs have, by comparison with lead-acid and lithium-ion batteries, lower energy densities, they are unencumbered by energy capacity limitations and become more economical with increasing power and energy balancing requirements [13,18]. For this reason, RFBs are well suited for grid level energy storage. To contextualize the work of this dissertation more broadly we can consider a simple system cost model where we describe the cost of an RFB system being controlled by two primary factors: electrolyte costs and stack costs [19]:

$$C_{system} \approx \frac{U_{electrolyte}}{V_{eff}} + \frac{U_{stack}}{t \times I \times V_{eff}} \tag{1.1}$$

where C_{system} is the RFB system cost; $U_{electrolyte}$ is the cost per unit capacity ($ per Ah) of electrolyte, which includes the electroactive elements and supporting electrolyte, U_{stack} is the cost per unit geometric area ($ m^{-2}) of the stack, which includes bipolar plates, membranes, and electrodes ;V_{eff} is the effective cell voltage during discharge; t is the duration of discharge at V_{eff}, in (h); and I is the cur-

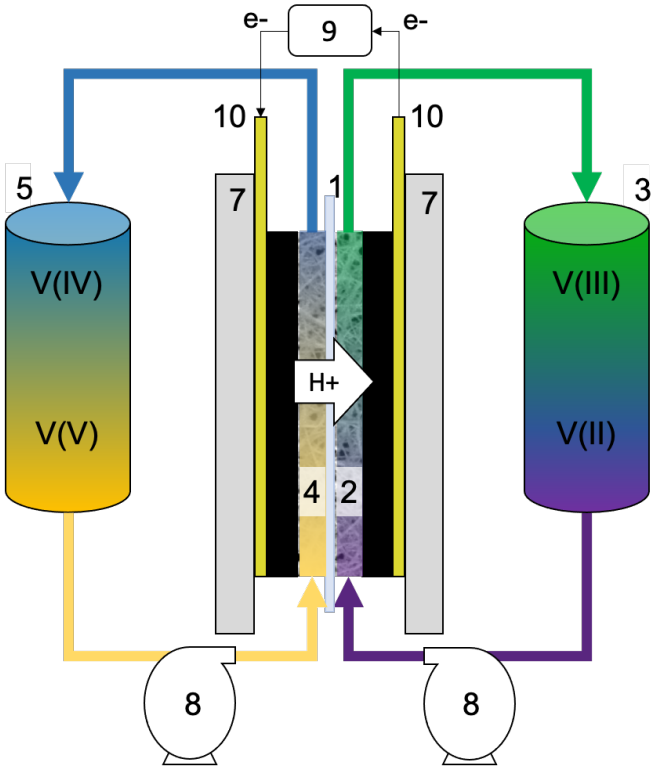

Figure 1.5: Schematic of a single cell VRFB (discharging): (1) Ion exchange membrane (2) anode (3) anolyte tank (4) cathode (5) catholyte tank (6) graphite flow fields (7) end plates (8) pumps (9) load (discharge) / source (charge), (10) current collectors

rent density (mA cm^{-2}). In the broad context of lowering system costs the VRFB electrode research focuses on **maximizing the effective discharge voltage in vanadium redox flow battery (VRFB) systems** by reducing parasitic losses at the anode.

VRFBs are a type of redox flow battery which utilizes vanadium as the electroactive chemical at both the anode and the cathode (Figure 1.5). For secondary batteries, the nominal anode-cathode distinction is kept with conventional battery terminology associated with the discharging process, where the negative electrode is referred to as the anode and the positive is referred to as the cathode [14]. Using this convention, it is likewise convenient to refer to the electrolyte that flows through the cathode as the catholyte and the anolyte through the anode.

1.2 Literature Review

Thermodynamic equilibrium for a half-cell of a reversible electrochemical reaction is described by the Nernst equation [20].

$$E = E^{0'} + \frac{RT}{nF} log\left(\frac{C_O}{C_R}\right) \tag{1.2}$$

where the formal potential $E^{0'}$ is the potential of the half-cell when the ratio of oxidized and reduced species is unity. Clearly from equation 1.2, when the ratio of the reactants is unity ($C_O = C_R \ \rightarrow log(1) = 0$), the potential ($E$) is equal to formal potential. For the anode of a VRFB system this potential is around -.26 V vs. a standard hydrogen electrode (SHE).

$$V^{+2} \underset{charge}{\overset{discharge}{\rightleftharpoons}} V^{+3} + e^- \ ; \text{ E = -.26 V vs. SHE} \tag{1.3}$$

Likewise the formal potential for the cathode is around 1.0 V.

$$VO_2^+ + 2H^+ + e^- \underset{charge}{\overset{discharge}{\rightleftharpoons}} VO^{2+} + H_2O \; ; \; \text{E = 1.0 V vs. SHE} \tag{1.4}$$

The potential across a cell composed of these two half-cells, then, is the difference between the cathode and anode potentials.

$$E_{cell} = E^{0'}_{cathode} - E^{0'}_{anode} + \frac{RT}{nF} \log \left(\frac{C_{VO_2^+} \cdot C_{V^{2+}}}{C_{VO^{2+}} \cdot C_{V^{3+}}} \right) \tag{1.5}$$

For VRFBs this value is around 1.26 V at 50% SoC. The Nernst equation has very low sensitivity with respect to SoC ($\frac{\partial E}{\partial SoC}$) over much of the SoC window and this sensitivity is minimized at 50% ($\frac{\partial^2 E}{\partial SoC^2}\big|_{SoC=50\%} = 0$), which means that small variations in the voltage in this vicinity can correspond with large variations in the SoC. Figure 1.6 shows the Nernst equation and its sensitivity with respect to SoC plotted as functions of SoC.

At 50% SoC the sensitivity of the Nernstian voltage to SoC is ~2 mV $\%^{-1}$ and is below 5 mV $\%^{-1}$ from ~12% to ~88%. For this reason, the open circuit voltage is a relatively low fidelity quantification of the electrolyte composition over most of the SoC range, however, it is a strong indicator of very high (~100% and very low (~0%) SoCs.

A discrepancy between this theoretical value at 50% SoC (1.26 V) and what is often measured experimentally (1.43 V) exists, which several researchers have attempted to rectify. Knehr *et al.* suggested incorporating both the proton concen-

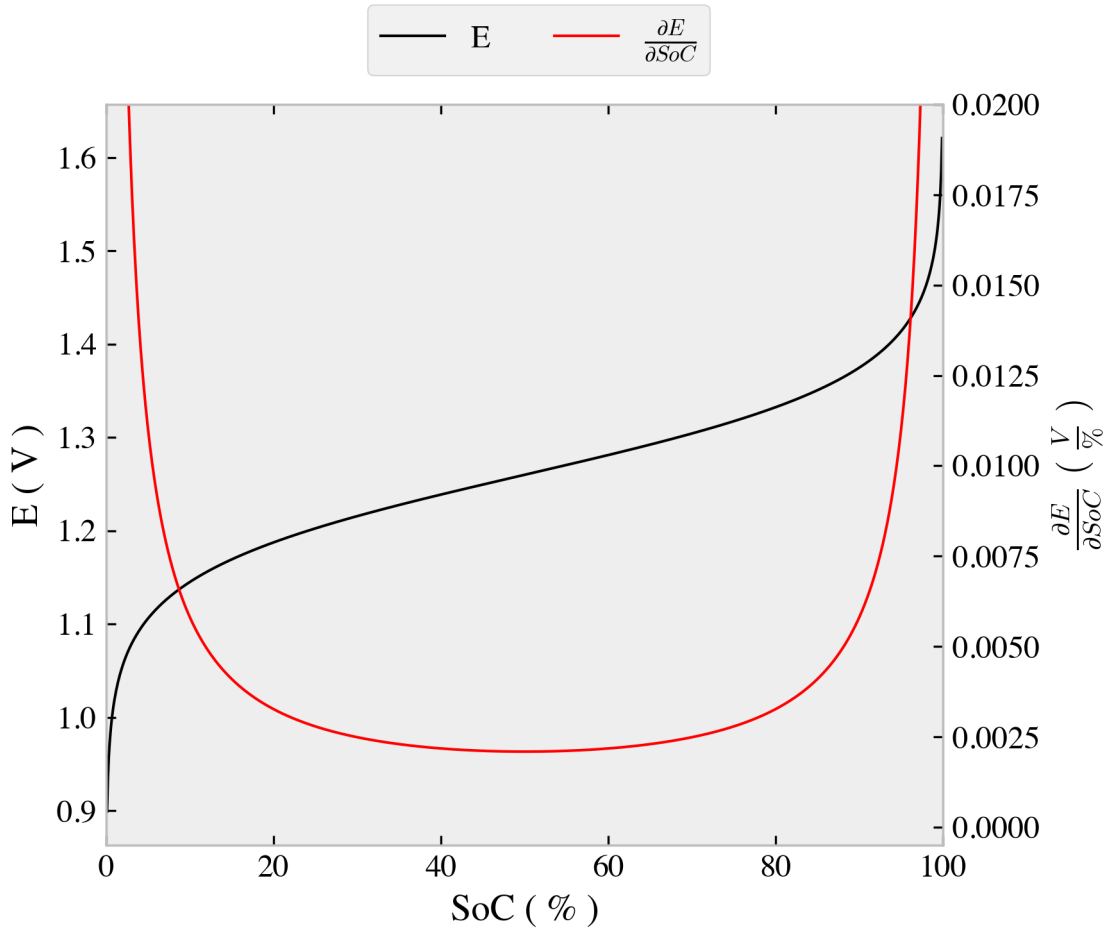

Figure 1.6: The Nernst equation (1.2) for the VRFB and its sensitivity with respect to SoC as a function of SoC.

tration at the cathode (see Equation 1.4) and the Donnan potential (a potential that manifests from unequal proton concentrations at the membrane interface) into the Nernst formulation to arrive at a *complete* Nernst equation (Equation 1.6).

$$E_{cell} = E^{0'}_{cathode} - E^{0'}_{anode} + \frac{RT}{nF} \log \left(\frac{C_{VO_2^+} \cdot C_{V^{2+}} \cdot (C^+_{H^+})^2 \cdot C^+_{H^+}}{C_{VO^{2+}} \cdot C_{V^{3+}} \cdot C^-_{H^+}} \right) \tag{1.6}$$

Here, the superscript for the proton concentrations refer to cathode (+) and anode (-) respectively. Several others [21, 22] have proposed modifications to the Nernst equation which bring the voltage closer to the common experimental value by incorporating water at the cathode (see Equation 1.4).

$$E_{cell} = E^{0'}_{cathode} - E^{0'}_{anode} + \frac{RT}{nF} \log \left(\frac{C_{VO_2^+} \cdot C_{V^{2+}} \cdot (C^+_{H^+})^2 \cdot C^+_{H^+}}{C_{VO^{2+}} \cdot C_{V^{3+}} \cdot C^-_{H^+} \cdot C^+_{H_2O}} \right) \tag{1.7}$$

These three models of thermodynamic equilibrium are shown in Figure 1.7.
This thermodynamic picture is a requirement for any kinetic theory, which must recover and agree with this representation in the limit of equilibrium [20]. For this reason, many models demonstrate the agreement between.

In electrochemical systems polarization refers to departure from the thermodynamic equilibrium potential, that is caused by the passage of current. Overpotential specifically refers to the magnitude of this drop in potential, which is manifested by resistance to current flow [23]. There are three primary sources of parasitic losses (overpotential) in VRFBs: ohmic, activation and concentration. Ohmic overpotential refers to the components of the overpotential which obey ohms law (V=IR) [24]. These components include the membrane, bipolar plates, wires, cur-

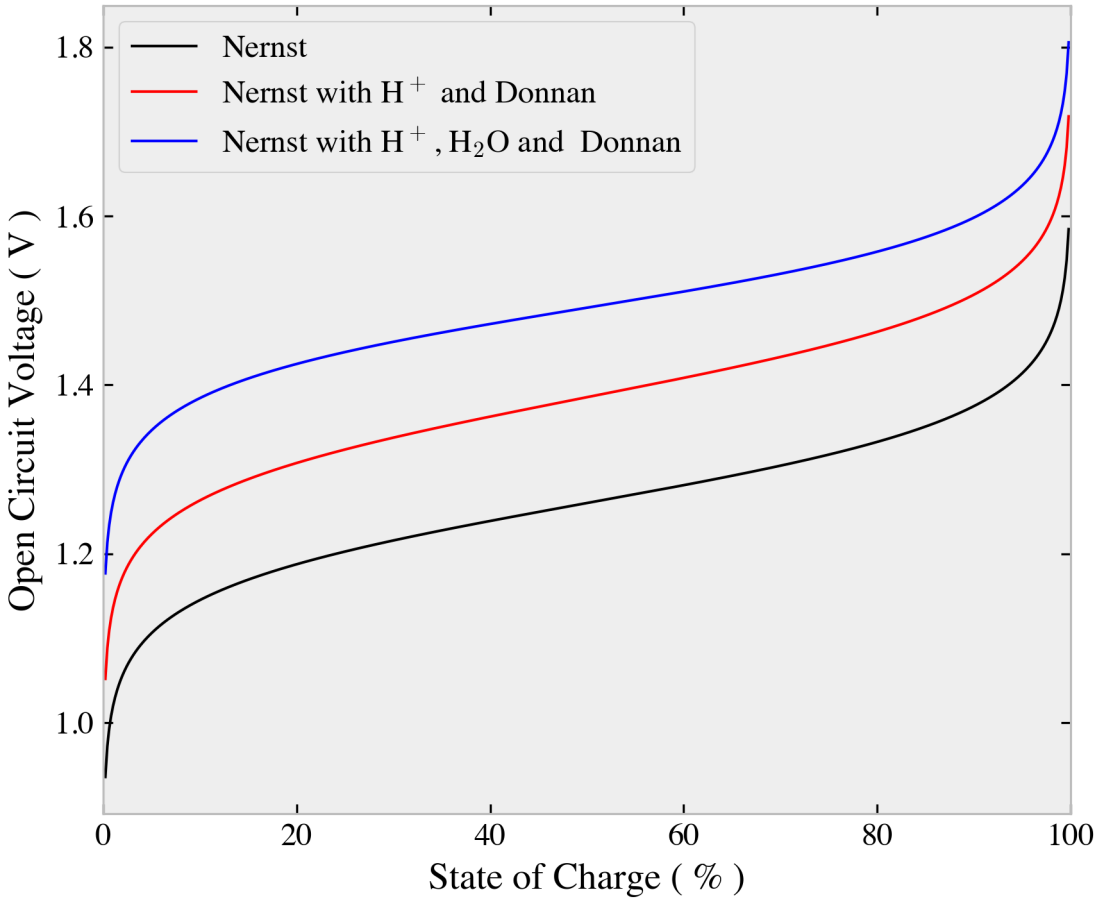

Figure 1.7: Three variations of the Nernst equation for the VRFB

rent collectors and electrode thickness. The activation overpotential, also referred to as charge transfer overpotential refers to the components of overpotential associated with kinetics, such as rate constant, exchange current density and electrochemical surface area [20]. Last, the concentration overpotential, which is also referred to as diffusion resistance is associated with the components of overpotential associated with mass transfer of charge carrying species to the electrode surface. The operating parameters that affect this overpotential component are the electrode porosity/permeability, the flow rate and the concentration of electroactive species [23].

1.2.1 Electrodes

Electrodes in VRFB systems play a central role in affecting the magnitude of each of the aforementioned overpotential components. Ideal VRFB electrodes must [25]:

1) Not be consumed in the reaction

2) Be stable in low pH environments

3) Be electrochemically stable inside the window of operating potential

4) Have high electrical conductivity

5) Be sufficiently permeable for electrolyte flow

In general, carbon-based papers and felts have been identified to satisfy these requirements most readily and have been the primary electrode material in VRFBs. A great deal of research has been performed on modifications and treatments to VRFB electrodes which can be generally categorized into three groups: 1) chemical/thermal treatments 2) doping with metals and 3) deposition of nanoscale carbon materials (e.g. graphene, carbon nanotubes). The goals of these treatments

are typically to enhance the kinetic activity of the electrode surface by catalyzing the reactions e.g. [26–28], or increasing the electrochemical surface area to provide more sites for reactions [29–31] typically by the addition of oxygen containing functional groups [32].

Studies on electrode kinetics for VRFBs have tended to focus on the cathode / catholyte e.g. [33–35], which is motivated by early speculation that the more complex reaction at the cathode (equation 1.4) was more kinetically limiting [36]. This inspired much of the early work on VRFBs electrode modifications to focus on improving the cathode kinetics particularly by the introduction of oxygen functional groups to facilitate the assumed rate limiting step of the positive reaction. Recently, however, the assumption of poor kinetics at the cathode has become debatable.

Fink *et al.* reported that the electrode composition determines which half-cell's rate constant is higher [37]. Recently, in the context of in-situ experiments with polyacrylonitrile (PAN)-based porous electrode in a full cell, results have generally indicated that the kinetics at the cathode are not limiting and are in fact highly superior to those at the anode [38–40]. Recent work has done in the field of developing electrode treatments and diagnostics for experimentally screening electrodes and delineating the sources of losses [41].

Treating of activated carbon via ammonia at elevated temperature, is a known method for introducing amine (amination) groups into porous carbon [42]. This is typically undertaken at temperatures below 500 °C. At higher temperatures ammonia treatments can induce etching as well as substitution of nitrogen into graphene layers to form pyrrole and pyrridine [43]. These methods are tangential

to VRFB research, but of importance to the proposed work.

Graphene quantum dots (GQDs) are a material that has gained popularity in recent years on account of the environmental friendliness of their synthesis technique (not including fluorescent semiconductors). GQDs are pieces of graphene (with particle sizes ranging from 3 nm to 20 nm) consisting of no more than 5 layers [44]. A solid-phase-microwave-assisted (SPMA) technique has been demonstrated by Gu and co-workers, that was used to synthesize N-doped GQDs and graphitic carbon nitride (g-C_3N_4) [45]. These GQDs exhibited attributes, which are favorable in VRFB systems e.g. improved wettability and improved electrical conductivity [46, 47].

1.2.2 Electrolyte

VRFB electrolyte composition dictates the separator conductivity, solubility of vanadium and the degradation rate of the electrode membrane and is therefore a central aspect of VRFB optimization and the topic of much research. Vanadium solubility is a function of both temperature and supporting electrolyte concentration and currently state-of-the-art flow batteries with sulfuric acid supporting electrolyte have vanadium concentrations in the range of 1.7 - 2M V in 4 - 5M H_2SO_4 [48]. Solubility is the primary parameter in determining the volume specific energy of VRFB electrolyte [49] and is, therefore, directly proportional to the footprint of a VRFB system. Several approaches have been taken to increase the solubility of vanadium, such as using mixed acid (sulfuric and hydrochloric) electrolyte [50], as well as using stabilizing agents such as polyacrylic acid [51] and potassium sulfate [52]. Concentrations as high as 3M have been achieved with

these approaches. Recently Mousa *et al.* investigated the precipitation mechanisms for V(III) and V(II) and reported that vanadium in both oxidation states (II and III) followed a first-order rate law for stagnant solutions. It was also reported that the activation energy increased for stirred solutions of V(III) and measurements indicated that upon stirring, that the precipitation process followed a second order rate-law [53].

Because electron transfer between the solution and electrode occurs by quantum mechanical tunneling, it is essential for the solution to be in extreme proximity to the electrode surface (10-20 Å) [54]. The primary roles of supporting electrolyte are dissolving the electroactive species and making the distance between the electrode surface and the charge carrying species is as small as possible in order to ensure that the gradient in potential (solution - electrode interface) is as small as possible. Supporting electrolytes also affect proton mobility in the membrane phase and the solution phase as well as the viscosity [55]. Sulfuric Acid (H_2SO_4) is the most commonly used supporting electrolyte in the VRFB literature (high conductivity, low capital costs). Most work on VRFBs has utilized aqueous electrolyte, however Liu *et al.* researched a non-aqueous VRFB electrolyte (vanadium acetylacetonate/acetonitrile) and were able to increase cell voltage by about 60% [56]. For electrolytes with aqueous solvents, the cell voltage range is restricted by the voltage window in which water is stable, this limits the maximum energy density of RFBs, which is proportional to the voltage of the cell. This is the primary reason for interest in non-aqueous electrolytes, however these systems tend to suffer from higher area-specific resistance (ASR) relative to aqueous solvents [16, 57].

1.2.3 Bipolar Plates

Bipolar plates in VRFB systems provide mechanical strength and channeling for fluid flow while also serving as a circuit component which electrons traverse during charge and discharge. Ideal bipolar plates (BPP) in VRFB systems should posses the attributes of impermeability to electrolyte leakage, high electrical conductivity to reduce ohmic resistance, mechanical stability to maintain stack geometry, and high chemical resistance to potentially corrosive electrolytes. [58]. The three primary types of BPPs that have been researched in literature are graphite, composite and metallic [59]. Graphite is the most commonly used BPP material in the literature for lab-scale work, however the difficulty of forming combined with is poor flexural strength make it unattractive as BPP material for VRFB stacks [60]. Composite plates are often primarily composed of a graphite matrix that is combined with fillers and epoxy resin in an effort to increase conductivity e.g. [61] or improve other aspect relating to permeability e.g. [62] or mechanical flexural strength [60]. While metallic bipolar plates can satisfy the need for high electrical conductivity and mechanical strength, resistance to corrosion is a significant problem [63] that renders most metals without proper treatments and coatings unsuitable for VRFBs. Although adequately stable in the corrosive conditions of an operating VRFB, Satola *et al.* observed that graphite and composite BPPs with can suffer from corrosion and damage when exposed to electrolyte at high state of charge [64]. In consideration of equation (1.1) the bipolar plates contribute to the overall system costs in category of stack components. It is in this context

that research is motivated to find composite BPP materials that are more easily formed than graphite but have similar conductivity and general corrosion resistance e.g. [65]. It is also desirable at stack-scale for VRFB BPPs to have sufficient flexural strength that fracture upon assembly or transportation of a system does not occur. Liao *et al.* developed novel BPP material which improved flexural strength to 48 MPa nearly double the target set by DOE (25 MPa) by supplementing a graphite-epoxy mixture with CF3 carbon fibers [60]. Tantalum has been demonstrated as a viable bipolar plate in high temperature electrolyzers operated over a variety of voltages [66] as well as in various industrial processes which necessitate materials, which can process highly corrosive media [67]. While companies such as Tantaline have suggested that their tantalum plating technology will enable corrosion resistant flow battery materials [68], there has not been a demonstration of the performance and corrosion resistance in the presence of vanadium electrolyte or operating potentials for VRFBs.

1.2.4 Degradation / Durability

In order for VRFBs to be viable options in the space of grid level energy storage they must be able to exhibit durability as they are expected to see usage for up to 10 years and potentially undergo thousands of charge/discharge cycles [15] Capacity fade is a type of degradation that occurs in all secondary batteries, in which the available capacity of the electrolyte diminishes over repeated charge-discharge cycles [69]. With the all-vanadium chemistry this form of degradation is reversible by remixing the electrolytes into a single solution and then separating the homogeneous solution back into the respective electrolyte reservoirs. This process does

result in, effectively, a complete discharge of the battery i.e. a temporary loss of the usable energy, however the electroactive species are conserved when undergoing this process, which means that while the electrolyte may need to undergo maintenance, the vanadium (which is one of the two most expensive components of VRFB systems) should last indefinitely and can be recharged once the solutions have been separated.

Crossover is a phenomenon which is the primary cause of capacity fade, and is caused by imperfect selectivity and permeability of ion exchange membranes. Water and undesirable charged ions are therefore able to penetrate the membrane and move to the other side as a result of the various gradients (e.g. concentration of electroactive species, sulfate, proton concentration) that exist across the cell and imperfect selectivity. Investigations of different membranes on the basis of ionic conductivity, selectivity and stability have been performed [70] as well as modeling of transport of active vanadium species across the membrane [71].

In recent years, several novel methods have been developed to bypass the problem of capacity fade such as using a hydraulic shunt which connects the two electrolyte reservoirs and disallows for an accumulation of water and ionic species on one side of the battery [69, 72]. Another novel method for VRFB capacity fade mitigation involves battery polarity inversion [73]. This method involves completely switching the role of anode and cathode i.e. increasing the oxidation state of the anolyte until it is the catholyte and conversely with the catholyte. Rudolph and co-workers found that this mitigated passivation caused by V^{+2} at the negative graphite plate surface and decreased cell internal resistance by a factor of 2,

resulting in higher capacity retention. Irreversible degradation in VRFB systems can manifest itself in a variety of ways (decrease in membrane and/or electrode conductivity), and must be disentangled from capacity fade specifically and even more generally from effects of exposure to VRFB electrolyte. As electrodes degrade in VRFBs it can cause the cell to reach the cutoff voltage for charging / discharging at a faster rate effectively reducing the useful capacity of the battery [41]. These effects have also been investigated by Derr and co-workers [74].

1.2.5 VRFB parameter estimation

Parameter estimation (inverse modeling problem) is most often done via ex-situ experiments e.g. (cyclic voltammetry [75], electrochemical impedance spectroscopy [30], materials characterization [76]). These are the data that inform modelers of the relevant parameters involved in simulating the physics of full VRFBs. Recently in-situ experimental methods have proven fruitful in determination of kinetics parameters [39, 77]. While these developments in VRFB experimental diagnostics are desirable, in that they are expected to be more representative of the parameters in an operating VRFB, convolution of other phenomena (beginning-of-life-degradation, multiple electrochemical interfaces) begin to occur at this scale.

1.2.6 VRFB modeling

Cell level VRFB modeling has generally been performed via multi-physics software packages where the interactions between mass transport phenomena and redox chemistry are resolved in a continuum e.g. [78–80]. Recently work has been done towards modeling RFBs at stack-scale in this manner [81, 82]. A more recent development in materials modeling has emerged in recent years when networks

of pores in an electrode are modeled e.g. [83, 84]. This type of modeling, known as pore network modeling (PNM) has been demonstrated with fuel cells and more recently with RFBs [85]. One of the primary benefits of PNM modeling is that, as opposed to volume-averaged models, which simulate electrochemical processes inside a continuum domain, PNM modeling distinguishes between solid electrode and liquid phase electrolyte, which highlights the critical impact of electrode geometry on performance [86]. While these methods have become popular recently there is one significant limitation to this approach which is the lack of experimental data for verification and validation of models [87].

Lattice Boltzmann models (LBM) are a class of numerical models which can be used to simulate (among others) fluid flows, mass transfer, heat transfer and many niche physical phenomena which occur in these fields [88]. LBM have been used to model pore-scale phenomena and in this context can be used to compute fluid and mass transport in PNMs. LBM is an explicit method that can be easily parallelized and has certain advantages over conventional conservation methods (finite difference and finite volume) the most prominent of which is its implementation of boundary conditions. The ease of implementing boundary conditions to arbitrarily shaped domains, is one of the greatest strengths of LBM [89]. Bounce-back boundaries can be used as no-slip boundary conditions for fluid flow as well as zero-flux boundary conditions for mass transfer [90]. The boundary conditions implementation method coupled with the ease of parallelization make LBM attractive for modeling electrochemical systems, which are often restricted to mass transfer in geometrically complex domains such as porous media. Indeed, LBM

has found a wide range of uses in the field of electrochemistry. Kang *et al.* derived a multi-component reactive boundary for LBM that has been utilized by others in the fuel cell, lithium battery and flow battery literature e.g. [85,91–94]

1.3 Objectives

Sluggish kinetics of PAN-based carbon felt anodes in VRFBs present a significant limitation to the commercialization of VRFB systems and a broad target for system improvement. Though there is no shortage of work that has been performed on improving kinetics of electrodes in VRFB systems, the work has tended to focus on the cathode. Likewise, EIS abounds in the literature with little care towards the interpretation of results. Based on these gaps in the literature, the objectives of this dissertation are:

1. Identify the viability of GQDs for improving kinetics and likewise to understand the durability of this modification.

2. Evaluate the impact of ultra-fast laser ablation on lowering the overpotential at the anode.

3. Probe impedance model sensitivity in the context of a series of treatments based on monte carlo simulations.

4. Evaluate the impact of graphitic bipolar plates on in-situ EIS measurements.

5. Elucidate the impact of electrolyte composition and state of charge on in-situ kinetics measurements.

6. Identify the interaction between pumping losses and limiting current in a power-flexibility analysis.

7. Identify the interaction between pumping losses and limiting current in a power-flexibility analysis.

8. Establish a micro-scale two-dimensional lattice Boltzmann model of a VRFB flow battery anode.

These contributions to the literature are intended to both highlight methods to enhance anodes and to demonstrate more rigorous methodologies for modeling approaches in VRFB systems. While these are not the only barriers to commercialization of VRFB systems, they represent an obstacle, of which overcoming is the purpose of this dissertation.

Chapter 2

Impedance Model Specific Parameter Estimation of Treated Carbon Felt Electrodes in Vanadium Redox Flow Batteries

This article has been submitted to the Journal of the Electrochemical Society (JES) under the same name as the title of this chapter and is currently under review. Its authorship is attributed to M. C. Daugherty, A. M. Pezeshki, R. L Sacci, D. S. Aaron, and M. M. Mench. Sacci, Aaron and Mench assisted with manuscript revisions, Pezeshki collected data. I reduced the data and composed the manuscript.

Abstract

The influence of chemical and thermal modification of carbon felts for use as anodes in the all-vanadium redox flow battery is presented in this work. Electrochemical impedance spectroscopy (EIS) with a symmetric cell was used to resolve the sources of overpotential and to quantify kinetic parameters for deeper insight into performance variation as a function of electrode pre-treatment. EIS data were analyzed with three different models: a Randles circuit over the full spectrum, a Randles circuit over a low pass spectrum and a macrohomogeneous porous electrode model. Monte Carlo simulations were utilized to investigate the impact of fitting error on parameter estimation. It was found that the macrohomogeneous porous electrode model and the low-pass Randles circuit share much of their parameter estimation distributions when the complex decay length is greater than or equal to the thickness of the porous medium. When the decay length is lower than the thickness, the parameter distributions become more exclusive as the distributed porous resistance and the charge transfer resistance begin to merge. An electrode pre-treatment involving an ammonia atmosphere at elevated temperature exhibited a dramatic improvement in kinetic performance corresponding to

an increase in electrochemical surface area of 180× greater than untreated carbon felt.

2.1 Introduction

The electrode in redox flow batteries (RFB) plays a central role in determining the ohmic, charge transfer, and concentration polarization. The cell architecture, electrode thickness, electronic conductivity, porosity, and ionic conductivity of the electrolyte solutions determine the distributed ohmic resistance through the electrode structure [38, 39, 95, 96]. The electrode surface area and activity toward a given redox reaction determine the charge transfer resistance while morphology plays an important role in determining concentration polarization. Characteristics of optimal electrodes include: large surface area, excellent activity, low ionic resistance, formation of low-resistance contacts, and an open pore structure with high permeability to maximize transport and mixing of reactants.

Vanadium redox flow batteries (VRFBs), commonly employ porous carbon materials as the electrode material. Rate constants ranging from 10^{-3} to 10^{-6} cm s^{-1} have been reported in the literature depending on the type of base-line carbon material used and which reaction is being investigated (V^{2+}/V^{3+} or VO^{2+}/VO_2^+). As such, there are conflicting reports as to the anode or cathode being limiting [37]. In the last 4 years, studies have suggested that the anode is more limiting (for polyacrylonitrile-based carbon felt), where exchange currents can be a factor of 40 lower than that of the cathode [39, 77]. Many works have studied the implementation of one and two-dimensional carbon materials (carbon nanotubes and

graphene) for their ability to increase surface area and facilitate kinetics; others have studied the impact on kinetics that doping with metal-based catalysts can provide [27,28,97–100].

Another method to facilitate kinetics has targeted improving the activity of the electrode surface through thermal, chemical, and radiation treatments [31,32,101–106]. Electrode modifications of this kind target the addition of oxygen-containing functional groups to the carbon surface. The effect of these groups, however, may differ between the anode and cathode where a study has suggested that they hamper the anode while improving the cathode [37]. There have also been electrode modification studies which specifically target improving electrode permeability and not surface-level morphology or electrochemical surface area [107].

Electrochemical impedance spectroscopy (EIS) is a commonly used technique in electrochemistry, which can give insights into each of the sources of losses (overpotential). Macdonald and co-workers [108] have used Monte Carlo simulations to estimate the precision of EIS fitting parameters by successive use of complex nonlinear least squares (CNLS) fitting. Their work demonstrated that there are certain limiting cases where CNLS is inadequate for parameter estimation depending on the model used and the error. Three primary sources of error are present in EIS data which constitute the difference between an experimental and a calculated impedance: *stochastic* (random) errors intrinsic to an experiment, *bias* errors which arise from artifacts in the instruments and *fitting* (model) error which is present from the use of an incorrect model [109].

The goal of this work is to quantify the impacts of a series of electrode modifi-

cations on a material with respect to parameter estimation. EIS is applied to understand the effect of electrode treatments on physical parameters determined by three related impedance models on the treated felts in VRFBs using Monte Carlo simulations. These simulations accentuate the fitting or *model* based error structure and give insight into the appropriate conditions for model selection.

2.2 Methods

2.2.1 Treatments

The control material for the current study was untreated GFD3 carbon felt (SGL, GmbH). The pretreatments that were utilized are listed in Table 2.1 where their associated abbreviations (used throughout the text) are listed alongside a brief description of the reactant, thermal, and temporal conditions. Heat treatments were performed in a quartz tube furnace (Lindberg/Blue M) which was purged for one hour with N_2 at 200 ml min^{-1} before the reactant gas began flow. The treatment atmosphere was flowing at a rate of 200 ml min^{-1} both during the approach to the set point temperature and for the duration of the hold time. For each treatment, the temperature began at room temperature and increased to achieve the set point after two hours (i.e. the ramp rate for HtO differed from that of Am4). Thermal treatments in oxidizing environments have been shown in the literature both as a standalone treatment and as a precursor for other treatments e.g. [29, 31, 36, 110, 111]. The nitrogen treatment was a control for the 900°C with ammonia to isolate temperature from treatment atmosphere.

Table 2.1: Electrode treatments

Treatment type	**Abbreviation**	**Reactants**	**Temperature°C**	**Hold time**
Untreated	Raw	-	-	-
Nitric Acid Soak	NAS	HNO_3	Ambient	10 minutes
Hydrothermal	HyA	1:3 HNO_3 | H_2SO_4	80	1 hour
Hydrothermal	HyB	1:3 HNO_3 | H_2SO_4	60	1 hour
Heat treat	HtO	42% O_2 | 58% N_2	400	15 hours
Heat treat	HtN	N_2	900	1 hour
Hydrothermal +Heat Treat	Hyt	1:3 HNO_3 | H_2SO_4 +NH_3	80 900	1 hour 4 hours
Heat treat	Am1	NH_3	900	1 hour
Heat treat	Am4	NH_3	900	4 hours

A PTFE-lined autoclave (50 mL Columbia International, HTC230-V50) was used for all hydrothermal treatments at 60°C (HyB) and 80°C (HyA, Hyt). Both hydrothermal treatments utilized a solution comprising 10 mL of concentrated nitric acid (HNO_3; Alfa Aesar, 70%) and 30 mL of concentrated sulfuric acid (H_2SO_4; Alfa Aesar, ACS grade, 96%). Following the addition of the felt to the HNO_3:H_2SO_4 solution, the autoclave was then closed and submerged in a water bath, which was preconditioned to the treatment temperature. The autoclave was given 30 minutes for the internal temperature to climb to the set point and was then held for a subsequent treatment period of 60 minutes. Following the thermal bath, the mixed acid solution was rinsed off of the samples by successive immersion in deionized (DI) water, followed by storage in DI water for 8 hours prior to cell assembly. This pretreatment protocol was based on a previous study where the treatment was performed on PAN-based carbon paper (TGP-H-060) [112].

The nitric acid soak (NAS) treatment was performed by submersion of the felt sample in a concentrated HNO_3 (Alfa Aesar, 70%) solution for 10 minutes. The nitric acid was then rinsed off of the sample by successive rinsing in DI water and then stored in DI water for 8 hours prior to cell assembly. The mixed hydrothermal/heat treatment (Hyt) was a serial combination of the HyA (described previously) and Am4 with an intermediate step between the hydrothermal treatment and insertion in the tube furnace where the electrode was dried at ambient temperature in a vacuum chamber. The protocol for the treatment in the tube furnace was identical to that of the four-hour NH_3 900°C sample (Am4).

2.2.2 Experimental

The cell architecture used in this work was an equal path rectangular flow-through design (see Figure 2.1). Nafion ® 117 was the membrane material used for all testing. The membrane was conditioned in a solution of 1M H_2SO_4 for 30 minutes at a temperature of 80°C. Following immersion in sulfuric acid it was treated in DI water for 30 minutes at 80°C. The base material for all the treatments was GFD3 carbon felt (SGL Carbon). Each experiment consisted of one layer of felt on each half-cell of the battery. In total there were nine samples tested, the eight modified/treated felts and the control (Raw).

For each electrode condition detailed in Section 2.2.1, an electrolyte solution of 0.5 M V / 4 M H_2SO_4 was prepared via dissolution of $VOSO_4$ (Alfa Aesar, 99.9%) in a sulfuric acid (Alfa Aesar, ACS grade) solution. The electrolyte was vacuum filtered through glass fiber filter paper (1 μm pores) with a Büchner funnel to remove impurities [113,114]. A separate charging cell (25cm^2 serpentine) was used to condition the stock solution. The electrolyte was brought to 100% SoC potentiostatically (1.8 V) with 100 mL of electrolyte on the cathode side and 50 mL on the anode side. After achieving 100% SoC, 50 mL was removed from the catholyte followed by coulometrically discharging to 50% SoC (0.25 M V^{2+} / 0.25 V^{3+}). The anolyte solution, which was kept under a nitrogen head space to prevent oxidation, was then circulated through the cell as in ref [39]. All experiments with faradaic reactions were with anolyte flowing in the symmetric cell.

In-situ measurements were performed in a symmetric cell configuration [38,39,

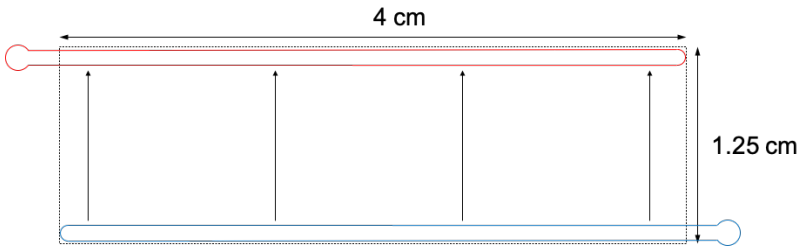

Figure 2.1: Rectangular flow-through flow-field (5 cm^2) schematic. The blue and red channels show the electrolyte inlet and outlet respectively.

77,115,116]. The symmetric cell utilizes a single electrolyte (catholyte or anolyte) on both half-cells of a battery to mitigate crossover effects and maintain a constant SoC. To improve the resolution at lower frequencies, a pulse dampener [39] was integrated into the flow path between the pump and the cell. The two-electrode cell configuration described in ref [39] was used for all measurements with all reported cell voltages being across the whole cell. Spectra were recorded over a frequency range from 50 kHz to 60 mHz with a sinusoidal perturbation of 5 mV. The cell was filled with 50% SoC vanadium solution (.5 M V, 4 M H_2SO_4) to evaluate the beginning-of-life electrochemical performance. SEM images were recorded with a Zeiss Gemini SEM. A non-faradaic impedance spectrum was recorded with the symmetric cell as described previously; however, the anolyte was replaced with 4M H_2SO_4. The use of the non-faradaic spectrum is explained in Section 2.3.2.

2.2.3 EIS data

Fit to physical models

Impedance spectra for each treatment were fit using three different impedance models to account for model bias in parameter estimation. The first model was a Randles circuit fitting the entire frequency spectrum (RFS). The second model was a Randles circuit fitting the spectrum below an approximation of the characteristic frequency (ω_1) referred to as Randles truncated spectrum (RTS). Third was the MHPE model [38,39,95] fitting the entire frequency spectrum. Both of the Randles circuit-based models have the exact same mathematical formulation and only differ in the portion of the spectrum that is used to fit. For this reason, they will not be

distinguished in the following treatment. The Randles circuit for a single electrode is described by the following equation:

$$Z_R = (Z_{ct}^{-1} + j\omega^P Q)^{-1} \tag{2.1}$$

All the symbols are defined in the nomenclature. The charge transfer impedance per unit length (Z_{ct}) at open circuit is given by [38,39]:

$$Z_{ct} = \frac{RuT}{A_t i_0 F} + \frac{RuT}{f A_t F^2 C_R \sqrt{j\omega D_R}} tanh\left(a\sqrt{\frac{j\omega}{D_R}}\right) + \frac{RuT}{f A_t F^2 C_O \sqrt{j\omega D_O}} tanh\left(a\sqrt{\frac{j\omega}{D_O}}\right) \tag{2.2}$$

The macrohomogeneous porous electrode derived by Paasch *et al.* [95] is:

$$\frac{AZ_{MHPE}}{b} = \frac{\rho_1^2 + \rho_2^2}{\rho_1 + \rho_2}\frac{\lambda}{b} coth\left(\frac{b}{\lambda}\right) + \frac{2\rho_1\rho_2}{\rho_1 + \rho_2}\frac{\lambda}{b}\left(sinh\left(\frac{b}{\lambda}\right)\right)^{-1} + \frac{\rho_1\rho_2}{\rho_1 + \rho_2} \tag{2.3}$$

The derivation of Equation 2.3 and the expression for λ are shown in the supplemental materials. λ is defined as the complex decay length (cm), which is a measure of the distance that the ac signal can penetrate through the porous medium at each frequency. The representation of Equation 2.3 in terms of the ratio of the complex decay length to the characteristic length, as previously done by Nguyen and co-workers [96], was deliberate in this case as this ratio determines the transition between finite and semi-infinite length behavior as is discussed in Section 2.2.3. The full cell impedance for both the Randles circuit and the MHPE are calculated

with [39]:

$$AZ(\omega) = AR_{\Omega} + 2A(Z_x^{-1} + j\omega^P Q)^{-1} + Aj\omega L \tag{2.4}$$

where Z_x is substituted with either Z_{ct} or Z_{MHPE}. It should also be clarified that in the derivation for Z_{MHPE} (shown in the supplemental material) the charge transfer admittance per unit length g_{ct} is the inverse of Z_{ct} ($g_{ct} = Z_{ct}^{-1}$) and is a component of the MHPE formulation where its value is embedded in the complex decay length (λ). This distinction highlights the effect of the MHPE model where the impedance response at every frequency is not solely a function of the charge transfer impedance, but a function of the resistivities, the electrode thickness and the complex decay length. For this reason, the same parameters can be fit with each of these models where the supplemental resistivities can be measured ex-situ and are not needed as floating parameters. The double layer capacitance in the presence of CPE behavior is calculated by [117]:

$$C_{eff} = Q^{\frac{1}{P}} \left[\frac{R_{\Omega} R_{ct}}{R_{\Omega} + R_{ct}} \right]^{\frac{1}{P}-1} \tag{2.5}$$

In the case where there are no reacting species at the electrode surface (i.e. $C_R \rightarrow 0$, $C_O \rightarrow 0$) the charge transfer impedance approaches infinity ($Z_{ct} \rightarrow \infty$). In such an instance Equation 2.5 reduces to:

$$C_{eff} = Q^{\frac{1}{P}} R_{\Omega}^{\frac{1}{P}-1} \tag{2.6}$$

Q is calculated as the product of A_t and C_{dl} and is termed the CPE parameter. C_{eff}

being the effective capacitance is then used to calculate the effective surface area by:

$$A_{eff} = \frac{C_{eff}}{C_{dl}} \tag{2.7}$$

The charge transfer resistance is calculated by [20]:

$$R_{ct} = \frac{RuT}{A_t i_0 F} \tag{2.8}$$

This is the first term in Equation 3.2; likewise, R_{fd} is calculated as the sum of the following two terms in Equation 3.2 in the limit as the frequency goes to zero:

$$\begin{aligned} \lim_{\omega \to 0} \frac{\tanh\left(a\sqrt{\frac{j\omega}{D_R}}\right)}{a\sqrt{\frac{j\omega}{D_R}}} &= 1 \\ R_{fd} = \frac{aRuT}{A_t f F^2}\left(\frac{1}{C_R D_R} + \frac{1}{C_O D_O}\right) & \end{aligned} \tag{2.9}$$

The resistive components in electrochemical systems are often specified on a geometric areal basis (i.e. $\mathrm{ASR}_x \rightarrow A_{geometric} \times R_x$). This normalizes the resistances so reactors of different geometric surface areas can be compared directly, and it is the form, which the data in this report are presented.

Frequency Analysis

The characteristic frequency ω_1 is calculated by:

$$\omega_1 = \frac{K}{b^2} \tag{2.10}$$

The ratio of the exchange current density to the double layer capacitance determines frequency k. Refer to [95] for further analysis of characteristic frequencies (the same nomenclature is used in this work). The expressions for both K and k are shown in the supplemental material where their values arise naturally from the derivation of the MHPE model. ω_1 is the frequency which describes the upper bound for the ability of the diffusive front to propagate through the thickness of the porous medium [96]. The selection of the maximum frequency to use for the RTS model was performed by using the K value from the RFS model to estimate the characteristic frequency (ω_1).

The characterization of semi-infinite porosity or qualitatively 'thick' electrodes in impedance is achieved by comparing the complex decay length to the characteristic length b (λ/b). Paasch *et al.* reported the following inequality for determination of $\lambda \ll b$:

$$\begin{gathered} \lambda \ll b \text{ if } \gamma \ll 1 \\ \text{where } \gamma = \frac{\frac{2\omega_1}{k}}{1+\sqrt{1+\frac{\omega^2}{k^2}}} \end{gathered} \tag{2.11}$$

CNLS procedure

All models were used to fit the experimental data with the CNLS method. The sum of squares (S) was minimized for each model:

$$S = \sum_{i=1}^{N} \left[AZ'_{i,exp} - AZ'_{i,model} \right]^2 + \left[AZ''_{i,exp} - AZ''_{i,model} \right]^2 \tag{2.12}$$

For each model there were seven parameters which were allowed to float for fitting: wetted surface area (A_t), membrane area specific resistance (ASR_{mem}), exchange current density (i_0), boundary layer thickness (a), scale factor (f) [38], inductance (L), and constant phase element exponent (P). The fixed parameters for the impedance models are shown in the appendix.

2.2.4 Monte Carlo Simulations

Monte Carlo simulations were performed based on the models' respective biases. The coefficient of variation was calculated for each model for each treatment according to:

$$
\begin{aligned}
c_v &= \frac{\sigma_d}{\mu_d} \\
\sigma_{dReal} &= \sqrt{\frac{\sum_{i=1}^{n}(Z'_{iexp} - Z'_{imodel})^2}{n-1}} \\
\sigma_{dImag} &= \sqrt{\frac{\sum_{i=1}^{n}(Z''_{iexp} - Z''_{imodel})^2}{n-1}} \\
\mu_{d,iReal} &= \frac{Z'_{iexp} - Z'_{imodel}}{2} \\
\mu_{d,iImag} &= \frac{Z''_{iexp} - Z''_{imodel}}{2}
\end{aligned}
\tag{2.13}
$$

The noise added to the impedance at each frequency was selected from a Gaussian distribution with zero mean and coefficient of variation of the respective model ($N(0,c_v)$). The spectra with the added noise were then reduced to give distributions for the fitted parameters.

2.3 Results and Discussion

2.3.1 Complex decay length

Distinguishing between spectra in which the ac signal penetration length (λ) can penetrate to the bottom of a pore is critical for parameter estimation. In cases where the penetration length is very small relative to the pore depth, the double layer capacitance is a function of frequency and cannot be separated from the charge transfer resistance [118]. Equation (2.11) shows the inequality from Paasch *et al.* [95] which qualifies an electrode porosity as semi-infinite. Figure (2.2) shows this value (γ) as a function of frequency over the entire spectrum. The Raw, NAS, HyB and HtN spectra do not satisfy this inequality as the value of γ reaches a value greater than 1. This manifests in the Nyquist plots (discussed in section 2.3.2) for these spectra which have a distinct break between the high frequency content at an angle of $\pi/4$. Spectra of this type admit a straightforward estimation of the characteristic frequency (ω_1) at this breaking frequency.

The spectra for HyA, Hyt, HtO exhibited values of γ in the low frequency content between 0.1 and 1. While these spectra do exhibit some overlapping between the pore resistance (characterized by an angle of $\pi/4$ at high frequency) and the charge transfer, from this test, we fail to accept the conclusion that the porosities are semi-infinite. The shape of these spectra (excluding the diffusion resistance) are qualitatively akin to a lemniscate (see Figure A.1) and the models of these spectra have a higher degree of sensitivity in the fitted parameters relating to capacitance and exchange current density as the charge transfer shape deviates more from a

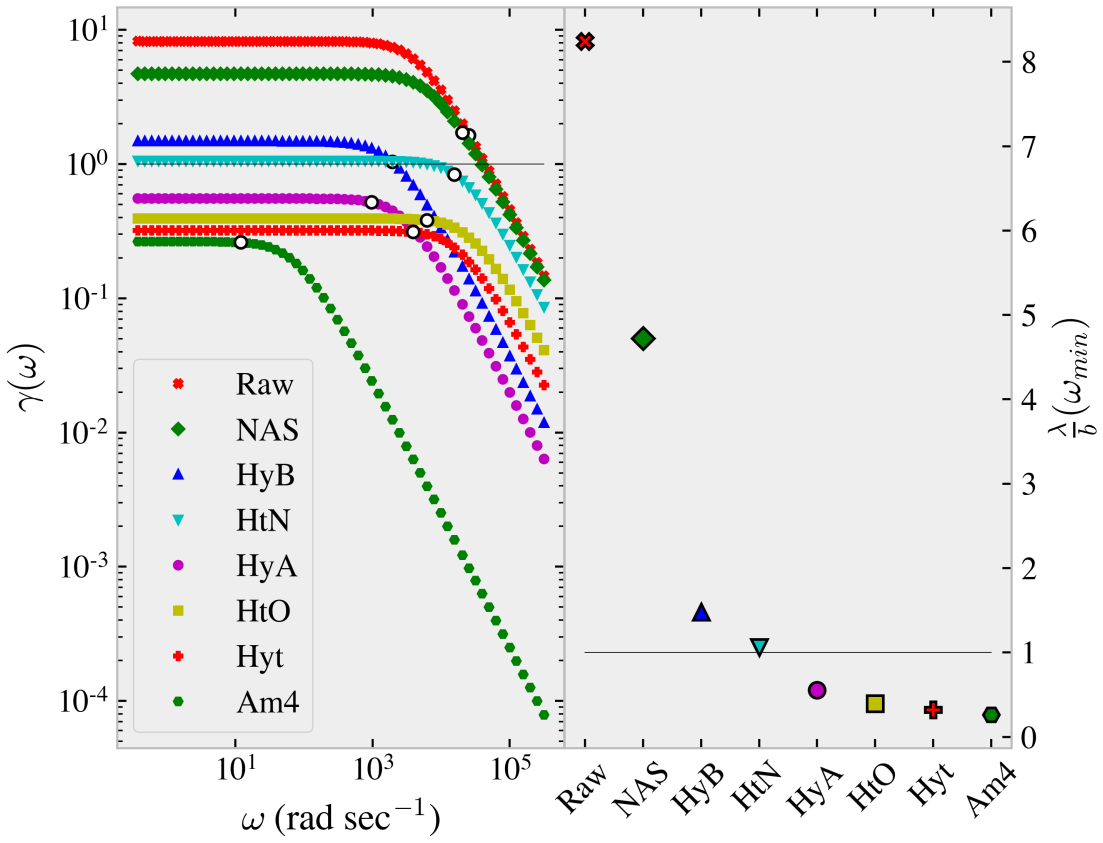

Figure 2.2: Impact of frequency on complex decay length (λ). The left figure shows $\gamma(\omega)$ with ω_1 labeled on each spectrum with a white circle. The right plot shows the ratio of λ to characteristic length b at the lowest measured frequency (ω_{min})

semi-circle. As seen on the right-hand plot of Figure 2.2 the complex decay length is less than b at the minimum frequency for each of these spectra. The spectrum for the ammonia treatment (Am4) has a very low characteristic frequency (2 Hz). Keiser *et al.* studied the effect of different pore geometry on the impedance response, demonstrating the deviation from $\pi/4$ radians as a function of different pore shapes [118]. A quantitative analysis of Am4 is presented later in Section 2.3.2. We speculate that the Am4 treatment has a strong effect on the surface area which becomes available in the recesses of this porosity. This is reinforced qualitatively by the SEM images (Figure 2.3) of the Am4 electrode surface; post-treatment SEM clearly shows the presence of nanopores with diameters below 50 nm.

2.3.2 Monte Carlo Simulations

Monte Carlo simulations were performed with N = 5,000 samples to get a distribution for the fitted parameters based on their respective model parameter estimation sensitivities. This section is divided into two subsections based on whether the parameter γ for an electrode is greater or less than 1 at moderate to low frequency. The results for the different models are shown in a consistent format: the left column shows the best fit for RFS (red), RTS (green) and MHPE (blue) respectively; characteristic frequency (ω_1) is shown as a white circle in all spectra. The column on the right has the different models as its x-axis and box plots for the ohmic, charge transfer and finite diffusion distributions in separate stacked subplots. Electrode analysis will proceed in descending order of maximum γ values from Figure 2.2. Table A.3 shows the aggregated parameter estimations for the charge transfer impedance per unit length (Z_{ct} Equation 3.2). In the case where the

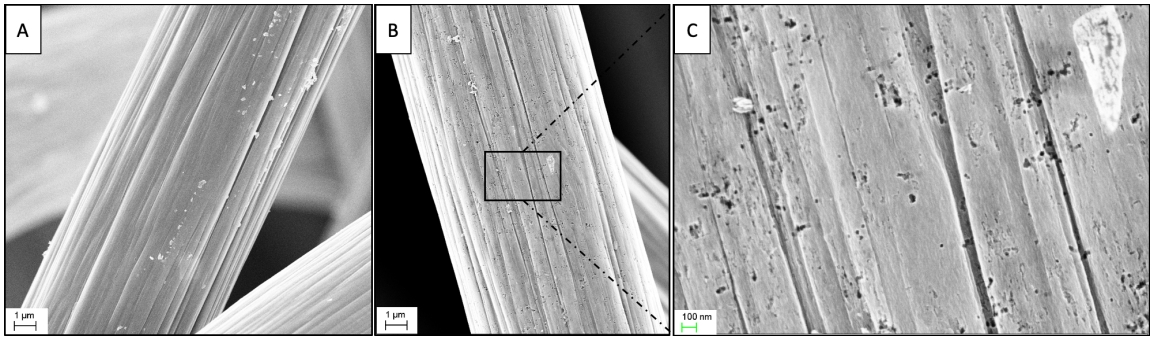

Figure 2.3: SEM Images: (A) Untreated (Raw) GFD3 fiber; (B) Am4 electrode fiber; (C) Inset increased magnification of porosity on fiber surface (fiber diameter ≈ 8 μm; pore diameter ≤ 50 nm)

95% confidence interval exceeds 66% of the mean (i.e. $\sigma > \frac{\mu}{3}$) the results are not shown and the parameter is considered poorly estimated by the model, except for the inductance. This separate perspective of the inductance is reflected in its separation from the other parameters in the table and is elaborated on in Section 2.3.2. The results for the one-hour ammonia treated electrodes (Am1) were qualitatively and quantitatively very similar to Am4 and therefore only the analysis for Am4 is presented here and can be considered to apply similarly to Am1.

$\gamma > 1$

In the case of the untreated electrode (Raw) the models all exhibit a relatively high agreement in terms of the magnitudes of the ohmic, charge transfer and finite diffusion resistances (see Figure 2.4). This low level of sensitivity is due to magnitude of the charge transfer resistance being approximately a factor of four larger than the diffusion resistance and a factor of 14 larger than the ohmic resistance. The basis for comparing the impedance models is the probability of estimating a parameter with the same magnitude between different models. Table (A.3) shows the model fitting parameters estimated with a 95% confidence interval ($2 \times \sigma$). Clearly the impact of the model is minimal for the untreated case and each of the parameters is within the 95% probability distribution of the others. Because of the high number of samples these data have statistically significant differences in their means, but their distributions have sufficient overlap to conclude that this spectrum is insensitive to the model used to estimate its parameters. The Raw electrodes also had both the highest characteristic frequency and the highest ratio

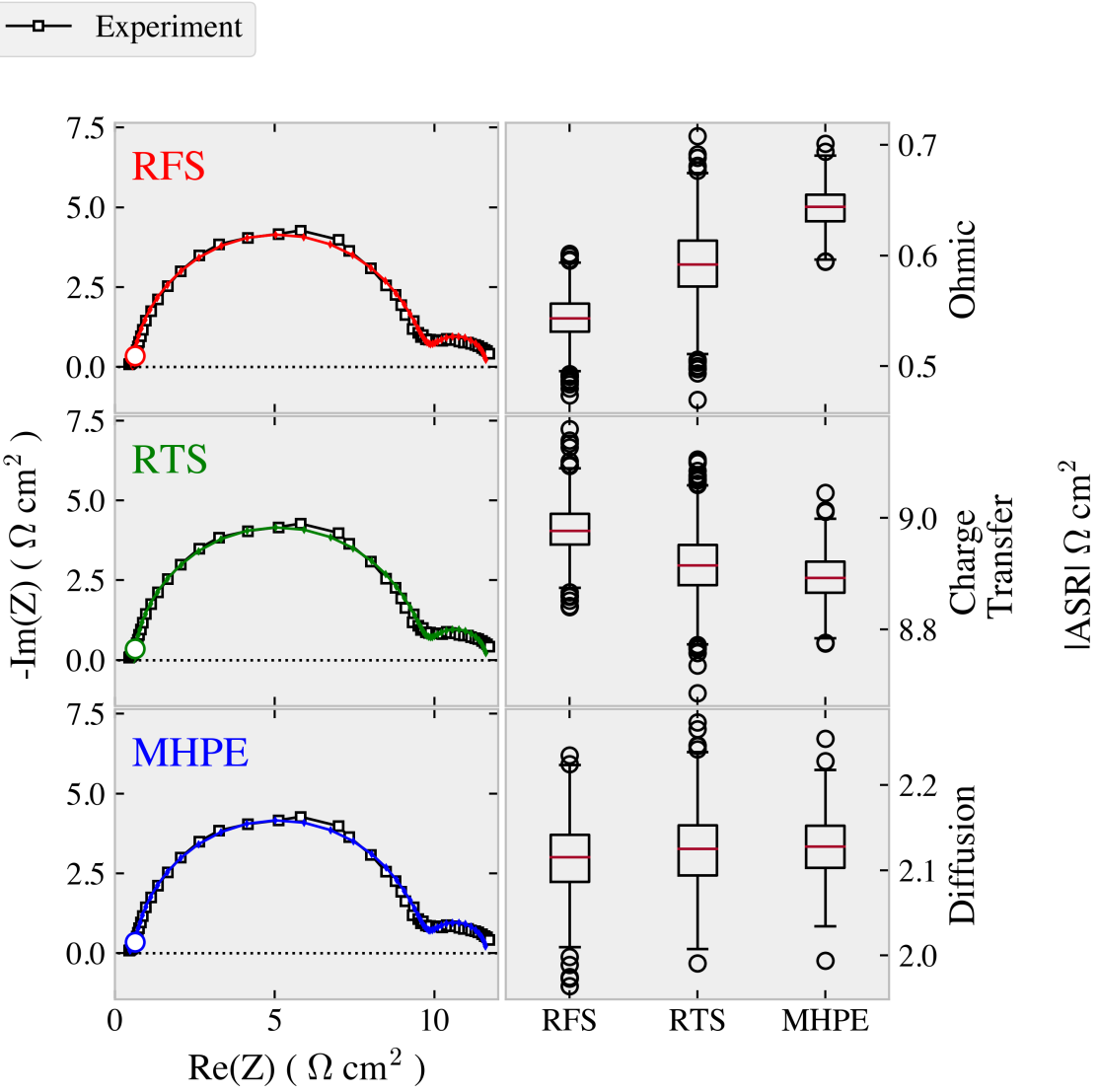

Figure 2.4: Monte Carlo Simulation for untreated (Raw) electrodes

of complex decay length to characteristic length ($\frac{\lambda}{b}$; Figure 2.2).

The nitric acid soaked (Figure 2.5) treatment produces a comparatively modest improvement in the impedance relative to Raw; however, it reduces the charge transfer resistance by almost a factor two and begins to demonstrate the variations in model bias. The RTS and MHPE have very minimal overlap in ohmic resistance (.002%); however, the RTS and MHPE share an overlap of 27% and 28% for the charge transfer and finite diffusion resistance respectively. The MHPE and RFS have mutually exclusive distributions for the ohmic resistance and only an overlap of .03% for the charge transfer resistance. Table A.3 shows that for the NAS treatment using the high frequency begins to affect the parameter estimation non-trivially. The probability distribution for the exchange current density no longer has any overlap between RFS and MHPE. Likewise, for the estimation of the effective surface area, each model converges to an exclusive distribution with relatively small coefficient of variation. It should be noted, however, that the difference between the mean surface area estimated with RTS and MHPE is on the order of 2% and likewise between MHPE and RFS the difference is 5%, which is an acceptable estimate in many instances.

The nitrogen heat treatment (2.6) was performed as a control for the ammonia treatment (Am4). The characteristic frequency ω_1 for HtN was lower than for Raw and NAS, but still relatively high (2245 Hz). As γ becomes smaller, the impact of the model bias becomes more pronounced. In this instance the probability of estimating the same charge transfer resistance and ohmic resistance is effectively

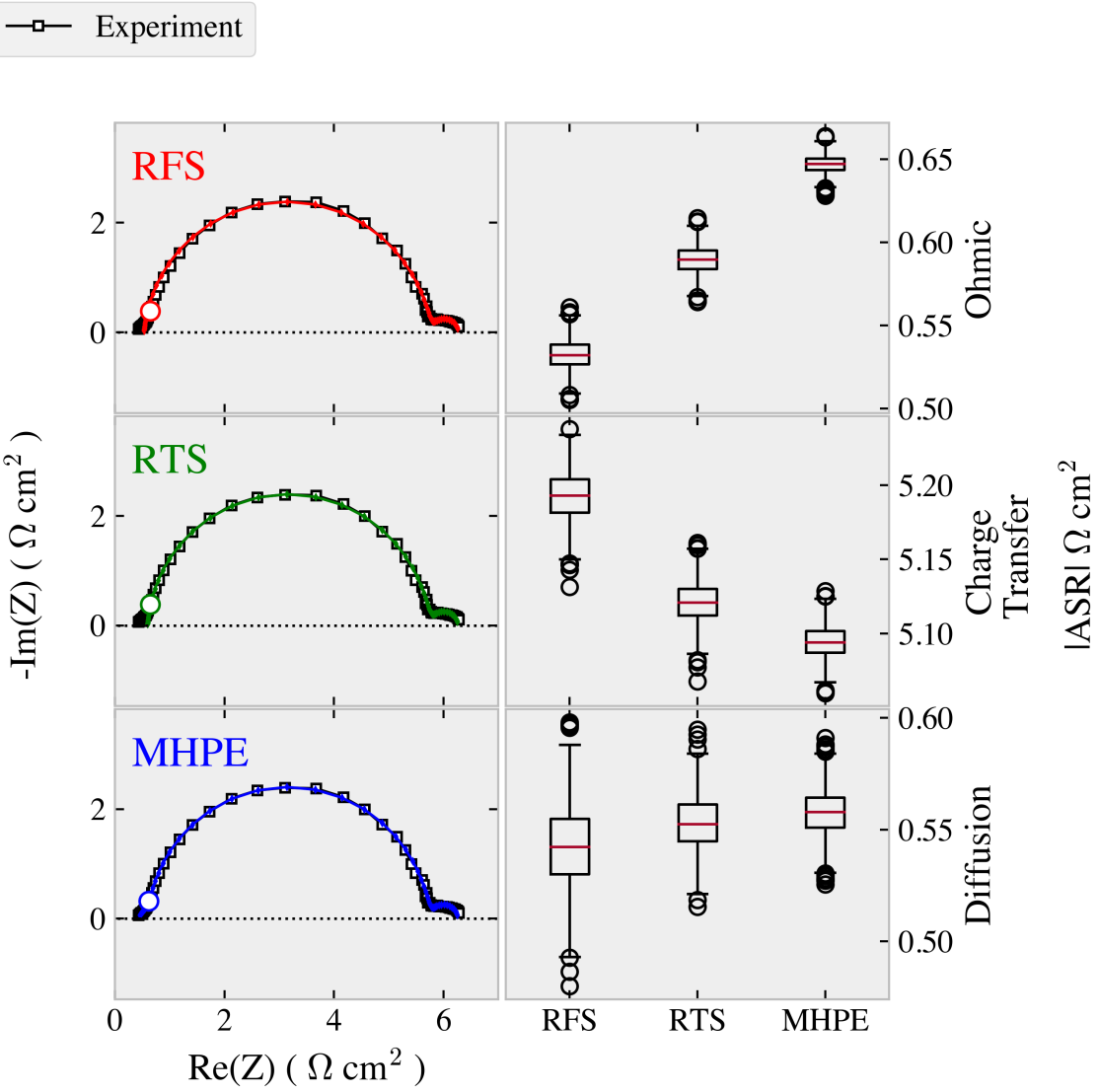

Figure 2.5: Monte Carlo Simulation for nitric acid soaked (NAS) electrodes

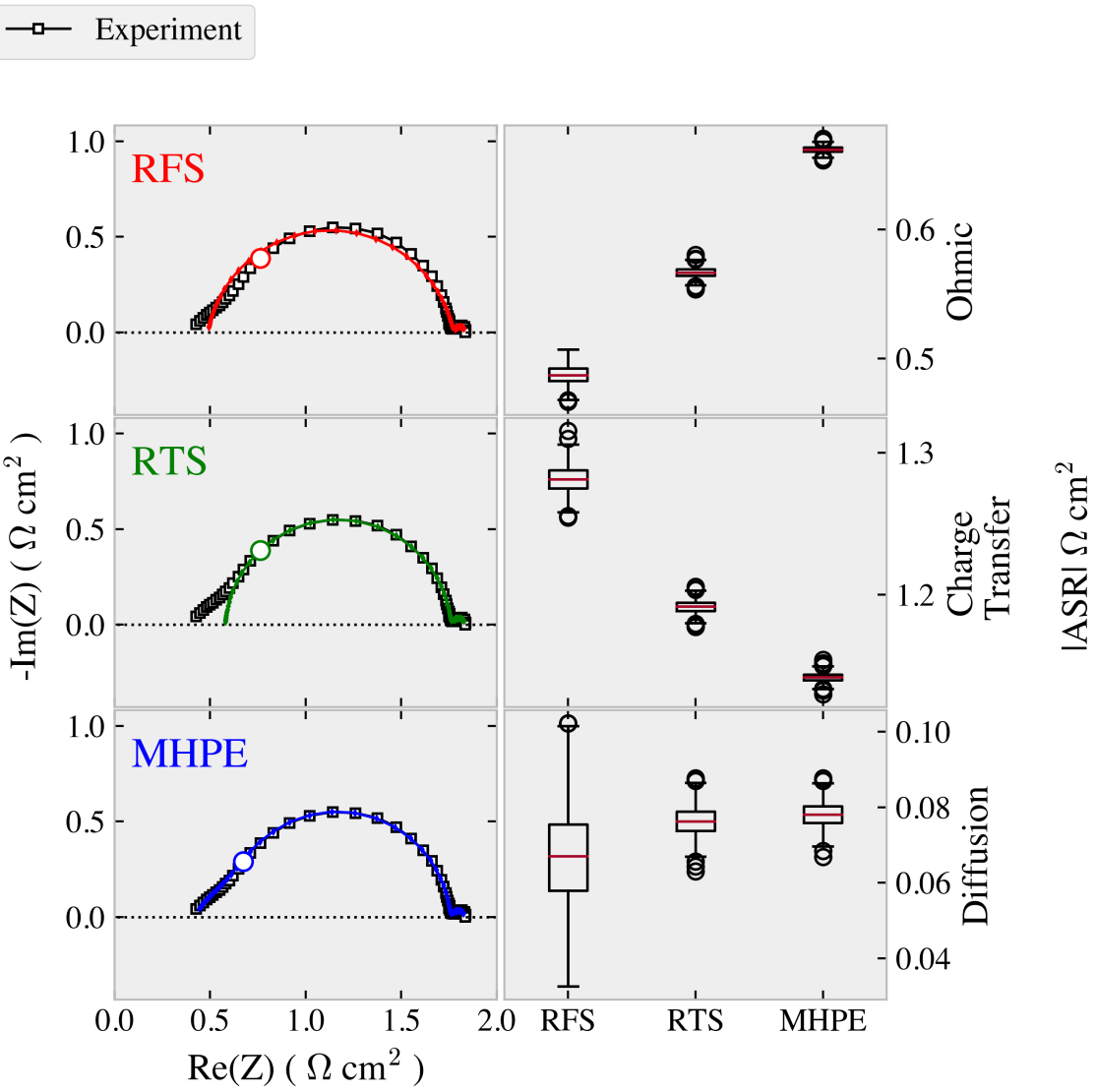

Figure 2.6: Monte Carlo Simulation for nitrogen heat treated (HtN) electrodes

zero between each model. The difference in means between the charge transfer resistance from RFS and MHPE (using a Tukey HSD test) is now on the order of 12%, while between RTS and MHPE the difference is around 3%. They each still converge to similar approximations of the finite diffusion resistance with the RTS and MHPE having a probability distribution overlap of 80%.

The significance of these deviations is emphasized in Table (A.3) where the effective surface areas are estimated at lower values using the two Randles-circuit models. These estimations are still of the same order of magnitude, but are significant when considering that the exchange current densities are also estimated at lower values. The mean exchange current density for RFS is almost a factor of two lower than the mean for the MHPE. The distribution overlap between RTS and MHPE, however, is on the order of 6%, meaning that the RTS is still capable of approximating the same exchange current density as the MHPE. It is with the HtN electrode that significant deviations in the approximation of the mass transfer parameters begin to manifest. Scale factor f exhibits a standard deviation that is 20.5% of the mean indicating that the parameter is not very well estimated by this model.

The 60°C hydrothermally treated electrode (HyB) exhibited the lowest characteristic frequency (296 Hz) of the electrodes with $\gamma > 1$. Examination of its Nyquist plot (Figure 2.7), however, shows evidence of a deviation between the high frequency semi-infinite behavior (characterized by an angle of $\frac{\pi}{4}$ at high frequency) and the charge transfer process. Again, the ohmic resistances estimated by each model are mutually exclusive; however, for HyB there is an overlap (2%) between the MHPE and RTS distributions. While this overlap is low, examination of Figure

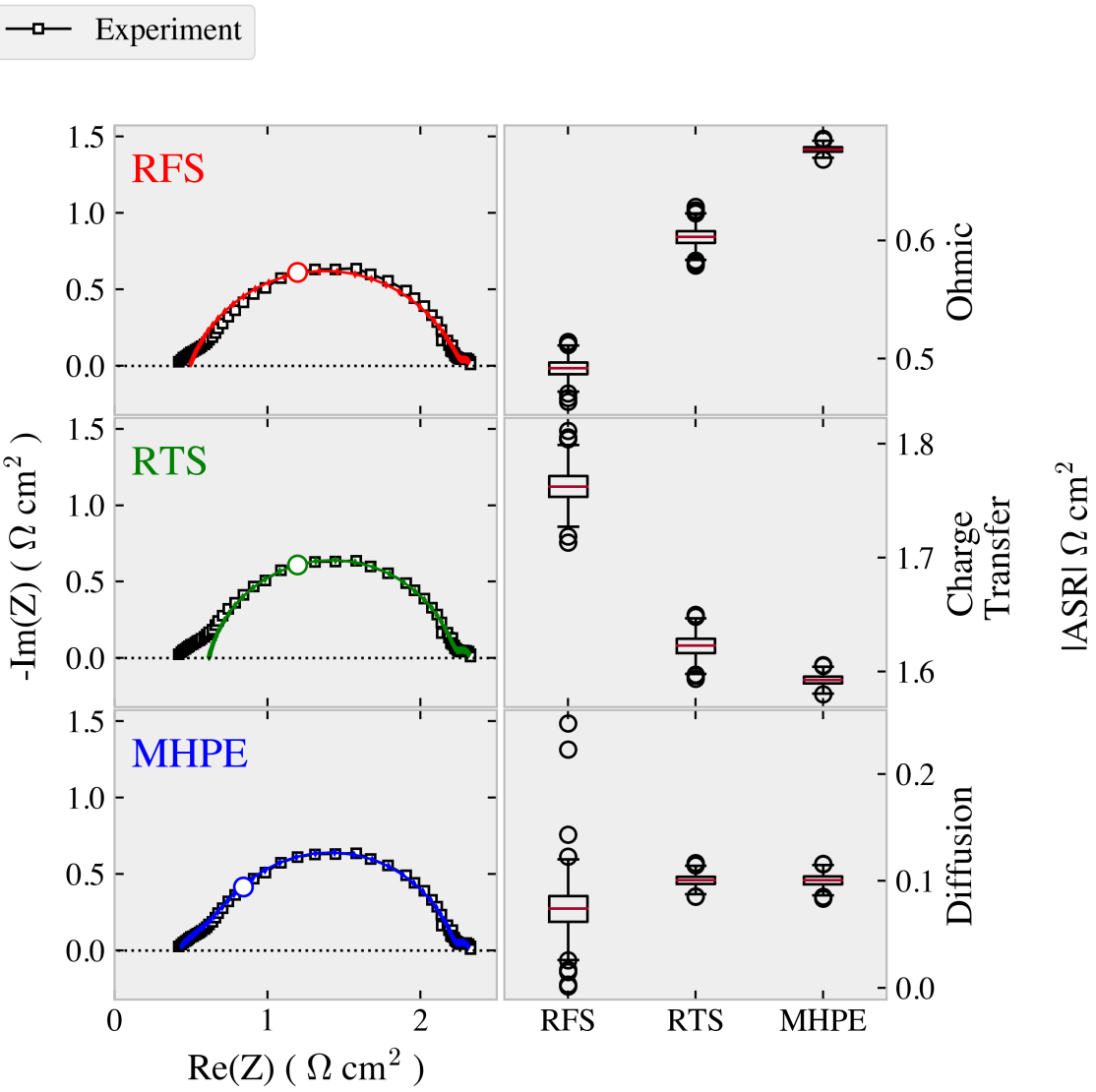

Figure 2.7: Monte Carlo Simulation for 60 °C hydrothermally treated (HyB) electrodes

2.7 indicates that the difference between their means is very small (2%). The finite diffusion resistance for this case is very small, and all three models have significant overlap: 96% between RTS and MHPE and 22% between RFS and MHPE. The significance of the perturbations for the RFS model is evident in the box plots; however, the variation in the diffusion layer thickness a and fitting parameter f are evidence that this model has a low ability to estimate these parameters. Estimations of the surface area between RTS and MHPE only differs by 5%, and the distributions for the exchange current density are statistically similar (95% probability that the means are equal).

$\gamma < 1$

The 80°C hydrothermally treated electrodes (HyA) showed an improvement in charge transfer over HyB (62% lower). Examination of Figure 2.8 shows that the separation between the charge transfer resistance and the distributed ohmic resistance is not obvious the way it is for HyB in Figure 2.7. Both the RTS and RFS have significant outliers; however the charge transfer of the RTS and MHPE have an overlap of 31.3 % and an overlap in diffusion resistance of 37%. Table A.3 reflects this agreement where there is 20% agreement on the effective surface area as well as 2% overlap in distributions for exchange current density. While the characteristic frequency of HyA is lower than HyB as seen in Figure 2.2 its γ value is not sufficiently small to be categorized as semi-infinite. The < 1 threshold for γ bounds the domain where the distributed resistance can be considered *sufficiently* small that it does not significantly impact the estimation of the charge transfer re-

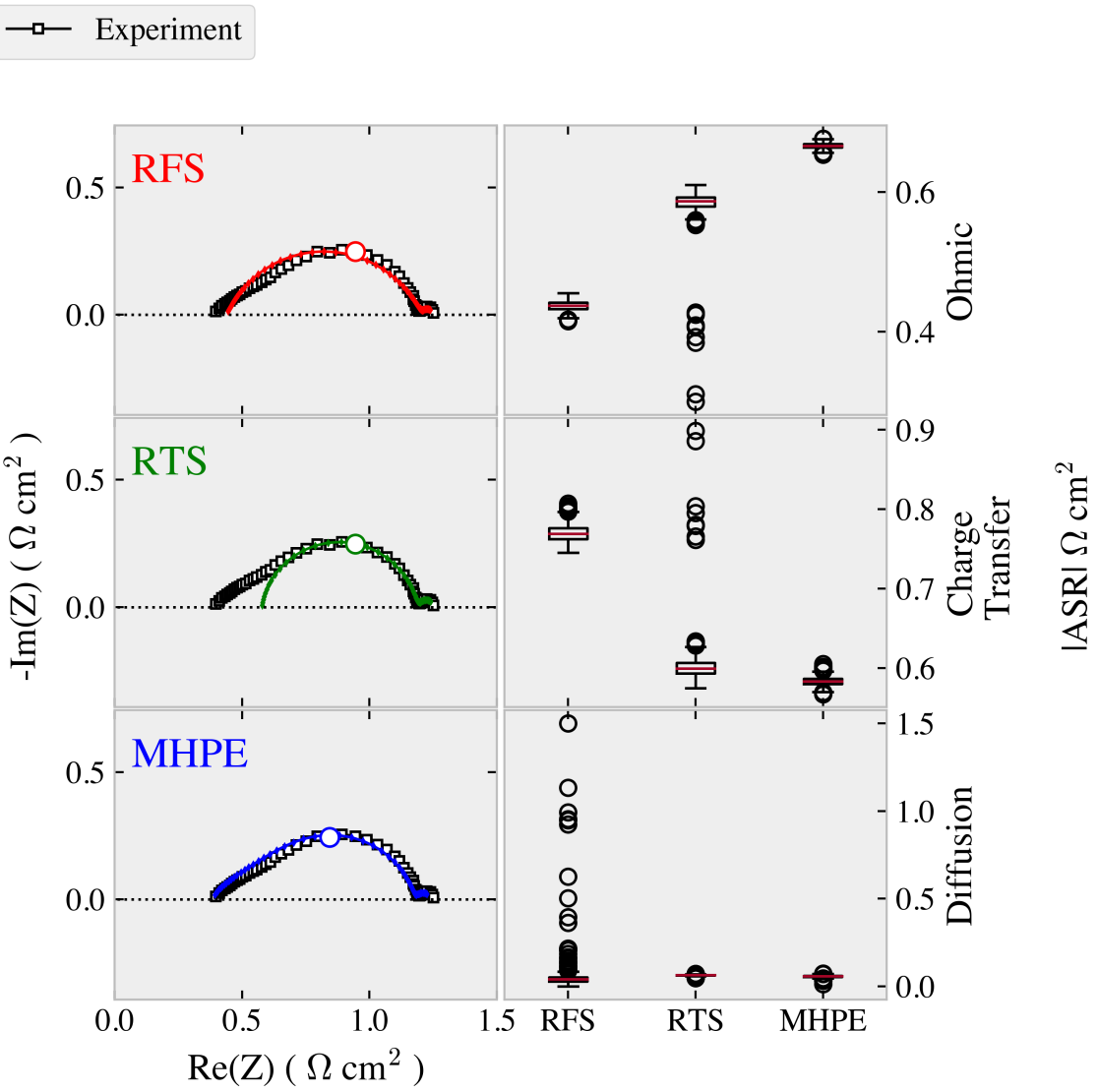

Figure 2.8: Monte Carlo Simulation for 80 °C hydrothermally treated (HyA) electrodes

sistance and its constituent parameters. For this instance, the surface areas differ by nearly a factor of two between the MHPE and RFS.

The oxygen heat treatment was previously demonstrated on carbon paper (SGL 10AA) [111]. Figure 2.9 shows the impact of the treatment on felt, where the charge transfer resistance is reduced even relative to HyA ($\approx$ 18% lower). The HtO electrodes show no indication of transition between the distributed ohmic component and the charge transfer resistance. For this treatment the overlap between the estimations of the charge transfer resistance is effectively zero between all the models, while the diffusion resistances between the models are in good agreement. The exchange current density distributions for RTS and MHPE (Table A.3) share an overlap of 37%; however, their surface area approximations are mutually exclusive, differing by 23%. The RFS shares little overlap with either of the other models for both the surface area and i_0. HtO has a higher characteristic frequency than both the hydrothermally treated electrodes, but its maximum γ value is smaller. This makes the RFS model extremely ineffective as it attributes the effect of both the distributed resistance and the charge transfer resistance into its value of the charge transfer resistance where parameters will inevitably be poorly estimated.

The mixed hydrothermally / heat treated electrodes (Hyt) again exhibited mutually exclusive charge transfer resistance distributions between the three models (see Figure 2.10), and high overlap between the finite diffusion distributions. Table A.3 indicates that, as was the case with HtO, there is effectively no overlap between MHPE and RTS in the surface area distributions, but high overlap between the exchange current densities. Differing by almost a third in their surface

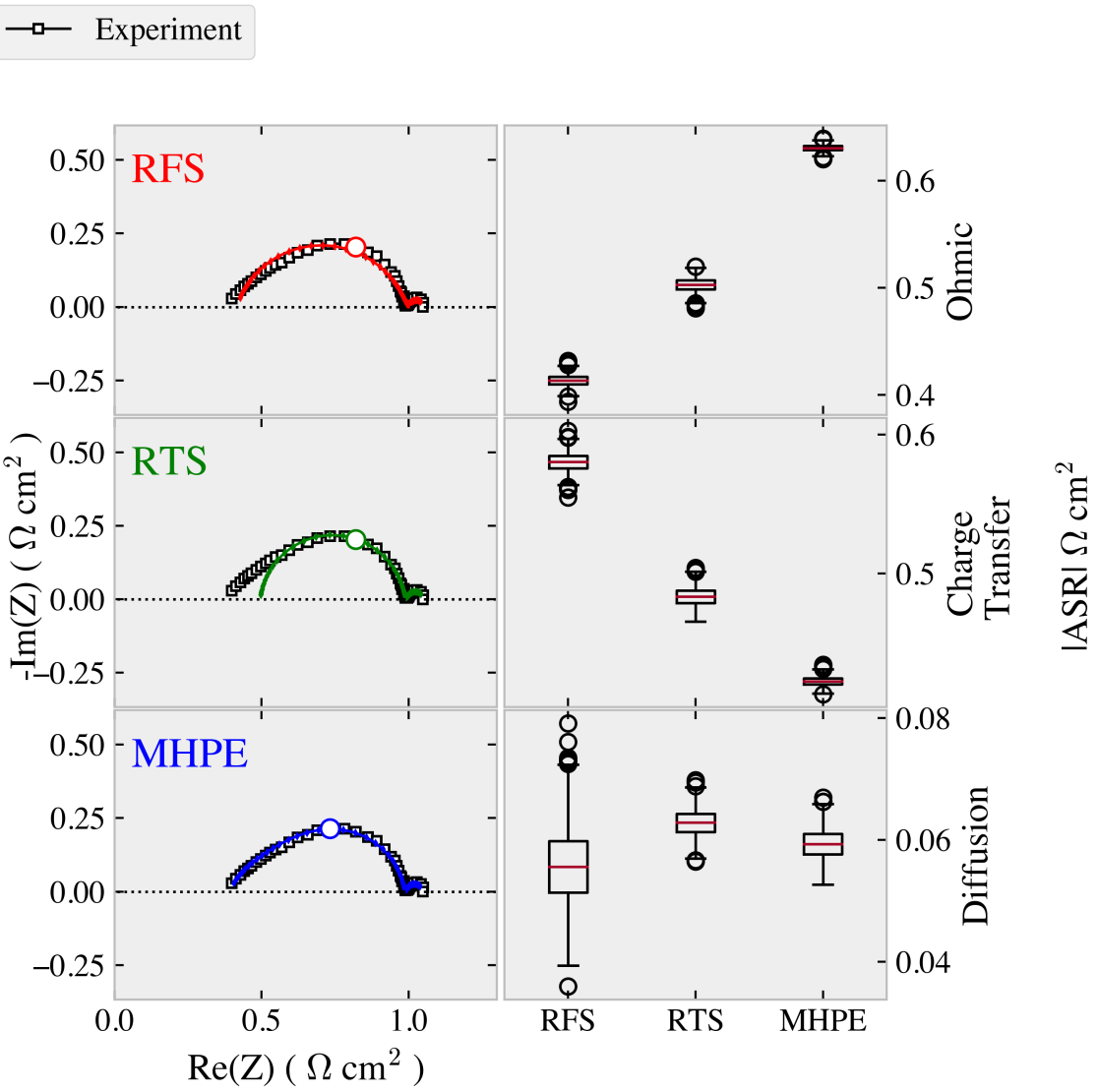

Figure 2.9: Monte Carlo Simulation for oxygen heat treated (HtO) electrodes

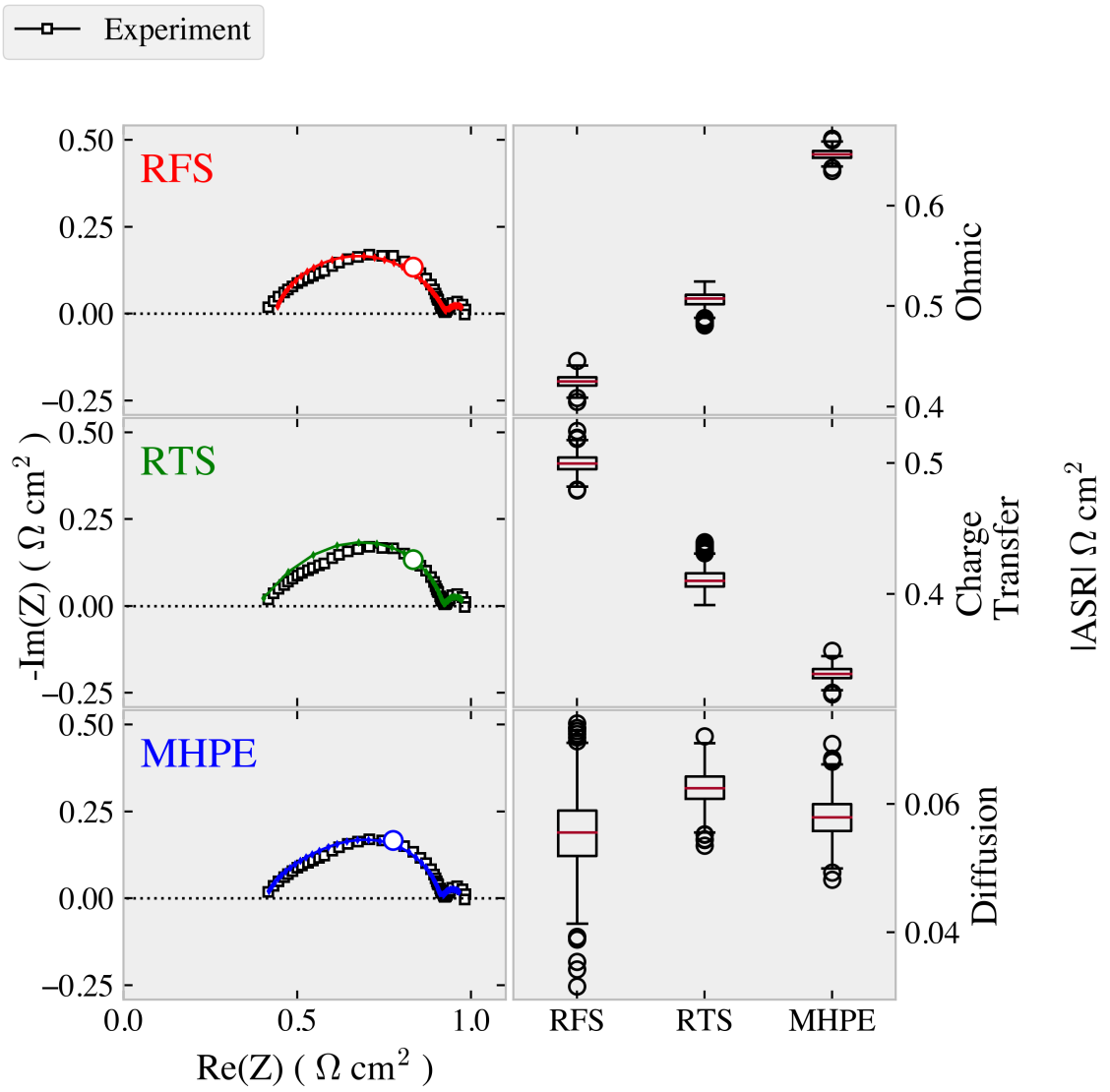

Figure 2.10: Monte Carlo Simulation for mixed hydrothermal / heat treated (Hyt) electrodes

area estimations are certainly non-trivial; however as the characteristic frequency is low, the kinetics are not well separated from distributed resistance. The effect of this phenomenon is even more pronounced with the RFS model, where it is the unquestionable outlier in the surface area and exchange current estimations.

Ammonia treated electrodes (Am4)

The ammonia treated electrodes (Am4) possessed the smallest impedance of all the treatments. Clearly from Figure 2.2 the Am4 electrode exhibits the smallest ratio between the characteristic length and the complex decay length (λ). With such a low characteristic frequency and a maximum γ value of .265, this electrode may have semi-infinite porosity where there is zero ability for CNLS-based impedance data reduction techniques to estimate kinetics parameters [118]. For this reason, the electrode was characterized capacitively with non-faradaic impedance in order to estimate the surface area (which is expected to have increased based on Figure 2.3).

Figure 2.11 differs from the template of the Monte Carlo results in very important ways. First, A) is the non-faradaic spectrum referred to in Section 2.2.2. This experiment was performed because, as can be seen in 2.11 B), the ammonia treated spectrum is qualitatively different from the other spectra, exhibiting a third semi-circular feature at high frequency. The presence of this extra impedance feature renders all the models incapable of parameter estimation without first approximating the capacitance in a non-faradaic cell. The MHPE model was used to estimate the effective surface area via Equation 2.6. For the Am4 electrodes the effective

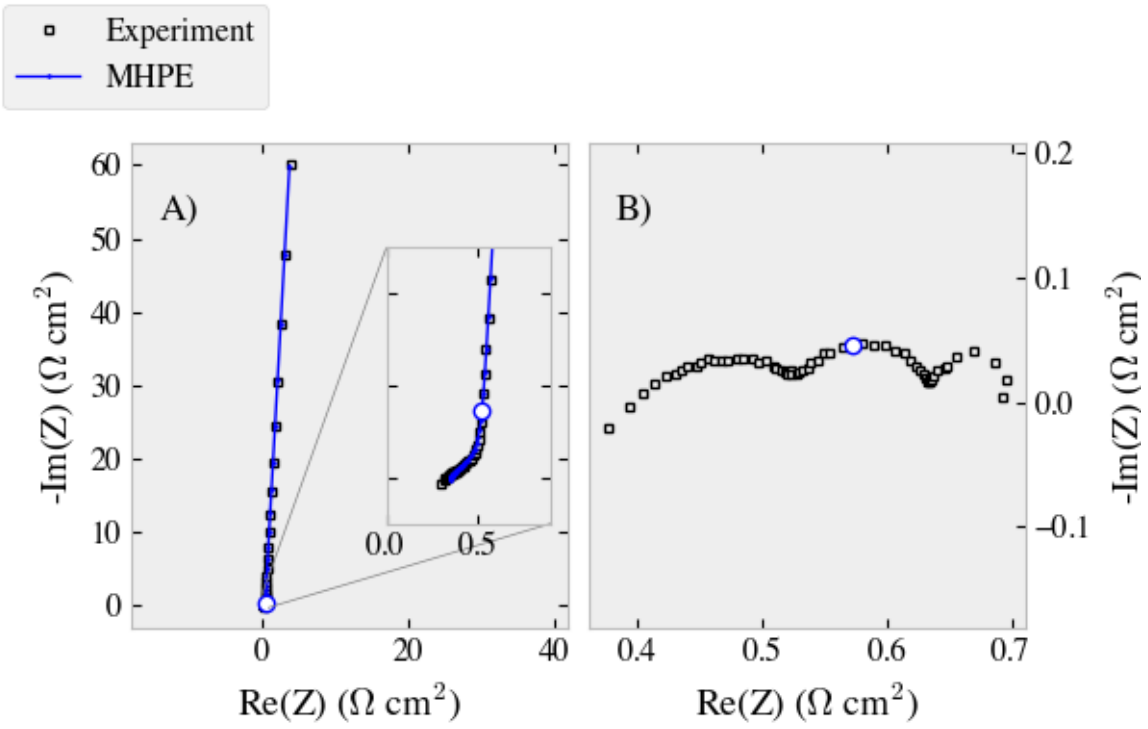

Figure 2.11: Nyquist plots for Am4 electrodes. A) shows the non-faradaic spectrum (measured in 4M H_2SO_4), fit with the MHPE model with $C_R \rightarrow 0$ and $C_O \rightarrow 0$. The inset shows the distributed resistance which is observed at high frequency. B) shows the spectrum measured in the presence of vanadium electrolyte. The characteristic frequency is labeled with the white circle in both figures.

surface area was estimated to be 15,662 $\pm$1.06% cm^2 (1044 cm^{-1}). Comparing this value with Table A.3 shows that with this approximation, the surface area of the ammonia-treated electrodes is an order of magnitude higher than each of the other treatments. This drastic increase in surface area is attributed to the morphological change to the surface, induced by the ammonia treatment (see Figure 2.3B and 2.3C).

Analysis

The purpose of this analysis is not to posit that one of these models is objectively correct over another; rather, it is to determine whether they can agree on the probability distributions of estimated parameters. For this reason the RTS and MHPE are the models that have the highest level of agreement (particularly in the cases where γ is greater than unity). Use of the full spectrum (RFS) to estimate parameters results in overestimation of the charge transfer resistance whenever the distributed resistance comes to constitute a larger component of the spectrum (i.e. HtN, HyB, etc.). As the ratio of the complex decay length to the characteristic length becomes smaller (γ becomes smaller) the distributions of surface area and exchange current density have smaller overlap. Table A.3 shows a significant difference between the hydrothermally treated electrode from the other treatments (aside from Am4): an increase in effective surface area by a factor of 6 coupled with a decrease in exchange current density of a factor of 0.5 (relative to Raw). The other (non-hydrothermal) treatments both increase the surface area (by a smaller factor) and the exchange current density. The parameter P (CPE exponent) is a

measure of the tilt of the charge transfer impedance below the real axis (i.e. P = 1 is a perfect capacitor). There is often some distribution in the effective time-constant throughout the electrode structure and P is a lumped parameter representing the entire electrode response. The estimates of P for RTS and MHPE have a minimum mean of .85, while RFS exhibited a minimum mean of .72. The incorporation of the high frequency content in the RFS model necessitates elongation of the charge transfer resistance, where the maximum reactance value (Z″) is disproportionately low compared to the width of the semi-circle (see Figure 2.8). Among the ways that the RFS model compensates for this (lower surface area / lower exchange current), P can take a lower value to accommodate the 'depressed' semi-circles. The scale factor f is a fitting parameter introduced by Sun and co-workers which functionally partitions the surface area [38]. These results demonstrate that for parameter estimation, the use of a Randles circuit can produce similar parameter estimates to the use of a MHPE model if the characteristic frequency (ω_1) is sufficiently high. The resistivities of the electrolyte and the electrode affect the impedance at every frequency; however, their effect is most significant at high frequency.

Inspection of equation 2.4 reveals a feature of the inductance (L), which elucidates its high level of sensitivity to the RFS and RTS for all treatments and to MHPE for Raw: its sensitivity to inductance is maximized at high frequency. As mentioned previously, the non-MHPE models have zero physics-based resolution of the high frequency content when there is a distributed ionic resistance (slope of $\approx \pi/4$ at high frequency). Parameter differentiation can be used to quantify the sensitivity of Equation 2.4 to an arbitrary parameter $q \in \{A_t, i_0, P, a, f, ASR_{mem}, L\}$.

$$U(AZ, q) \equiv A\frac{\partial Z}{\partial q} \tag{2.14}$$

Applying Equation 2.14 to the inductance, its sensitivity coefficient is:

$$U(AZ, L) = A\frac{\partial Z}{\partial L} = Aj\omega \tag{2.15}$$

Inspection of Equation 2.15 reveals: AZ' has no sensitivity to inductance (as it is a complex number with no real component) and the sensitivity of AZ" is a function of frequency which is maximized at the highest frequency. This is the portion of the spectrum that is deliberately removed for RTS, which is reflected in the extremely large variance seen in Table A.3. RFS, on the other hand, is limited because it physically represents a planar surface without the ability to resolve the distributed resistance (which manifests at the maximum frequencies). For these reasons, the model perturbations of RTS and RFS result in an inability to resolve the inductance consistently. The MHPE model, however, maintains the smallest variance for the inductance (for each of the models) as it has the highest resolution at the maximum frequency. The Raw and NAS treatments have relatively high variance for MHPE compared to the other treatments because the MHPE model can resolve this high frequency content, therefore, when it constitutes a relatively small portion of the spectrum, its resolution is constricted.

2.4 Conclusions

These results illustrate, first, that symmetric cell impedance combined with Monte Carlo simulations can be utilized to understand the impacts of electrode modifications on kinetics and transport parameter estimation. The ratio of the complex decay length to the characteristic length has a very strong impact on the ability for RTS to approximate the parameter values that MHPE produces. This is because when this ratio is at or above unity the ac signal can penetrate the entire porosity and the double layer capacitance can be decoupled from the charge transfer resistance. In cases where this ratio is too small, the charge transfer and the distributed ohmic resistance begin to overlap in the Nyquist plot, where estimation of the characteristic frequency becomes ambiguous. The hydrothermal treatments (HyA and HyB) resulted in both an apparent surface area increase and a decrease in charge transfer resistance. The Am4 treatment required special analysis on account of its ultra-low characteristic frequency and irregular Nyquist plot. Its effective surface area (measured in 4M H_2SO_4) was estimated to be 15,662 cm^2 ($\approx$ 10,400 cm^{-1}), which is approximately 180 $\times$ higher than untreated (Raw). This increase in surface area is expected to be due to morphological changes on the electrode surface due to ammonia treatment. The use of different models is most accentuated by the ability (or inability) to resolve the inductance, which the models are most sensitive to at the maximum frequency. Because these frequencies are removed from RTS it has an enormous variance for the inductance when it is perturbed. The MHPE model is the only one, which can resolve high frequency content because its formu-

lation accounts for the distributed resistance at high frequency, which also gives it the ability to resolve the inductance consistently. These findings demonstrate that electrode morphology modification can be a viable method to develop suitably low-impedance materials for the negative electrode for the all-vanadium battery.

Chapter 3

Contributions from graphitic plates to in-situ kinetics measurements in all vanadium redox flow batteries

This article has been submitted to the Journal of the Electrochemical Society (JES) under the same name as the title of this chapter and is currently under review. Its authorship is attributed to M. C. Daugherty, D. S. Aaron, and M. M. Mench. Aaron and Mench assisted with manuscript revisions. I devised experimental protocol, collected and reduced data, and composed the manuscript.

Abstract

The impact of bipolar plate contributions to the capacitance and activity of vanadium redox flow battery kinetics are explored and quantified in this work. The parallel reaction pathway between the graphite felt (GF) electrode and the bipolar plate was systematically quantified, elucidating the impact of the plate kinetics on the global signal that is measured using a symmetric cell. Tafel analysis was then used to compare the geometric exchange current density informed by a non-open circuit voltage (OCV) estimation to distributions generated using Monte Carlo simulations of an OCV Randles circuit. The cathode was found be to controlled by mass transport polarization at open circuit, indicating that the current supported by the plate is nonuniform at all overpotentials. It was also found that, in the limit as the overvoltage goes to zero, 34% of the current is supported by the plates at the anode. This phenomenon distorts the quantification of kinetics parameters measured at OCV.

3.1 Introduction

Interest in incorporation of renewable energy sources onto grids has necessitated development of novel technologies and solutions to challenges associated

with stable grid operation. Redox flow batteries (RFBs) are a technology which has been studied [12, 15] and demonstrated [119] as a viable energy storage technology for grid-level applications. RFB systems in this context are expected to undergo thousands of charge/discharge cycles and see service lifetimes greater than 10 years [120].

The all vanadium redox flow battery (VRFB), which is the topic of this work, has the advantage over other RFBs in that crossover-induced capacity fade is reversible. However, degradation of other components such as the membrane, electrode, and bipolar plates can be permanent. Derr and co-workers investigated the trade-offs between cutoff voltage, degradation, and SoC utilization; despite greater degradation with cutoff at 1.8 V, greater SoC utilization ultimately yielded better performance than 1.65 V. Derr *et al.* also observed the effects of electroless chemical aging of electrode materials for VRFBs [74]. A significant loss in capacitance was observed for electrodes exposed to anolyte (particularly V(III)), whereas the catholyte induced oxidation, but did not show significant performance loss. Pezeshki *et al.* developed a novel method for accelerating electrode degradation by utilizing a 'cell-in-series' configuration which allows for constant overcharging of a cell at high SoC [41]. Many chemical [32,112] and thermal [36,111] treatments have been studied for the VRFB system as well as deposition-based treatments which focus on doping with metals [97, 121] and graphene/carbon nanotubes [122–124]. Treatments often involve combinations of these processes in attempts to engineer nano-scale effects of the morphology and activity of electrode surfaces.

Bipolar plates (BPP) in VRFB systems provide mechanical strength and channel-

ing for fluid flow while also serving as a circuit component for electron conduction during charge and discharge. Ideal BPPs in VRFB systems should be impermeable to electrolyte leakage, have high electrical conductivity to reduce ohmic resistance, and have both mechanical stability and high chemical resistance to potentially corrosive electrolytes [58]. The three primary types of BPPs that have been researched in literature are graphite, composite and metallic [59]. Graphite is the most commonly used BPP material in the literature for lab-scale work; however the difficulty of manufacturing combined with poor flexural strength make it unattractive as BPP material for VRFB stacks [60]. Composite plates are often primarily composed of a graphite matrix that is combined with fillers and epoxy resin in an effort to increase conductivity [61] or improve other metrics relating to impermeability [62] or mechanical flexural strength [60]. While metallic bipolar plates can satisfy the need for high electrical conductivity and mechanical strength, resistance to corrosion is a significant problem that renders most metals without proper treatments and coatings unsuitable for VRFBs. Although adequately stable in the corrosive conditions of an operating VRFB, Satola *et al.* observed that graphite and composite BPPs can suffer from corrosion and damage when exposed to electrolyte at high SoC [64] or overcharge. It is also desirable at stack-scale for VRFB BPPs to have sufficient flexural strength that fracture upon assembly or transportation of a system does not occur. Liao *et al.* developed novel BPP material which improved flexural strength to 48 MPa, nearly double the target set by DOE (25 MPa) by supplementing a graphite-epoxy mixture with CF3 carbon fibers [60].

The dependence on the uniformity of current distribution across electrodes in

VRFBs has been studied by Clement and co-workers [125]. It was found that deviation from the mean current density is minimal ($\pm$ 5%) in cases where mass transport polarization is non-dominant; however that range jumps to $\pm$ 20% as mass transport begins to dominate the polarization. In this work, the assumption of uniformity (of current) is essential to decoupling the channel electrode contributions to kinetics. Levich derived closed-form solutions for the convection-diffusion equation in many geometric domains, including the channel electrode which is used in this work [126].

3.2 Methods

3.2.1 Experimental

Cell configuration and architecture

Experiments were conducted on a 2.5 cm^2 rectangular (2.82 cm x 0.88 cm) flow through cell which was machined from Bulk Molding Compounds (BMC) graphite. For the experiments which involved porous felt electrodes, carbon felt was utilized (SGL GFD3; 3 mm nominal thickness). Isolation of each half-cell was achieved by the use of a symmetric cell, which has been demonstrated in the literature [39,116] as a means to operate at approximately steady state SoC conditions and with no net crossover effects. A reference electrode (Hg/Hg_2SO_4; E°=0.64V vs. NHE at 25°C) was in contact with the membrane edge in a small reservoir of 0.5M H_2SO_4 to ensure the consistency of the electrolyte composition and the symmetry of the overpotential distribution between the two half-cells. The voltages reported herein are across the whole cell, but should be recognized as consisting of two times the

contribution of a half-cell. A Nafion ^{TM}117 membrane was used for all testing, with the same break-in protocol as described in [39].

Electrochemical Protocol

All experiments in this work were conducted with electrolyte composed of 1 M vanadium ($VOSO_4$ Alfa Aesar, 99.9%), 3.3 M sulfuric acid (H_2SO_4 Alfa Aesar, ACS grade) at 50% state of charge (SoC). 100 mL of $VOSO_4$ on the cathode and 50 mL on the anode were charged potentiostatically at 1.8 V in a 25 cm^2 charging cell until the current density decayed to less than 1 mA cm^2. 50 mL was then removed from the catholyte followed by discharge of 25% of the charged capacity to achieve 50% SoC. Temperature of the tanks and the cell was controlled at 30°C with type T thermocouples (Omega).

The experimental protocol consisted of a 5-hour dwell period to allow for beginning-of-life degradation to begin to stabilize and the electrode to become wetted. Following the stabilization period, staircase potentiostatic electrochemical impedance spectroscopy (SPEIS) was performed (0–600 mV in 15 mV increments; 100 kHz to 60 mHz; 6 points per decade). A Biologic VSP potentiostat with a 20A booster was used for all electrochemical experiments.

Electrode Configurations

Systematic quantification of the effects of multiple layers of electrode material was achieved by comparing the channel (just the bipolar plate) to one and two layers of GFD3. The single and double layers of electrode were each compressed to 64% of their original thickness. Testing for the channel configuration was performed with the same hardware as used in the case for the GFD3 electrode testing;

however, in this instance the porous electrode was removed so that the electrode consisted of the bipolar plate with an equivalent volume of flowing electrolyte adjacent to the plate. The flow conditions of this situation are certainly dissimilar to those with GFD3 material in the reactor; however, the analysis of the channel flow is summarized in 10.2 and it was concluded that these effects are small with regard to characterization of the electrochemical surface. For determination of the impact of mass transport limitation, the flow rates tested were 10, 17.5, 25, 32.5, and 40 mL min^{-1} (corresponding to area normalized flow rates of 4, 7, 10, 13 and 16 ml min^{-1} cm^{-2}).

3.2.2 Impedance

Impedance spectra were fit using a Randles circuit model which was modified and demonstrated for a symmetric cell by Pezeshki and co-workers [38, 39, 95].

$$AZ_{cell} = 2 \times AZ_{ct} + ASR_{ohmic} \tag{3.1}$$

The charge transfer impedance (Z_{ct}) is modeled by the charge transfer resistance in series with a Warburg impedance element [38]:

$$Z_{ct}(\omega) = R_{ct} + \frac{\delta_{eff}}{f} W \tag{3.2}$$

where the charge transfer resistance (R_{ct}) and Warburg impedance (W) are defined

as:

$$R_{ct} = \frac{RuT}{A_t i_0 F}$$

$$W = \frac{RuT}{A_t F^2 \sqrt{j\omega}} \left[\frac{1}{C_R \sqrt{D_R}} \tanh\left(\delta_{eff} \sqrt{\frac{j\omega}{D_R}} \right) + \frac{1}{C_O \sqrt{D_O}} \tanh\left(\delta_{eff} \sqrt{\frac{j\omega}{D_O}} \right) \right] \tag{3.3}$$

Low frequency approximation of the Warburg element (W) in Equation 3.3 gives the area specific finite diffusion resistance (ASR_{fd}) as:

$$ASR_{fd} = \frac{\delta_{eff}}{f} \frac{ARuT}{A_t F^2} \left(\frac{1}{C_R D_R} + \frac{1}{C_O D_O} \right) \tag{3.4}$$

The charge transfer ASR (ASR_{ct}) is defined by:

$$ASR_{ct} = \frac{ARuT}{A_t i_0 F} \tag{3.5}$$

This is the area specific version of the charge transfer resistance term (R_{ct}) in Equation 3.3. The effective capacitance was calculated as a constant phase element (CPE) according the relationship proposed by Brug and co-workers [117]:

$$C_{eff} = Q^{\frac{1}{p}} \left(\frac{R_{ohmic} R_{ct}}{R_{ohmic} + R_{ct}} \right)^{\frac{1}{p} - 1} \tag{3.6}$$

Likewise, the effective surface area is the ratio of the effective capacitance to the

typical double layer capacitance per unit area of the electrode (C_{dl}):

$$A_{eff} = \frac{C_{eff}}{C_{dl}} \tag{3.7}$$

A complex nonlinear least-squares (CNLS) regression was utilized to minimize the difference between the experimental values and the modeled values for each frequency in the spectrum.

$$S = \sum_{k=1}^{n} \left[AZ'_{k,exp} - AZ'_{k,model} \right]^2 + \left[AZ''_{k,exp} - AZ''_{k,model} \right]^2 \tag{3.8}$$

The independent variables for the curve fitting were: A_t, i_0, δ_{eff}, P, f and ASR_{ohmic} (membrane ASR + distributed ohmic ASR). The impedance resolved polarization curves were calculated by integrating the individual ASR components (ohmic, charge transfer and finite diffusion) with respect to current density.

$$\eta_x = \int_0^j ASR_x(j)dj \tag{3.9}$$

This process was also used for isolation of the charge transfer polarization in the Tafel analysis. It should be noted that when the cell is polarized (deviating from open circuit), the Randles model is used to estimate the ASR components used in Equation 3.9; however the non-ohmic fitted parameters (A_t, i_0, δ_{eff}, P, f) have no meaning as the boundary conditions used to derive Equation 3.2 differ when the cell is polarized. Thus, these values are used only to estimate the different components for integration.

3.2.3 Mass transport at the channel electrode

Without the use of the current distribution diagnostic, we seek a relationship between the limiting current and the impedance signal to characterize an electrode as having a uniform (non-mass transport limited) or non-uniform (mass transport limited) current distribution. Solving the convection-diffusion equation at steady state, for laminar flow in a channel with minimal edge effects, the relationship between the diffusion layer thickness and velocity in the center of the channel can be derived [54]:

$$\delta_{eff} = \frac{3\Gamma(\frac{1}{3})}{4\sqrt[3]{6}} \left(\frac{LhD}{V_O} \right)^{\frac{1}{3}} \tag{3.10}$$

Likewise, in this geometric setting, the relationship between the volumetric flow rate and the velocity at the center of the channel can be calculated by integrating a parabolic velocity profile across the flow domain (assuming negligible edge effects):

$$V_f = \frac{4}{3} V_O bd \tag{3.11}$$

The relationships in Equations 3.4, 3.10 and 3.11 indicate that for incompressible laminar flow, a channel with constant dimensions will have an average diffusion layer thickness (and by proxy diffusion ASR) that is proportional to the inverse cube root of the volumetric flow rate ($\text{ASR}_{fd} \propto V_f^{-1/3}$). This relationship is used to determine if a channel is in a mass transport limited regime.

3.3 Results and discussion

3.3.1 Mass transport analysis

In order for the contribution from the channel to be decoupled from the electrode, the current on the channel must be approximately uniform. IR Polarization curves for the symmetric cell with catholyte (left) and anolyte (right) are displayed in Figure 3.1. Because these polarization curves are performed with a symmetric cell, their open circuit potential goes to zero due to having electrolyte of the same composition on both half-cells. The catholyte curves show the onset of mass transfer dominated overpotential at low current, exhibiting almost no ohmic or kinetic controlled regions. The anolyte, however, shows no variation as a function of flow rate up to around 20 mA cm^{-2}. This lack of mass transfer-controlled polarization at low current indicates that the current distribution is approximately uniform for the anode at low overpotentials [125].

To estimate if there is any regime where mass transfer is non-dominant for the cathode, the open circuit impedance spectra were analyzed. Equations 3.4 and 3.10 indicate that under mass transfer control, the diffusion layer thickness (and by proxy the diffusion resistance) is proportional to ${V_f}^{-1/3}$. Figure 3.2 shows this relationship for the catholyte symmetric cell where there is a linear correlation between the diffusion resistance and ${V_f}^{-1/3}$. This proportionality indicates that the cathode channel has sufficiently facile kinetics to be mass transport controlled at open circuit and therefore will have a non-uniform current distribution across the channel when polarized by any degree.

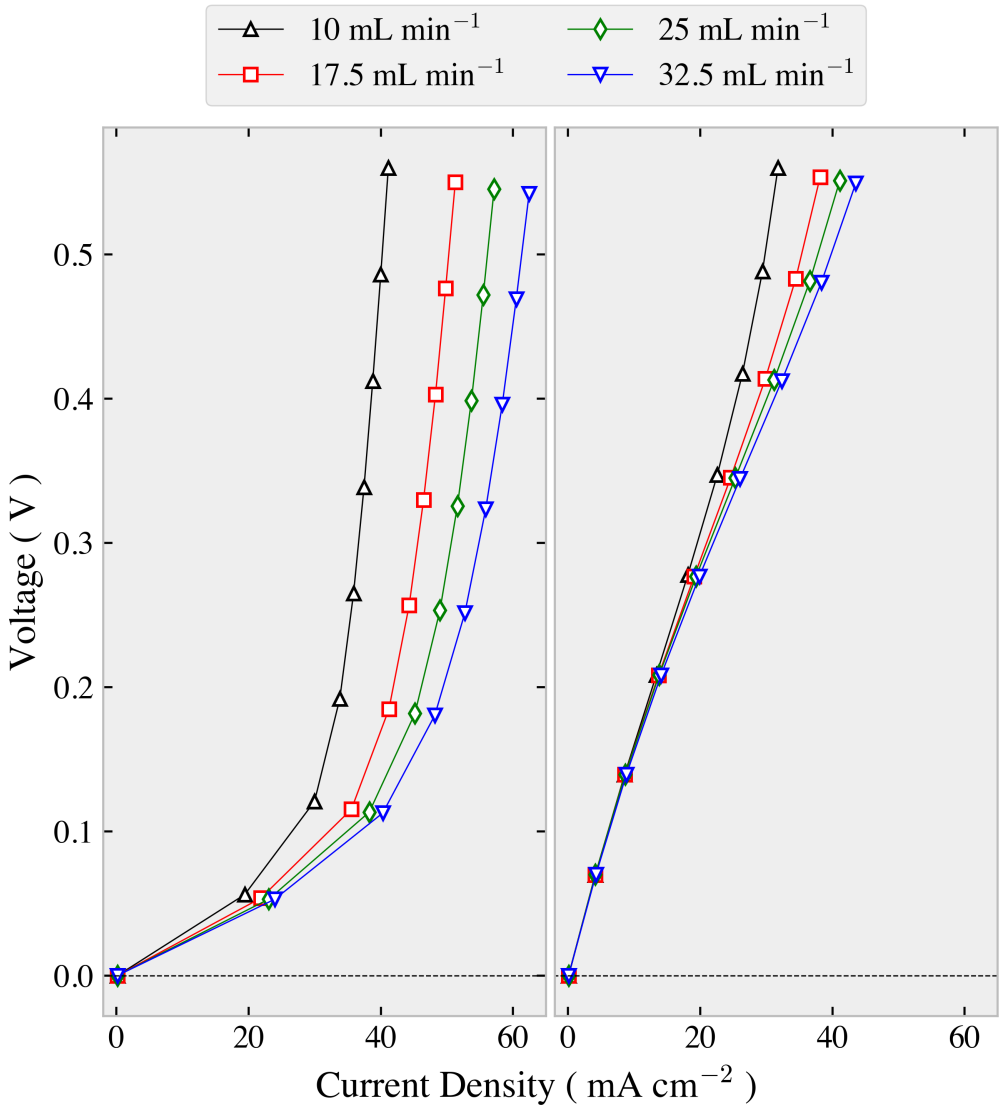

Figure 3.1: IR corrected polarization curves for symmetric cell between 10 and 32.5 $mLmin^{-1}$. The left shows the catholyte as a function of flow rate where the onset of mass transport dominated polarization begins at low current. The right shows the anolyte as a function of flow rate where mass transport polarization is non-dominant up to $\approx$ 20 mA cm^{-2}.

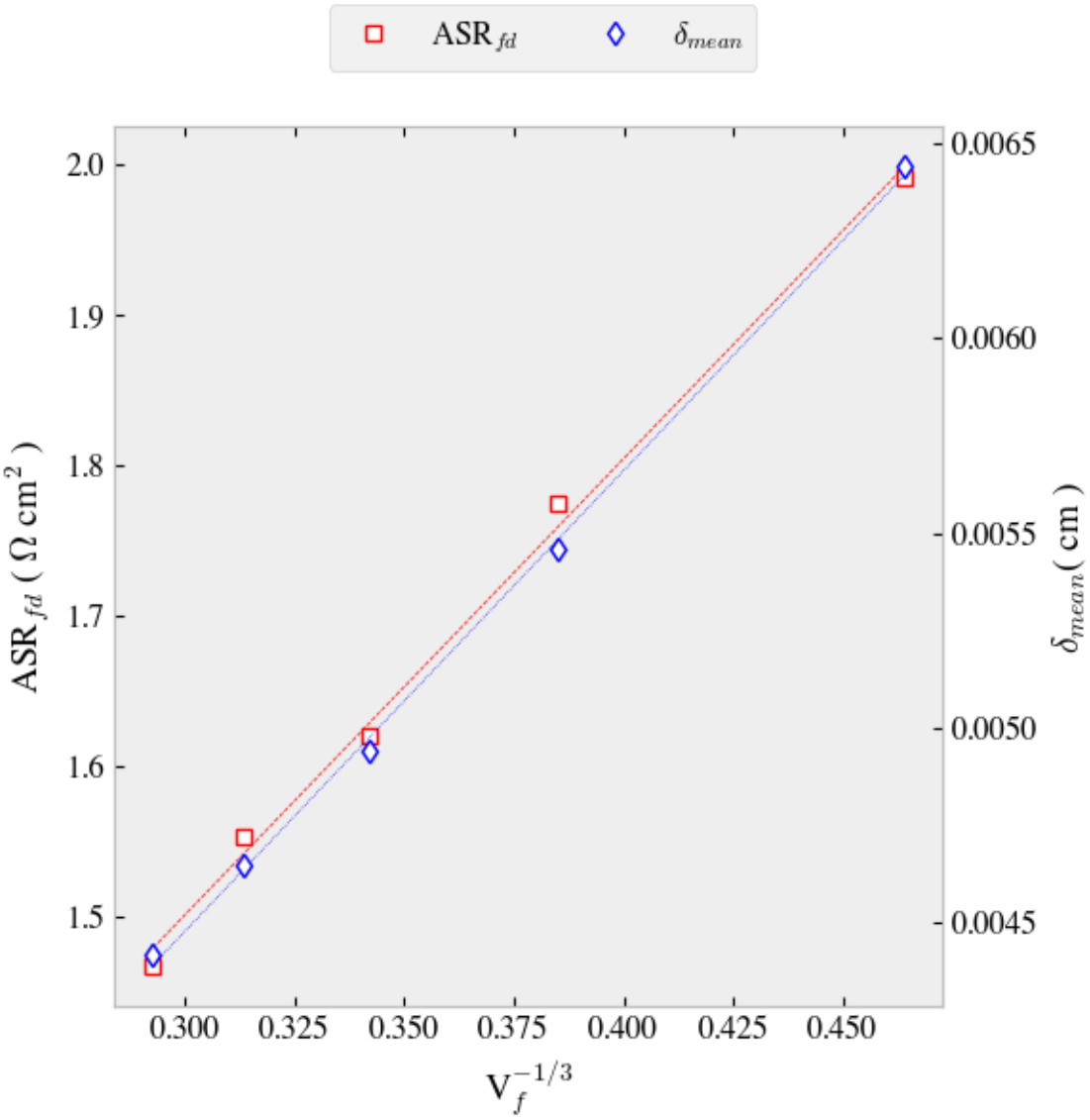

Figure 3.2: Open circuit catholyte diffusion ASR and mean diffusion layer thickness as a function of $V_f^{-\frac{1}{3}}$. This relationship indicates onset of mass transport control is at OCV.

While this analysis is less precise than using in-situ current distribution, it indicates that even at open circuit the kinetics are non-limiting at the cathode, which implies that even at low overpotential the current would be distributed preferentially nearer to the inlet where the SoC is higher owing to active species concentration depletion down the channel.

3.3.2 Frequency analysis

To ensure that the distributed ohmic resistance was not large enough to perturb the estimations of the ASR components, the characteristic frequency and complex decay length were calculated as shown in Table 3.1. Clearly, ratio of the complex decay length to the characteristic length (λ/b) is greater than unity at both the characteristic frequency ω_1 and the minimum frequency indicating that these spectra do not possess semi-infinite porosities. With these results the use of the macrohomogeneous porous electrode model (MHPE) [38, 95, 96] is not necessary to use for ASR magnitude estimation [manuscript under review by JES].

3.3.3 Anode Polarization Curves

Determination of the potential at which mass transport polarization begins to limit the anode is essential to determining the voltage range where the kinetics of the channel and electrode can be separated; thus integrated polarization curves were recorded at successively higher flow rates as seen in Figure 3.3.

The overlay shows the current and potential at which all the polarization curves converge (≈ 0.28 V) as well as the agreement between the sources of overpotential at these current densities. Clearly the charge transfer and ohmic overpotentials are unaffected by the flow rate as their portions of the integrated curves extends

Table 3.1: Characteristic frequency and complex decay length for different electrode configurations. The actual thickness of the porosity of the channel electrode has not been measured so the thickness of 1 Layer of felt was use (.18 cm) to give a lower bound for $\frac{\lambda}{b}$.

Configuration	$\boldsymbol{\omega_1}$	$\boldsymbol{\lambda}(\omega_1)$	$\frac{\boldsymbol{\lambda}(\omega_1)}{\mathbf{b}}$	$\boldsymbol{\lambda}(\omega_{min})$	$\frac{\boldsymbol{\lambda}(\omega_{min})}{\mathbf{b}}$
Channel *	13481.04	0.33	1.85	0.72	4.00
1 Layer GFD3	8237.74	0.30	1.68	0.45	2.48
2 Layers GFD3	953.74	0.54	1.50	0.66	1.84

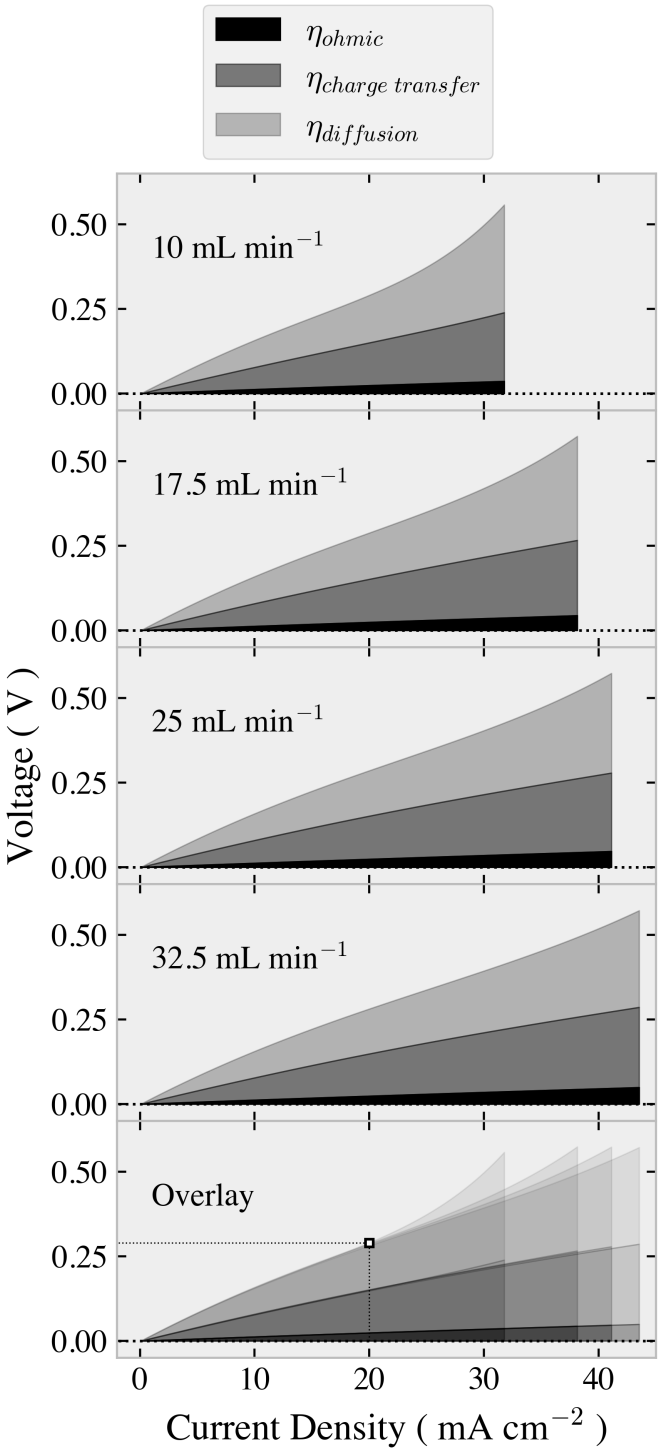

Figure 3.3: Impedance resolved anolyte channel polarization curves as a function of flow rate, the semi-transparent Overlay shows the convergence of the polarization curves to the potential where mass transport limitation starts.

linearly. Below this potential, the plates consistently behave as a parallel reaction-hosting pathway and contribute predictably to the global current signal.

In order to analyze the effect of the additional kinetics that are provided by the BPPs, the electrode layering experiments were performed. The polarization curves as a function of flow rate and number of electrodes are shown in Figure 3.4. Each of these integrated plots is shown with the measured voltage at each current as a white circle to confirm the accuracy of the impedance calculated overpotential integration. The x-axis is fixed for all three columns of curves to show the difference in magnitude of the three configurations. As expected, the plates are much more limited than the cells with one layer and two layers (columns two and three respectively). With the addition of more electrode material the thickness increases, which increases the distributed ohmic ASR ([95] [manuscript under review by JES]), however, the surface area is also increased which lowers both the charge transfer and finite diffusion ASRs.

The experiments with one and two layers of felt have effectively no functionality with respect to flow rate and examination of Figure 3.4 shows that the diffusion ASR is a small source of loss compared to charge transfer. Because of these minor mass transfer losses, we expect the current distribution to be uniform. Under these conditions, the assumption the plates and electrodes form a parallel pathway for reactions is valid. Further investigation of this claim can be accomplished by comparing the overall polarization results for channel-only, one layer of felt, and two layers of felt, shown in Figure 3.5. Inside this potential range the current supplied by the plates and the electrodes is additive, and as seen in Figure 3.5, this

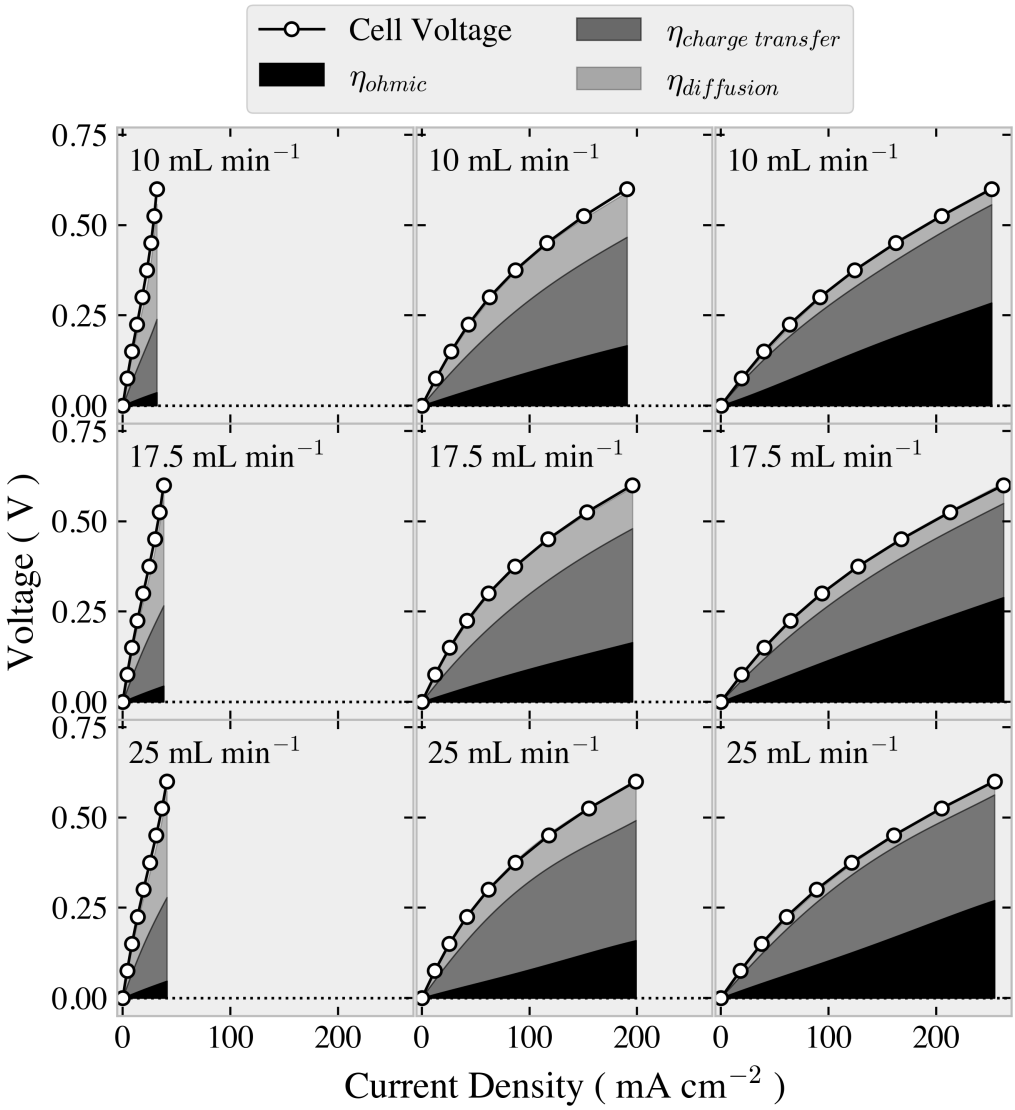

Figure 3.4: Impedance resolved polarization curves for each electrode configuration (channel, 1 Layer, 2 Layers) with increasing flow rate. Cell voltage is shown in white circles to confirm the sum of the overpotential components.

represents the physical situation accurately. The top figure shows the three different iR-corrected experimental polarization curves (*Channel*: green squares; *1x experiment* : magenta circles; *2x experiment* : blue diamonds). Here the 'x' indicates the number of layers of GFD3. Because the plates are in parallel with the single electrode, the current generated solely on the electrodes is calculated by subtracting the current on the plates, which forms the *1x isolated* curve. This result is the current that a single layer of electrode provides.

Extension of the one layer of felt case to two layers of felt leads to the assumption that the current will be the sum of both the plates and two times this *1x isolated* current, which forms the *2x predicted* curve. The predicted curve is in very close agreement with the experimental case of two electrode layers. The bottom portion of Figure 3.5 shows the percentage of the current that is on the plates inside the uniform current distribution regime. Extrapolating down to open circuit, the percentage that the plates support is $\approx$ 34% (of the *1x experiment* case). Voltages of this magnitude (and likewise current densities) are not representative of any type of working cell condition; however, these are the conditions in which the simplest and most commonly used EIS models are valid (i.e. open circuit at 50% SoC) and experimentally observed e.g. [38, 74]. Not all impedance-based analysis attempts to separate the surface area and the activity; however, in-situ analysis does run the risk of estimating kinetics parameters poorly since the double layer capacitance and rate constant of the graphite and felt may be dissimilar. Degradation studies, which seek to diagnose the transient state of electrodes necessitate periodic characterization of in-situ electrodes [127, 128], which might be affected by this.

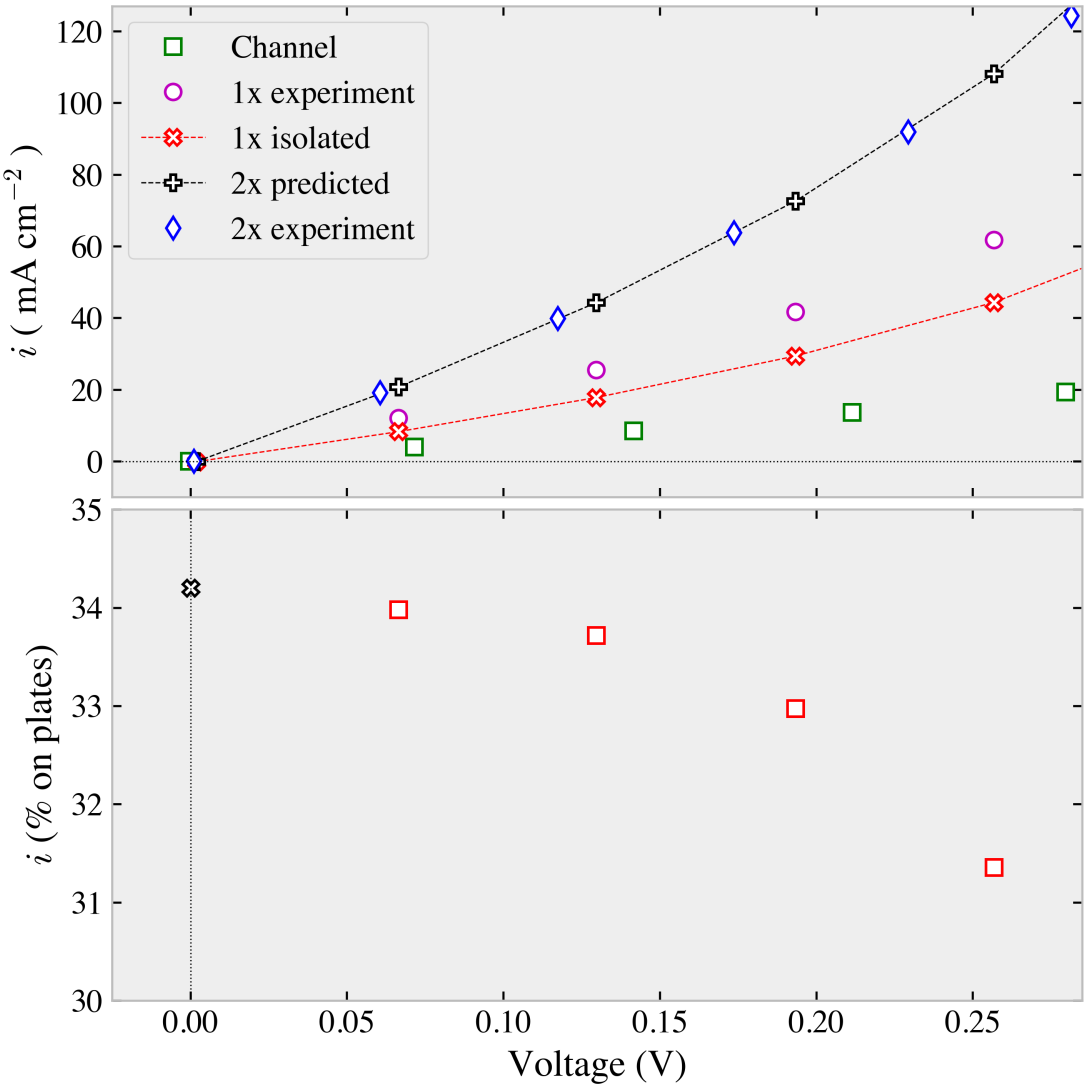

Figure 3.5: Parallel combination of plates and one layer of electrode predicts polarization of two layers of electrode. The bottom figure shows the percentage of current that is supported by the plates as the overpotential goes to zero. This is for the instance of a volumetric flow rate of 10 mL min $^{-1}$.

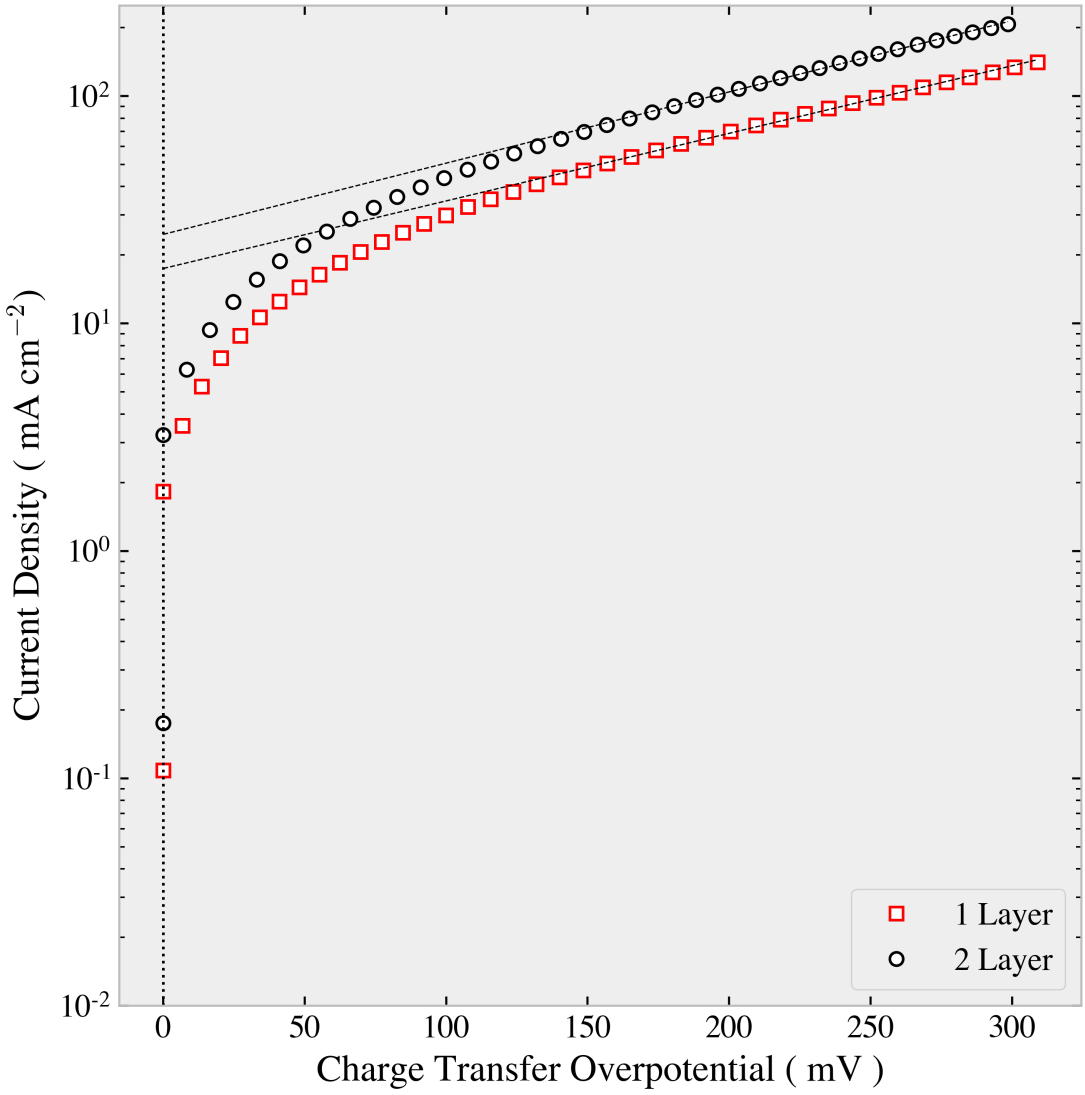

Figure 3.6: Tafel plots for one and two layers of electrode thickness for estimation of the geometric exchange current density.

3.3.4 Capacitance and exchange current density

To gain deeper insight into the kinetics behavior in the limit as the overpotential approaches zero, the geometric exchange current density was estimated using Tafel plots as shown in Figure 3.6. As shown on the x-axis of this figure, both the ohmic and finite diffusion resistances have been removed and the log of current density is shown only as a function of charge transfer overpotential. At these current densities there is still minimal mass transfer polarization seen in the global EIS signal of the resolved polarization curves; however, at higher currents the mass transfer overpotential on the channel becomes infinite and the reaction shifts to the electrode, where we expect the current distribution to be roughly uniform. Because the channel electrode is mass transport limited at such a low overpotential, it does not achieve a true (charge transfer controlled polarization [129]) Tafel slope.

For Figures 3.7 and 3.8 the box plots correspond to the Randles circuit Monte Carlo simulations (referred to as MC data). Figure 3.7 shows the Monte Carlo simulation estimations for the charge transfer (A) and finite diffusion (B) ASRs. The MC data are shown in the box plots, which correspond to the 95% confidence intervals of estimates of the geometric exchange current density, calculated using MC data in the process described in [manuscript under review by JES].

Extrapolated values are calculated by fitting a line to the median of 1 layer and 2 layers and extrapolating to zero thickness. The MC data distributions for the charge transfer ASR show an extrapolation to the median value that is estimated for the channel. While the distribution for the channel is broader than the that

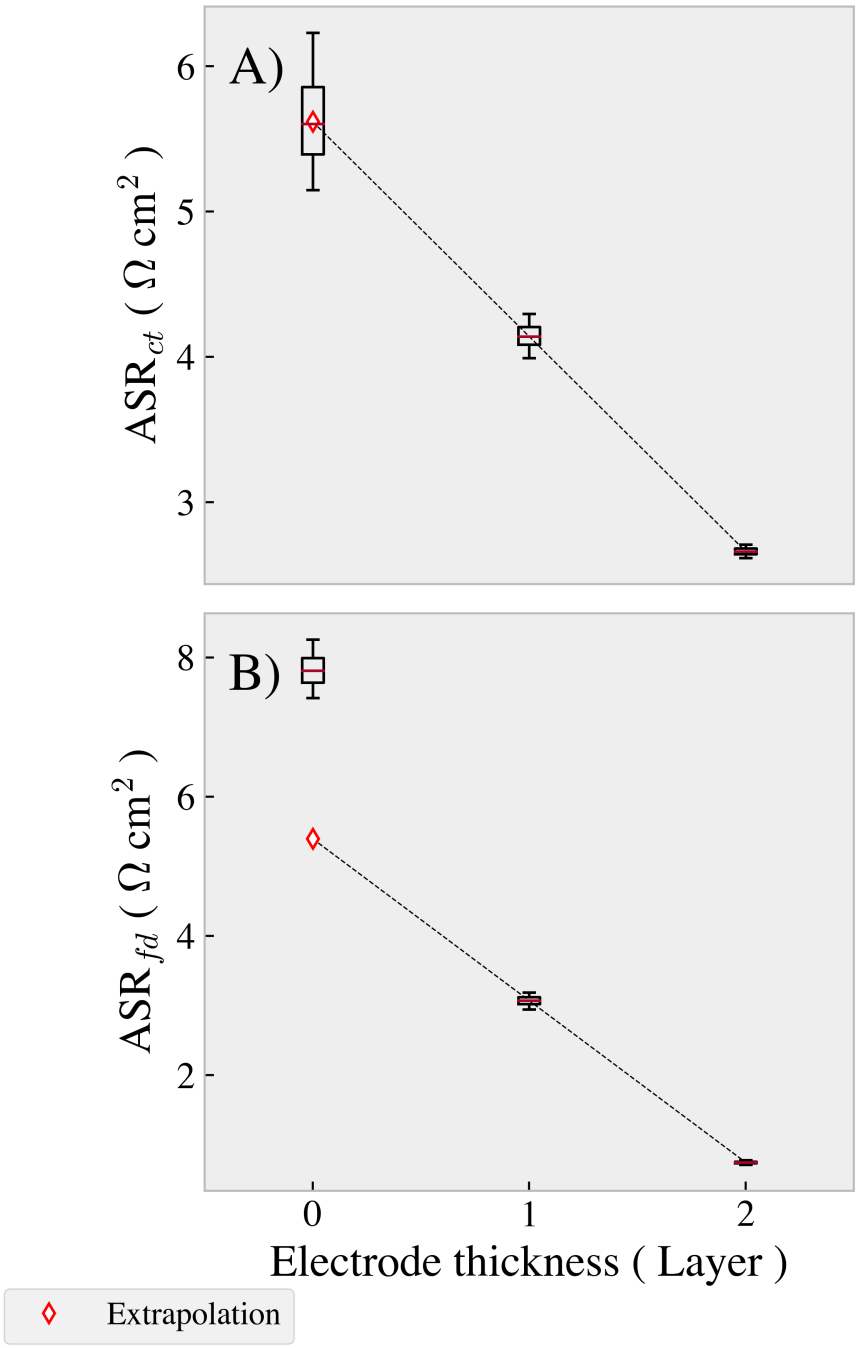

Figure 3.7: Effect of stacked electrodes on (A) charge transfer ASR and (B) finite diffusion ASR measured at open circuit.

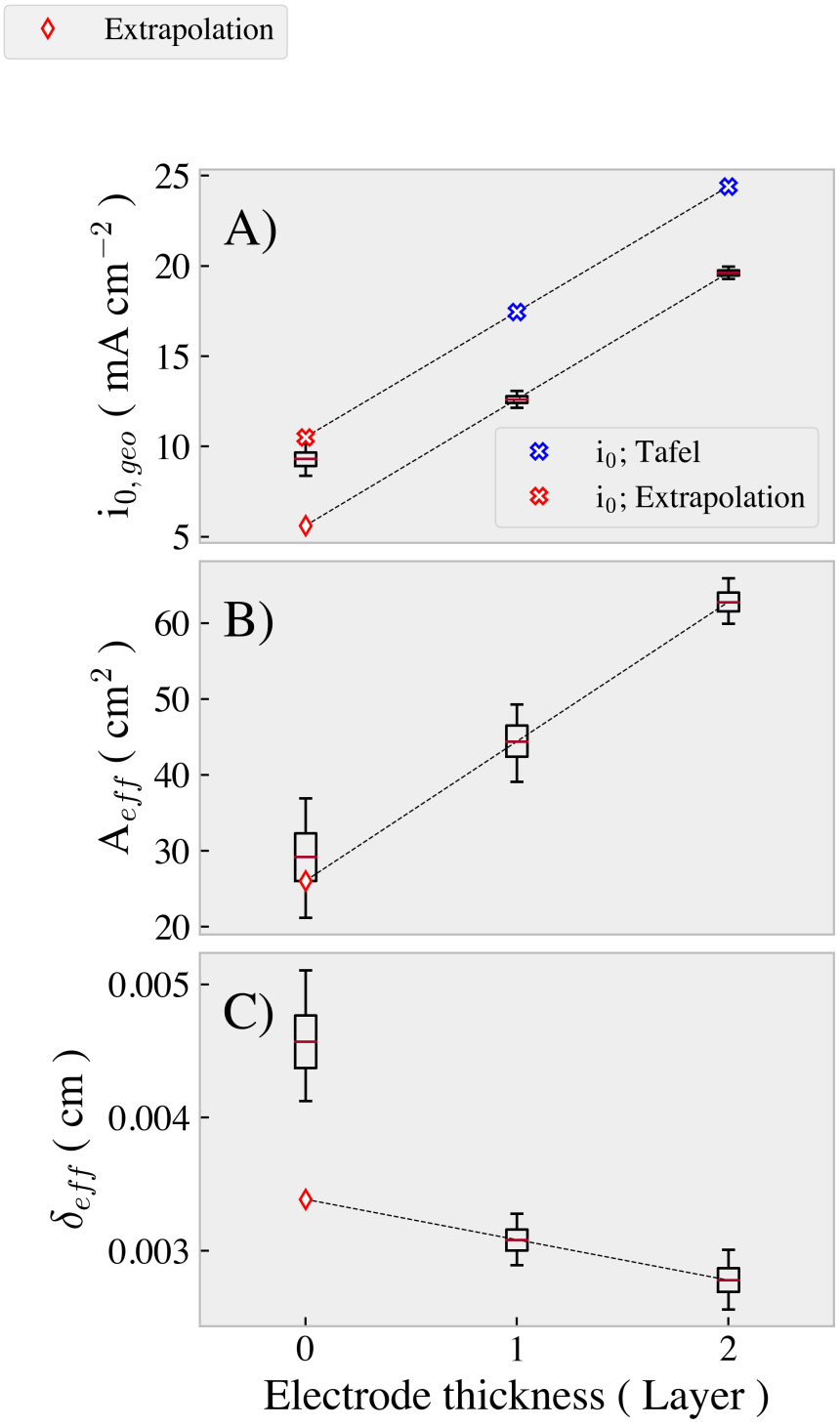

Figure 3.8: Effect of stacked electrodes on (A) geometric exchange current density ($i_{0,geo}$), (B) effective surface area (A_{eff}), and (C) diffusion boundary layer thickness (δ_{eff}). The linear fits are the values projected to zero thickness using one and two layers.

for the GFD3 layers, the projection is at the center of the distribution, where it is expected that a background signal exists (from Figure 3.5). Because the channel electrode is approximately planar, it is expected that the diffusion ASR will be larger than it is for the layered electrodes because its exposed surface area is approximately planar as opposed to the porous matrix of the GFD3 electrodes. This is the case in Figure 3.7 (B) where the diffusion resistance is large and dissimilar from the extrapolation of the stacked GFD3 electrodes.

Recall from Figure 3.3 that the charge transfer overpotential of the channel is nearly a linear function of current. Figure 3.8 (A) shows the comparison between the geometric exchange current densities estimated with the Randles circuit as well as with the Tafel-estimated values. Clearly the Tafel and Randles extrapolations disagree, differing by almost 100%. The Tafel-extrapolation, however, is inside the 95% confidence interval for the MC data estimated geometric exchange current density calculated on the channel electrode.

Figure 3.8 (B) shows the MC data distributions for the effective surface area. The extrapolation to zero thickness lies well inside the second quartile of the distribution for the effective surface area. Figure 3.8 illustrates some very important aspects of the combination of the electrodes with the channel. First, the effect of the nonlinear coupling of the activities makes the activity of the electrodes inaccurately estimated at open circuit. It was observed in Section 3.3.3 that the channel can account for up to a third of the current as the electrode begins to deviate from open circuit. There is no reason to assume that the specific properties of the channel are similar to those of the layers of graphite felt. Indeed, the MC data results

suggest that the channel has a higher geometric exchange current density than a single layer of felt with an almost vanishingly small thickness. Second, analysis of (C) in Figure 3.8 shows the Randles circuit confirming that the larger diffusion resistance for the channel is highly correlated to the diffusion layer thickness. In the case where the diffusion layer thickness is large, it can make the channel surface less-accessible than the porous matrix of the GFD3 electrodes. When the porous electrode + channel is polarized, such as it is in the conditions for the Tafel polarization, the channel component becomes completely mass transport limited and the shorter diffusion length (to the porous surface) becomes the favorable pathway for the reaction to proceed and the kinetics of the GFD3 electrode can be quantified. The higher capacitance and exchange current density form a more favorable interface at open circuit and the kinetics of the electrode are heavily biased by this.

Because the cell exhibits virtually no mass transfer polarization at all the measured potentials, we hypothesize that the surface area at open circuit underestimates the true surface area of the graphite felt layers. The previous analysis suggests the question: *are the surface area data valid if the exchange current densities are estimated with low accuracy*? Sensitivity analysis of Equation 3.2 shows that the Randles circuit model is far more sensitive to the wetted surface area (orders of magnitude), than it is to the exchange current density. The purpose of this analysis is not to posit objectively about the magnitude of the electrochemical surface area and activity, but rather to point out the inconsistencies that can arise when analyzing data at open circuit where the channel capacitance and activity can be coupled in the signal. Such analysis is useful when parameter estimations are needed for

more comprehensive models.

3.4 Conclusions

In this work, the contributions of the graphite BPPs to the estimation of kinetics parameters at the anode were observed and quantified. The contributions to the cathode in this instance could not be reliably quantified, as the cathode channel is mass transport limited at open circuit which implies a non-uniform current distribution upon polarization. The approximate magnitude of the current supported by the plates ($\approx$ 34%) was estimated by determination of the onset potential for mass transport overpotential at the anode channel which allowed for decoupling of the polarization curves with one and two layers of felt. Finally, the plate and porous electrode kinetics were decoupled by comparing the Randles circuit estimated values for the geometric exchange current density to those estimated with Tafel analysis. It was found that using an unmodified Randles circuit yields a geometric exchange current density that differs by $\approx$ 36% from the Tafel-estimated value. The nonlinear relationship between the addition of electrode material at open circuit was proposed to be an effect of the coupling between the double layer capacitance and rate constant of the channel with the electrode. These results indicate that when a reaction has sluggish kinetics, the decoupling of the effects from bipolar plates can be helpful in estimating kinetics parameters accurately.

Chapter 4

Graphene and Graphitic Carbon Nitride Quantum Dot Decorated Carbon Electrodes for Energy Storage in Vanadium Redox Flow Batteries

This chapter is a revised version of the published paper: [130]

M. C. Daugherty, S. Gu, D. S. Aaron, R. E. Kelly, Y. Ashraf Gandomi, and C.-T. Hsieh. Graphene quantum dot-decorated carbon electrodes for energy storage in vanadium redox flow batteries.Nanoscale, 12(14):7834–7842, 2020.

My contributions to this work were collection, reduction , and analysis of data and manuscript composition. Gu and Kelly assisted with data collection. Hsieh assisted with manuscript composition.

Abstract

Nitrogen-doped graphene quantum dots (GQDs) and graphitic carbon nitride (g-C_3N_4) quantum dots were synthesized via a solid-phase-microwave-assisted (SPMA) technique. The resulting GQDs were deposited on graphite felt (GF) and were employed as high-performance electrodes for all-vanadium redox flow batteries (VRFBs). The SPMA method is capable of synthesizing highly oxidized and amidized GQDs using citric acid and urea as the precursor. As-prepared GQDs contain an ultrahigh O/C (56-61%) and N/C (34-66%) atomic ratio, much higher than the values reported for other carbon-based nano-materials (e.g. oxidized activated carbon, carbon nanotubes, and graphene oxide). Three types of quantum dots, having an average particle size of 2.8-.2 nm, were homogeneously dispersed onto graphite felt electrodes, forming GQD/GF composite electrodes. Polarization curves and electrochemical impedance spectroscopy were utilized to assess the durability and capacity retention for VRFBs with hybrid GQD/GF electrodes. Through deposition of GQDs onto the electrode structure, the catalytic

activity, equivalent series resistance, durability, and voltage efficiency were improved. The theoretical capacity utilization using GQD/GF electrode was substantially enhanced (~69% increase within 40 cycles). The improved performance was attributed to the synergistic effect of GQDs containing oxygen functionalities (epoxy, phenolic and carboxylic groups) and lattice N atoms (quaternary, pyrrolic and pyridinic N) which resulted in enhanced wettability and increased surface electrochemical surface area providing increased reaction sites.

4.1 Introduction

The environmental issues associated with the use of fossil fuels as well as energy security have necessitated the integration of renewable energy sources onto electrical grids [131, 132]. Rapidly decreasing costs associated with wind and solar energy sources further motivates stationary energy storage systems to be designed based on renewables for maintaining a reliable energy economy [46]. Thus, there exists a significant need for advanced energy storage devices capable of reliable integration within the grid. Redox flow batteries (RFBs), due to a flexible architecture, are promising devices for independently scaling power as well as energy storage capacity for various applications [133–136]. The all-vanadium redox flow battery (VRFB), which utilizes vanadium in different oxidation states at the anode and cathode, has been studied and proposed for this purpose.

Carbon-based materials are most commonly used as electrodes in VRFB architecture supplying an electrically conductive open porous structure for electrolyte flow [124, 137]. Graphite felt (GF) is a commonly used electrode material with

average fibers diameters of 8-10 μm, capable of a wide voltage stability window and chemically robust; however, low surface area and low electrocatalytic activity (i.e., poor kinetics) limit its application as high-performance VRFB electrodes [101, 102, 112]. Therefore, an appropriate treatment strategy (e.g. chemical, thermal, and electrochemical) must be implemented on GF electrodes for promoting higher electrocatalytic activity toward the redox reactions occurring within a VRFB system. Previous efforts have been dedicated to a variety of strategies such as heat treatment of as-received electrodes [36, 138], hydroxylation [112], modification with graphene sheets [132,139], utilization of carbon nanotubes [101], metallic electrodes [121], graphite oxide [140], and mesoporous carbon [141].

Recently, graphene quantum dots (GQDs) have garnered significant attention due to their environmental friendliness, green synthesis route, and excellent biocompatibility, compared to that of fluorescent semiconductor quantum dots, which typically consist of toxic heavy metals (e.g., Cd) to achieve high-intensity fluorescence [142, 143]. GQDs are ultra-small pieces of graphene (particle sizes range from 3 to 20 nm) consisting of no more than 5 layers [44]. These favorable characteristics of GQDs inspired the present work where GF electrodes were doped via homogeneous dispersion of GQDs along with Nafion ^{TM} (serving as a binder and proton exchange layer) onto the GF microstructure. The resulting electrode morphology resulted in improved activity toward the negative redox couple employed in VRFBs (i.e., V^{2+}/V^{3+}).

The GQD configuration, however, must be engineered for increasing the accessible surface area (i.e., electrochemically wetted surface) as well as enhancing

the surface functionalities (i.e. increased number of active sites) for high oxidation/amidation level. Recently, a solid-phase-microwave-assisted (SPMA) technique for synthesizing N-doped GQDs and graphitic carbon nitride (g-C_3N_4) quantum dots using various carbon precursors was demonstrated by Gu *et al.* [45]. The as-prepared GQDs exhibited high oxidation/amidation due to the increased presence of oxygen (e.g., hydroxyl (-OH), carbonyl (C=O), and carboxyl (O=C- OH) groups) / nitrogen functionalities (e.g., amide-carbonyl group(O=C-NH_2), pyridine, pyrrole, and quaternary type N sites) at the edges or on basal planes of the GQDs.

For VRFBs, the determination of which half-cell has a higher rate constant is dependent on the electrode composition [37]. It is, however, established that the kinetics associated with the untreated PAN-based carbon electrodes is particularly sluggish at the anode [77]. The electrocatalytic activity of the electrodes can be enhanced via improving the surface hydrophilicity (i.e. surface wetting) as well as creating oxygen functional groups serving as active sites for catalyzing redox reactions [36, 46, 47]. Doping graphene with nitrogen has also been suggested for increasing the the electrical conductivity of the carbon structures [144–146].

These favorable characteristics of GQDs inspired the design and fabrication of the hybrid GQD/GF electrodes in this work. To the best of our knowledge, there are very limited prior reports on improving the catalytic activities of the GF electrodes modified by N-doped GQDs and CNQDs for VRFBs.

4.2 Experimental

4.2.1 Synthesis of quantum dots by SPMA method

N-doped GQD and CNQD samples were synthesized using the SPMA technique outlined in reference [45]. Employing the SPMA method, the citric acid (C source), urea (N source) and distilled water were uniformly mixed and subsequently heated at 280 °C for five minutes. Three electrolyte configurations were prepared where the citric acid/urea precursor was adjusted at 2:1, 1:1, and 1:2 with the solid content of 100 g per electrolyte treatment. A microwave reactor (total volume of 60 L) equipped with a microwave emitter (maximal power: 6,000 W) and a rotary sample plate was employed for synthesizing the samples. The entire SPMA process was carried out in air, resulting in a high production yield of 40-50 wt%. Upon cooling to ambient temperature, the N-doped GQD and CNQD samples were collected and sieved through a metallic screen (# 200 mesh). The solid precipitate was repeatedly dispersed and washed using deionized water. The powders were then centrifuged at 15,000 rpm for 10 min.

4.2.2 Materials characterization of quantum dots

Field-emission scanning electron microscope (FE-SEM) images were taken using a JEOL JSM-6701F electron microscope at an accelerated voltage of 10 kV. An X-ray diffraction (XRD; Shimadzu Labx XRD-6000) spectroscope, equipped with Cu-Kα radiation emitter, was employed to characterize the crystalline structures of the carbon samples. Raman spectra of carbon samples were recorded using a Renishaw Micro-Raman spectrometer. An inductively-coupled plasma optical emis-

sion spectroscopy/mass spectrometry (ICP-OES/MS) was used to characterize the chemical compositions of GQD samples. X-ray photoelectron spectroscopy (XPS, Fison VG ECSA210) equipped with Mg-Kα radiation emitter, was used for analyzing the chemical composition of the samples. The C 1s, N 1s and O 1s spectra were deconvoluted using a non-linear least square fitting algorithm with a symmetric Gaussian function. The surface compositions of the NGQD and CNQD powders were further quantified by applying a sensitivity factor.

4.2.3 VRFB cell architecture and GQD / GF composite electrode fabrication

To fabricate the composite electrodes, the GF sheets (electrode area: 5 cm^2; thickness: 3 mm; SGL GFD3) were impregnated in GQD/Nafion ^{TM} (Nafion ^{TM} 117, Sigma-Aldrich) suspension. The suspension (100 mL) contained 500 mg GQD powder and 2 vol.% Nafion monomer suspended in DI water. The chemical impregnation process was conducted at ambient temperature for 2 hours. The treated GF sheets were then dehydrated at 110°C in a vacuum oven to ensure that the GQDs were bonded with the GF, and the GQD/GF catalyst composite electrodes were coherently formed.

The cell architecture utilized in this work for all in-situ experiments was a 5 cm^2 (4 cm x 1.25 cm) rectangular flow through flow field. The cell and external electrolyte reservoirs were maintained at 30°C. Electrodes were compressed to 66% of their original thickness (1.98 mm) via teflon gaskets. The area specific electrolyte flow rate for all tests was 10 mL min^{-1} cm^{-2}. A Nafion ^{TM} 117 (Ion-Power Inc.)

membrane was used as the separator. The membrane was pre-treated via immersion in 3.3 M H_2SO_4 at 80°C for 30 minutes followed by immersion in 80°C DI water for 30 minutes. A reference electrode (Hg/Hg_2SO_4) was kept in contact with the membrane to assess the half-cell potential. A schematic of the cell architecture is included in the supplementary materials (Figure A.4).

4.2.4 Electrochemical performance of VRFBs using GQD/GF electrodes

All electrochemical measurements were performed with a BioLogic VSP potentiostat connected to a VMP3B-20 booster.

Symmetric Cell

A symmetric cell was utilized to characterize the behavior of the anode, which has been observed to be more limiting than the cathode for untreated GFD3 [77]. Electrolyte (1 M VO^{2+}3.3 M H_2SO_4) was coulometrically tuned to 50% SoC (.0005 mol cm^{-3} V^{2+}; .0005 mol cm^{-3} V^{3+}) with a 25 cm^2 charging cell. The anolyte was then used in symmetric cell experiments. In the symmetric cell configuration, one redox couple flows through both half-cells. This allows an approximation of steady state, with no crossover and constant SoC (barring side reactions). A reference electrode was kept in contact with the membrane to ensure that the overpotential was split approximately evenly between the two half cells. Schematics of the symmetric cell configuration and the full cell configuration are included in the supplemental materials (Figure A.7 and A.8 respectively). During the first four hours of electrolyte flow open circuit EIS was performed once per hour over a frequency

range of 100 kHz to 25 mHz with 10 points per decade at an amplitude of 5 mV. This allows the electrolyte and cell to reach the operating temperature (30°C) and for quantification of beginning-of-life (BoL) electroless performance degradation (degradation due solely to the exposure of electrolyte with no applied overpotential). Staircase potentiostatic electrochemical impedance spectroscopy (SPEIS) was then performed in voltage increments of 50 mV from 0 to 400 mV for the acquisition of impedance resolved polarization curves. Polarization curves were recorded three times to quantify BoL electrochemical degradation.

Full Cell

Following the identification of the highest performing citric acid/urea ratio, a full cell was assembled with the superior ratio to characterize full cell efficiencies and cycling performance. A full cell with untreated GFD3 was also cycled as a control for the treated electrodes. Cycling was performed galvanostatically at a current density of 100 mA cm^{-2} between 1.8V and 0.6V. It has been shown that using a cut-off voltage of 1.8 V degrades electrodes faster, however it allows higher SoC utilization than lower cut-off voltages and does not suffer greatly from gas-generation [147].

4.2.5 Impedance modeling and parameter estimation

EIS spectra were fit with a Randles circuit as shown in Equation (4.1)

$$AZ_{model,cell} = 2 \times AZ_{electrode} + ASR_{ohmic} \tag{4.1}$$

The symbols used in defining the mathematical model are listed in Table A.6. Because the overpotential is split approximately evenly between the two half-cells the single-electrode response is multiplied by 2. The single electrode is modelled as a faradaic impedance in parallel with a constant phase element.

$$Z_{electrode} = [Z_f^{-1} + (j\omega)^p Q]^{-1} \tag{4.2}$$

The faradaic impedance element (Z_f) consists of a charge transfer resistance in series with a Warburg element with a transmissive boundary as seen in Equation (4.3) [38,39].

$$A_t Z_f = \frac{RT}{i_0 F} + \frac{RTa}{fF^2 C_R D_R} \frac{tanh\left(a\sqrt{\frac{j\omega}{D_R}}\right)}{a\sqrt{\frac{j\omega}{D_R}}} + \frac{RTa}{fF^2 C_O D_O} \frac{tanh\left(a\sqrt{\frac{j\omega}{D_O}}\right)}{a\sqrt{\frac{j\omega}{D_O}}} \tag{4.3}$$

The Faradaic impedance given in Equation (4.3) is associated with a differential element of electrode surface. Calculation of the individual area specific resistance components is achieved by taking the limit of (4.3) as the frequency approaches zero. The first term in (4.3) is the differential charge transfer resistance.

$$ASR_{charge\ transfer} = \frac{ART}{A_t F i_0} \tag{4.4}$$

Likewise, the transmissive boundary Warburg element is given by the second and

third terms in (4.3). Note that,

$$\lim_{\omega \to 0} \frac{tanh\left(a\sqrt{\frac{j\omega}{D_O}}\right)}{a\sqrt{\frac{j\omega}{D_O}}} = 1 \tag{4.5}$$

Which leads to the expression for the diffusion ASR:

$$ASR_{diffusion} = \frac{ARTa}{A_t f F^2}\left(\frac{1}{D_R C_R} + \frac{1}{D_O C_O}\right) \tag{4.6}$$

The ohmic ASR includes both the series and distributed (pore electrolyte resistance) ohmic components. Because an unmodified Randles circuit does not capture the distributed resistance feature at high frequency, which manifests as a 45°line on Nyquist plots, spectra were fit at frequencies below this feature. It is noted that the intercept of the fitted spectra with the real axis at high frequency is constituted of both of these ohmic components. The double layer capacitance (CPE_{dl}) is calculated as a constant phase element as given by Brug et al. [117].

$$CPE_{dl} = Q^{\frac{1}{p}}\left(\frac{R_{ohmic}R_{ct}}{R_{ohmic} + R_{ct}}\right)^{\frac{1}{p}-1} \tag{4.7}$$

Impedance resolved polarization curves were calculated by integrating each of the area specific resistances (ASR) with respect to current density i.

$$\eta_x(i) = \int_0^i ASR_x(i)di \tag{4.8}$$

where the subscript x represents charge transfer, diffusion, and ohmic overpoten-

tial components. The cell voltage (V_{cell}) at a given current, then, is the sum of these overpotentials.

$$V_{cell}(i) = \sum \eta_x(i) \tag{4.9}$$

4.3 Results and discussion

Three different configurations of GQD electrodes were prepared; QD-1, QD-2, and QD-3, with the weight ratio of citric acid to urea adjusted at 2:1, 1:1, and 1:2, respectively. Figure 4.1(a) depicts typical XRD patterns of all GQD samples, where a major peak around 26-29°can be identified. As illustrated in Figure 4.1, both QD-1 and QD-2 samples contain one feature at 27.3-27.5°demonstrating sp2-layered stacking crystals with an average $d_{(002)}$ = 0.324-0.327 nm.

For quantifying the crystal size, Bragg's Law was employed [148]. In contrast, the QD-3 sample had twin-peaks at 27.5 and 28.1°, mainly originating from the (002) inter-layer planes of graphite and g-C_3N_4 crystals [45, 149]. The corresponding average crystal size at 27.5°and 28.1°were $d_{(002)}$ = 0.324 and 0.317 nm; respectively. In a recent publication detailed analysis was provided on the structural change during crystallization due to the pyrolysis of citric acid and urea precursors [150].

The degree of graphitization of carbon-based materials can be characterized using Raman spectroscopy. The Raman spectra of GQD samples were recorded (see Figure 4.1(b)) using a laser at an excitation wavelength of 1048 nm. Three major peaks can be identified in the Raman spectra: the D band (ca. 1350 cm^{-1}), the G

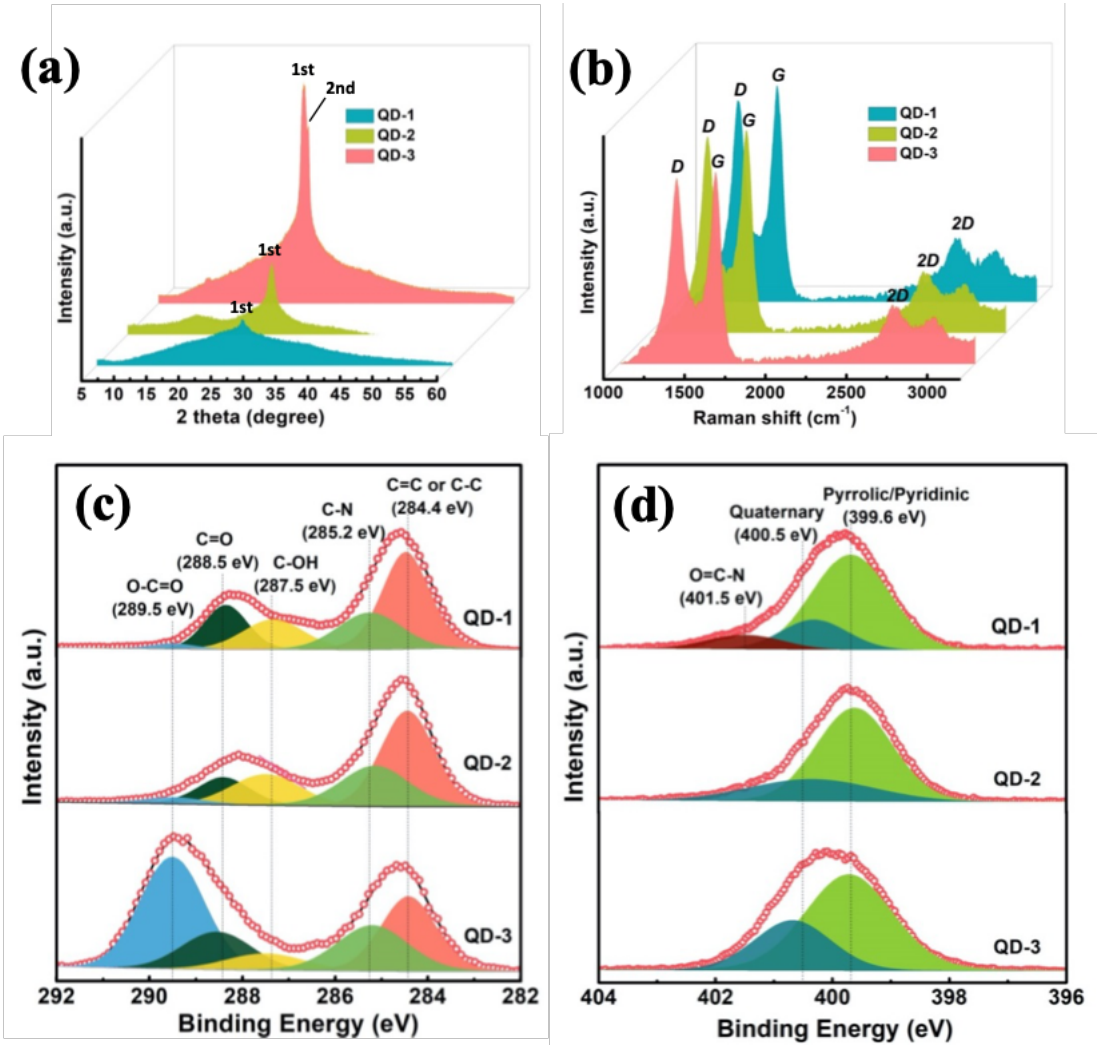

Figure 4.1: (a) XRD patterns and (b) Raman spectra of QD-1,Qd-2, and QD-3 samples. XPS (c) 1s and (d) N 1s peaks of QD-1, QD-2 and QD-3 samples

band (ca. 1580 cm^{-1}), and the 2D band (ca. 2700 cm^{-1}). The intensity ratio of the D to G band, ID/IG, can be used for assessing the graphitic quality of carbon-based materials [151]. The ID/IG ratios were within the range of 0.94-0.97 for all GQD samples. Thus, all the samples synthesized via the SPMA method possess a similar crystalline microstructure, confirming a non-detrimental influence of the precursor configuration (i.e., the weight ratio of citric acid to urea) on the crystallinity.

XPS was carried out to investigate the chemical composition of the GQD samples. Figures 4.1(c) and (d) present a detailed scan and C 1s and N 1s spectra of all the samples. In the XPS spectra, both the C 1s and N 1s peaks were deconvoluted using a multiple Gaussian function. First, the C 1s spectra was decomposed into five peaks at 284.4 eV (C=C or C-C), 285.2 eV (C-N), 286.5 eV (C-O), 288.5 eV (C=O), and 289.5 eV (O-C=O), respectively. Therefore, a large amount of surface oxygen functional groups were added to the edge sites or basal plane of the carbon surface, improving hydrophilicity. Commonly, the carboxyl (O-C=O) and carbonyl (C=O) groups tends to attach to the edge sites of the graphene sheet, while phenolic (C-OH) and epoxy (C-O-C) groups favor bonding to the basal planes [152]. Of note, the fraction of C-O and O-C=O groups demonstrate the following order: QD-2 (57.9%) > QD-3 (42.2%) > QD-1 (31.3%). This decreasing trend is primarily caused by the functional groups containing -OH that serve as the active sites for catalyzing VO^{2+}/VO_2^+ and V^{2+}/V^{3+} reactions [32, 36].

Deconvolution of N 1s peaks into three components at pyrrolic/pyridinic N at 399.6 eV, quaternary N at 400.4 eV, and N-oxides (e.g., O=C-N) at 401.4 eV [145,153] has been illustrated in Figure 4.1(d). All the GQD samples mainly possess pyri-

dine/pyrrole and quaternary N groups. Accordingly, during the SPMA process, the intramolecular dehydration or decarbonylation is more likely to occur promoting the generation of thermally-stable heterocyclic aromatic moieties such as pyridine, pyrrole, and quaternary type N sites ("lattice N") [154]. The SPMA method facilitates the insertion of nitrogen atoms into the graphene sheets (i.e., the formation of pyridinic N and pyrrolic N). The post-insertion analysis reveals that the ratio of pyridinic/pyrrolic N to quaternary N has a following order: QD-1 (3.5) > QD-2 (3.1) > QD-3 (1.4), where the last one approaches that of triazine-based g-C_3N_4 [153]. This observation confirms the presence of g-C_3N_4 within QD-3 sample, which is in good agreement with the XRD analysis.

Figures 4.2(a)-(c) show HR-TEM micrographs of the samples. As illustrated in Figure 4.2, the GQDs have been homogeneously dispersed within the samples. The corresponding diagrams of particle size distribution are also shown in Figures 4.2(d)-(f). According to Figure 4.2, the QD-3 sample demonstrates the narrowest distribution with the smallest average particle size among all the samples. The average particle sizes were ca. 4.2, 4.1, and 2.8 nm for QD-1, QD-2, and QD-3 samples, respectively. It is important to note that the composition of the carbon precursor strongly influences the particle size as well as the lattice fringe, as shown in the inset of Figures 2(a)-2(c). Herein the dashed white curves were used to outline the edges for each particle. The patterns confirm superb crystallinity with a lattice distance of 0.21-0.22 nm, assigned to the (1120) lattice fringes of the graphene sheets [155]. In a previous study [45], molecular dynamics (MD) simulations have been employed to confirm the atomic structures at ambient temperature, as shown

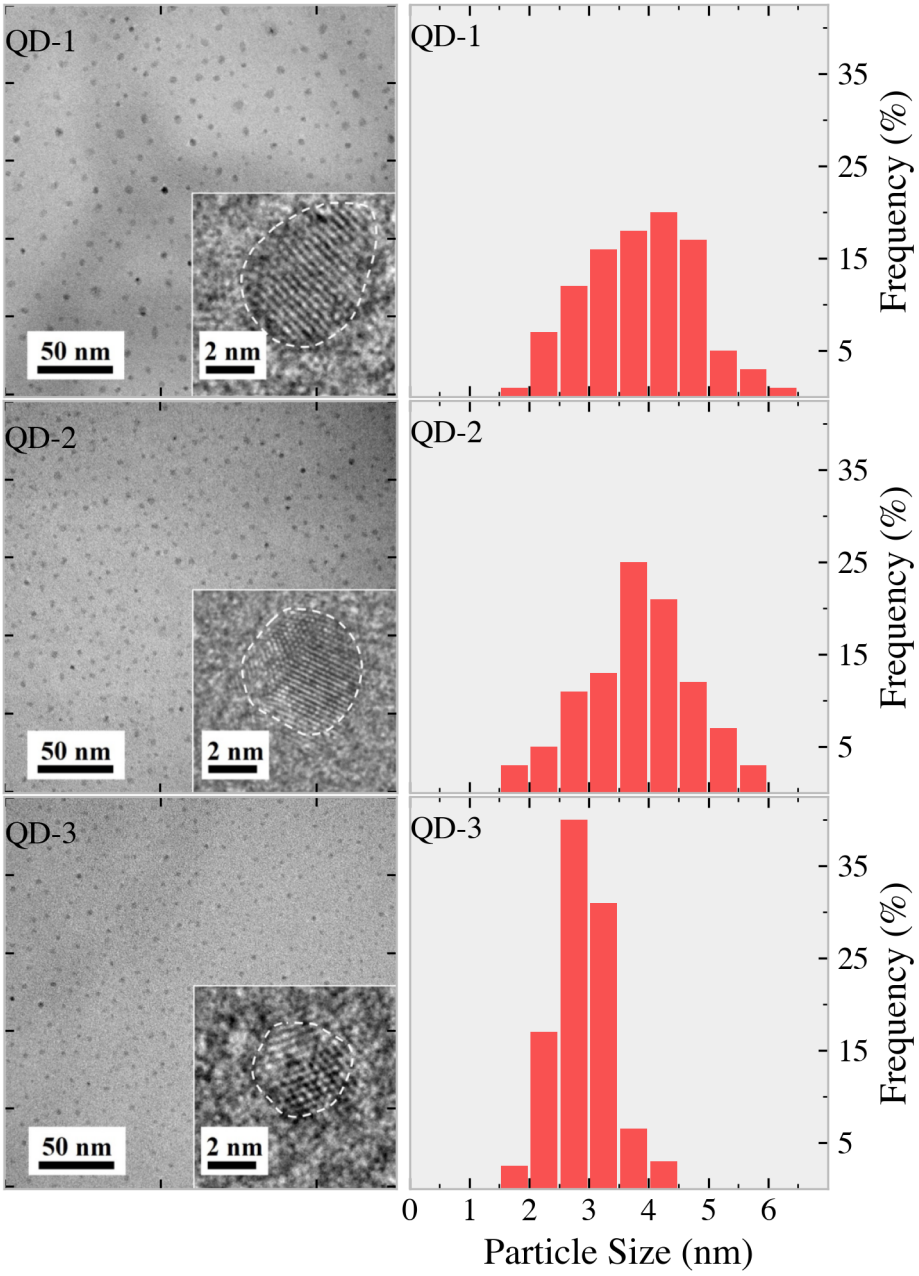

Figure 4.2: HR-TEM micrographs of QD-1, QD-2 and QD-3 samples, where inset shows their corresponding lattice fringes. Particle size distributions are shown in the histograms on the right for the respective treatments

in the Electronic Supporting Information (see Figure A.3).

Figure 4.3(a) illustrates the schematic diagram of the synthesis route for the hybrid GQD/GF catalyst electrode where homogeneous dispersion of GQDs within the microscaled carbon fibers can be identified. In the GQD/GF electrodes, GQDs serve as active sites for catalyzing the negative redox couple (i.e. V^{2+}/V^{3+} at anode) as shown in Figure 4.3(c), respectively. Polarization and EIS analysis were employed on the symmetric cell to evaluate the overpotential distributions at the anode and to gain insights into transient behavior of the different treatments. Figure 4.4 demonstrates the quality of the model fit on these spectra in the complex plane. The column on the right illustrates the progression from the initial spectrum to the final for each of the treated electrodes as well as the untreated GFD3. The ASR magnitudes and values for the fitted parameters for each spectrum are shown in Table 4.1. The model suggests a slight decrease in the exchange current density for the treated electrodes over the untreated, however, increasing the double layer capacitance by almost two (from untreated to QD-2) is the source of kinetic improvement. This result is in agreement with a previous report that the addition of oxygen functional groups can improve hydrophilicity, it can also lead to a loss of electrochemical activity [156].

The symmetric cell protocol captures two different degradation phases referred to as: electroless and electrochemical. Figure 4.5 illustrates the transient behavior of the open circuit impedance of the electrodes during these different stages in the experiment: electroless (first 5 points) and electrochemical (final 4 points). The

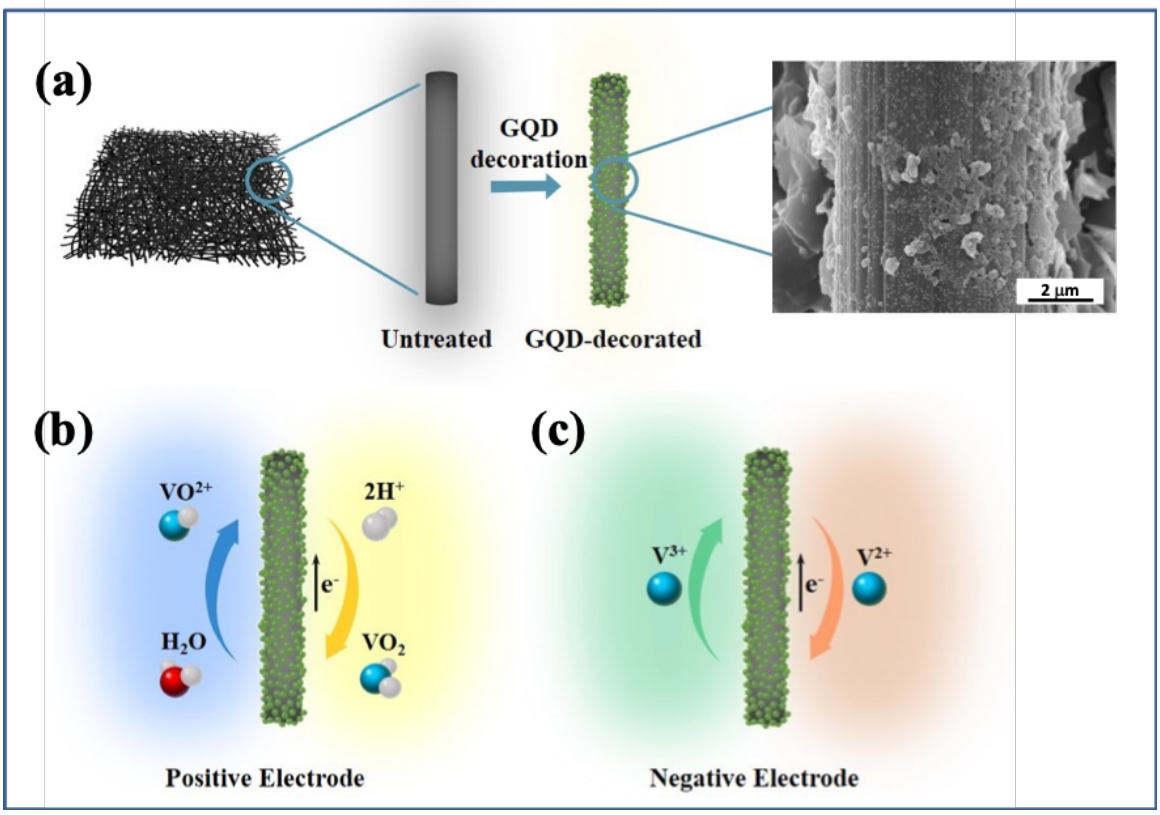

Figure 4.3: Schematic diagram illustrating (a) the procedure of GQD/GF composite electrode for VRFBs and reversible redox pairs at (b) positive and (c) negative electrodes, where GQDs serve as active sites for catalyzing the redox couples.

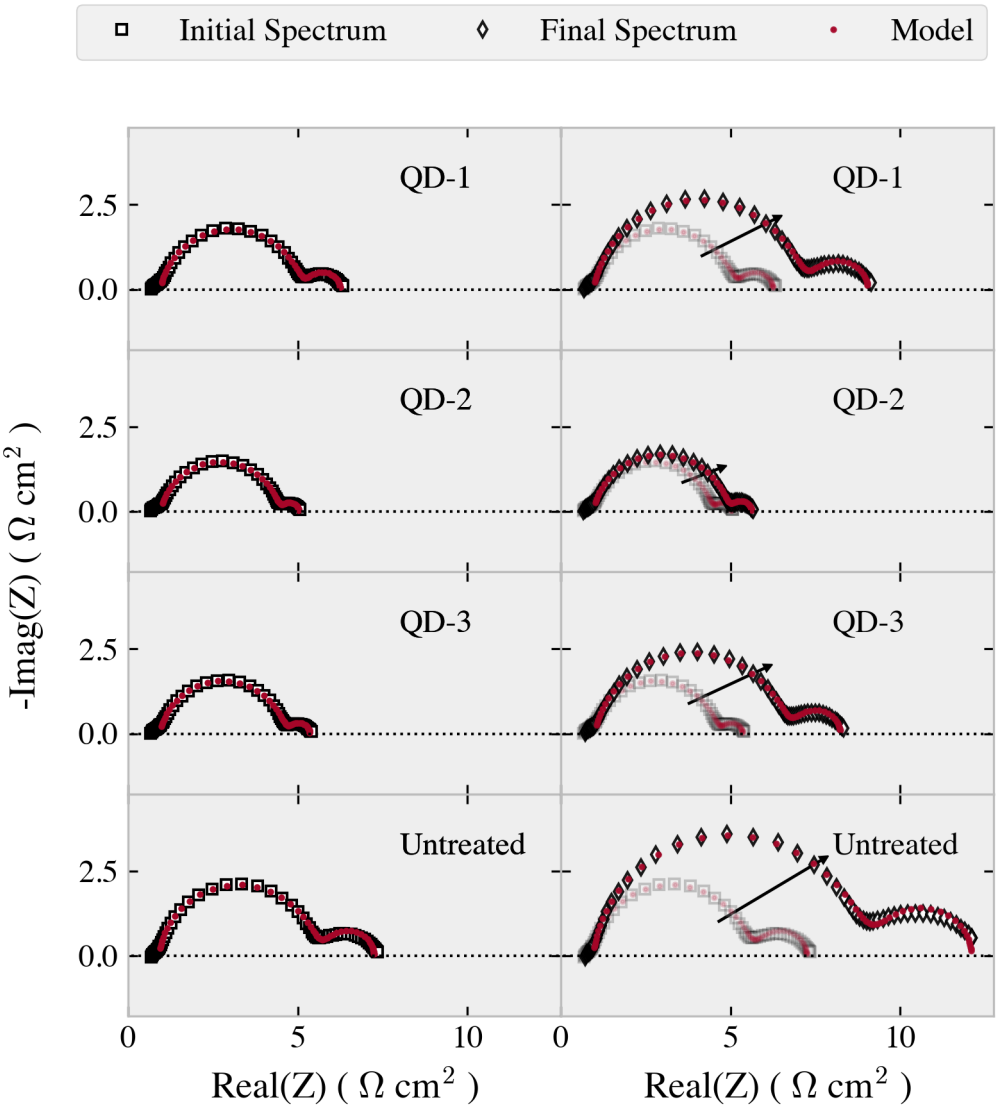

Figure 4.4: EIS Spectra and fits fo reach electrode treatment. The left column shows the initial spectrum and the right shows the initial (semi-transparent) and the final spectra

Table 4.1: ASR magnitudes and fitted parameters for the spectra shown in Figure 4.4

	QD-1	**QD-2**	**Qd-3**	**Untreated**
ASR charge transfer ($\Omega\ cm^2$)	4.09	3.46	3.67	4.56
ASR diffusion ($\Omega\ cm^2$)	1.20	0.60	0.74	1.76
ASR ohmic ($\Omega\ cm^2$)	0.95	0.95	0.93	0.93
Double layer capacitance (mF)	2.62	3.39	2.98	1.98
Exchange current density ($\mu A\ cm^{-2}$)	0.25	0.22	0.23	0.37
Diffusion layer thickness (μm)	7.90	8.17	8.18	6.36
P (CPE exponent)	0.90	0.89	0.89	0.93
f (Scale factor)	0.03	0.05	0.05	0.03

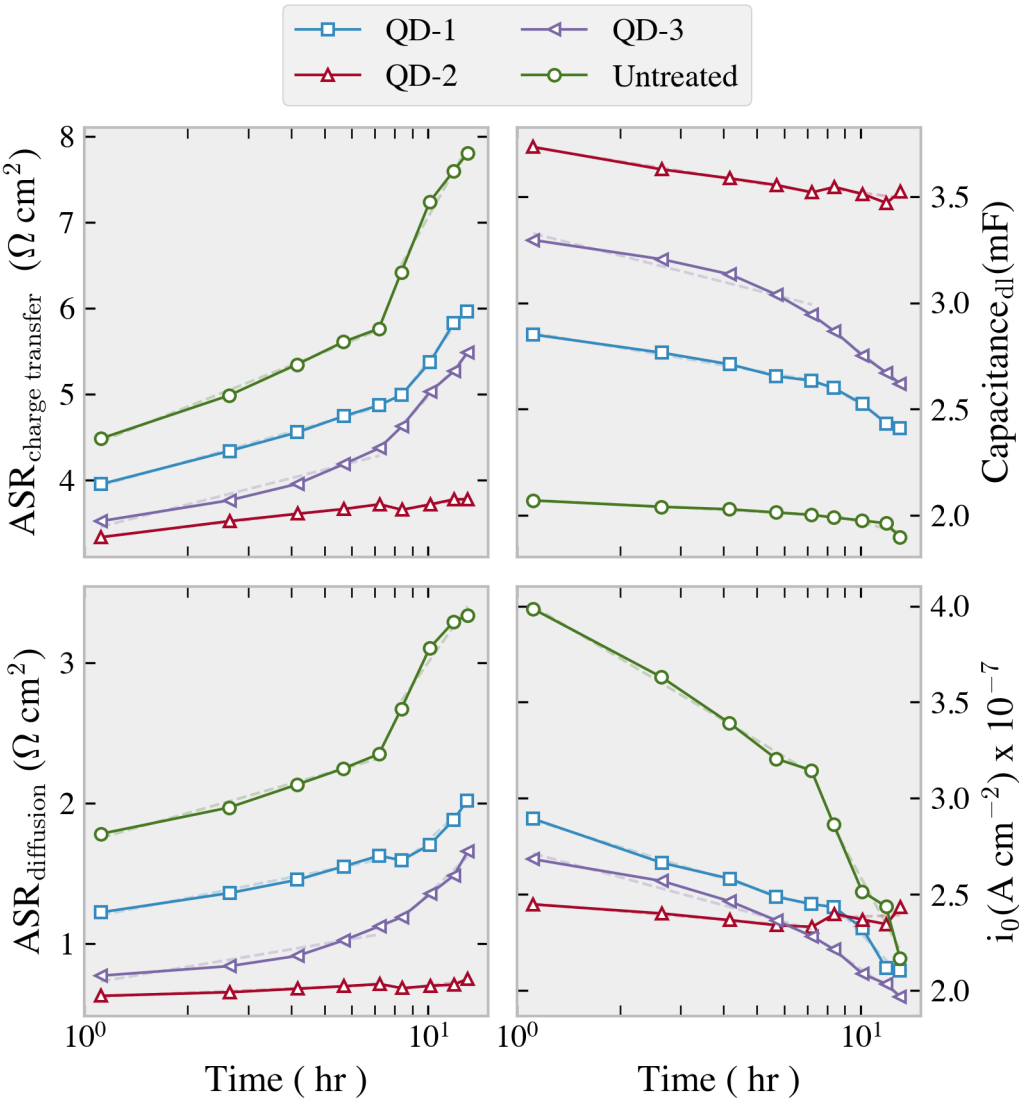

Figure 4.5: Evolution of open circuit charge transfer ASR, diffusion ASR, capacitance and exchange current density with respect to time. Each treatment is shown with 2 linear fits: 1) electroless degradation regime (first 5 points) and 2) electrochemical degradation regime (final 4 points).

plots on the left side show the progression of the diffusion and charge transfer ASR components. The separation between the degradation regimes is highlighted by independent curve fits. All the electrodes exhibited some electroless degradation, which has been observed in VRFBs and is more detrimental in anolyte than in catholyte [74]. During the electroless degradation period the QD-1, QD-3 and untreated electrodes each saw an increase in charge transfer between 23-27% as well as an increase in diffusion ASR of between 33-45%, while the QD-2 had charge transfer and diffusion ASR increases of 12 and 13% respectively. The plots on the right side of Figure 4.5 show the double layer capacitance and exchange current density as a function of time. During the electroless degradation phase each of the electrodes experienced a decrease in double layer capacitance between 5-11%. The QD-1, QD-3 and untreated electrodes each had declines in exchange current density of 15-22%, while QD-2 had a decline of only 5%. These findings suggest that exposure to electrolyte reduces both the electrochemical surface area and the activity of the surface, manifesting in an increase in both charge transfer and diffusion resistances.

The electrochemical degradation regime was marked by increased decay rates for each of the electrodes aside from QD-2. The QD-1, QD-3 and untreated each experienced an additional increase in charge transfer ASR of 18-20% and an increase in diffusion ASR of 28-40%. Likewise, the double layer capacitance and exchange current density for QD-1 and QD-3 decayed an extra 9% and 12 % respectively. The untreated electrodes had the most significant decrease in activity during electrochemical cycling, decaying an extra 26% upon the onset of cycling.

These results suggest that integration of the GQDs into the electrode structure primarily enhances the electrochemical surface area and not the activity of the electrode surface.

The symmetric cell impedance resolved polarization curves are shown in Figure 4.6. The arrows indicate the progression from the first curve to the final curve. The maximum current density of 81 mA cm^{-2} at 0.4 V was recorded for VRFBs utilizing untreated electrodes. For the VRFBs with hybrid GQD/GF electrodes, improvement in the performance was achieved (i.e. the current density at 0.4 V for the hybrid electrodes were: QD-2 (120 mA cm^{-2}) > QD-3 (100 mA cm^{-2}) > QD-1 (90 mA cm^{-2}). Therefore, a ~50% increase in power density is achieved via decorating GQDs within pristine GF electrodes. It is important to note that the QD-2 hybrid electrodes demonstrated higher stability over extended polarization stress testing of the electrodes (i.e. the current retention associated with the samples were: QD-2 (98.5%) > QD-3 (91.1%) > QD-1 (90.8%)> untreated (90.7%)). For QD-1, QD-3 and the untreated electrodes the semi-transparent polarization curves show that the ohmic (blue) component remains consistent across the cycles, While Figure 4.5 shows an increase in diffusion resistance, it is clear from the impedance resolved polarization curves that the source of increased overpotential is primarily manifested in worsening kinetics (gray), which constitutes a higher portion of the overpotential at a lower current for each electrode. This behavior manifests in a full cell as more overpotential is required to maintain a given current resulting in achieving a cut-off voltage faster and at a lower SoC, which results in both lower SoC utilization and decreased voltage efficiency [111].

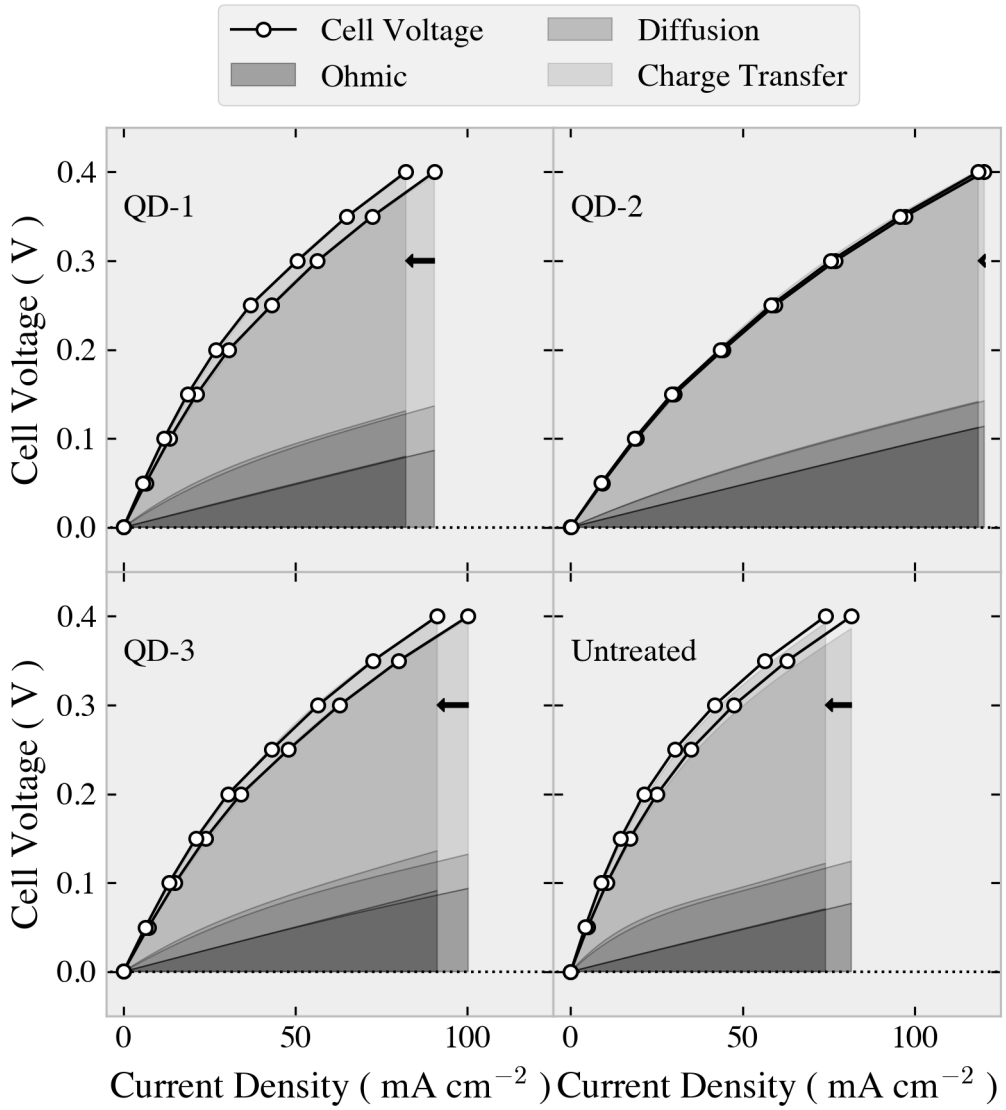

Figure 4.6: Impedance resolved polarization curves with QD-1, QD-2, QD-3, untreated GF electrodes at 50% SOC.

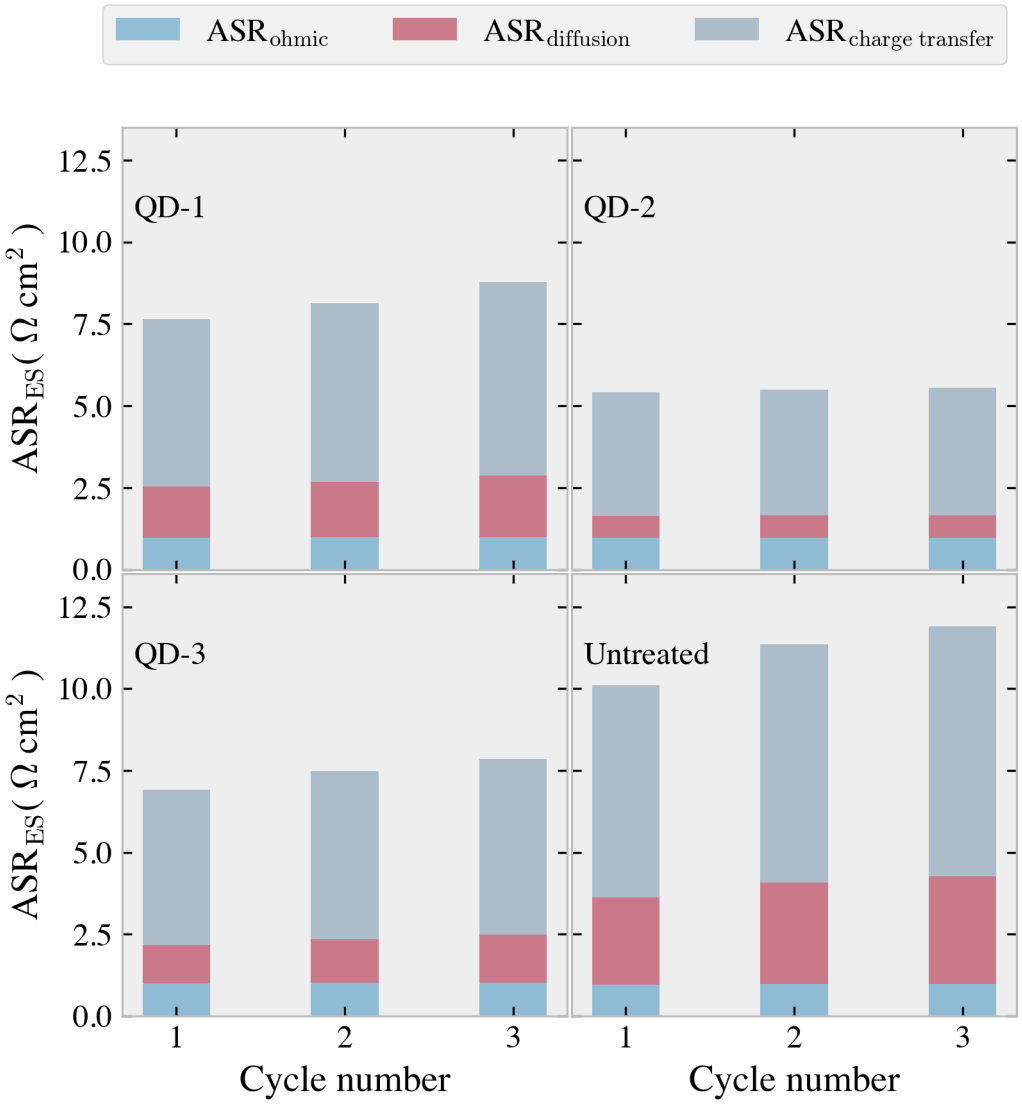

Figure 4.7: Distributions of equivalent series area specific resistance components by diffusion, charge transfer, and ohmic components at open circuit of the VRFBs based on the EIS analysis.

Figure 4.7 demonstrates overpotential distribution for various electrode configurations including pristine and hybrid GQD/GF electrodes. As shown in Figure 4.7, the equivalent series area specific resistance (ASRES), sum of ASRohmic + ASRcharge transfer + ASRdiffusion, for untreated GF electrode increases with increased cycle number, i.e., 9.7 Ω cm^2 (1st pol-curve cycle) and 11.9 Ω cm^2 (3rd pol-curve cycle). This is due to both lower electrochemical surface area and comparatively inferior kinetics which together lead to higher cell resistance of untreated GF electrode. In contrast, the ASRES value for QD-2 electrodes remains relatively unchanged during cycling confirming a durable catalytic activity achieved via decorating the GQDs within the electrode microstructure. In particular, the application of QD-2 electrode not only results in the lowest charge transfer resistance (ca. 3.65 Ω cm^2) among samples; but also demonstrates miniscule degradation during extended cycling. This improved durability can be attributed to the fact that QD-2 electrode possesses the largest amount of hydroxyl and carboxyl groups among the GQD/GF electrodes [138].

It is important to note that increased fraction of C-O groups (including phenolic, epoxy, and carboxylic groups) on the GQDs directly decreases the equivalent series resistance and subsequently improves the performance, as depicted in Figure 4.8(a). To further analyze the influence of GQDs on the improved performance, the distribution of active sites on highly O-/N-functionalized GQDs (i.e. basal plane: (i) dual phenolic groups (ring opening of one epoxy group in acid solution) and (ii) phenolic group and edge: (iii) carboxylic group) have been shown in Figure 4.8(b). The catalytic activity on the electrode surface increases as a function of

electrode wettability, which is typically due to the presence of oxygen functional groups [30, 138, 157]. The implantation of GQD/GF hybrid electrodes discussed in this work improves the kinetics for negative redox reactions. Reaction steps of V^{2+}/V^{3+} redox couple on the phenolic groups are provided in Figure A.6 [32]. Uniformly dispersed GQDs on GF electrode provide an increased number of active sites, and subsequently enhance the active surface coverage of GF electrode.

To explore the longer-term durability of the hybrid GQD/GF electrodes, extended charge-discharge cycling was performed at 100 $mA{\cdot}cm^{-2}$ (see Figure 4.9 (a) and 4.8(b)). As shown in Figure 4.9, utilizing hybrid GQD/GF electrodes increases the capacity utilization. The discharge capacity increased from 660 mAh (untreated electrodes) to 879 mAh (QD-2) resulting in 33% enhancement in capacity utilization. After 20 cycles, the discharge capacity of the untreated GF electrode decreases to 527 mAh (the capacity retention: < 80%), while the capacity retention of QD-2 electrode still remained as high as 91%. The voltage efficiencies for the untreated GF electrodes were 67.6% and 62.4% at 1st and 20th cycle, respectively. The voltage efficiencies were improved through the decoration of QD-2 sample, i.e., 78.7% (1st cycle) and 74.0% (20th cycle). Capacity retention and coulombic efficiency as a function of cycle number are depicted in Figure 9(c). After 40 cycles, the capacity of the battery assembled with untreated GF electrodes dropped by ~32%. Aside from crossover effects, one of the major contributors to the decreased voltage efficiency is associated with the cell reaching cutoff voltages at a lower SoC on account of increased overpotentials [127, 158, 159]. The VRFB cell utilizing QD-2 electrodes demonstrated improved capacity retention (~86%) dur-

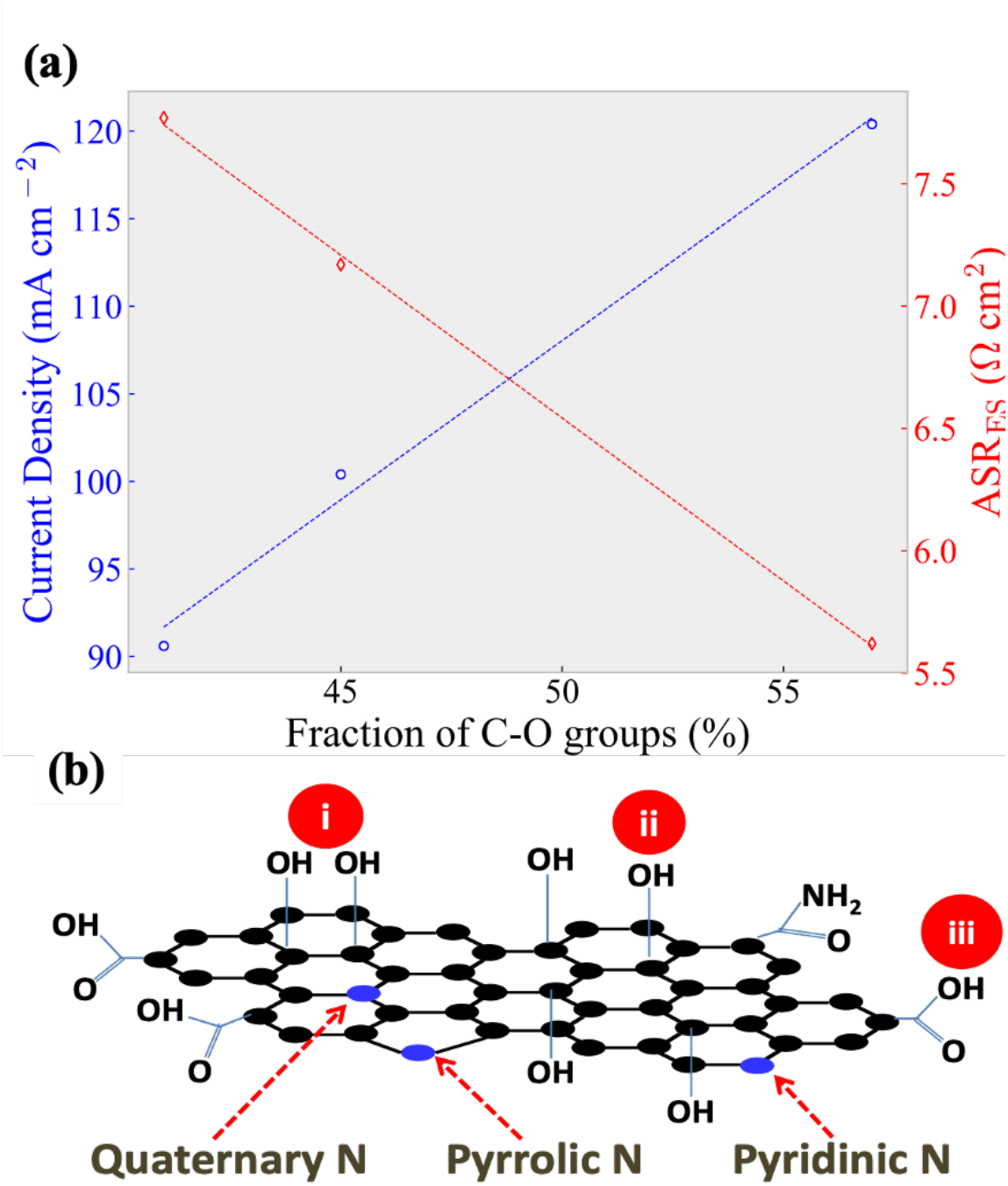

Figure 4.8: (a) Variation of current density (blue circles) and equivalent series resistance (red diamonds) with fraction of C-O groups on GQD/GF electrodes. The operating conditions of the VRFBs were overpotential of 0.4 V, 50% SOC, ambient temperature, and the first polarization curve cycle. Schematic illustration regarding the distribution of active sites on highly O-/N-functionalized GQDs, i.e., basal plane: (i) dual phenolic groups and (ii) phenolic group and edge: (iii) carboxyl group. The lattice "N" atoms induces a smaller charge transfer resistance during the redox reactions of VO^{2+}/VO_2^+ and V^{2+}/V^{3+} pairs.

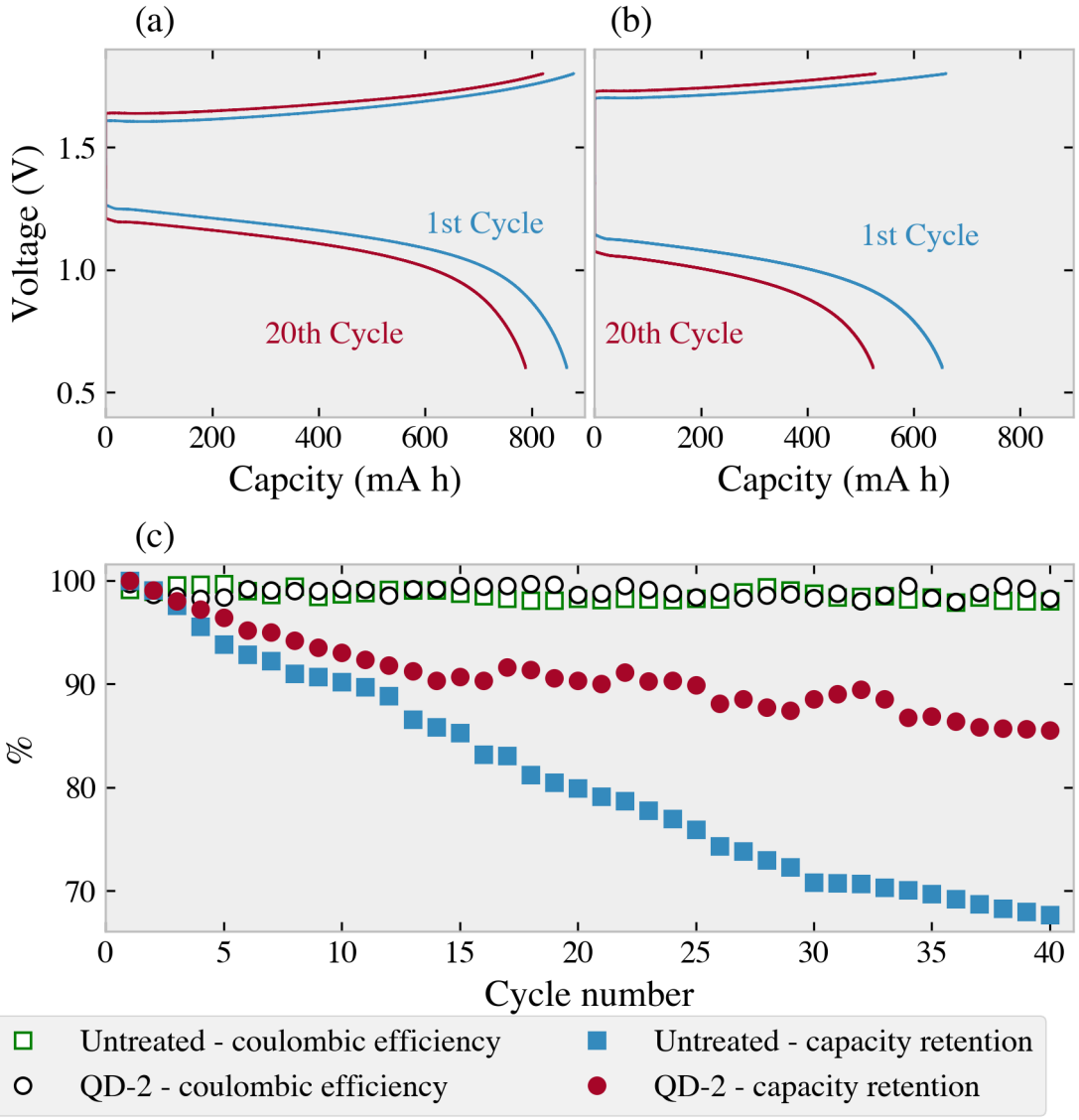

Figure 4.9: Charge-discharge curves of the VRFBs equipped with (a) QD-2 and (b) untreated GF at a constant current density of 100 mA cm^{-2}. Variation of capacity retention and Coulombic efficiency with cycle number shown in (c).

ing charge/discharge cycling thanks to improved catalytic activity and superior durability. The coulombic efficiency was also maintained at high values for both pristine (~98%) and hybrid GQD/GF electrodes (> 98.5%) upon extended cycling confirming excellent reversibility towards the redox reactions of V^{2+}/V^{3+} couple with GQD decorated electrodes.

4.4 Conclusions

We have improved the performance of all-vanadium redox flow batteries using GF electrodes decorated with N-doped GQDs and g-C_3N_4 quantum dots prepared by the SPMA technique. The SPMA method is very efficient, fast, and inexpensive, and results in highly crystalline GQD microstructure. Uniformly dispersed GQDs within the GF electrode form a hierarchical GQD/GF hybrid nano-structure. The as-prepared GQDs contained ultra-high O/C (56-61%) and N/C (34-66%) atomic ratio, exhibiting a synergistic effect toward increasing the surface area thereby decreasing the faradaic impedance for the redox reactions of the V^{2+}/V^{3+} couple. Through decorating GQDs, the durability and voltage efficiency of GF electrodes were improved during extended cycling by 3% and 11% respectively. Accordingly, the design of GQD/GF electrode provides a pathway towards nano-engineering electrode structure for improved durability in various energy storage devices including redox flow batteries.

Chapter 5

Decorating Sulfur and Nitrogen Co-doped Graphene Quantum Dots on Graphite Felt as High-Performance Electrodes for Vanadium Redox Flow Batteries

This chapter is a revised version of the published paper: [160]

M. C. Daugherty, S. Gu, D. S. Aaron, B. Chandra Mallick, Y. A. Gandomi, and C.-T. Hsieh. Decorating sulfur and nitrogen co-doped graphene quantum dots on graphite felt as high-performance electrodes for vanadium redox flow batteries. Journal of Power Sources, 477:228709, 2020.

My contributions to this work were collection, reduction, and analysis of data and manuscript composition. Gu and Hsieh assisted with data collection. Hsieh assisted with manuscript composition.

Abstract

This paper reports on decorating sulfur (S)/nitrogen (N) co-doped graphene quantum dots (S/N co-doped GQDs) on graphite felt as high-performance electrodes for vanadium redox flow batteries (VRFBs). The S/N co-doped GQDs are synthesized through an efficient infrared-assisted pyrolysis of glucose, urea, and ammonia sulfate at 280 °C. The S/N co-doped GQDs, having an average diameter of 6.2 nm, contain high oxidation, amidation, and sulfonation levels (45.8 (O/C), 22.7 (N/C), and 7.8 at.% (S/C), respectively). Electrochemical impedance spectroscopy is utilized to assess the overpotential distributions for VRFBs equipped with untreated GF and S/N co-doped GQDs/GF. With the aid of S/N co-doped GQDs, the catalytic activity, equivalent series resistance, durability, and voltage efficiency are substantially improved. The improved performance is attributed to the synergistic effect of GQDs containing O functionalities, lattice N atoms, and S dopants, facilitating surface catalytic activity and accelerating charge transfer

across the anode/anolyte interface for the vanadium redox couples (V(II)/V(III)). Accordingly, hierarchical S/N co-doped GQD/GF electrode paves the pathway for engineering the electrodes' nano-structure with improved catalytic activity and enhanced durability for redox flow batteries.

5.1 Introduction

Reliable, cost-effective, and high-performance energy storage technologies are needed for accelerating the integration of renewable energy sources (e.g. solar and wind) into the power grid. Redox flow batteries (RFBs) have gained considerable attention as a promising energy storage technology. Scalability, enhanced safety, and vast design flexibility are the most notable characteristics of RFBs. Different classes of electroactive materials (e.g. organic and inorganic) have been developed for RFB electrolytes; among them, all-vanadium redox flow batteries (VRFBs) have been the focus of major research and improvement in recent years. VRFBs utilize the same element (vanadium) in different oxidation states within the anolyte (V(II)/V(III)) and catholyte (V(IV)/V(V)). Therefore, VRFBs can be cycled extensively with no irreversible capacity decay due to cross-contamination (i.e. via undesired transport of vanadium ions through the membrane) [112, 161–164]. A typical all-vanadium redox flow battery reactor includes two half-cells separated by an ion exchange membrane/separator. Each half-cell contains a flow field for distributing the electrolyte across the electrode. Among various components used within VRFB architecture, the electrodes play a crucial role influencing the performance and long-term durability [165].

The surface functional groups along with the internal morphology are the key characteristics dictating the catalytic activity and species transport within the electrode's micro- and nano-structure. Carbon-based porous electrodes (e.g. carbon paper and carbon felt or graphite felt (GF)) are commonly used electrode materials for VRFBs [101, 166, 167]. However, utilizing pristine carbon-based porous electrodes usually results in sluggish kinetics for the negative and positive redox reactions. Therefore, extensive attempts have been made to improve the electrochemical performance of carbon-based electrodes through chemical modification (e.g. surface oxidation and functionalization) [168, 169]. The introduction of oxygen functionalities such as hydroxyl (C-OH), carbonyl (C=0), and carboxyl (O-C=O) have been explored as a promising approach for improving the kinetics. In addition to surface oxidation, nitrogen doping into carbon lattice has been shown to significantly improve the electrochemical properties of carbonaceous host materials due to an enhanced electronic structure [170–172]. Accordingly, N-doped carbon electrodes such as nanospheres [173] and carbon black [174] demonstrate excellent conductivity and superior catalytic activity. This is expected to be a result of the catalytic improvements being a function of state of charge, which was held constant at 50 % (minimum charge transfer resistance) during experimental characterization. Despite the enhancement in catalytic activity, the implementation of the N-doped carbon electrodes has not been shown to be very effective in boosting the power density of VRFBs. Recently, both carbon nanodots [175] and graphitic carbon nitride [176] decorated GF electrodes were confirmed to exhibit excellent wettability and enhanced activity towards vanadium redox couples (V(IV)/V(V)

and V(II)/V(III)).

Improved activity was mainly attributed to the surface functionalization and nano-scaled architecture facilitating mass transport within the electrode structure. Therefore, engineering electrodes' nano-structure is a feasible pathway for promoting the kinetics of the negative and positive redox reactions in VRFBs. Graphene quantum dots (GQDs), zero-dimensional materials with combined attributes of graphene and carbon nanodots, are remarkable catalytic materials with superior electrocatalytic performance and unique photoelectrochemical properties [45,177]. Recently, sulfur (S) doping into carbon materials has been explored as a promising route for enhancing the catalytic activity [178]. As a result of S doping, a mismatch of the outermost orbitals of S and C imparts a non-uniform spin density distribution in S-doped graphene [178]. Theoretically, there is a slight difference between the electronegativity of S atoms (2.58) and C atoms (2.55); thus, a significant polarization in the S-C composites is formed [179,180]. Theoretical studies have also demonstrated that doping graphene with N is an effective approach for tailoring the electronic property as well as chemical reactivity due to stronger electronegativity of N (3.05) compared to that of C (2.55) atom from one side and conjugation between the nitrogen lone pair electrons and the graphite π-system from the other side [181–183]. Thus, the unique design of S and N co-doped GQDs (S/N co-doped GQDs) enables high carrier transport mobility and superior chemical stability [184]. Accordingly, in this work, we have developed high-performance electrodes (i.e. improved kinetics and catalytic durability) for all-vanadium redox flow batteries via decorating S/N-co-doped GQDs on GF electrodes. In previous

work, an infrared (IR)-assisted heating technique for synthesizing S/N co-doped GQD samples [184] was demonstrated, with a large amount of surface functionalities (e.g. oxygen, nitrogen, and sulfur-containing functional groups). With the aid of the functionalized GQDs, the electrocatalytic activity of S/N co-doped GQD electrodes can be largely enhanced due to improved surface hydrophilicity (i.e. surface wetting) as well as the functional groups serving as the active sites for catalyzing the redox reactions during oxidation/reduction processes. To the best of our knowledge, the novel design of S/N co-doped GQD/GF electrode for improving the catalytic activity in VRFBs has not been reported in prior literature. The merit of this work is to shed some light on how the decoration of S-/N-co-doped GQDs effectively improves the catalytic activity on GF electrodes for high performance VRFBs.

5.2 Experimental

5.2.1 IR-assisted synthesis of S/N co-doped GQDs

To synthesize the S/N co-doped GQD samples, we followed the procedure outlined in a previous study [184]. In short, the precursors including citric acid ($C_6H_8O_7$, Acros Organics, Purity: > 99.5 %), urea (CON2H4, J.T. Baker, Purity: 99 %), and ammonia sulfate ($(NH_4)_2SO_4$, Acros Organics, Purity: 99.5 %) were used. All the chemicals were of analytical reagents. First, a solid mixture of citric acid (10 g), urea (10 g), and ammonia sulfate (15 g) was homogeneously blended for 5 min using a three-dimensional mixer with Zr spheres. After that, the mixture was placed within a home-made IR furnace equipped with six medium-wave IR heaters. The

maximum power density of the heaters was 80 kW m^{-2} with a near-IR wavelength range of 1.4−3.2 μm. The thermal pyrolysis process was carried out in air at 280 °C for 30 min. Upon naturally cooling down to ambient temperature, the as-prepared powders were sieved through a stainless foil mesh (Type: 200 mesh). Finally, the samples were washed using distilled water, and subsequently were centrifuged at 15,000 rpm for 30 min, collecting the S/N co-doped GQD samples.

5.2.2 Materials characterization of S/N co-doped GQDs

The formation of the functional groups on the S/N co-doped GQD samples was characterized by Fourier-transform infrared spectroscopy (FT-IR, Varican 1000-FT-IR). A high-resolution transmission electron microscope (HR-TEM, FEI Talos F200s) operating at 200 kV was employed for capturing the micrographs. Field-emission scanning electron microscope spectra (FE-SEM) were taken using a JEOL JSM-6701F electron microscope at an accelerated voltage of 10 kV. X-ray photo-electron spectroscopy (XPS, Fison VG ECSA210) equipped with Mg-Kα radiation emitter, was employed for analyzing the chemical composition of the samples. The C 1s, N 1s and S 2p spectra were deconvoluted using a non-linear least square fitting algorithm with a multiple Gaussian function. The surface composition of the GQD powders was analyzed considering an appropriate sensitivity factor.

5.2.3 Electrochemical characterization of VRFBs

To prepare the S/N co-doped GQD/GF electrodes, a colloidal solution (100 mL) containing 500 mg S/N co-doped GQD powder and 2 vol.% Nafion ® monomer suspended within distilled water was used. Commercially available GF sheets (electrode area: 5 cm^2; thickness: 3 mm; Sigracell, SGL Carbon) were impregnated

with the GQD solution. The chemical impregnation process was performed at ambient temperature for 2 h. Finally, the S/N co-doped GQD/GF sheets were dried at 90 °C in a vacuum oven to ensure the formation of the chemical bonds between the GQDs and GF sheets.

A 5 cm^2 rectangular (4 cm $\times$ 1.25 cm) flow through flow field was used for all in-situ experiments to both improve the pressure drop and enforce even electrolyte distribution. The Nafion ® 117 (Ion-Power Inc.) ionomer was used as the separator, which was exposed to a pre-treatment consisting of a 30-minute immersion in 3.3 M H_2SO_4 at 80 °C followed by an immersion for 30 minutes in DI water at 80oC. Electrochemical impedance spectroscopy (EIS) was performed utilizing a Bio-Logic (model number: HCP-803) potentiostat. The EIS analysis was performed within the frequency range of 25 mHz to 100 kHz with an amplitude of 5 mV. To explore the catalytic activity and durability, the VRFBs assembled with S/N co-doped GQD/GF electrodes were cycled symmetrically at 0.3 V for 40 cycles.

A symmetric cell configuration was used for isolating the anode to measure the impedance [38, 39]. At 50 % state of charge (SoC), the charge transfer impedance is minimized relative to all other electrolyte compositions. The anolyte was coulometrically tuned to 50 % SoC for these experiments. The EIS results at 50 % SoC commonly served as a crucial indicator to evaluate the electrochemical performance of carbon electrodes in VRFBs. We believe that the EIS experiments would have different results at 0 % and 100 %, and the expression for the charge transfer impedance has dependence on the product of the concentrations (raised to the power of the charge-transfer coefficients) in the denominator (i.e., the charge trans-

fer impedance is generally minimal at 50 % SoC). This is an idealization of the full cell. The symmetric cell was potentiostatically cycled at 0.6 V for 40 cycles to simulate cycling stress in this configuration. Cycles consisted of 30-minute holds on account of the inability for the symmetric cell to charge/discharge electrolyte. Because the anolyte flows through both sides of the reactor in the symmetric cell configuration, the open circuit voltage is zero, also, it is assumed that the voltage is equally distributed between the two half-cells, i.e. the application of 0.6 V across the symmetric cell results in approximately 0.3 V per half-cell.

A full cell was also utilized for cycling experiments to calculate efficiencies and electrolyte utilization. For these experiments the cell was cycled galvanostatically at 150 mA cm^{-2} between a max cutoff voltage of 1.8 V and a minimum cutoff voltage of 0.6 V.

5.3 Results and discussion

The FT-IR spectrum of the S/N co-doped GQDs is illustrated in Figure 5.1(a) confirming the presence of S-containing groups on the GQDs. As shown in Figure 5.1(a), a noticeable transmittance occurring at 570–600 cm^{-1} (i.e. C-S bonding) confirms the S doping into the GQD samples [185]. The strong peak in 1150-1300 cm^{-1} mainly originates from C-O stretch of -COOH or S-O stretch of sulfones. Transmittance peaks within the range of 1400 to 1706 cm^{-1} can be assigned to the existence of C-N and C=O/S=O functional groups, respectively [186]. The weak band at ca. 3400 cm^{-1} is ascribed to the physically adsorbed water molecules on the surface of the GQDs. This finding reveals that an effective doping of sulfur

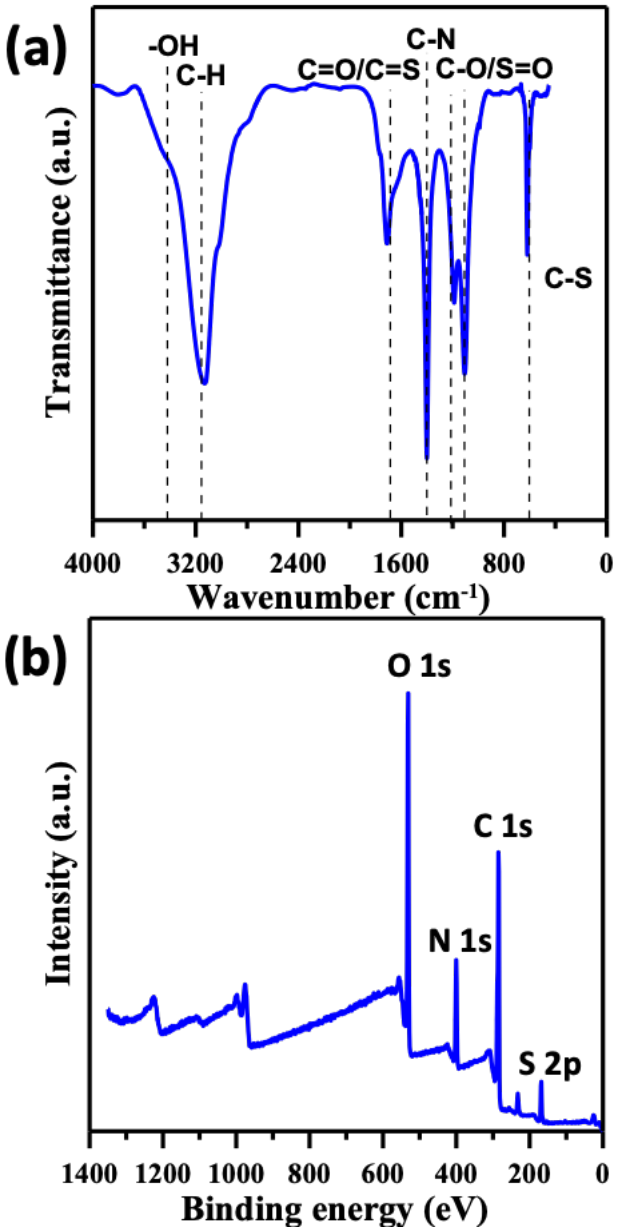

Figure 5.1: (a) FT-IR spectrum and (b) survey-scan XPS spectrum of N/S co-doped GQD sample.

and nitrogen is accomplished with the decoration of oxygen functionalities and the formation of S-/N-related defects on the GQD sample through the IR-assisted synthesis method.

A survey-scan XPS spectrum of the S/N co-doped GQD samples is depicted in Figure 5.1(b), presenting four major peaks at ca. 169, 285, 400, and 532 eV corresponding to S 2p, C 1s, N 1s, and O 1s, respectively. The S/C, N/C, and O/C atomic ratios are estimated to be 7.8, 22.7, and 45.8 at.%, respectively. Such high magnitude of atomic ratios reflects high heterogeneity on the S/N co-doped GQDs. To explore the surface heterogeneity, high-resolution XPS spectra of C 1s, N 1s, O 1s, and S 2p, as shown in Figure 5.2, can be deconvoluted to analyze functional group distributions on the S/N co-doped GQD samples. As shown in Figure 5.2(a), the C 1s spectrum is decomposed into five peaks including C-C/C=C (ca. 284.6 eV), C-N/C-S (ca. 285.2 eV), C-OH (ca. 287.5 eV), C=O (ca. 288.5 eV), and O-C=O (ca. 289.5 eV) [184]. The N 1s XPS spectra in Figure 5.2(b) can be divided into three main signals: pyrrolic/pyridinic N (ca. 399.6 eV), quaternary N (ca. 400.2 eV), and N oxides (ca. 401.5 eV) [145, 150]. This finding reveals that the IR-assisted technique enables "lattice N" doping into the graphene sheets (i.e. the formation of pyrrolic/pyridinic N and quaternary N), favoring electrical conductivity in the N-doped graphitic structure. It is important to note that the S/N co-doped GQD samples also contain amino group ("chemical N"), originates from the amide-carbonyl group (O=C-NH2) located at the edges of graphene sheets [187, 188]. The O 1s peak, as shown in Figure 5.2(c), reflects the presence of C-O/S-O, C=O, and O-C=O groups. High resolution of S 2p XPS spectrum (see

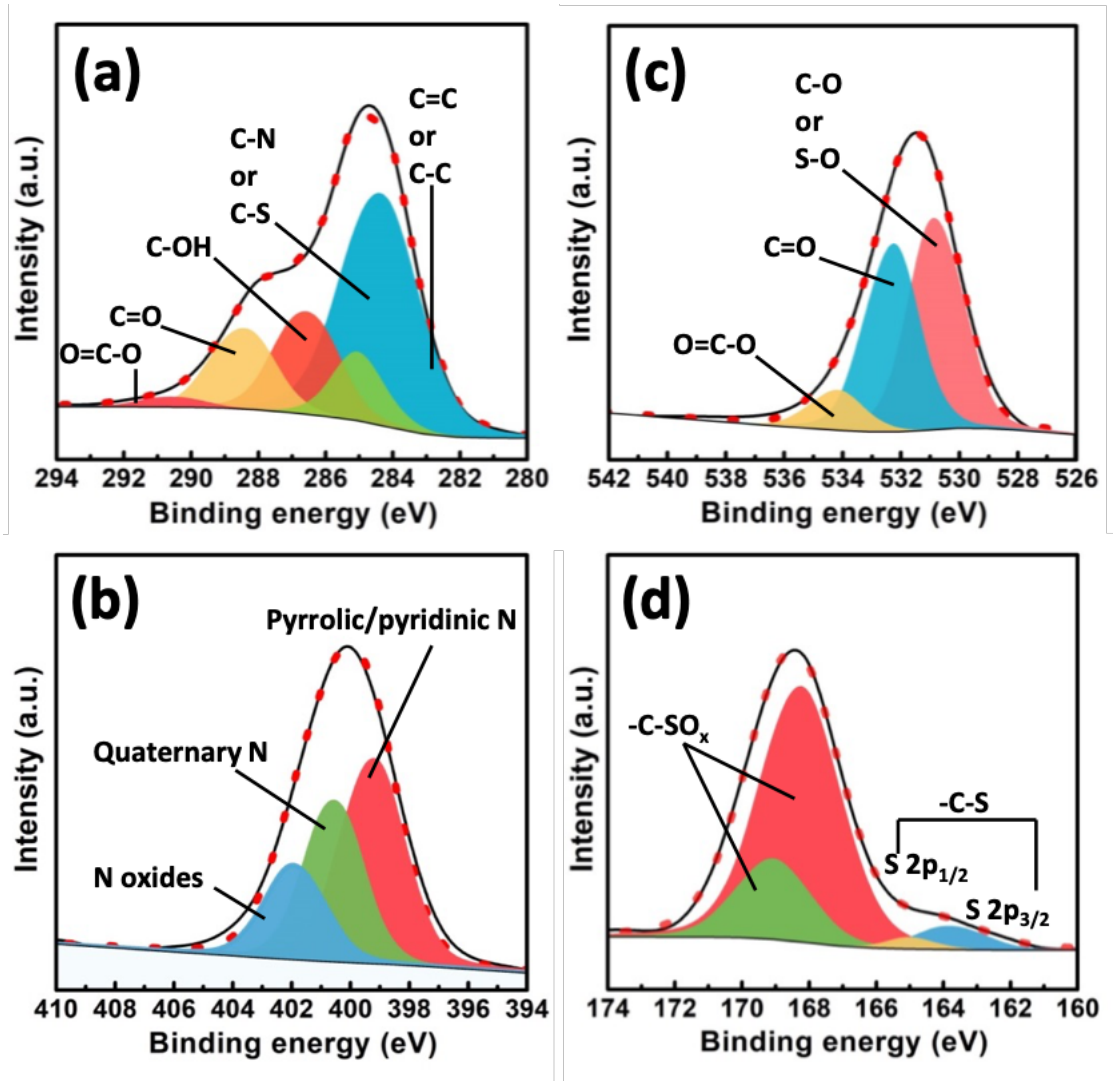

Figure 5.2: High-resolution XPS spectra of (a) C 1s, (b) O 1s, (c) N 1s, and (d) S 2p peaks of N/S co-doped GQD sample, deconvoluted by a multiple Gaussian function.

Figure 5.2(d)) shows three signals: ca. 163.9, 165.1, and 168.3 eV; these can be attributed to the S 2p3/2 and S 2p1/2 of thiophene and C-SOx bonding [189, 190]. Accordingly, two various configurations are feasible for the S dopant into the S/N co-doped GQDs: (i) thiophene-S and (ii) oxide-S [191], which is consistent with the FTIR results.

Figures 5.3(a) and (b) present HR-TEM micrographs of S/N co-doped GQD samples with low and high magnification, respectively. Figure 5.3 shows the GQDs possess a homogeneous dispersion with a narrow particle size distribution. The GQDs particle size distribution was in the range of 4 to 10 nm with the average particle size of ~6.2 nm. The selected-area diffraction pattern, located at the inset of Figure 5.3(b), shows the bright diffraction spots along with diffraction rings. The pattern of such bright rings reveals that the GQDs consisted of nanocrystallites due to a high concentration of dopants (i.e., S and N atoms) within the functionalized GQDs. Figure 5.3(b) shows a single S/N co-doped GQD nanoparticle, having a round shape. Also, as illustrated in the inset of Figure 5.3(b), well-ordered lattice fringes in the individual GQD crystal can be identified confirming superior crystallinity with a lattice distance of ca. 0.22 nm, corresponding to the (1120) lattice fringe of graphene-based materials [145].

Figure 5.4 depicts typical XRD patterns for the untreated GF as well as S/N co-doped GQD/GF electrodes. The pristine GF contains well-indexed diffraction peaks of graphitic crystallites. The (002) peak of the pristine GF electrode occurs at 25.6°; therefore, the interlayer distance, d(002), can be quantified as ca. 0.347 nm, according to the Bragg's equation [192].

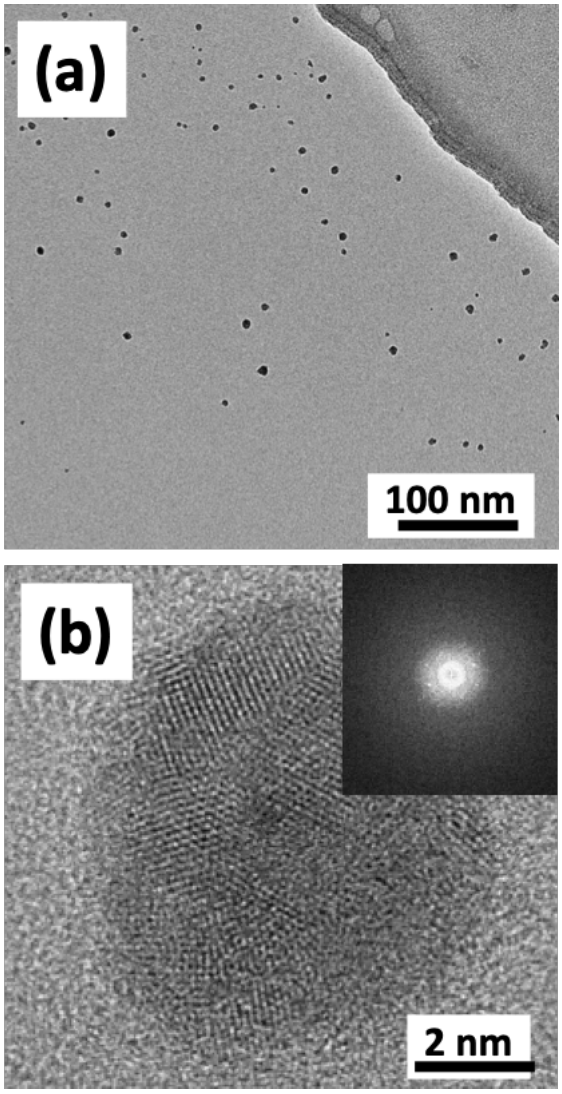

Figure 5.3: (a) HR-TEM micrograph and (b) lattice fringes of N/S co-doped GQD sample. The inset of (b) shows selected area diffraction of individual N/S co-doped GQD.

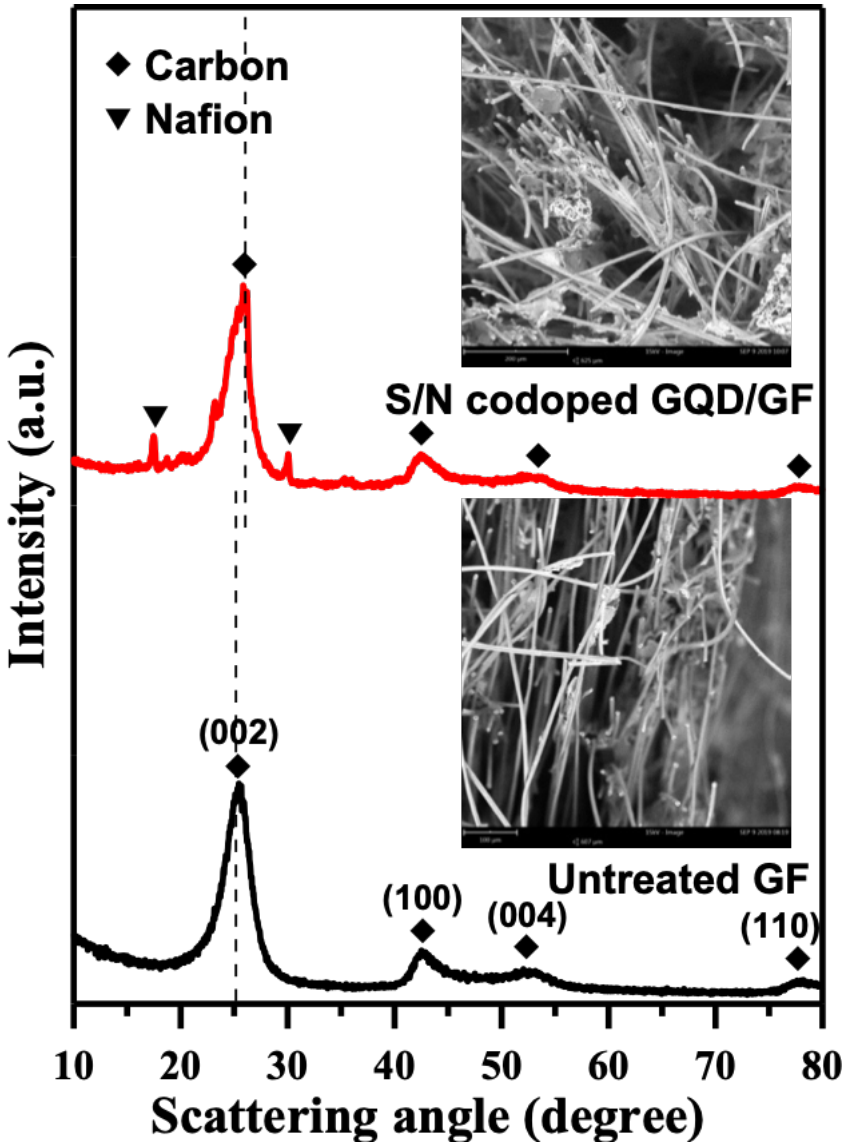

Figure 5.4: Typical XRD patterns of untreated GF and N/S co-doped GQD/GF samples. The inset shows their corresponding FE-SEM images.

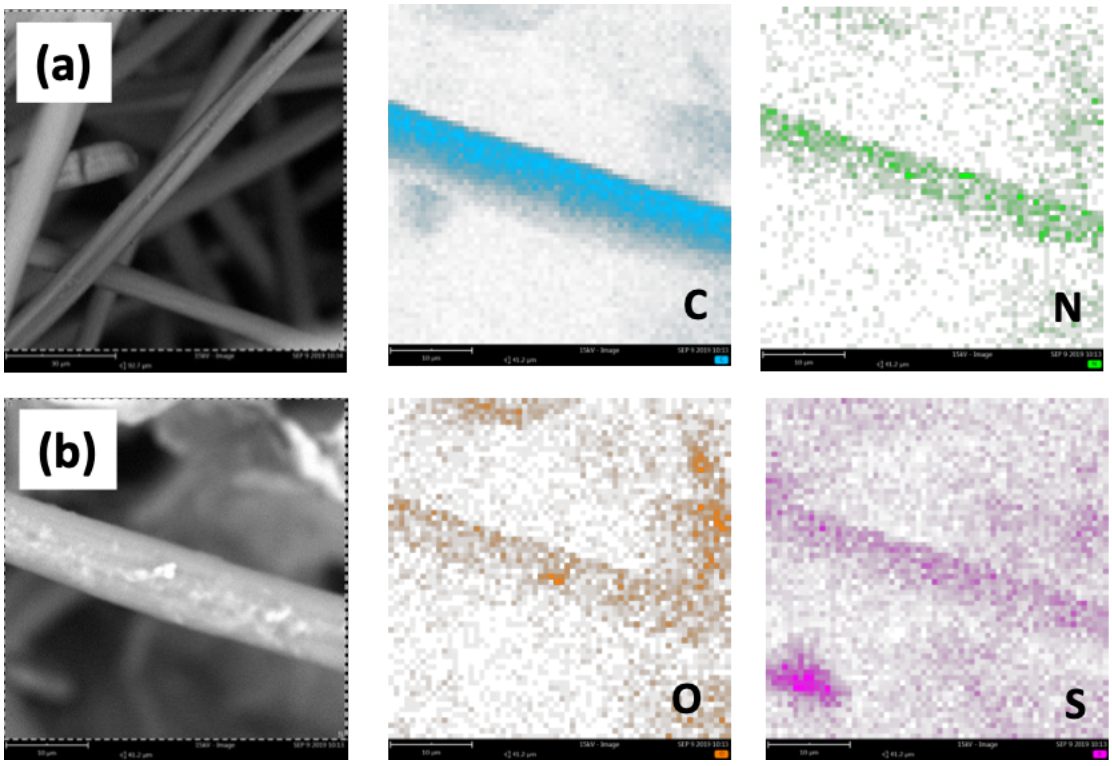

Figure 5.5: FE-SEM images of N/S co-doped GQD/GF composite with (a) low and (b) high magnification. The left shows elemental mapping of C, N, O, and S on the individual carbon fiber.

Through decorating S/N co-doped GQDs, two additional peaks, originating from the Nafion crystals, can be identified [193]. Notably, the (002) peak shifts to ca. 26.0°, approaching an interlayer spacing distance d(002)= 0.342 nm, which is close to that of a perfect graphite (i.e. d(002)= 0.334 nm). The smaller d(002) value implies that the S/N co-doped GQDs have been attached to the surface of GF electrodes; thus, the S/N co-doped GQDs have highly crystalline microstructure. FE-SEM images of untreated GF and S/N co-doped GQD/GF electrodes are illustrated in the inset of Figure 5.4(a) and 4(b). As shown in Figure 5.4, the GF electrodes are composed of a stack of carbon fibers randomly distributed across the entire 3D structure with an average diameter of 6-10 μm for a single fiber. According to Figure 5.4, the GF electrodes maintain their original topography before and after the S/N co-doped GQDs. To inspect the dispersion of S/N co-doped GQDs, FE-SEM elemental mapping imaging technique was utilized (Figure 5.5). According to Figure 5.5, the FE-SEM elemental mapping images demonstrate a homogeneous distribution of C, N, O, and S elements, indicating the preservation of N/O/S functionality in the S/N co-doped GQD/GF hybrid electrodes. This also reflects that a uniform dispersion of S/N co-doped GQDs within the micro-scaled carbon fibers has been achieved.

EIS was used to characterize the electrode polarization (i.e. overpotential distribution) at SoC of 50 %. Nyquist plots of the VRFBs fabricated with the pristine/untreated GF (labelled as "U") and the S/N co-doped GQD/GF electrodes (labelled as "C") were assessed at open circuit as illustrated in Figure 5.6(a). The Nyquist plots can be divided into three regions: (i) real-axis intercept: ohmic re-

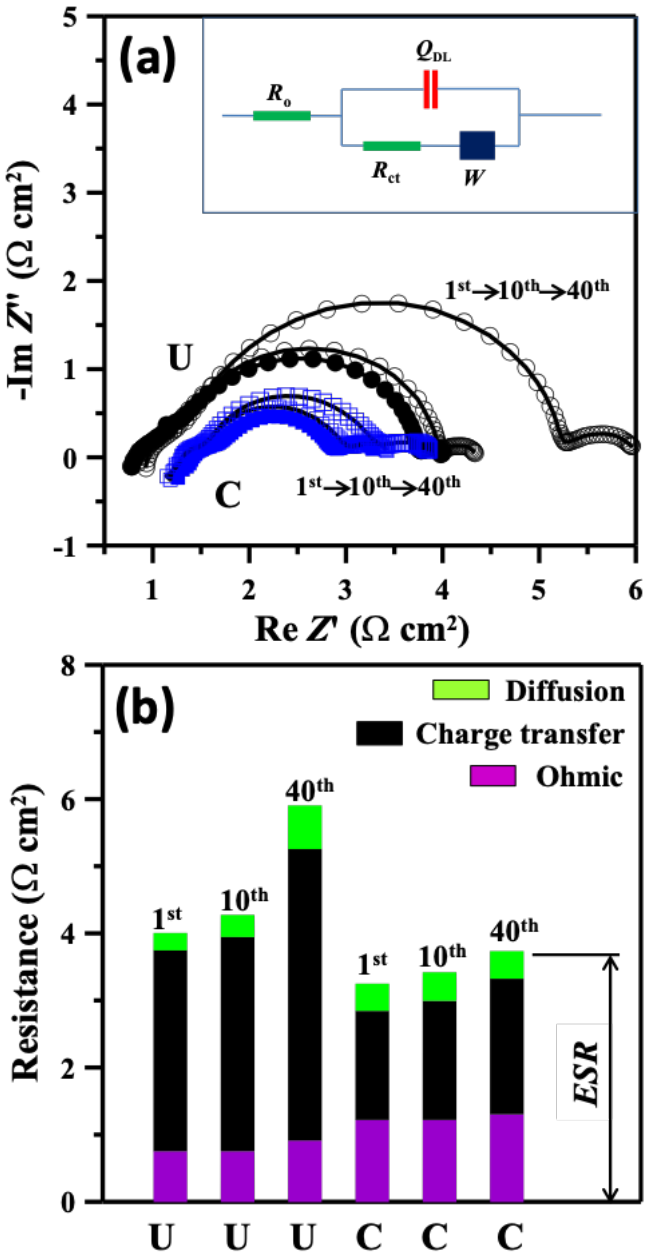

Figure 5.6: (a) Open circuit Nyquist plots of untreated and N/S co-doped GQD-coated GFs at 1st, 10th, and 40th cycle, where the inset shows an equivalent circuit. (b) Resistance analysis of untreated and N/S co-doped GQD-coated GFs at 1st, 10th, and 40th cycle, where ESR is the sum of ohmic, charge transfer, and diffusion resistance.

sistance at high-frequency region, (ii) first semicircle: charge-transfer (kinetic) resistance at moderate frequency, and (iii) second semicircle: mass transfer (finite diffusion) resistance in the low frequency region [38,138,194,195].

To quantify the overpotential distributions, a Randles circuit was used to model the EIS spectra (see the inset of Figure 5.6(a)). The equivalent circuit model consists of four components: (i) ohmic resistance (RO) for the ohmic resistance associated with the electrolyte, membrane, electrodes, and contact resistances, (ii) charge transfer resistance (RCT) for simulating faradaic charge transfer at the electrode surface, (iii) constant phase element (QDL) for quantifying the charge transfer across the electrode/solution interface, and (iv) mass transport resistance (RD) to account for the ionic finite diffusion within the electrolyte phase.

According to Figure 5.6, the open-circuit equivalent series resistance (ESR = RO + RCT + RD) is substantially lower for the S/N co-doped GQDs. Discrepancy between the experiments and model was less than 10 %. The kinetic parameters and overpotential distribution for both electrode configurations are illustrated in Figure 5.6(b). The ESR values of U electrodes were 4.0, 4.3, and 5.93 Ω cm^2 at the end of 1st, 10th, and 40th cycle, respectively. Therefore, the increase in ESR for the VRFBs assembled with the U electrodes was 48.3 % at the end of cycling. For the S/N co-doped GQDs, the ESR values were decreased to 3.2, 3.4, and 3.74 Ω cm^2 at the end of 1st, 10th, and 40th cycle, respectively (only 16.9 % increase in ESR after 40 cycles).

As shown in Figure 5.6, the application of the S/N co-doped GQDs improves kinetic, and mass transport overvoltages compared to pristine electrodes; how-

ever, the reduction in the charge transfer resistance is significantly higher with the S/N co-doped GQDs. According to Figure 5.6, the charge transfer overpotential reduces by ~53 % with the S/N co-doped GQDs after 40 cycles. It is important to note that the reduction in the charge transfer resistance remains relatively unchanged even after extended cycling (~53 % reduction in charge-transfer overvoltage); thus, the performance improvements via the implementation of the S/N co-doped GQDs is stable during cycling. This finding confirms a substantial and stable improvement in the catalytic activity and the catalytic durability of S/N co-doped GQD/GF electrodes.

The synergistic effect that combines O functionalities, lattice N atoms, and S dopants includes the following steps. First, the S/N co-doped GQDs possess a large amount of hydroxyl and carboxyl groups, facilitate the chemical redox kinetics, and subsequently reduce the charge transfer overpotentials [32, 36, 196]. The presence of oxygen functionalities (O/C ratio: 45.8 at.%) also imparts an affinity to the aqueous electrolytes and create a hydrophilic surface toward the solvent. Second, due to high amidation levels on the GQDs (N/C ratio: 22.7 at.%), the lattice "N" atoms replace the carbon atoms residing in the graphene lattice and such a substitution in the lattice structure maintains the sp2 hybridization of C atoms. Therefore, the electrical conductivity within the graphene nanostructure is improved via donating delocalized electrons [196–198]. Third, the S dopants in the GQD framework further improves the carrier transport mobility and enhances the chemical stability. The S dopant shares doping configurations such as C-S-C, C-SOx-C (x = 2, 3, and 4), and C-SH, where the sulfone bridges enable increased

adsorption of metal ions onto S/N co-doped GQD surface. Since the S-doping effectively adjusts the Fermi level and localized electronic state [178, 179], this interaction induces S/N co-doped GQDs' affinity toward V-containing ions, leading to increased reactivity toward the redox couples. Therefore, the catalytic activity as well as the durability of GF electrodes was improved via integration of S/N co-doped GQDs within the pristine electrode's microstructure.

To inspect the cyclic stability, the cyclic voltammetry (CV) measurement was conducted to investigate the electrochemical surface area (ESA) of N/S co-doped GQD/GF electrode in 1 M H_2SO_4 at 50 mV s^{-1}, as shown in Figure A.2. The CV profiles start from the open circuit potential and the potential window ranges from 0 to 1 V with Ag/AgCl. The CV feature of the electrode consists of three regions: (i) adsorption-desorption of hydrogen (0–0.4 V), (ii) double-layer formation (0.4–0.9 V), and (iii) oxidation-reduction of N/S co-doped GQDs (0.9–1.0 V). The CV feature is basically analogous with that of Pt-based catalyst electrodes [199]. Interestingly, the capacitive double-layer behavior within 0.4-0.9 V vs. Ag/AgCl can be viewed, indicating that N/S co-doped GQD/GF electrode are electrochemically active for the formation of a double layer. This is attributable to an improved surface hydrophilicity due to the presence of hydrophilic functional groups on the N/S co-doped GQD surface. The pair of redox peaks in the potential region of 0–0.4 V originates from the adsorption-desorption of hydrogen. After cycling, the electrode maintains ~90 % ESA retention as compared to its initial value at the first cycle. As a result, N/S co-doped GQD/GF electrode offers excellent ESA durability in acid electrolyte.

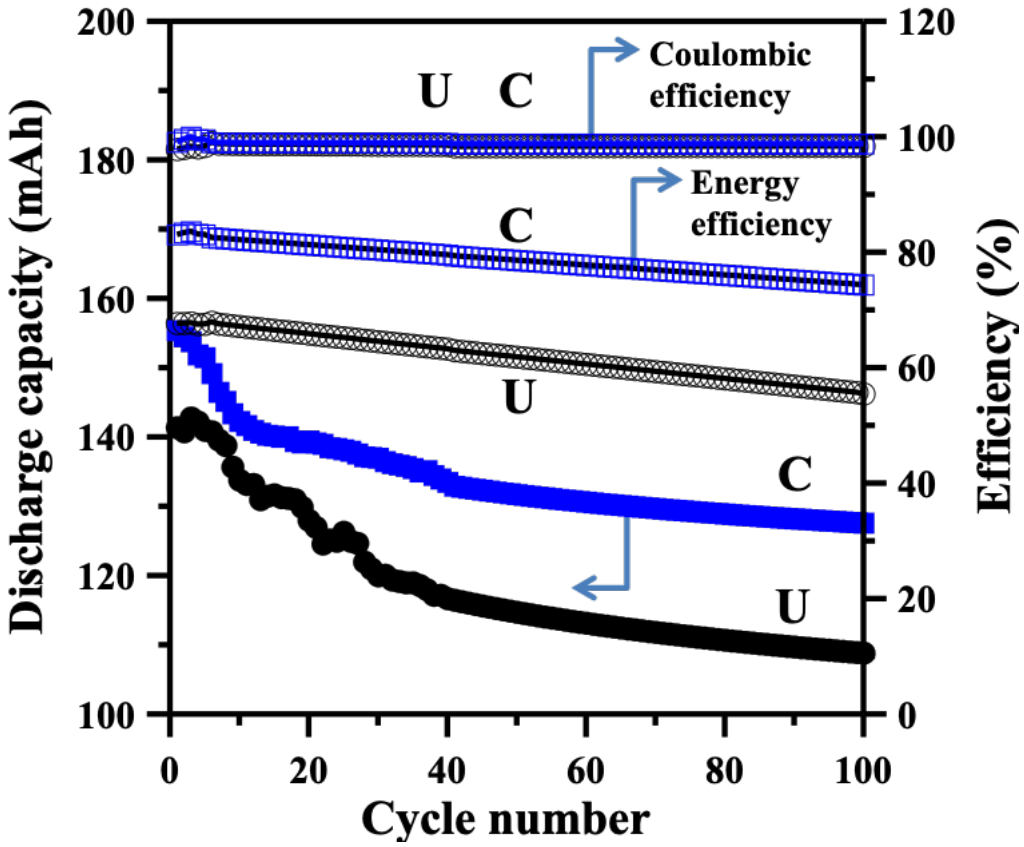

Figure 5.7: Discharge capacity, Coulombic efficiency, and energy efficiency as a function of cycle number.

To explore the long-term durability of the S/N co-doped GQDs, extended charge-discharge cycling was performed, as shown in Figure 5.7. As illustrated in Figure 5.7, the VRFBs with the S/N co-doped GQDs as the electrode, maintain an ultra-high coulombic efficiency during long-term cycling (> 98.8 %). Also, as illustrated in Figure 5.7, the VRFB equipped with S/N co-doped GQD/GF electrodes exhibit higher capacity utilization compared to untreated electrodes. The discharge capacity increases from 144 mAh (U electrode) to 157 mAh (C electrode) resulting in ca. 9 % enhancement in capacity utilization. After 100 cycles, the discharge capacity of U electrode decreases to 111 mAh, while the capacity retention of C electrode remains as high as ca. 82 %. The voltage efficiency (η_{VE}) was also assessed for both GF electrode configurations. The voltage efficiency associated with U electrode was 56.4 % at the end of 100th cycle. It was significantly enhanced through the decoration of S/N co-doped GQDs, i.e., 73.7 % (100th cycle).

The energy efficiency (η_{EE}) is defined here as the product of voltage and Coulombic efficiencies, also called round-trip energy efficiency in a battery system (often excluding system losses, e.g., pumps, electronics, etc.). A survey of the specifications provided by the companies active in VRFBs shows that commercial flow battery systems operate in the 70–80 % round-trip efficiency regime (including the losses from auxiliary systems), though battery systems can be considered competitive even in the 60–70 % energy efficiency range, depending on cost [24, 161]. As shown in Figure 5.7, the η_{EE} value of U electrode was 67.7 % at 1st cycle, whereas the η_{EE} value of C electrode can reach as high as 83.1 %. The η_{EE} decay was also significantly alleviated by the decoration of S/N co-doped GQDs, i.e., only

~12 % decay after 100 cycles. Accordingly, the VRFBs utilizing S/N co-doped GQD/GF electrode demonstrate superior capacity retention and satisfactory energy efficiency during charge/discharge cycling. The improvement in capacity retention is attributed to lower overpotentials resulting in higher depth of discharge, which is evidenced by the treated electrodes having on average 7 % longer cycles (e.g., 2.6 h vs. 2.4 h at 100 mA cm^{-2}). The coulombic efficiency was also maintained at ultra-high values (98.8 %) upon extended cycling, confirming excellent reversibility towards the vanadium redox reactions (V(IV)/V(V) and V(II)/V(III) couples) with the S/N co-doped GQD-decorated electrodes.

5.4 Conclusions

In this work, we demonstrated the robust design of the S/N co-doped GQD/GF hybrid structure as a high-performance electrode for all-vanadium redox flow batteries. S/N co-doped GQD/GF electrodes improve the catalytic activity toward the V(II)/V(III) redox reactions with excellent reversibility and durability during extended cycling. The IR-assisted method is extremely efficient and time-saving for synthesizing highly crystalline GQD samples. The S/N co-doped GQDs, having an average diameter of 6.2 nm, possessed high oxidation, amidation, and sulfonation level (45.8 (O/C), 22.7 (N/C), and 7.8 at.% (S/C), respectively). Uniformly dispersed S/N co-doped GQDs onto the GF enabled the formation of 3D nanostructures as the high-performance electrode for VRFBs. Through the deposition of S/N co-doped GQDs, the catalytic activity, equivalent series resistance, durability, and voltage efficiency of the treated GF electrode were enhanced. The synergistic

effect induced by the oxygen functionalities, lattice N atoms, and S dopants, effectively improves the surface catalytic activity and reduces charge transfer resistance for the redox reactions (V(IV)/V(V) and V(II)/V(III) couples). Accordingly, the design of GQD/GF electrode paves the pathway towards nano-engineering electrode structure for improved catalytic activity and durability in various energy storage devices including redox flow batteries.

Chapter 6

In-situ state-of-charge dependent parameter estimation for all vanadium redox flow battery

This chapter will not be published as a stand-alone article prior to submission of my ETD, therefore a publication statement was not included. The content of this chapter will be submitted for a publication authored by Michael. C. Daugherty, Douglas S. Aaron and Matthew M. Mench.

My contributions to this work were: experiment design, acquisition of data, data reduction and composition of the manuscript. Aaron and Mench assisted in manuscript preparation.

6.1 Introduction

State of charge (SoC) in all vanadium redox flow batteries impacts not only the open circuit potential, but also aspects of the kinetics and mass transfer when a cell is polarized. Although there are parameters such as the rate constant, which are invariant to composition, in-situ measurements of kinetics parameters as a function of continuously decreasing SoC has not been fully explored to this author's knowledge. This work presents a novel experimental configuration, which can continuously change the SoC of the electrolyte while measuring half-cell kinetics and mass transfer parameters. The goal of this work is to investigate these parameters and to identify if there are operational conditions, which can leverage favorable aspects of operating in a specific SoC range.

6.2 Experimental Methods

6.2.1 Novel in-situ cell-in-series configuration

Estimation of parameters as a function of state of charge was performed with a novel experimental configuration. This configuration, shown in Figure 6.1 utilizes

three separate cells: 1) a control cell (full cell) 2) an anolyte symmetric cell and 3) a catholyte symmetric cell.

The control cell was equipped with 2 Nafion ^{TM}117 membranes to mitigate crossover, while the symmetric cells were equipped with a single membrane. The anolyte and catholyte symmetric cells were connected serially to the anode and cathode respectively. This configuration was motivated by the ability to continuously vary the state of charge while maintaining half-cell resolution for quantifying kinetics parameters.

6.2.2 Electrochemical experiment procedure

Electrolyte was synthesized via dissolution of $VOSO_4$ (Alfa Aesar, 99.9%) in sulfuric acid (H_2SO_4, Alfa Aesar, ACS grade). Three different electrolyte compositions were tested 0.5 M V, 1 M V and 1.5 M V, each solution was composed of the same sulfuric acid concentration: 3.3 M. N117 ^{TM}was used as the membrane for all experiments All cells were equipped with a single layer of as received carbon felt (SGL GFD3, 3 mm nominal thickness). The electrodes were compressed to 66% of their original thickness via PTFE gaskets. A rectangular (4×1.25 cm^2) flow-through flow field was used for each cell [39, 200] with gold-plated current collectors. The temperature of each cell and the electrolyte tanks was maintained at 30°C with type T thermocouples.

6.2.3 Experiment Protocol

Electrolyte (100 mL on the cathode side and 50 mL on the anode side) was potentiostatically charged to 100% state of charge (SoC) at a voltage of 1.8 V with the control cell. After the cutoff voltage was reached, half of the volume of the

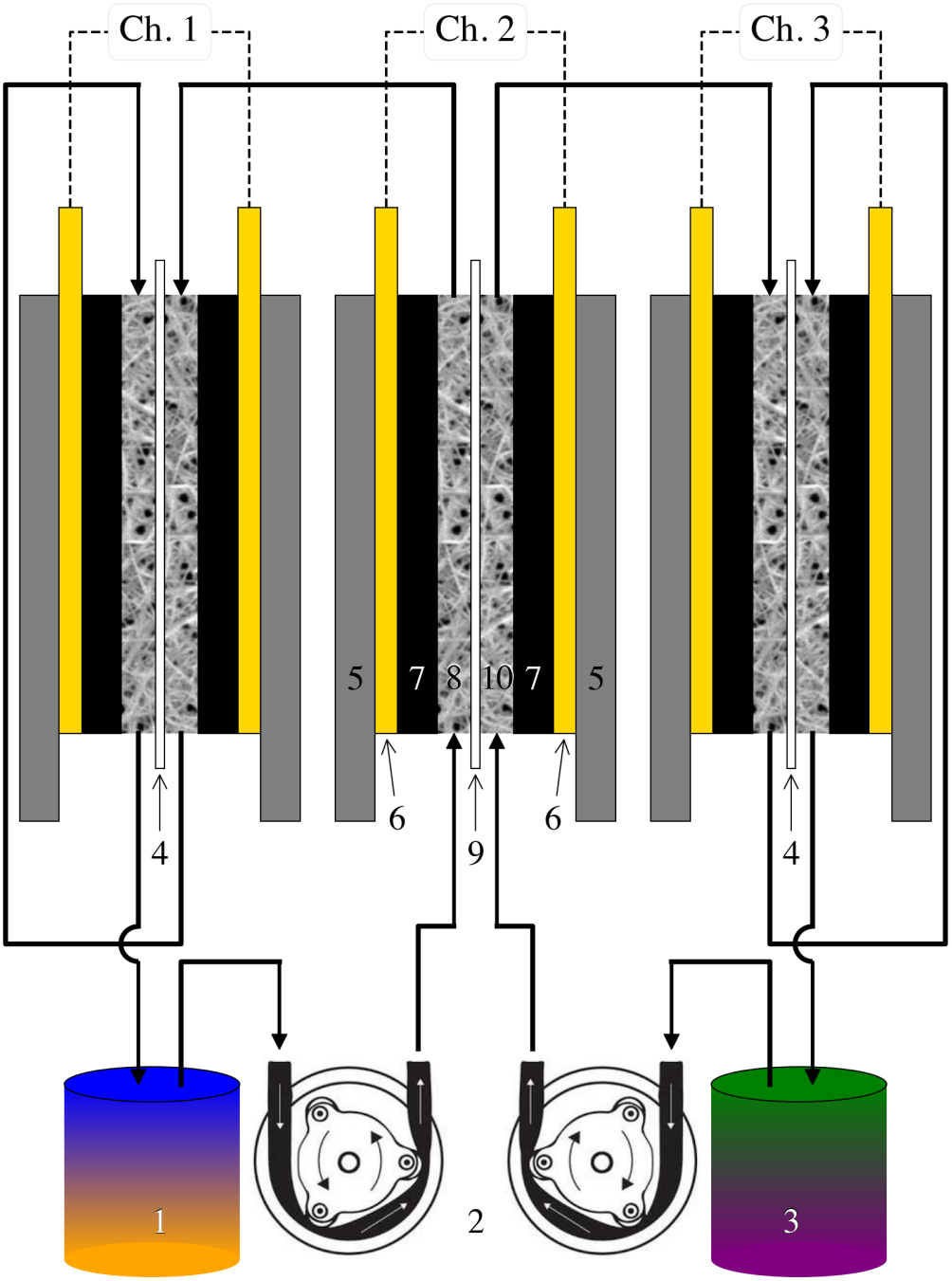

Figure 6.1: Schematic of experimental configuration. 1) catholyte tank, 2) peristaltic pump (2 channels), 3) anolyte tank, 4) symmetric cell membrane (1 x Nafion 117), 5) end plate, 6) current collector, 7) flow field, 8) control cell cathode, 9) Control Cell Membrane (2 x Nafion 117), 10) control cell anode. Each cell is connected to a separate potentiostat channel

catholyte (50 mL) was removed. During the charging the fluid circuit was fully connected (i.e. flowing through the symmetric cells); however these cells were inactive during this step. Following the charging step, a protocol was generated (via Python script), which synchronized the cells in the following manner: control cell discharging → symmetric cell dwell (record OCV); control cell dwell (record OCV) → symmetric cells record 2 consecutive impedance spectra (amplitude = 5 mV, 100 kHz to 100 mHz, 10 points per decade). The control cell was discharged galvanostatically at -50 mA cm^2 to 90% SoC then in increments of 2.66% down to 10% for a total of 30 samples. Each discharge—OCV step of this experiment was synchronized to yield impedance spectra spanning this SoC range. Figure A.14 illustrates this synchronous behavior highlighting both the voltage profile of the control cell, and the synchronous spectra recorded by the symmetric cells. All electrochemical measurements were performed with a Bio-Logic VSP potentiostat. Each experiment was performed twice to ensure repeatability.

6.2.4 Electrochemical Impedance Modeling

Electrochemical Impedance spectra were modeled using the macro homogeneous porous electrode model derived by Paasch *et al.* and demonstrated by others on the VRFB symmetric cell [38,39,95].

$$\frac{AZ_{MHPE}}{b} = \frac{\rho_1^2+\rho_2^2}{\rho_1+\rho_2}\frac{\lambda}{b}coth\left(\frac{b}{\lambda}\right) + \frac{2\rho_1\rho_2}{\rho_1+\rho_2}\frac{\lambda}{b}\left(sinh\left(\frac{b}{\lambda}\right)\right)^{-1} + \frac{\rho_1\rho_2}{\rho_1+\rho_2} \tag{6.1}$$

The charge transfer ASR is the product of the charge transfer resistance and the

geometric surface area:

$$ASR_{ct} = \frac{AR_uT}{nA_tj_0F} \tag{6.2}$$

where the exchange current density (j_0) is [20]:

$$j_0 = Fk_0C_O^{(1-\alpha)}C_R^{\alpha} \tag{6.3}$$

Likewise, the diffusion resistance was calculated by taking the limit of a Warburg diffusion element as the frequency goes to zero.

$$ASR_{fd} = \frac{AaRuT}{A_tfF^2}\left(\frac{1}{C_RD_R} + \frac{1}{C_OD_O}\right) \tag{6.4}$$

The calculation of the effective surface area was achieved by utilizing the relationship derived by Brug and co-workers and used by others [39,117,201].

$$A_{effective} = \frac{(A_tC_{dl})^{1/P}}{C_{dl}}\left(\frac{1}{A}\frac{R_{ohmic}R_{ct}}{R_{ohmic}+R_{ct}}\right)^{1/P-1} \tag{6.5}$$

The calculation of the ohmic resistance for the MHPE (Equation 6.1) is shown in the appendix. ASR magnitude ($|\,\text{ASR}\,|$) is calculated by summing the ohmic, charge transfer and finite diffusion ASRs:

$$\begin{gathered} |ASR| = \sum_q ASR_q \\ q \in \{\text{Ohmic, Charge Transfer, Finite Diffusion}\} \end{gathered} \tag{6.6}$$

The overpotential as a function of current is determined by integrating the $|\,\text{ASR}\,|$

with respect to current. This is true for both the magnitude of the overpotential and the components that constitute it.

$$\begin{aligned} \eta(i) &= \int_0^i |ASR(i)|di \\ \eta_q(i) &= \int_0^i ASR_q(i)di \end{aligned} \tag{6.7}$$

6.2.5 Modeling the efficiency as a function of electrolyte composition

The voltage efficiency (V_E) is the ratio of the average voltage during discharging to the average voltage during charging:

$$V_E = \frac{t_{ch}\int_0^{t_{dch}} V(t)dt}{t_{dch}\int_0^{t_{ch}} V(t)dt} \tag{6.8}$$

For galvanostatic charge/discharge with no crossover the state of charge can be linearly mapped to time

$$SoC(t) = \frac{Q_i + it}{Q_1} \tag{6.9}$$

Note we are expressing SoC from 0-1 not 0-100%. If $Q_i = Q_1$ at $t = 0$ then it is starting at 100% SoC, this point can be non-100 however in the case of varying the depth of discharge. Substituting SoC for time (u-substitution): $\frac{dSoC}{dt} = -\frac{i}{Q_1} \rightarrow$

$dt = -\frac{Q_1 dSoC}{i}$

$$discharging: \begin{cases} SoC(0) = \frac{Q_i}{Q_1} \\ SoC(t_{dch}) = \frac{Q_i}{Q_1} - DoD \\ t_{dch} = \frac{Q_1 DoD}{i} \end{cases} \tag{6.10}$$

$$charging: \begin{cases} SoC(0) = \frac{Q_i}{Q_1} - DoD \\ SoC(t_{ch}) = \frac{Q_i}{Q_1} \\ t_{ch} = t \rightarrow SoC_i = blank \end{cases} \tag{6.11}$$

Using the substitutions from Equations 6.10 and 6.11 in Equation 6.8 the voltage efficiency (and implied energy efficiency on account of the no crossover assumption) is:

$$V_E = \frac{\int_{\frac{Q_i}{Q_1} - DoD}^{\frac{Q_i}{Q_1}} V_{dch}(SoC) dSoC}{\int_{\frac{Q_i}{Q_1} - DoD}^{\frac{Q_i}{Q_1}} V_{ch}(SoC) dSoC} \tag{6.12}$$

Since we are operating at low current we assume:

$$\begin{aligned} V_{dch}(SoC) &= OCV(SoC) - \eta(SoC) \\ V_{ch}(SoC) &= OCV(SoC) + \eta(SoC) \end{aligned} \tag{6.13}$$

The assumption of no crossover is an idealization, however often the coulombic efficiency for vrfb systems is close to 100% even for systems operating at more ideal system-level currents e.g. [52, 202].

6.3 Results and discussion

6.3.1 Area Specific Resistance

The coarsest measure of the variation in the electrochemical parameters from the macro perspective is the change in the area specific resistance (ASR) as a function of state of charge. Figure 6.2 shows the ASR magnitudes as a function of electrolyte composition for each of the vanadium concentrations (the calculation of the vertical and horizontal error bars is defined in the appendix).

As expected for GFD3 felt electrodes, the anode is more limiting than the cathode at all states of charge and for all electrolyte concentrations. As the state of charge approaches zero both the anode and the cathode begin to show dramatic increases in ASR magnitude. Figure 6.2 illustrates that both the anode and cathode exhibit ASR magnitudes at open circuit that are not completely symmetric with respect to 50% SoC. Both equations 6.2 and 6.4 have dependence on reactant concentrations in the denominator, so as either of these approach zero these overpotential components grow larger ($C_{Ox,SoC=100} \rightarrow 0$; $C_{Red,SoC=0} \rightarrow 0$). Considering equation 6.7, we know that the overpotential (η) is determined by integrating the impedance. However, as the cell becomes polarized the deviation from equilibrium is not necessarily linear and can be a function of composition. Indeed, Figure 6.3 illustrates this phenomenon, where, as the state of charge is decreased there are two distinct overpotential branches. Here the state of charge is annotated to illustrate the dependence of the overpotential on the electrolyte composition.

While the spectra must be measured while the control cell is not actively chang-

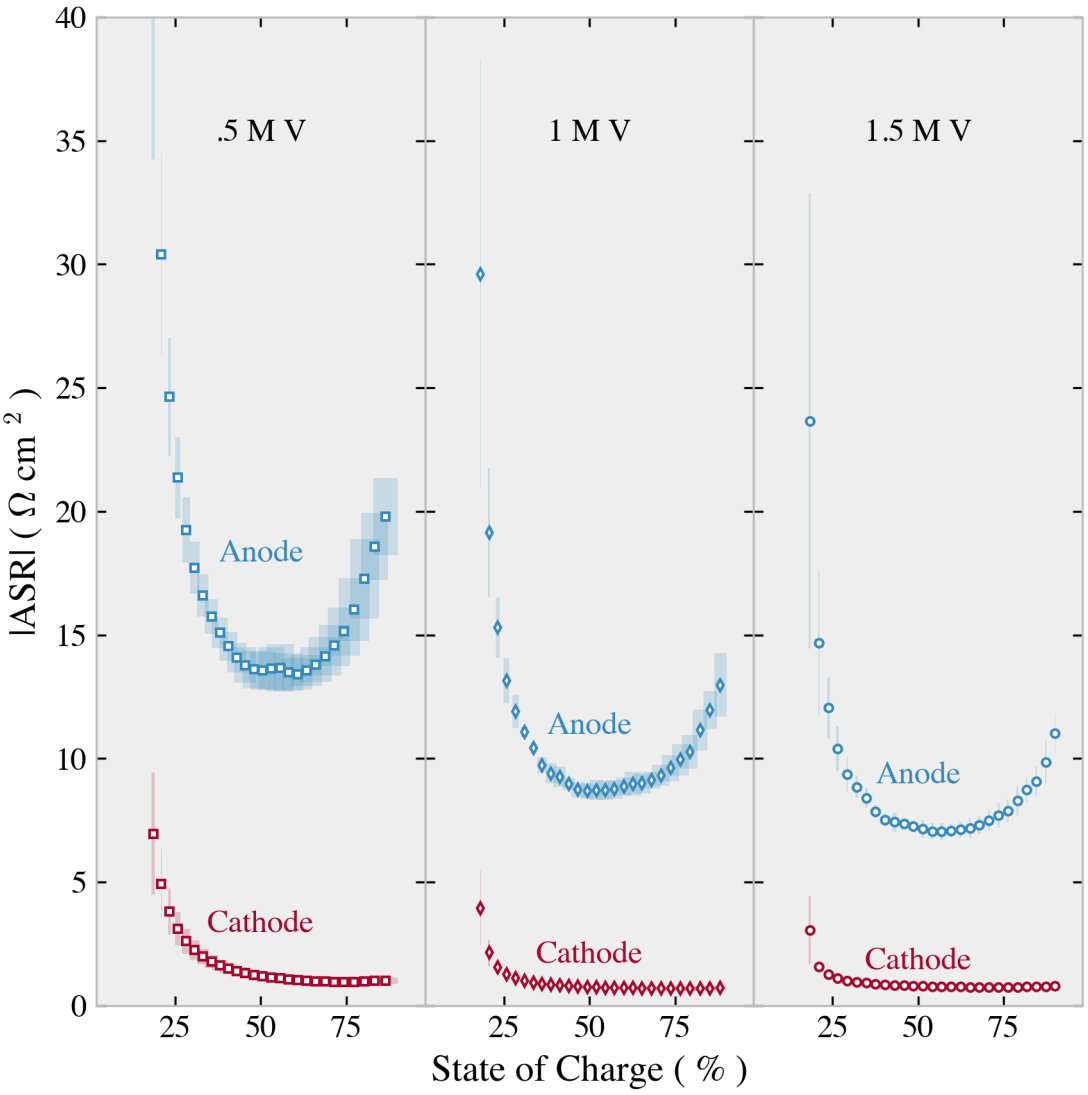

Figure 6.2: ASR magnitudes for the anode and cathode as a function of composition.

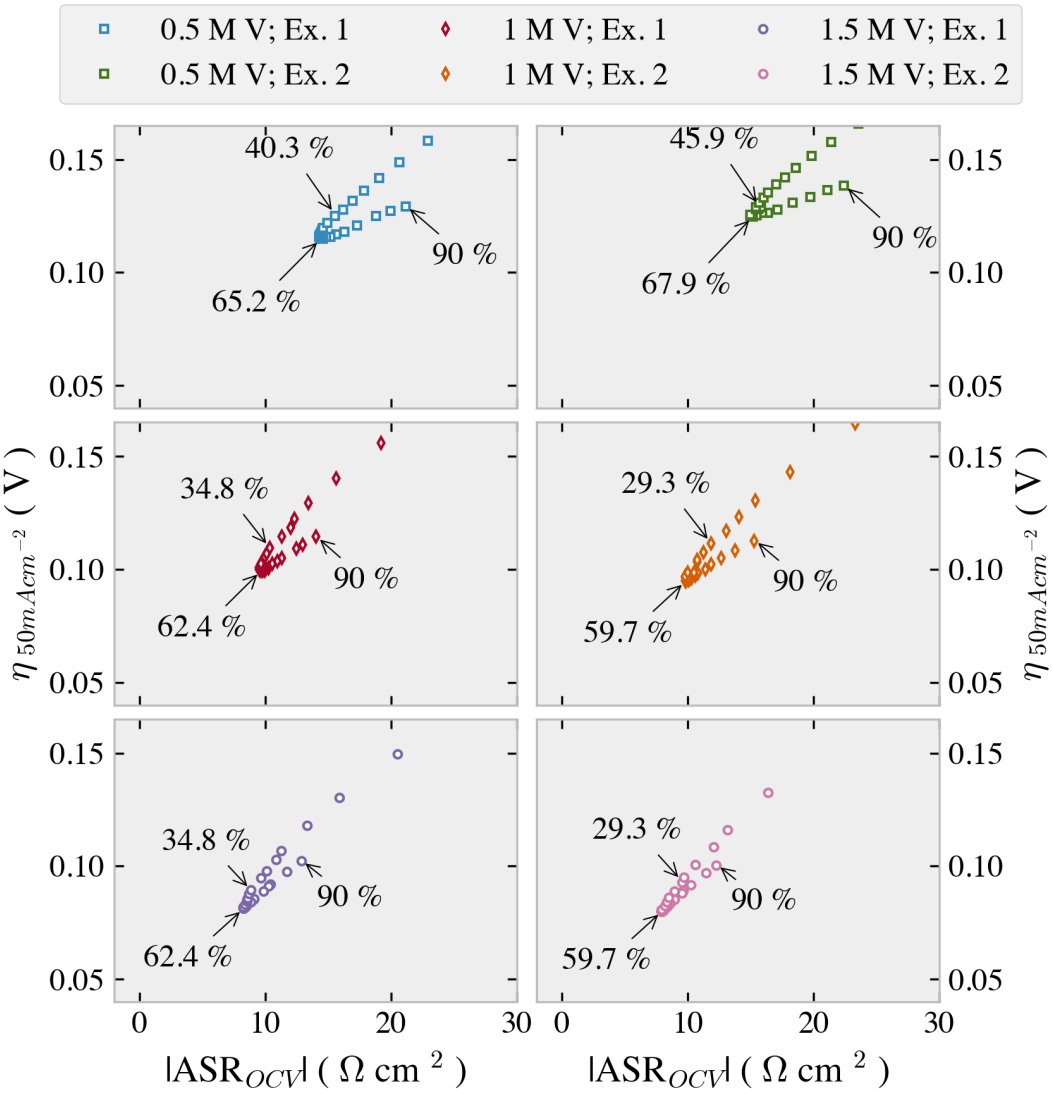

Figure 6.3: Overpotential at 50 mA cm^{-2} as a function of open circuit |ASR|, theoretical SoCs are annotated. Each row shows two instances with equivalent concentration of vanadium; the columns indicate the two separate experiments

ing the electrolyte composition in order to have consistent electrolyte composition for the duration of a spectrum, there is a trend that elucidates an asymmetry in the polarization behavior of the cell. Figure 6.3 indicates that the losses are greater (the cell will operate at a lower voltage efficiency) by operating on the lower portion of the SoC range. The annotations on this figure illustrate that the local minimum overpotential is achieved around ~60-65% SoC for each of these compositions. Figures 6.2 and 6.3 illustrate the asymmetry that arises as a function of composition (with respect to 50% SoC). This suggests that efficiency as a function of depth of discharge passes through an optimal value.

Cathode analysis

We have observed in figure 6.2 that the overpotential dedicated to the cathode is lower than the anode (~15 $\times$ lower at 90% SoC for 0.5 M V; see Figure A.11). For this reason the focus herein will be primarily on the anode, however, a brief analysis of the cathode is presented in the appendix. Figure A.13 shows the ASR components as a function of state of charge.

6.3.2 Anode analysis

Inspecting the anode ASR components in isolation (Figure 6.4) we can see that the ohmic ASR remains approximately constant over the course of the experiments, while the charge transfer and finite diffusion ASRs follow qualitatively parabolic profiles.

First, looking at the slight decrease in ohmic ASR as the SoC becomes small, we note that as the impedance becomes very large due to severe concentration po-

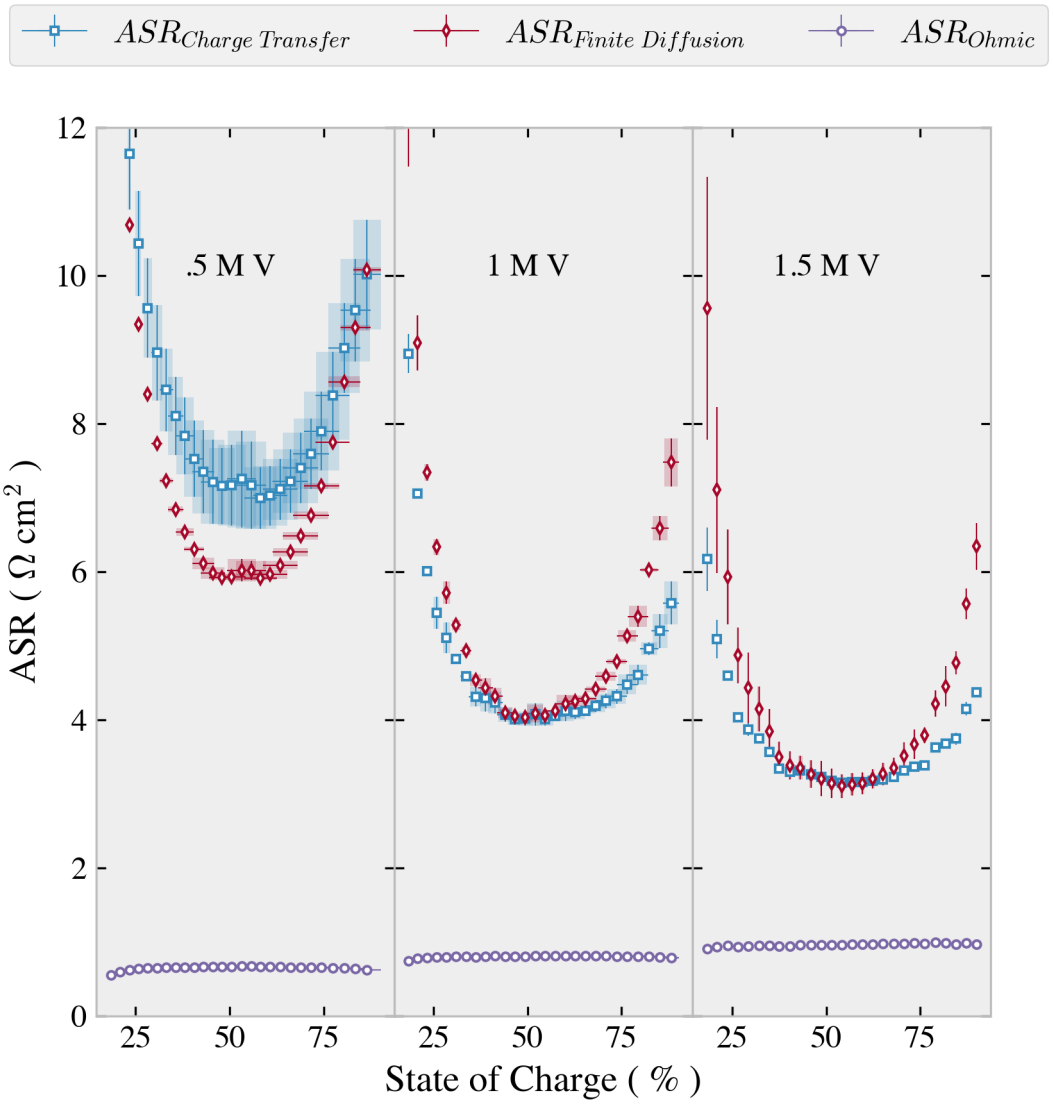

Figure 6.4: ASR components for the anode as a function of SoC.

larization, the resolution of ASR components becomes smaller meaning that we expect this to be an artifact and do not expect that the ohmic ASR becomes smaller as the SoC approaches zero. Indeed, for each of the experiments there is some stochastic error, and this was the reason for which multiple experiments were performed at each electrolyte composition. Inspecting equation 6.2 we can see that at constant temperature and wetted surface area the charge transfer ASR is minimized when j_0 is at its maximum value. Because α must lie between 0 and 1, equation 6.3 indicates, that the maximum value for j_0 occurs when the state of charge (on a 0-1 scale) is equal to α. α can be thought of as a measure of the symmetry of the energy barrier for the redox reaction [20], and is assumed to be 0.5 in many models and analysis in the VRFB literature e.g. [78, 203]. We see that for the 1 M V and the 1.5 M V there is a slight asymmetry in the charge transfer ASR with respect to 50% SoC. While this does not prove that $\alpha \neq 0.5$, it does warrant further investigation. Equation 6.4 indicates that the diffusion resistance has no dependence on alpha and, as a function of composition, is minimized at 50% SoC, which is observed in Figure 6.4.

Kinetics parameters

To investigate the manifestation of the anode response to changing the SoC, we next analyze the fitted kinetics parameters of the impedance spectra. Figure 6.5 shows both the exchange current density and the effective surface area as functions of SoC.

The top subplot of Figure 6.5 shows the exchange current density. Here we see the expected behavior described by equation 6.3 where the exchange current

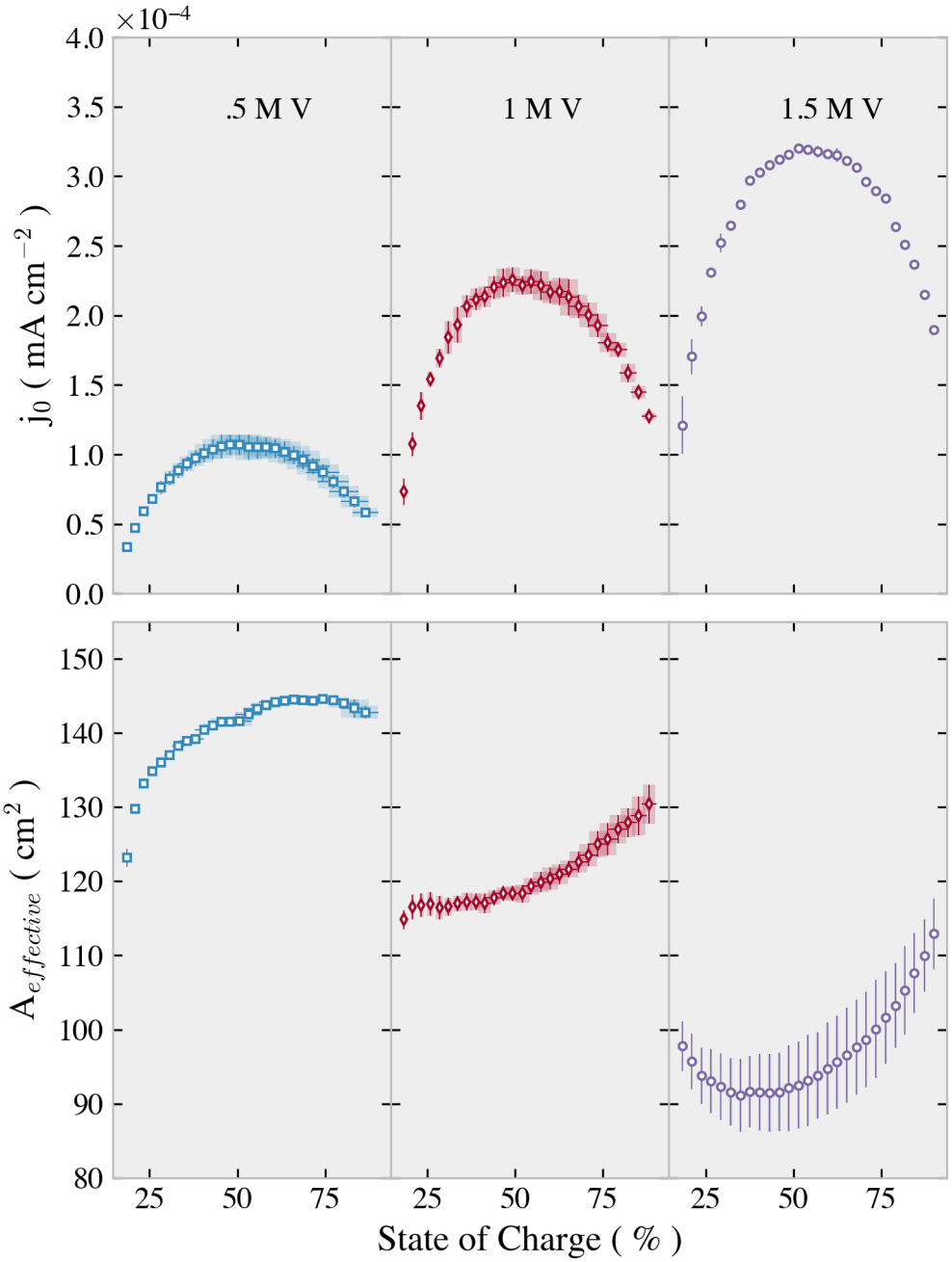

Figure 6.5: Exchange current density (j_0) and effective surface area ($Area_{effective}$) as functions of state of charge.

passes through a maximum value and becomes smaller at the extreme SoCs. As mentioned previously, the maximum value of j_0 corresponds with α; however, the sensitivity of j_0 to α is minimized where $j_0 = \alpha$. We note, however, that the trend of maximum j_0 observed across these experiments suggest that α is closer to 0.57 than 0.5.

The lower subplot of 6.5 conveys the effective surface area variation as a function of SoC. This subplot indicates behavior that is not symmetric with respect to 50% SoC. We can see that for each electrolyte composition (0.5, 1 and 1.5 M V) $A_{effective}$ is higher in the high SoC range than the low range. The 0.5 M V passes through a maximum around 75% SoC while both the 1 and 1.5 M V cases are maximized at the highest SoC. This trend in $A_{effective}$ suggests that the behavior observed in Figure 6.3 where the polarization dependence on open circuit ASR magnitude is not one-to-one could be related to the effective surface area which is preferentially higher at higher SoC.

Efficiency estimation for 1.5 M V

The uncertainty in electrolyte composition for the 1 M V and 0.5 M V cases raises concerns about the effect of crossover. Using equation 1.2 as an estimate, we can see that even if the crossover rate is not dependent on concentration, the lower concentration cases have less total mass so the fractional changes that occur on account of crossover impact the OCV to a higher degree. For this reason we have only performed the system efficiency estimation with the 1.5 M V data set, where the impact of crossover is minimal, and we assume to be approximately zero. Figure 6.6 shows the efficiency profile calculated with equations 6.12 and 6.13.

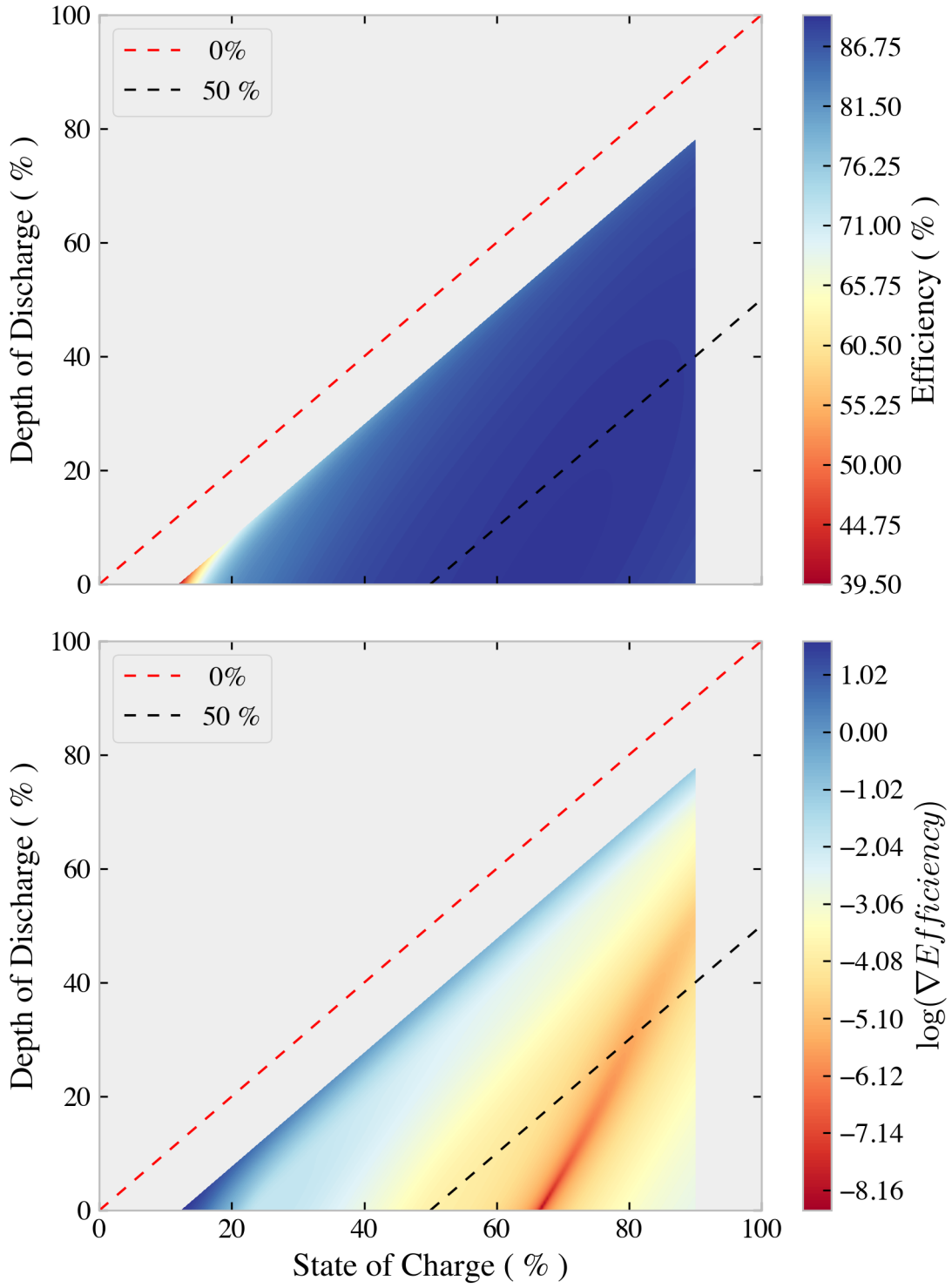

Figure 6.6: System efficiency predictions using 1.5 M V. The black and red dashed lines indicates 50 and 0% SoC references respectively.

much lower degree of uncertainty (than VRE smoothing).

6.4 Conclusions

Through this analysis we have related the manifestation of nonlinearities in system parameters as a function of composition to a system scale model of efficiency. A novel experimental configuration was utilized to probe the VRFB anode and cathode over a range of electrolyte compositions. The anode was investigated in greater depth than the cathode on account of constituting a much larger portion of the total cell |ASR|. The effective surface area for all experiments was found to be higher in the high SoC range (SoC > 75%) trending downward from this point. A (limited) novel representation of energy efficiency was derived and utilized to generalize an operating conditions over a range of SoCs and depths of discharge. It was found that the depth of discharge can be optimized for conditions with an initial SoC above 67%. While, we do not expect this behavior to be generally true of all operating conditions (charge/discharge currents), equation 6.12 can be used to profile a system when crossover is minimal, and importantly, can be determined with a single lab-scale battery (i.e not using the setup if Figure 6.1).

Chapter 7

Improved rate capability and low internal resistance for vanadium redox flow batteries utilizing ultrafast laser structured graphite felt

This chapter is a revised version of the published paper: [204]

M. C. Daugherty, C. T. Hsieh, D. S. Aaron, Y. Ashraf Gandomi, J. Li, Y. Zheng, and W. Pfleging. Enabling high rate capability, low internal resistance, and excellent cyclability for vanadium redox flow batteries utilizing ultrafast laser-structured graphite felt. Electrochimica Acta, 344, 2020.

My contributions to this work were collection, reduction, and analysis of data and manuscript composition. Pfleging assisted with sample preparation. Hsieh assisted with manuscript composition. Li and Zheng assisted with data collection.

Abstract

The electrochemical performance of vanadium redox flow batteries (VRFBs) was enhanced via laser-patterned graphite felt (GF) electrodes. The laser-structured GF electrodes engineered via preparing a series of well-ordered microscopic channel structures with an average width of 200 μm, creating a three-dimensional carbon framework. The ultra-fast laser patterning increased the porosity by 10%, as compared to pristine electrode. Analysis of the overpotential distribution using electrochemical impedance spectroscopy revealed that the electrode polarization involving charge transfer and diffusion resistance is strongly alleviated with the aid of carbon micro perforation. The advanced design of laser-structured GF electrode also exhibits high rate capability, low internal resistance, and excellent cyclability. The improved performance was attributed to the synergistic effect involving (i) high electrochemically active surface area for rapid electrochemical reactions (i.e. V(II)/V(III) and V(IV)/V(V) redox couples) and (ii) excellent transport prop-

erties for facile electron/ion/species transport. The micro-scale channels created with the laser-ablation technique act as capillary structures and enabled homogeneous and rapid wetting of GF electrodes as formulated with the classical Washburn equation. The VRFB equipped with the laser-structured GF electrodes delivered a high discharge capacity with exceptional capacity retention upon extended cycling (>84.9%). Accordingly, the design of laser-structured electrode paves the pathway towards finely tuning the electrode internal microstructure for improved cyclability, durability, and capacity retention in various electrochemical energy storage/conversion devices (e.g. all-vanadium redox flow batteries).

7.1 Introduction

Redox flow batteries (RFBs) have emerged as a promising technology for large scale energy storage [12, 132]. RFBs decouple energy capacity from power rating, thus, are well suited for scaling. Relatively long cycle life along with improved safety are other notable advantages of RFBs. Numerous chemistries have been developed for RFBs; among those, all-vanadium redox chemistry has been the focus of significant research and improvement in recent years [12]. All-vanadium redox flow batteries (VRFBs) utilize vanadium ions in different oxidation states in the negative electrolyte (V(II)/V(III)) and positive electrolyte (V(IV)/V(V)). VRFBs, therefore, do not suffer from irreversible cross contamination due to undesired transport of vanadium ions through the membrane during cycling [136].

Among different components used within VRFB reactors, the electrodes play a significant role influencing the performance as well as the durability. The elec-

trode's surface chemistry affects the kinetics and its microstructure can modulate transport [205]. Graphitic carbon has been widely used as the electrode material for negative and positive half-cells [124, 137]. Graphitic carbon is capable of catalyzing the redox reactions (i.e., V(II)/V(III) and V(IV)/V(V)); thus, no noble catalyst is needed for the half-cell reactions. Several other carbon-based materials including carbon nanotubes [206], activated carbons [207], activated carbon felt [208], and carbon fibers [112] have also been employed as the electrode material for VRFBs. In VRFBs determination of which half-cell has a higher rate constant is dependent on electrode composition [37], however, for untreated polyacrylonitrile (PAN)-based felt, the anode kinetics are more limiting than the cathode [77]. Therefore, developing low cost, durable, and high efficiency electrode materials with improved surface chemistry and microstructure is of significant importance.

Decorating the carbon felt electrodes with carbon nanodots [175] and carbon nitride nanoparticles [176] has been explored for boosting the catalytic activity since it promotes the formation of a hierarchical electrode microstructure. Various chemical, thermal, and electrochemical treatments have also been implemented for altering the physical morphology of the carbon electrodes and subsequently improving the performance and durability [209–211]. These techniques, despite being very efficient, are not capable of finely tuning the microstructure as well as the surface morphology of the electrodes.

Here, we have adopted a high frequency ultrafast laser ablation technique for preparing a well-ordered porous microstructure within the graphite felt (GF) electrodes. Graphite felt is a commonly used electrode material with an average car-

bon fiber diameter of 8–10 μm and a wide potential window in which it is stable. However, low electrochemical surface area and low electrocatalytic activity (i.e., poor kinetics and reversibility) severely limits the application of GFs as high performance electrode materials for VRFBs [101,102]. Therefore, via laser patterning, we have improved the catalytic activity along with transport properties within the electrode nanostructure. Recently, ultrafast laser processing has emerged as a high quality and cost effective approach for engineering various materials [212]. The laser patterning technique has been successfully employed for preparing a $LiNi_{1/3}Co_{1/3}Mn_{1/3}O_2$ cathode [213], graphite and silicon/graphite anodes [214, 215], and Li metal foils [216], with superior power/energy density for lithium-ion batteries (LIBs). The enhanced performance has been attributed to increased electrochemical active surface area, improved mechanical properties during electrochemical cycling (i.e., reduced degradation), and decreased charge-transfer impedance. In this context, attempts have been made to use laser (e.g., CO_2) to open transport pathways of varying size and number in the electrode structure. By varying the diameter and density of these transport channels, they studied the effects of perforation size and the critical transport length for electrolyte flowing through the bulk electrode material in VRFBs [107,217,218].

Inspired by these prior observations, we prepared a series of laser-patterned electrode microstructures to be used as high-performance electrodes for VRFBs. Herein we employed an ultrafast fiber laser to fabricate different electrode structures with various micro-pore internal morphologies. Subsequently, we utilized the as-prepared electrodes within all-vanadium flow battery configuration and ex-

plored the performance along with cyclability. The findings of this work will pave the pathway for designing laser-patterned GF electrodes for high performance RFBs.

7.2 Methods

7.2.1 Laser treatment of GF electrodes

To prepare the laser-patterned electrodes, the GF sheets (SIGRACELL®, nominal dry thickness: 3 mm) were purchased from SGL Carbon Cooperation (Germany). A laser micromachining system PS450-TO (Optec s. a., Belgium), equipped with an ultrafast fiber laser (Tangerine, Amplitude Systèmes, France), was applied in order to realize a cold laser ablation. The ultrafast fiber laser system has a maximal average power of 35 W and a maximum pulse energy of 175 μJ (M2 < 1.2). The laser pattern induced channels with a width of 200 μm and a depth of 1.2 mm. Pitch between each channel was set at 800 μm on the GF electrode with the projected area of 5 cm^2. Accordingly, the channel density was 12.5 channels per cm^2.

Subsequently, the perforation of pristine GF was carried out using the laser micromachining system. During the laser ablation, a sheet of GF was fixed to a graphite backing plate with tape in order to ensure a flat surface along with a well focused laser beam. The ablation process was performed five times to achieve a clean structure without debris formation. The laser structuring process was carried out at a scan rate of 200 mm s^{-1}, laser repetition rate of 200 kHz, wavelength of 515 nm, and at an average power of 2.2 W.

Throughout the entire paper, the untreated and laser treated GF electrodes were labelled with letters "U" and "L", respectively. To inspect a possible impact of laser ablation, a scanning electron microscope (SEM, Zeiss ULTRA 55) was employed to capture the micrographs. An X-ray diffraction (XRD: Shimadzu Labx XRD-6000) spectroscope, equipped with Cu-Kα radiation emitter, was also employed to characterize the crystalline structures of the GF samples. To figure out the porosity change due to the laser patterning, the apparent density of GFs, defined as the mass of materials divided by the total volume they occupy, was calculated. The apparent densities of U and L electrodes were ca. 0.180 and 0.162 g cm^{-3}, respectively. Accordingly, an increased porosity (approximately 10%) of L electrode was thus obtained.

Contact angle (CA) measurement was performed to evaluate the hydrophilicity on U and L electrodes. Deionized water (surface tension: 72.3 mN m^{-1}) was used to evaluate the water repellency on U and L electrodes. An optical meter was applied for measuring the CAs of water droplets on the GF electrodes. A 12 μL water drop was dropped on the electrodes using a micropipette. Five drops of water were placed at different locations on a horizontal GF surface, and five readings were then taken. The derivation of the CAs measured in this study was within 2.4°. All CA measurements were performed at ambient temperature.

7.2.2 Assembly of VRFBs

For the baseline conditions, the GF electrodes (Sigracell GFD3 SGL, Carbon Group, Germany) with the nominal thickness of 3 mm were used. More details of L electrodes were given as follows: (i) pore channels positioned on the current collector

side, and (ii) pore channels were parallel to the direction of flow. Polytetrafluoroethylene gaskets were employed to assure an appropriate compression of the porous electrodes (~25% compression), reduce the contact impedance, and prevent electrolyte leakage. Nafion® 117 (Dupont) was used as the ion exchange membrane to separate the half cells.

The VRFB architecture used in this study consisted of a rectangular flow through flow field (4×1.25 cm^2). Gold-plated current collectors were also utilized within the cell architecture and a two channel peristaltic pump (Cole Parmer) was used to circulate the electrolyte at a constant volumetric flow rate (25 mL min-1). The electrolyte (1.5 M V; 3.3 M H_2SO_4) was prepared via dissolution of vanadium (IV) oxide sulfate hydrate ($VOSO_4 \cdot xH_2O$, Sigma Aldrich) in a solution of sulfuric acid and deionized (DI) water. Starting with 100 mL of positive electrolyte and 50 mL of negative electrolyte, the electrolytes were potentiostatically (1.8 V) brought to 100% state of charge (SoC) followed by the removal of 50 mL of positive electrolyte. The negative electrolyte reservoir was under a continuous nitrogen gas flow throughout the entire experiment to prevent oxidation. For the impedance measurements, the VRFB was operated in the symmetric cell configuration in order to isolate a half cell and eliminate crossover effects. The electrolyte for all symmetric cell measurements was maintained at 50% SoC. The symmetric cell has been demonstrated and validated by others [38]. For cycling experiments, the full cell configuration was used, which is the standard arrangement (positive electrolyte at the cathode; negative electrolyte at the anode).

7.2.3 Electrochemical characterization of VRFBs

Prior to any electrochemical test, the VRFBs were exposed to electrolyte for 4 h, allowing total electrolyte wetting. The electrochemical impedance spectroscopy (EIS) was performed using a Bio-Logic potentiostat (model number: HCP-803). The EIS analysis was carried out within the frequency range of 100 kHz to 25 mHz. Spectra were fit with an equivalent circuit model (Randles Circuit), which consists of an ohmic resistor in series with a parallel combination of a constant phase element (Q) and a charge transfer impedance (Z_{ct}) [105, 109, 118, 219]. Equation 7.1 represents the Randles circuit for the symmetric cell.

$$AZ_{model,cell} = AR_o + 2A[Z_{ct}^{-1} + (j\omega)^P Q]^{-1} \tag{7.1}$$

where R_o is ohmic resistance. This model accounts for the response of the symmetric cell consisting of two electrodes and is area specific (normalized by area A). The charge transfer impedance consisted of a charge transfer resistance (R_{ct}) in series with a Warburg element (W).

$$Z_{ct} = R_{ct} + W \tag{7.2}$$

To explore high rate capability, the VRFBs were cycled within the voltage range of 0.6–1.8 V at different current densities (50, 100, and 150 mA cm^{-2}).

7.3 Results and discussion

Top view SEM micrographs of L electrode with low and high magnifications are illustrated in Figure 7.1 (a) and (b), respectively. As shown in Figure 7.1, the SEM images clearly confirm the formation of microscale channels across the entire GF electrodes. The laser-patterned channels had an average width of 200 μm with 800 μm pitch, creating a three-dimensional carbon framework. Also, as shown in Figure 7.1, the GF electrodes were composed of carbon fibers, with an average diameter of 8–10 μm. It is important to note that the GF electrodes maintained their original morphology even upon laser-patterning of the channel arrays within the microstructure (Figure7.1).

Typical XRD patterns of both GF electrodes are shown in Figure 7.2. Both U and L electrodes contain well indexed diffraction peaks of graphitic crystallites.
The interlayer distance, $d_{(002)}$, of graphitic crystalline can be obtained using the Bragg's equation [192]. The $d_{(002)}$ peak of the U electrode takes place at 25.6°($d_{(002)}$ = 0.347 nm) whereas the L sample possesses the $d_{(002)}$ peak appearing at 2θ = 25.4°($d_{(002)}$ = 0.350 nm). Values of interlayer spacings of L and U sample are within the measurement accuracy. This observation confirms that the so-called "cold" laser ablation does not alter the crystalline structure of the GF electrodes. The inset of Figure 7.1 (a) and 7.2 presents the SEM and optical microscopy image of L electrode. As illustrated in Figure 7.1 (a) and 7.2, the height of each laser-patterned channel is slightly smaller than half of the thickness of U electrode, i.e., 1.2 mm. Therefore, it can be deduced that the porosity of L electrodes was further

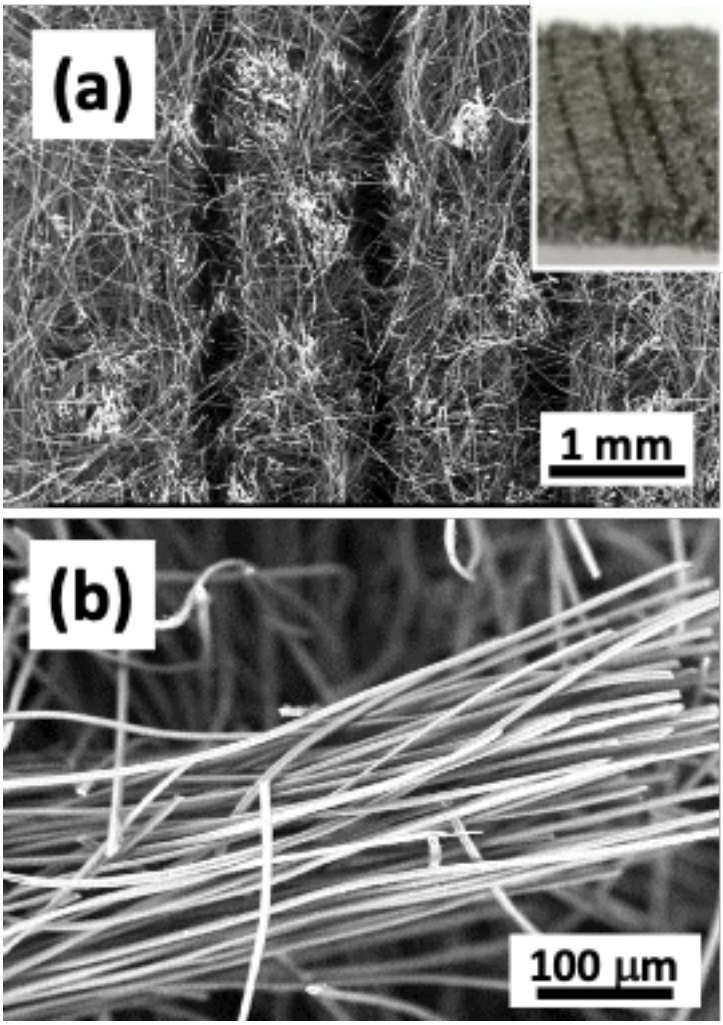

Figure 7.1: FE-SEM images of L electrode with (a) low and (b) high magnification. The inset (a) shows tilted view of FE-SEM image of L electrode.

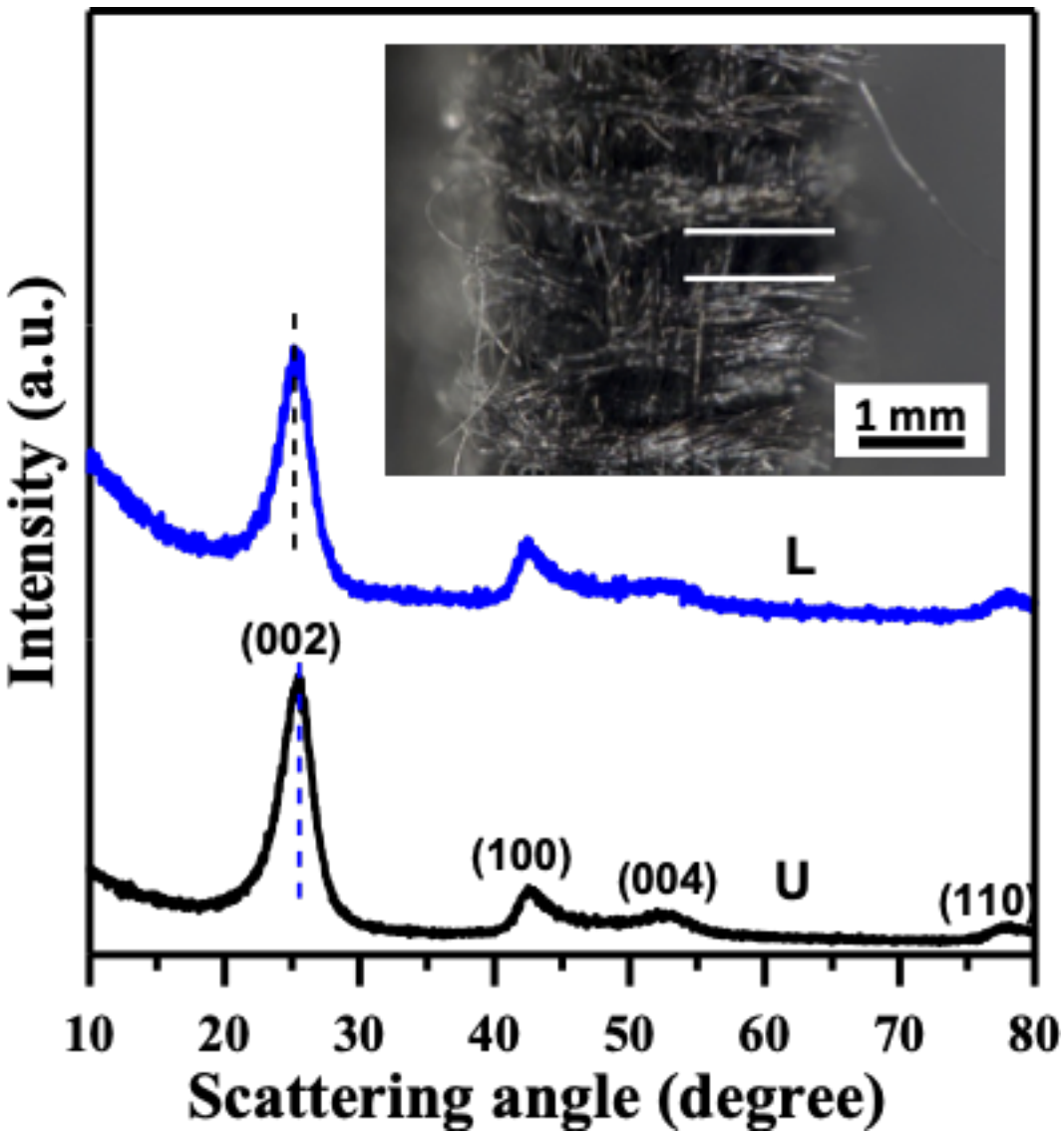

Figure 7.2: Typical XRD patterns of U and L electrodes. The inset shows cross-sectional view of optical microscopy image of L electrode.

increased (10% increase compared to the U electrode) due to laser patterning. EIS was employed to analyze the anode polarization and overpotential distribution of both U and L electrodes. For comparison reasons it was focused at the 1st and 10th cycle. Nyquist plots of the VRFBs assembled with U and L electrodes are shown in Figure 7.3(a).

According to the Nyquist plots illustrated in Figure 7.3(a), qualitative attributes of the EIS spectra are similar for U and L electrodes; however, quantitatively, their characteristics differ significantly. For the EIS spectra shown in Figure 7.3, the first semi-circle at high frequency region is attributed to the charge transfer (kinetics) resistance, the second semicircle, at low frequency, is ascribed to the mass transfer (finite length diffusion) resistance, and high frequency x-interface is related to the ohmic impedance [82,195]. The ohmic resistance includes the ionic resistance of the membrane, electrolyte, and interfacial interface between the cell components (e.g. membrane/electrode, electrode/flow filed). The contribution of the electronic resistance to overall ohmic impedance is usually minor by comparison to the membrane and distributed porous resistance. To describe the impedance behavior, a Randles circuit model was used to fit the EIS spectra, as shown in equation 7.1 and the inset of Figure 7.3(a). The equivalent circuit involves four components: (i) R_o for modeling the ohmic resistance associated with the solution, electrode, and the contact resistances, (ii) R_{ct} for faradaic charge transfer at the electrode surface, (iii) constant phase element (QDL) for simulating the charge transfer across the electrode/solution interface, and (iv) a Warburg diffusion element (W) which accounts for the ionic finite length diffusion within the electrolyte phase. Fitting the exper-

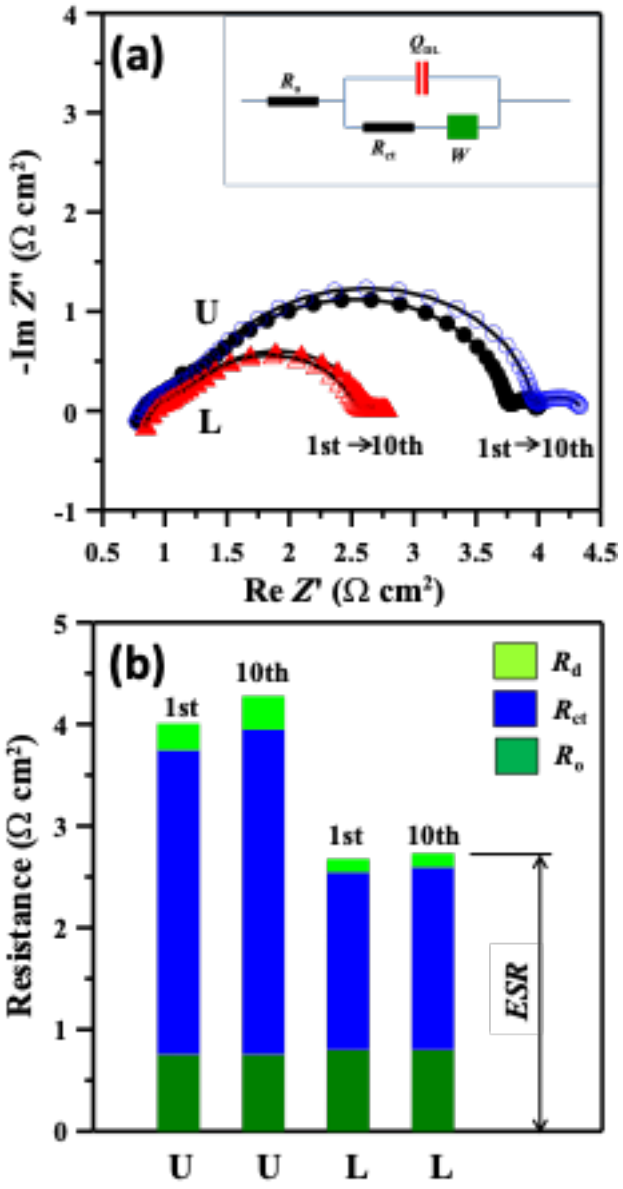

Figure 7.3: (A) Nyquist plots of U and L electrodes at 1st and 10th cycle at open circuit volt- age, where the inset shows a Randles circuit. (b) Resistance analysis of U and L electrodes at 1st and 10th cycle, where ESR is the sum of ohmic, charge transfer, and diffusion resistance.

imentally measured EIS spectra with the equivalent circuit model (Figure 7.3(a)) using a complex nonlinear least squares algorithm resulted in a good agreement between the experiment and the model with less than 10% deviation.

Analyzing the EIS spectra for both U and L electrodes, the variations in overpotential distribution were assessed (Figure 7.3(b)). As shown in Figure 3(b), the influence of laser patterning on the ohmic resistance is insignificant. The distributed ohmic resistance for U and L electrodes was in the range of 0.75–0.8 Ω cm^2. A slight increase in the distributed ohmic resistance might be due to decreased loss of direct carbon contact between L electrodes and flow plates, as compared to the base case.

According to Figure 7.3, the charge transfer resistance is reduced due the laser treatment (U electrode: R_{ct} = 3 Ω cm^2, L electrode: R_{ct} = 1.75 Ω cm^2). The improvement in the charge-transfer is mainly due to the increased electrochemically active surface area after the laser structuring. It is important to note that the mass transport was also im- proved via laser patterning. As shown in Figure 7.3, the mass transport overpotential was decreased from 0.26 to 0.13 Ω cm^2 with the aid of laser treatment. After 10 cycles, the Rd value of U electrode increases to 0.33 Ω cm^2, while the L electrodes demonstrate a relatively stable Rd value even after extended cycling. Therefore, it can be concluded that the improvements in the charge and mass transport achieved via laser patterning is stable and does not diminish during cycling. The equivalent series resistance (ESR), the sum of R_{ohmic}, R_{ct}, and R_d, is an important index for quantifying overall inner resistance of the electrodes. The variations of ESR with cycle number and electrode type are provided in Figure

7.3(b). As quantified in Figure 7.3, the ESR value for the L electrode is significantly lower compared to the U electrode. The ESR value for the U electrode increases by ~6.7% after 10 cycles, whereas the increase in the value for the L electrodes is significantly lower (only ~2.1%); thus, the cyclic stability was improved with L electrodes. It is important to note that the laser-patterning also enhances the wettability of the electrodes. The design of L electrodes facilitates the electrode wetting and decreases the mass-transport overpotential. The laser-generated microscopic capillary structures push up the diffusion limit of vanadium ions and decrease the diffusion length via enhanced convective mass transport [82]. The synergistic effect is thus the key for boosting the rate capability for VRFB applications [218]. Additional micro-scale channels, formed via laser ablation, enable efficient mass transport in concentrated solutions [107], facilitate the charge transfer on the electrode surface, and boost the catalytic activity for the vanadium redox couples within the negative electrolyte.

To explore the cyclability of L electrodes, charge-discharge cycling was conducted for the VRFBs equipped with U and L electrodes at 150 mA cm^{-2}, as depicted in Figure 7.4(a). As shown in Figure 7.4(a), utilizing the L electrodes, the discharge capacity along with the voltage efficiency was improved. To further explore the cyclability, both VRFB configurations were cycled at various current densities. The discharge capacity as a function of current density is illustrated in Figure 7.4(b). As shown in, Figure 7.4(b), the accessible capacity decreases with increased current density for both electrode configurations. However, the accessible capacity varies significantly between the U and L electrodes. Utilizing U electrode,

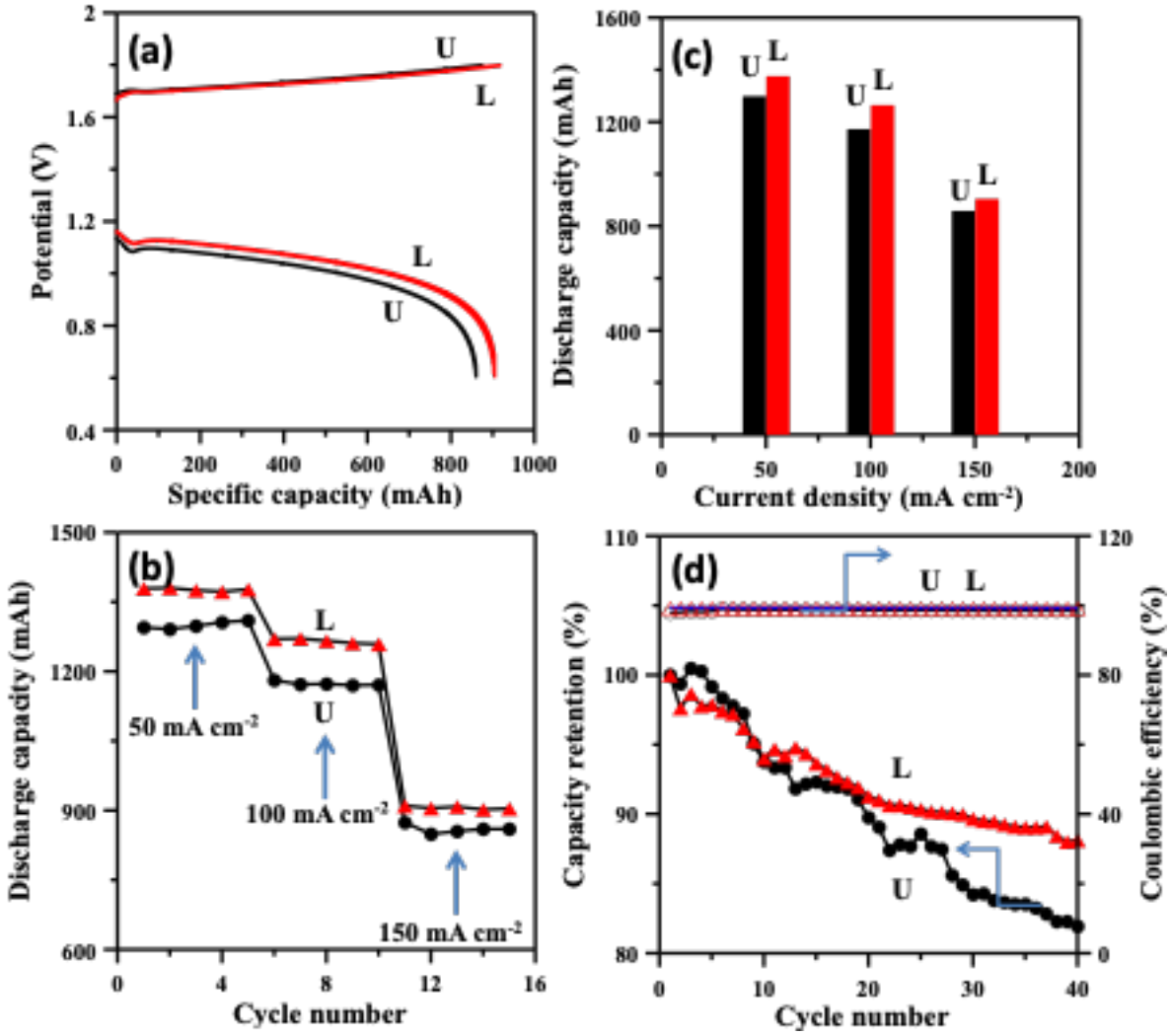

Figure 7.4: (A) Charge-discharge curves of U and L electrodes at a constant current density of 150 mA cm^{-2}, (b) specific capacity as a function of cycle number at different current density, (c) average capacity as a function of current density, and (d) both capacity retention and coulombic efficiency as a function of cycle number.

the discharge capacity within the entire SoC window was 1300, 1173, and 860 mAh at 50, 100, and 150 mA cm^{-2}, respectively. Through the laser patterning, the accessible capacity was increased to 1377, 1265, and 906 mAh at 50, 100, and 150 mA cm^{-2}, respectively (Figure 7.4 (c)). Increased theoretical capacity utilization via L electrodes is primarily due to improved wettability, enhanced charge transfer, and reduced mass transport overpotential due to the laser-assisted formation of new diffusion pathways, compared to the baseline conditions (U electrode).

The catalytic activity on the electrode surface also increases as a function of electrode wettability as demonstrated in some other works as well [30,157]. The liquid electrolyte must permeate micro and nano pores of the electrode. Generally, if the electrodes are prepared via some electrolyte filling processes, full wetting may not be achieved; thus, the capacity utilization would be lower [101]. Therefore, wetting of porous electrodes can be directly correlated to the capillary forces. The capillary rise (h) of the electrolyte liquids along the laser-generated micro-capillary structures can be formulated through the Washburn equation [220]. By neglecting the gravity and assuming that the capillary structure is filled at the beginning (h_0 = h at t = 0), the h value can be written as:

$$h = h_0 + (0.5 r \sigma cos(\theta)/\mu)^{0.5} \cdot t_h = h_0 + K\, t_h^{0.5} \tag{7.3}$$

where t [s] is the capillary rise time, r [m] is the capillary radius (i.e., half channel width), θ [°] is the contact angle between the wall and the meniscus, and σ [kg s^{-2}] and μ [kg $m^{-1}s^{-1}$] are the surface tension and viscosity of the liquid, respec-

tively. Note that K [m $s^{-0.5}$] describes the penetration ability of the liquid. Herein equation 7.3 expresses t_h [s] the capillary rise time for achieving the height h [m]. The capillary rise of liquid electrolyte in laser-generated micro-channels within the L electrodes can be described using equation 7.3 [220]. Employing the Washburn equation, the pore channels timing index can be approximated as 0.9 ms for the L electrodes with a water-based electrolyte. Since the water molecules possess a strong bipolarity, the GF electrode tends to be totally wetted by the vanadium-enriched aqueous electrolyte, as shown in Figure A.15.

To inspect the wettability, both GF electrodes were used to examine their repellency by measuring its static CAs with water droplets. Figure 7.5 shows cross view photographs of water droplets on both GF electrodes varied with time. At initial stage (1 min), it is apparent that the U electrode displays a hydrophobicity, i.e., CA of water: 155°, whereas the L electrode delivers better hydrophilicity (CA: 87°) as compared to the U one. The aqueous affinity of the L electrode toward the water drop can be attributed to the presence of pore channels, leading to an accessible penetration of water into the GF electrode due to the capillary force. The L electrode tends to be wetted easily by the water droplet. We also observe that the water volume dramatically reduces with time, as shown in Figure 7.5. After 20 min, the water drop disappears on the L electrode, confirming an easy wetting due to the existence of pore channels created by the laser treatment. This result is in good agreement with the schematic diagram in Figure A.15. Accordingly, it is concluded that the pore channels via the laser patterning enable the improvements in the charge and mass transport achieved. The mass transfer is thus improved over

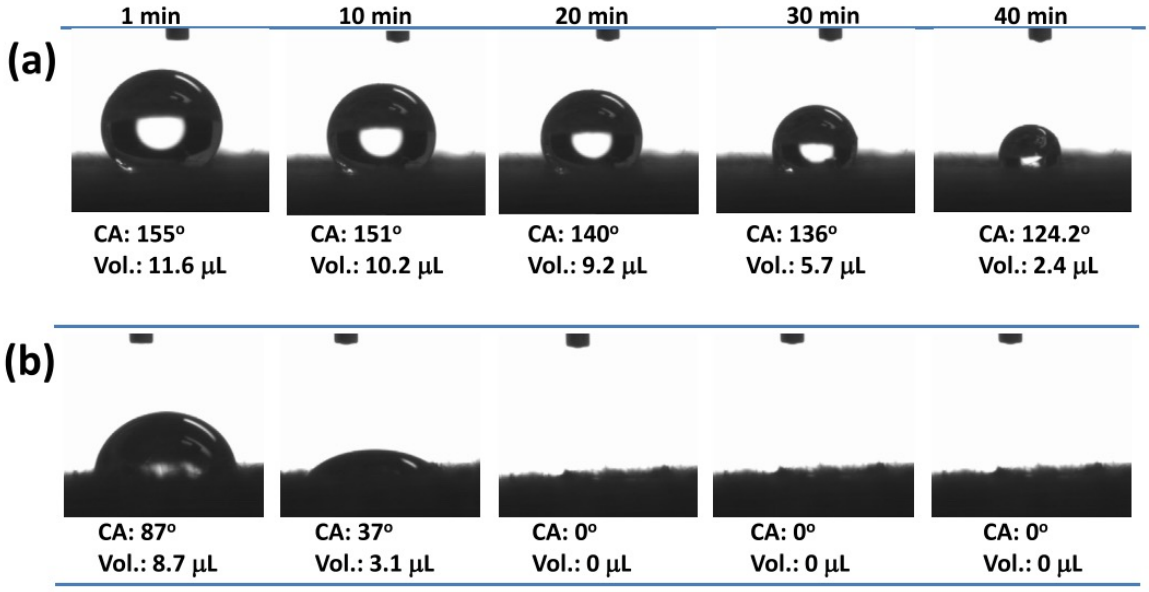

Figure 7.5: Variation of contact angle of water droplet and liquid volume with time for (a) U and (b) L electrodes.

a non-structured electrode in flow through mode.

To analyze the durability of L electrodes, cycling experiments were conducted at 100 mA cm^{-2} covering a very wide SoC window, as shown in Figure 4(d). Significant capacity fluctuations can be observed, mainly originated from ongoing gassing and electrolyte flow problems that induce excessive transfer of electrolyte from the positive into the negative electrode. This was periodically adjusted by manually transferring solution back to restore electrolyte volumes. Since this process causes an imbalance in the oxidation states of the two half-cell solutions however, the cell capacity is not immediately restored, taking several cycles to reach a new equilibrium [69, 221, 222]. After 100 cycles, the discharge capacity of U electrode decreases to 892 mAh (capacity retention: 76.0%), whereas with the L electrode, the accessible capacity was substantially higher (1073 mAh, determined from the capacity retention curve fit) confirming a superior capacity retention via the L electrodes upon extended cycling (84.9%). Therefore, the capacity loss during long-term cycling is lower with L electrodes. The major contributors to the capacity loss for VRFBs during cycling are the transport of vanadium ions through the membrane (i.e. crossover), degradation of cell components, and gas-generating side reactions. The gas-generating side reaction also do not contribute to the capacity loss in our experiments due to the cutoff voltage values considered for the cycling experiments. Thus, the major contributor to the irreversible capacity loss during long duration cycling is the degradation of the electrodes [111, 127, 158]. Therefore, according to Figure 7.4(d), it can be concluded that L electrodes are

more stable and prevent degradation or inactivation of the GF electrodes. Thus, this demonstrates that the framework of L electrode not only improves catalytic activity but also facilitates catalytic durability.

It is worth noting that the straight line shaped pattern is one of the options in increasing electrochemical surface area for the redox reaction. The crossover pattern is the other option that could contribute to more active surface area. Herein U electrode contains numerous carbon fibers with an average diameter of 8–10 μm and a length of several millimeters. The carbon fibers tend to suspend and easily peel out of the L electrode when using a crossover cutting with an average width of 200 μm in the laser pattern. The separated carbon fibers would reduce active surface area after the extended cycling, leading to a poor cyclic performance. To keep the original morphology, a straight line shaped pattern can be considered as a promising design to stabilize the cyclability of L electrode in VRFBs. The coulombic efficiency as a function of cycle number is also depicted in Figure 7.4(d). The coulombic efficiency was also maintained at ultra-high values for L electrodes (~99.2%), confirming high reversibility towards the redox reactions (V(II)/V(III) and V(IV)/V(V) redox couples) during extended cycling.

7.4 Conclusions

In this study, we demonstrated an advanced design of L electrodes with high rate capability, low internal resistance, and long duration cyclability tailored for redox flow battery applications. The micro-channels generated by the ultrafast laser ablation enhanced the porosity by about 10%, as compared to U electrode.

Laser-patterned macroscopic channels exhibited an average width of 200 μm and a height of 1.5 mm, creating a three-dimensional carbon framework. The overpotential distribution analyzed by the EIS technique revealed that the electrode polarization involving charge transfer and ionic diffusion resistance was strongly alleviated in the presence of carbon perforation. The enhancement could be attributed to the design of L electrode that contains vast porous/ geometrical structures to render (i) high electrochemically active surface area for rapid electrochemical reactions (i.e., V(II)/V(III) at the anode) and (ii) improved transport properties for fast electron/ion/species transport. A synergistic effect between the L electrodes and the flow fields boosts the rate capability and cyclability. The channels created by ultrafast laser ablation technique enabled complete and rapid wetting of GF materials with liquid electrolyte, as formulated by the classical Washburn equation. All vanadium redox flow batteries assembled with the L electrodes demonstrated improved capacity retention upon extended cycling (84.9%). Accordingly, the design of L electrodes paves the way for micro engineering the electrode internal morphology for improved durability and cyclability in various energy storage devices (e.g. redox flow batteries).

Chapter 8

Lattice Boltzmann modeling of 2D element of all vanadium redox flow battery electrode: Part I

This chapter will not be published as a stand-alone article prior to submission of my ETD, therefore a publication statement was not included. The content of this chapter will be part one in a two part manuscript, which will focus on the lattice Boltzmann model. Part two will focus on a machine learning (neural network) approach with this model as input data. It will be submitted for publication authored by Michael. C. Daugherty, Douglas S. Aaron and Matthew M. Mench.

My contributions to this work were: programming the model, acquisition of data, data reduction and composition of the manuscript. Contributions from co-authors will be added prior to submitting for publication.

8.1 Introduction

Lattice Boltzmann models (LBM) are a class of numerical models which can be used to simulate (among others) fluid flows, mass transfer, heat transfer and many niche physical phenomena which occur in these fields [88]. LBM is an explicit method that can be easily parallelized and has certain advantages over conventional conservation methods (finite difference and finite volume) the most prominent of which is its implementation of boundary conditions. The ease of implementing boundary conditions to arbitrarily shaped domains, is one of the greatest strengths of LBM [89]. Bounce-back boundaries can be used as no-slip boundary conditions for fluid flow as well as zero-flux boundary conditions for mass transfer [90]. The boundary conditions implementation method coupled with the ease of parallelization make LBM attractive for modeling electrochemical systems, which are often restricted to mass transfer in geometrically complex domains such

as porous media. Indeed, LBM has found a wide range of uses in the field of electrochemistry. Kang *et. al* derived a multi-component reactive boundary for LBM that has been utilized by others in the fuel cell, lithium battery and flow battery literature e.g. [85, 91–94].

The implementation of machine learning in the context of electrochemistry is still fairly novel. Ye *et al.* demonstrated the ability to identify the presence of heavy metals in solution based on voltammetric data [223]. While other work has focused on chemical physics looking specifically to model atomistic systems for both molecules and materials [224]. In the battery space it has been used to optimize lithium-ion cathodes [225] and has been used to model redox flow battery cathodes at multiple scales [22]. Bao and co-workers used LBM to generate high-fidelity simulations, which were used to train their network. This work aims to validate a two-dimensional model of a micron-scale flow battery electrode element, which can be swept over a higher parameter space than a 3d model. The intended use of the model in this work will be for training a neural network with a richer parametric space than work previously done on flow batteries.

8.2 Lattice Boltzmann Model

The lattice Boltzmann model used in this work involves a velocity field coupling to a species distribution field. First we will discuss the resolution of the fluid transport.

8.2.1 Fluid Transport

The continuity (8.1) and Navier Stokes equations (8.2) in their incompressible forms ($\rho = const$) were solved to resolve the fluid field.

$$\nabla \cdot u = 0 \tag{8.1}$$

$$\rho \frac{\partial u}{\partial t} = -\nabla p + \nu \Delta u + F \tag{8.2}$$

where Δ is the Laplace operator, u is the fluid velocity, ρ is the density, p is the pressure, ν is the kinematic viscosity and F is the body force. The single relaxation time Bhatnagar-Gross-Krook (BGK) model is a common LBM, which was used to solve equations 8.1 and 8.2. The BGK model is expressed as:

$$f_i\left(x + c_i \Delta t, t + \Delta t\right) - f_i(x,t) = -\frac{1}{\tau}\left(f_i(x,t) - f_i^{eq}(x,t)\right) \tag{8.3}$$

where $f_i(x,t)$ is the particle distribution function at lattice point x, for direction i ($i \in [0,1,..,8]$), at time t, c_i is the lattice speed, τ^{-1} is the relaxation frequency and $f_i^{eq}(x,t)$ is the equilibrium distribution. The left side of the equality in Equation 8.3 represents the *streaming* of the particle distribution function to its adjacent lattice points, while the right half represents the *collision* between the incoming particles from the adjacent lattice points [88]. LBMs are classified by a lattice nomenclature that specifies the number of spatial dimensions (D) and the number of streaming directions (Q). The equilibrium distribution function for a D2Q9 lattice is defined

as:

$$f_i^{eq} = w_i \rho \left(1 + 3\frac{c_i \cdot u}{c^2} + \frac{9}{2}\frac{(c_i \cdot u)^2}{c^4} - \frac{3}{2}\frac{u^2}{c^2}\right) \tag{8.4}$$

where the weights (w_i) are:

$$w_i = \begin{cases} \frac{4}{9}\ ;\ i = 0 \\ \frac{1}{9}\ ;\ i = 1,2,3,4 \\ \frac{1}{36}\ ;\ i = 5,6,7,8 \end{cases} \tag{8.5}$$

The lattice velocities (c_i) are:

$$c_i = \begin{cases} (0,0)\ ;\ i = 0 \\ \left(\cos\left(\frac{(i-1)\pi}{2}\right), \sin\left(\frac{(i-1)\pi}{2}\right)\right), i = 1,2,3,4 \\ \sqrt{2}\left(\cos\left(\frac{(i-5)\pi}{2} + \frac{\pi}{4}\right), \sin\left(\frac{(i-5)\pi}{2} + \frac{\pi}{4}\right)\right), i = 5,6,7,8 \end{cases} \tag{8.6}$$

Note the different lattice directions in 8.6 have two dimensional velocity vectors. Chapman-Enskog expansion is used to recover equations 8.1 and 8.2 and to relate the macroscopic fluid variables (ρ and u) to the LBM. ρ and u are recovered by computing the first and second moments of the particle distribution function f.

$$\rho = \sum_i f_i \tag{8.7}$$

$$\rho u = \sum_i f_i c_i \tag{8.8}$$

While the viscosity is related to the relaxation frequency (τ^{-1}) by:

$$\nu = c_s^2 \left(\tau - \frac{1}{2} \right) \frac{\delta x^2}{\delta t} \tag{8.9}$$

where c_s is the lattice speed of sound, which is typically set to $\frac{1}{\sqrt{3}}$, δx and δt are the lattice spacing and time step. Figure 8.1 illustrates the D2Q9 lattice with the streaming directions labeled.

8.2.2 Species Transport

The advection/diffusion equation describes the evolution of a scalar field (e.g. temperature, species concentration, etc.) and is governed by the equation:

$$\frac{\partial C}{\partial t} = -\nabla \cdot (Cu) + \nabla \cdot (D \nabla C) + q \tag{8.10}$$

Where C is a scalar quantity, u is the fluid velocity, D is the diffusion coefficient and q is a source term. This equation is very similar to equation (8.2) and is formulated similarly in the framework of lattice Boltzmann. The use of a D2Q5 lattice (see Figure 8.1) for solving equation 8.10 has been studied and determined to be of an equal level of accuracy to using a D2Q9 model [91,94,226] and is used herein for the species distribution lattices. We will use the variable g (instead of f) to represent the species distribution function. The BGK single relaxation time model was used again for the species distribution and has the exact same form as equation 8.3

$$g_i \left(x + c_i \Delta t, t + \Delta t \right) - g_i(x,t) = -\frac{1}{\tau} \left(g_i(x,t) - g_i^{eq}(x,t) \right) \tag{8.11}$$

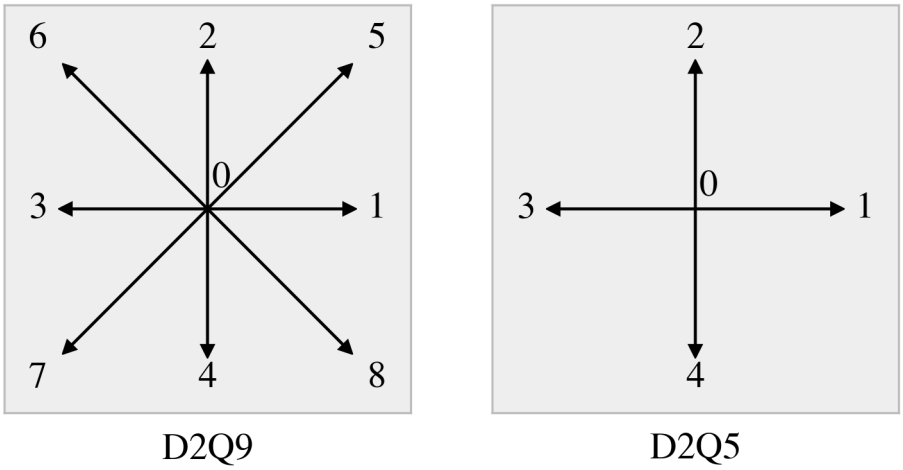

Figure 8.1: The two lattices used in this work were D2Q9 (for solving the fluid flow) and D2Q5 (for solving species transport).

The equilibrium distribution function for equation 8.11 is simpler than the equilibrium distribution function for the fluid transport (8.4) and is expressed as:

$$g_i^{eq} = w_i C \left(1 + \frac{c_i \cdot u}{c_s^2}\right) \tag{8.12}$$

The weights for any LBM must add up to 1 $\left(\sum_0^i w_i = 1\right)$, therefore the weights (w_i) for the D2Q5 lattice differ from the D2Q9 lattice and are defined as:

$$w_i = \begin{cases} \frac{1}{3} \; ; \; i = 0 \\ \\ \frac{1}{6} \; ; \; i = 1, 2, 3, 4 \end{cases} \tag{8.13}$$

The lattice velocities, for the D2Q5 model are the same as the lattice velocities for the D2Q9 model (for D2Q5 $i \in [0, 1, .., 4]$). Similar to Equation 8.7, the macroscopic scalar quantity (C) is recovered by computing the first moment of g:

$$C = \sum_i g_i \tag{8.14}$$

Similar to the viscosity, the diffusion coefficient is related to the relaxation frequency by:

$$D = \frac{(1 - J_0)}{2} \left(\tau - \frac{1}{2}\right) \frac{\delta x^2}{\delta t} \tag{8.15}$$

8.2.3 Boundary Conditions

The boundary conditions utilized in the LBM simulations are shown in Equation 8.16.

$$\begin{aligned} C\big|_{x=0} &= Constant \\ \left.\frac{\partial C}{\partial x}\right|_{x=x_{max}} &= 0 \end{aligned} \tag{8.16}$$

The boundaries at $y = 0$ and $y = y_{max}$ were periodic for the solutions in porous media and were zero-flux for the validation cases (these cases will be expounded upon in the next section). The electrochemical boundary proposed by Kang and co. workers [91] was utilized in this work (8.17)

$$\begin{cases} g_{u,Red} - g_{kn,Red} = -kC_{Red}^{\alpha} C_{Ox}^{1-\alpha} \left(\exp((1-\alpha)\bar{\eta}) - \exp(\alpha\bar{\eta})\right) \\ g_{u,Red} + g_{kn,Red} = \frac{1-J_0}{2} C_{Red} \\ g_{u,Ox} - g_{kn,Ox} = kC_{Red}^{\alpha} C_{Ox}^{1-\alpha} \left(\exp((1-\alpha)\bar{\eta}) - \exp(\alpha\bar{\eta})\right) \\ g_{u,Ox} + g_{kn,Ox} = \frac{1-J_0}{2} C_{Ox} \end{cases} \tag{8.17}$$

A schematic of the node identification is shown in Figure A.9 where the orientation of electrochemical boundary is clarified. The corner node equations are likewise specified in equation A.51 in the appendix. These systems of equations (edge nodes and corner nodes) were solved via Newton-Raphson method where the Jacobian was explicitly calculated. This was done to improve efficiency as every interfacial node in the domain solves one of these two systems of equations.

8.3 Results and discussion

8.3.1 Model validation: diffusion field

The model was validated against a known analytic solution for a pure diffusion case solving Laplace's equation on the rectangular domain $n_x \times n_y$ [91,94,227].

$$\begin{gathered} \frac{\partial^2 C}{\partial x^2} + \frac{\partial^2 C}{\partial y^2} = 0 \\ 0 < x < n_x \\ 0 < y < n_y \end{gathered} \tag{8.18}$$

Subject to the boundary conditions:

$$\begin{aligned} C\big|_{x=0} &= C_1 \\ \left.\frac{\partial C}{\partial x}\right|_{y=0} &= 0 \\ \left.\frac{\partial C}{\partial y}\right|_{x=n_x} &= 0 \\ D\left.\frac{\partial C}{\partial y}\right|_{y=n_y} &= -kC \end{aligned} \tag{8.19}$$

Equation 8.18 subject to boundaries 8.19 has the analytic solution:

$$C_1(x,y) = (C_0 - C_{eq}) \sum_{n=0}^{\infty} \frac{\sin(\beta_n n_y)}{N_n^2 \beta_n} \frac{\cosh(\beta_n (x - n_x))}{\cosh(\beta_n n_x)} \tag{8.20}$$

With:

$$N_n^2 = \frac{n_y}{2}\left(1 + \frac{\sin(2\beta_n n_y)}{2\beta_n n_y}\right)$$
$$(\beta_n b)\tan(\beta_n n_y) = D_a = \frac{k n_y}{D} \tag{8.21}$$

Comparisons of the lattice Boltzmann model and the analytic solution (Equation 8.18) are shown in Figure 8.2 where the normalized concentration is calculated with equation by:

$$C_{normalized} = \frac{C - C_{eq}}{C_1 - C_{eq}} \tag{8.22}$$

The parameters used in figure 8.2 are shown in Table A.7. The D2Q5 LBM is in very high agreement with the analytic solution, where the dashed lines (analytic solution) are hardly distinguishable from the LBM (RMSE $\approx$ 0.019, 0.029 for Da = 3.0, 30.0 respectively).

8.3.2 Model validation: advection and diffusion

The model was likewise validated in a field with both advection and diffusion with the Levesque analytical solution, which is valid for high Péclet (Pe) numbers ($u_{max}L \gg D$) [92,228].

$$\frac{\partial C}{\partial y} = \frac{1}{\Gamma(4/3)9^{1/3}}\left(\frac{4Pe}{x n_y^{-1}}\right)^{1/3} \tag{8.23}$$

To model the solution of equation 8.23 the Poiseuille parabolic velocity profile is used as the velocity field with the velocity u_{max} at the center of the channel. Both

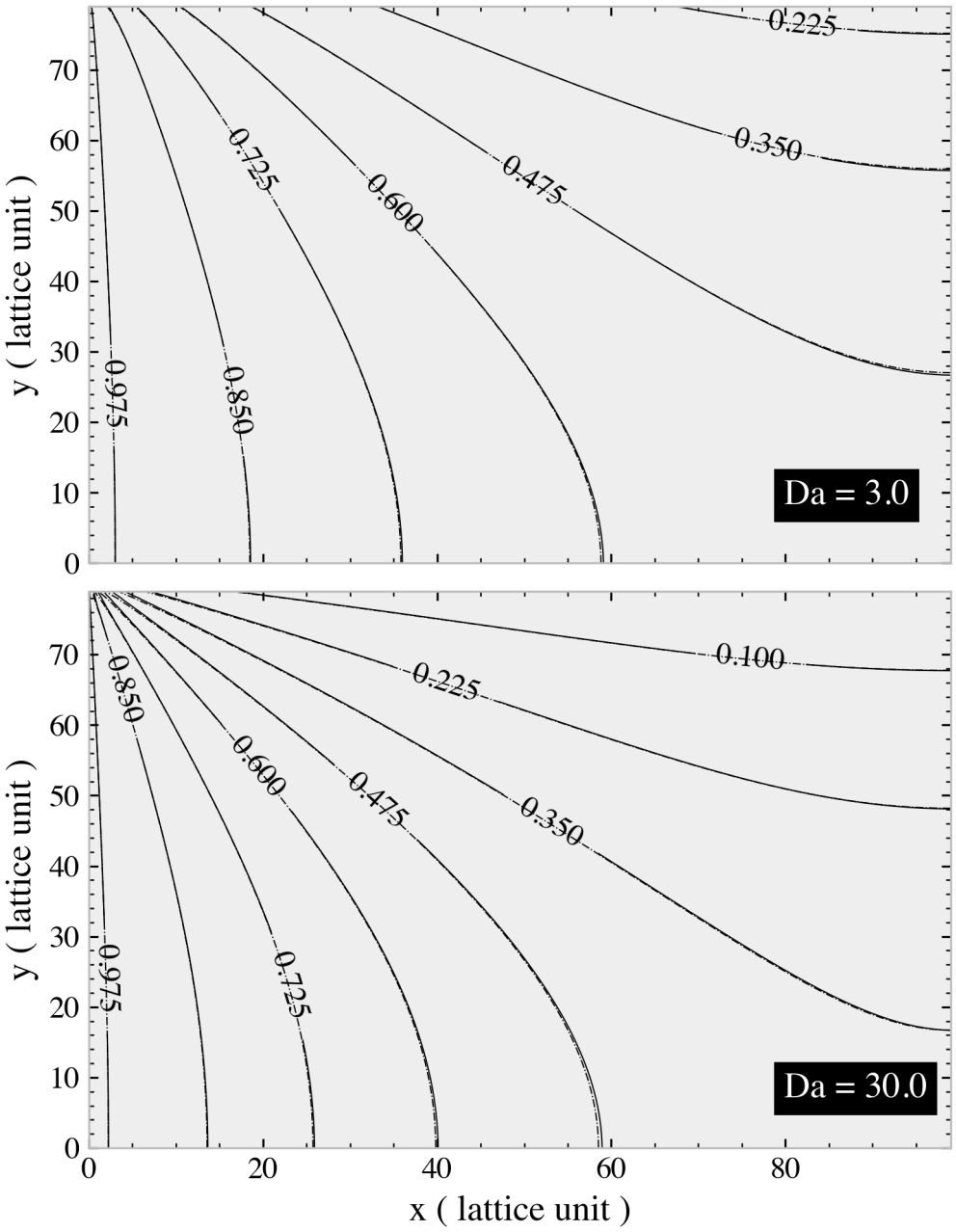

Figure 8.2: Analytic solution vs. D2Q5 LBM solution for Da = 3.0 and Da 30.0. The solid line is the LBM solution and the dashed line is the analytic. Parameters used in these simulations are shown in Table A.7.

the upper boundary of the domain and the outlet were zero-gradient boundaries while the inlet boundary is held at constant concentration. The boundary conditions for the solution of equation 8.23 are shown in equation 8.24:

$$\begin{aligned} C\big|_{x=0} &= C_{in} \\ \left.\frac{\partial C}{\partial y}\right|_{y=n_y} &= 0 \\ \left.\frac{\partial C}{\partial x}\right|_{x=n_x} &= 0 \\ D\left.\frac{\partial C}{\partial y}\right|_{y=0} &= -kC \end{aligned} \tag{8.24}$$

Figure 8.3 shows the comparison between the LBM and equation 8.23. Clearly equation 8.23 has a singularity at the inlet where x = 0. The solution approaches infinity at this leading edge, and the LBM solution is least accurate in this vicinity. The agreement between the LBM and the analytic solution is higher moving down the channel away from x = 0 (RMSE $\approx$ .414).

8.3.3 Porous media

Investigation of the response of the model was carried out by sweeping the inlet state of charge, the dimensionless overpotential ($\bar{\eta}$) and generating pseudo-random porous media for the boundaries. The purpose of this parametric sweep was to generate a three-dimensional data set for training a neural network with, which will be the content of the follow-up work. A Sobol sequence was utilized to sweep these parameters in a pseudorandom sequence that evenly samples the two-dimensional space (SoC $\times$ flow rate) [22]. The inlet velocity was held con-

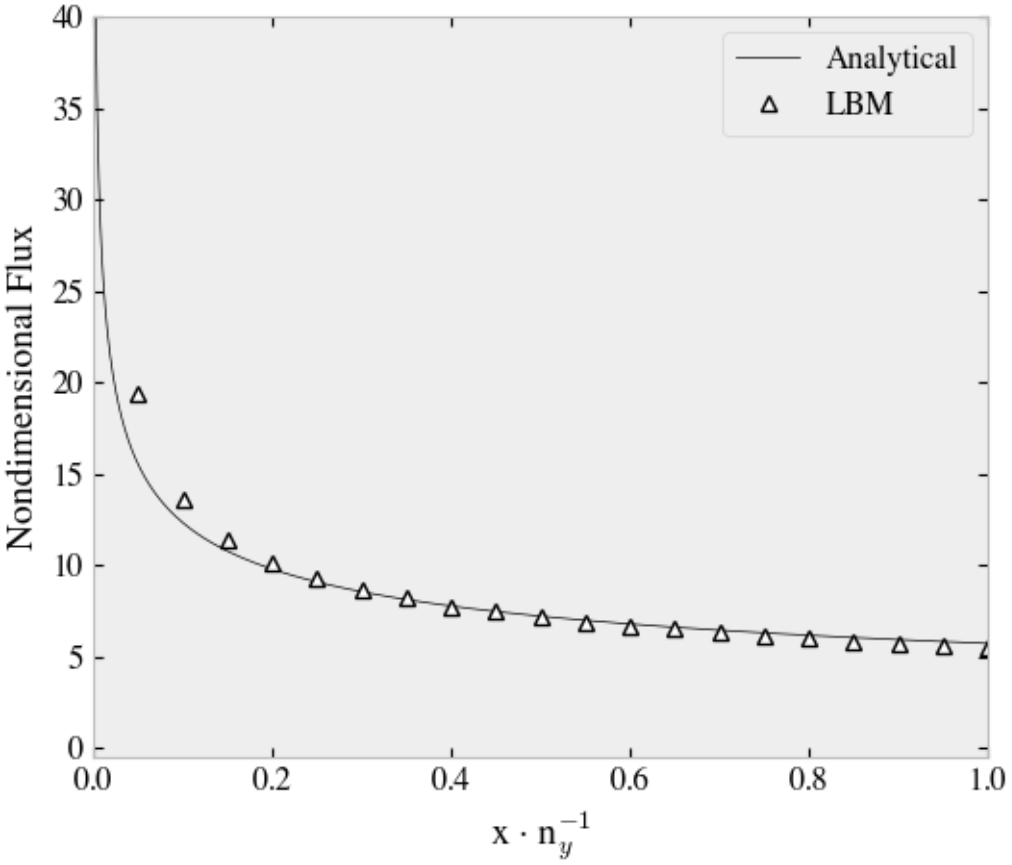

Figure 8.3: Comparison of the LBM solution to the Levesque analytic solution. Parameters used for this simulation are shown in Table A.8

stant at the inlet where its magnitude was calculated from a flow rate of 20 mL min^{-1}. Based on the inlet width (.04 m), gasket height (.0018 m) and a porosity of .9, this velocity was $\approx$ 0.0051 m s^{-1}. With a characteristic length of 200 μm and a kinematic viscosity of $2.4\times10^{-6} m^2 s^{-1}$, the Reynolds number for these simulations was ~0.211. While some LBMs include the electrolyte phase potential and resolve the overpotential locally across the fiber-electrolyte interface, here we have assumed that the electrolyte phase potential is constant and therefore the overpotential across the entire domain is constant. Work by Gandomi and co- workers has shown that the variation in overpotential throughout the thickness of the porous domain does not vary to a high degree [79]. The fluid velocity field was resolved first, solving the Navier stokes equations (8.1 and 8.2). After this, the species distribution was resolved with the supplied velocity field for the advection diffusion transport (equation 8.10). The C++ software Palabos was utilized to solve the lattice Boltzmann equations, while Porespy (porous media visualization software) was utilized to generate porous media for LBM simulations, which were scaled to 200 μm with a porosity of 0.9 consisting of fibers with average equivalent diameters of 8 μm (approximate diameter of GFD3 fiber; see Figure A.10). It should be noted that only the arrangement of the fibers is random, the porosity is maintained at a constant value. The boundaries for the electrode element are shown in Figure 8.4. The Sobol sequence mentioned previously was used to generate the inlet flow rates (which were converted to velocities) and inlet electrolyte compositions.

First, we inspect the behavior of the model as we increase the overpotential ($\bar{\eta}$). Figure 8.5 shows three porous media samples with the same flow rate and inlet

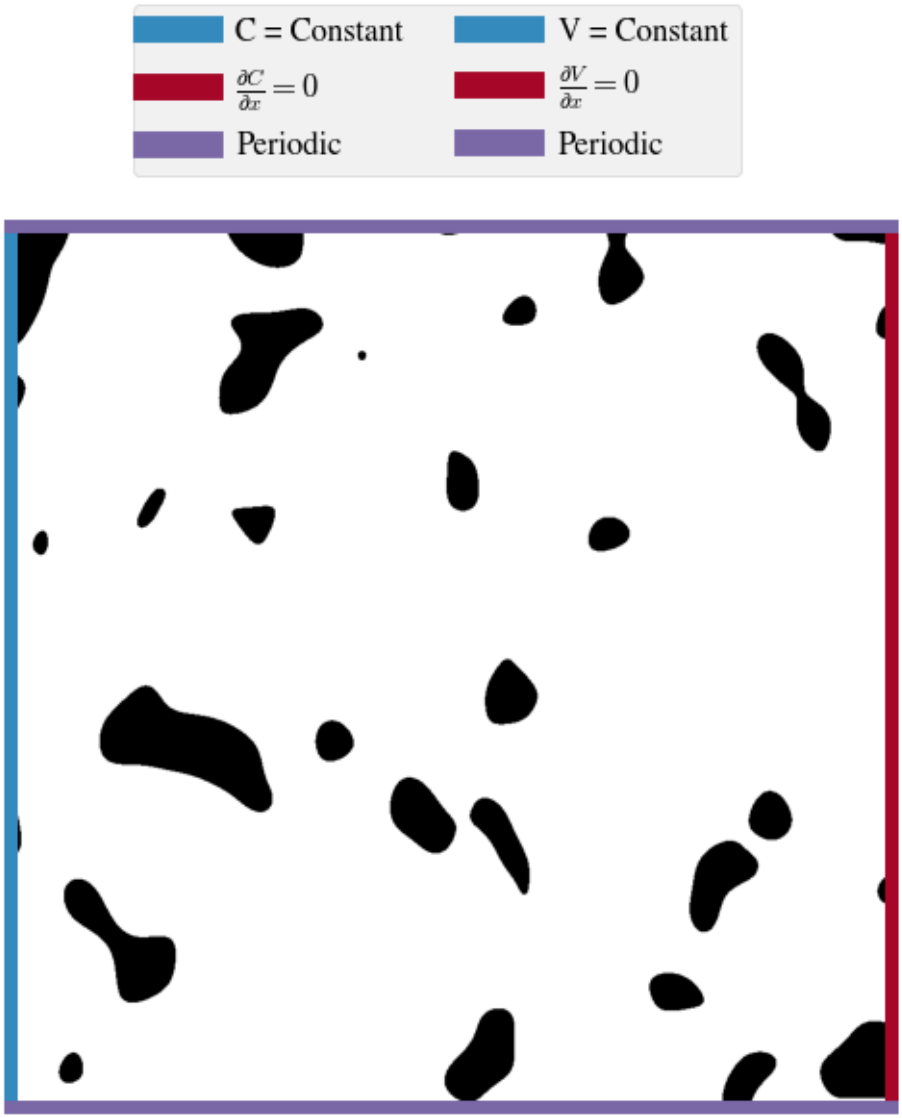

Figure 8.4: Boundaries for lattice Boltzmann simulations. The solid internal obstacles were bounce-back boundaries for solving Navier Stokes, and Kang boundary (Equations 8.17 and A.51) for species transport.

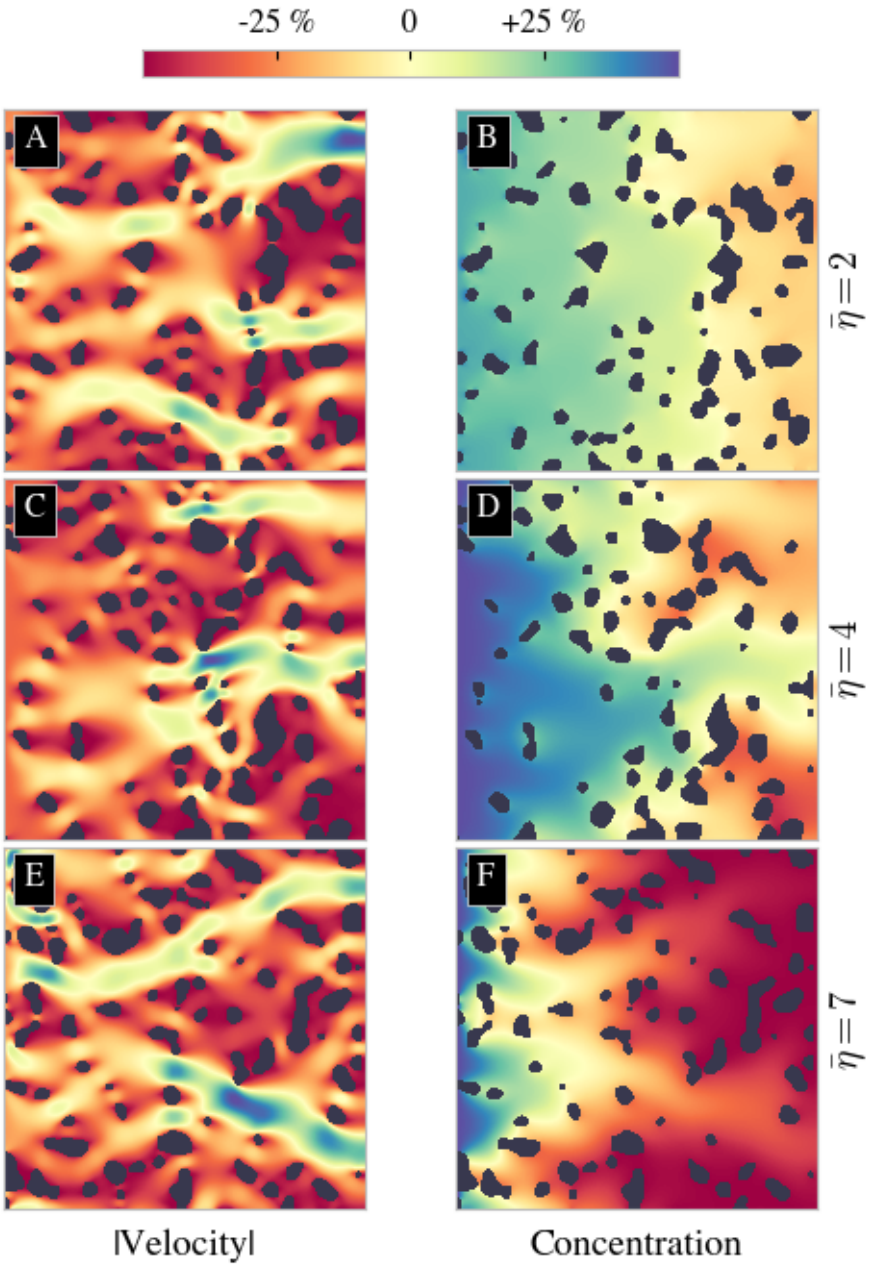

Figure 8.5: Impact of $\bar{\eta}$ on concentration distribution. The three plots were scaled to a single normal distribution with a mean centered at zero and a standard deviation of 1. [Re = 0.211. Da = 0.141, inlet SoC = 50%].

SoC at different overpotentials.

The lattice velocity and dimensionless concentration are shown in the left and right columns respectively. The values are scaled to a single normal distribution centered with a mean at 0 and a standard deviation of 1 (this will be the data format on which the neural network will be trained). We can see that, qualitatively, the behavior we have observed is that as the cell becomes more polarized the cell moves from a state of minimal mass transfer polarization, to one where this behavior dominates the polarization (bottom row). In the middle row of Figure 8.5 (subplots C and D), we observe most clearly the impact of the velocity on the local concentration distribution. There is a region in the center of the height of the electrode where the velocity is maximized (see 8.5:C). This velocity stream corresponds with the increased concentration observed in 8.5:D. Likewise, the local concentration polarization in 8.5:D corresponds with both being further from the inlet and being in the low velocity regions. While the lower overpotential case ($\bar{\eta}$ = 2; A and B) has some concentration depletion along the x-axis, it has, the lowest variation between the inlet and outlet. The highest overpotential case (F) shows the local concentration polarization becoming dominant. The high velocity region in the upper quadrant (of Figure 8.5:E) can be seen to correlate with the lower concentration depletion in this vicinity (of F). While this analysis is mostly qualitative, we have observed that the expected physical behavior is recovered and invariant to the specific porous domain. The averaged concentration depletion as a function of SoC and dimensionless overpotential is shown in Figure 8.6.

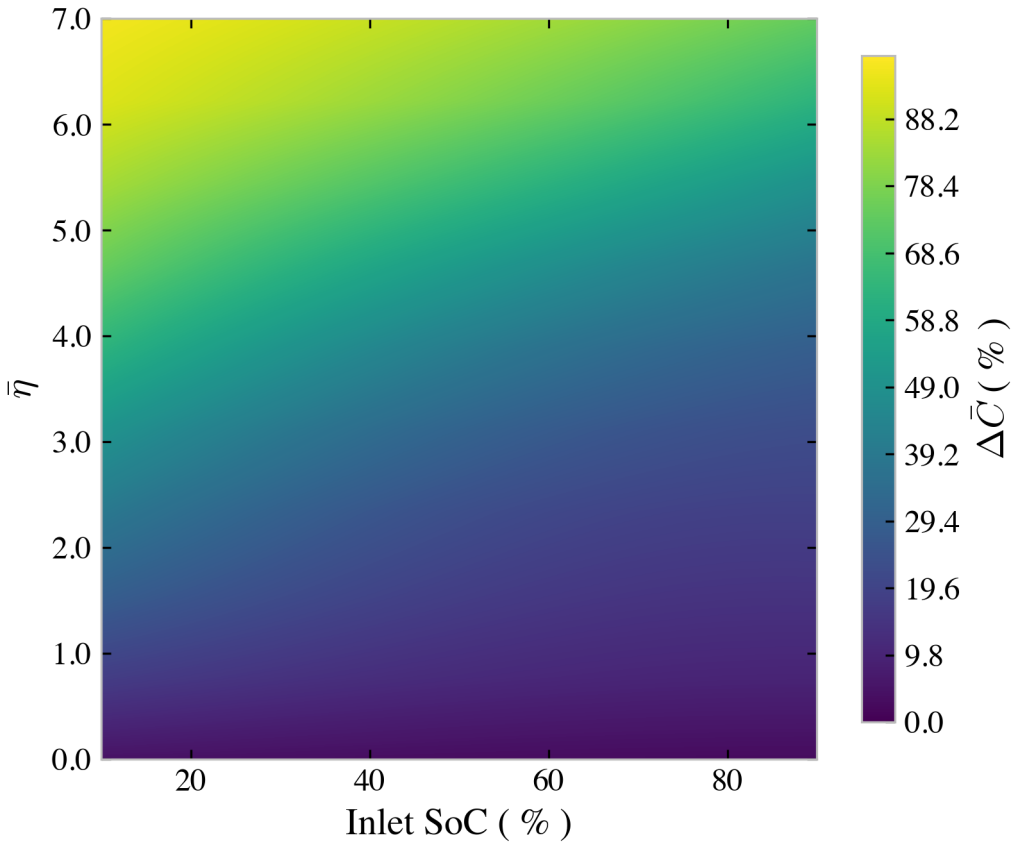

Figure 8.6: Percentage change in inlet concentration as a function of inlet SoC and dimensionless overpotential $\bar{\eta}$

The impact of the overpotential as seen in Figure 8.6 is, as expected, that the increasing dimensionless overpotential results in higher levels of concentration depletion. We also observe that the gradient is not purely in the direction of the dimensionless overpotential, but also has a component that is a function of the SoC. This behavior shows sensitivity of the model to not just the dimensionless overpotential, but also to the electrolyte SoC. The ability to recover this behavior (sensitivity to SoC and $\bar{\eta}$) indicates that the model responds with sufficient dynamic to the input parameters to be utilized in the context of a machine learning based model.

8.4 Conclusions

In this work we have demonstrated the use of the lattice Boltzmann method for modeling a two-dimensional micron scale electrode element. The electrochemical boundary was validated in both a pure diffusion field and a field with advection and diffusion (RMSE of .029 and .414 respectively). The model was used to simulate a sweep over the inlet state of charge (10-90%), the flow rate (10-50 mL min^{-1}) and with pseudorandom porous media generated for each simulation. We have also observed sensitivity of the model to the inlet composition at different dimensionless overpotentials. This work is the first part of an exploration of the utilization of the lattice Boltzmann method as a generator for a broader data set for training a neural network, which will be the focus of part II.

Chapter 9

Power flexibility analysis for strip cell vanadium redox flow battery

Abstract

This chapter will not be published as a stand-alone article prior to submission of my ETD, therefore a publication statement was not included. The content of this chapter will be submitted for a short communication authored by Michael. C. Daugherty, Tugrul Y. Ertugrul, Douglas S. Aaron and Matthew M. Mench.

My contributions to this work were data reduction, analysis and composition of the manuscript. Ertugrul collected data and assisted with data reduction and manuscript preparation. Aaron and Mench assisted in manuscript preparation.

9.1 Introduction

The strip cell architecture [229] represents a geometrically simplified redox flow cell where uncertainty over second-order mass transport effects can be minimized. These transport effects manifest as interactions between porous media and a flow field such as electrolyte jumping over lands in a serpentine flow field [200], forcing electrolyte into the electrode via interdigitated architecture, or introducing obstructions to induce higher electrode velocities [230]. Electrolyte flow in the electrode is a desirable effect in RFB systems (increasing mass transfer coefficient in the electrode), however these obstruction-based electrolyte distribution methods manifest in a highly distributed spatial domain that is non-ideal for understanding the fundamental relationship between the cell architecture and the mass transport in the electrode. The strip cell provides a generic 1-D architecture template that allows control of the flow directed into the electrode. This is achieved by varying the channel depth, which forces electrolyte to flow through the electrode [229, 231].

Understanding the nonlinear tradeoff between channel depth, mass transfer and pumping losses is critical for system optimization and is the goal of this work.

9.2 Methods

Efficiency in the context of laboratory scale redox flow battery systems is often quantified by coulombic, voltage and energy efficiency e.g. [31, 232]. These are assessed on a per-cycle basis where the coulombic efficiency represents the ratio of coulombs discharged to coulombs charged.

$$\text{Coulombic Efficiency} = \frac{\int_0^{t_d} i_d dt}{\int_0^{t_c} i_c dt} \tag{9.1}$$

The symbols used in this chapter are shown in Table A.11. The voltage efficiency, is the ratio of the average voltage during discharging to the average voltage during charging.

$$\text{Voltage Efficiency} = \frac{t_c \int_0^{t_d} V_d dt}{t_d \int_0^{t_c} V_c dt} \tag{9.2}$$

The energy efficiency is the product of these two efficiencies.

$$\text{Energy Efficiency} = \text{Coulombic Efficiency} \times \text{Voltage Efficiency} \tag{9.3}$$

These metrics, however, do not address the variations that can occur in power inputs to the system, which are required to achieve these conditions. While gravity driven flow batteries have been demonstrated at lab-scale [38], most flow batteries are driven with pumps which incur some degree of losses to the overall system

performance.

The maximum current that can be supplied with a given set of mass transfer conditions constitutes the *limiting current* [20]. This current is defined by the equation:

$$i_{lim} = \frac{nFADC}{\delta} \tag{9.4}$$

In the conditions where a limiting current flows, there is no additional current that can be gained from increasing the polarization, i.e. the current is completely dominated by mass transfer polarization. In the context of redox flow batteries, the ability to modify mass transfer is most directly controlled via pumps external to a cell; however, analysis of the equation for the limiting current (9.4) reveals that there is no term for flow rate or velocity. The ratio of the diffusion coefficient to the nernstian diffusion layer thickness is referred to as the mass transfer coefficient ($m_o = D\delta^{-1}$), which carries units of velocity, but this is only indirectly related to the volumetric flow rate at an electrochemical interface [54].

A more general relationship can be quantified between the mass transfer controlled current and the flow rate by comparing these values on a power-basis. Let the mass transfer controlled cell power be defined:

$$P_{cell} = i_{lim} \times V_{@\ i_{lim}} \times A \tag{9.5}$$

The pump power is then the product of the pressure drop and the volumetric flow rate.

$$P_{pump} = \Delta P \times V_f \tag{9.6}$$

The experimental configuration and data used for this analysis are described in reference [231]. Table A.10 shows the subset of data used for the present analysis.

9.3 Results and discussion

Convection in the electrode is the dominating mass transfer mechanism for controlling cell performance. The complex interactions between the electrode surface and the liquid phase electrolyte, however, make achieving this a problem of balancing the pressure drop across a cell. Figure 9.1 shows the relationships between P_{cell}, $\sqrt{P_{pump}}$ and the volumetric flow rate (note the y-scale is square root for P_{pump}).

In the simplified geometry of the strip cell, a linear relationship is observed between the volumetric flow rate and P_{cell}. As mentioned previously, the mass transfer coefficient is increased by decreasing the boundary layer thickness (δ) in the vicinity of the electrochemical surface. The Navier stokes equations indicate that the pressure drop will increase with the square of the velocity, and we observe in the bottom portion of Figure 9.1 that indeed the pressure drop increases with the square of volumetric flow rate (velocity $\propto \mathrm{V}_f$).

While increasing the mass transfer coefficient clearly increases P_{cell} (all channel depths have positive slopes with respect to flow rate), we see that P_{pump} will grow with the square of the increase in P_{cell}. Naturally we see that the use of P_{cell} as a proxy for velocity in the electrode lends itself to a direct comparison between

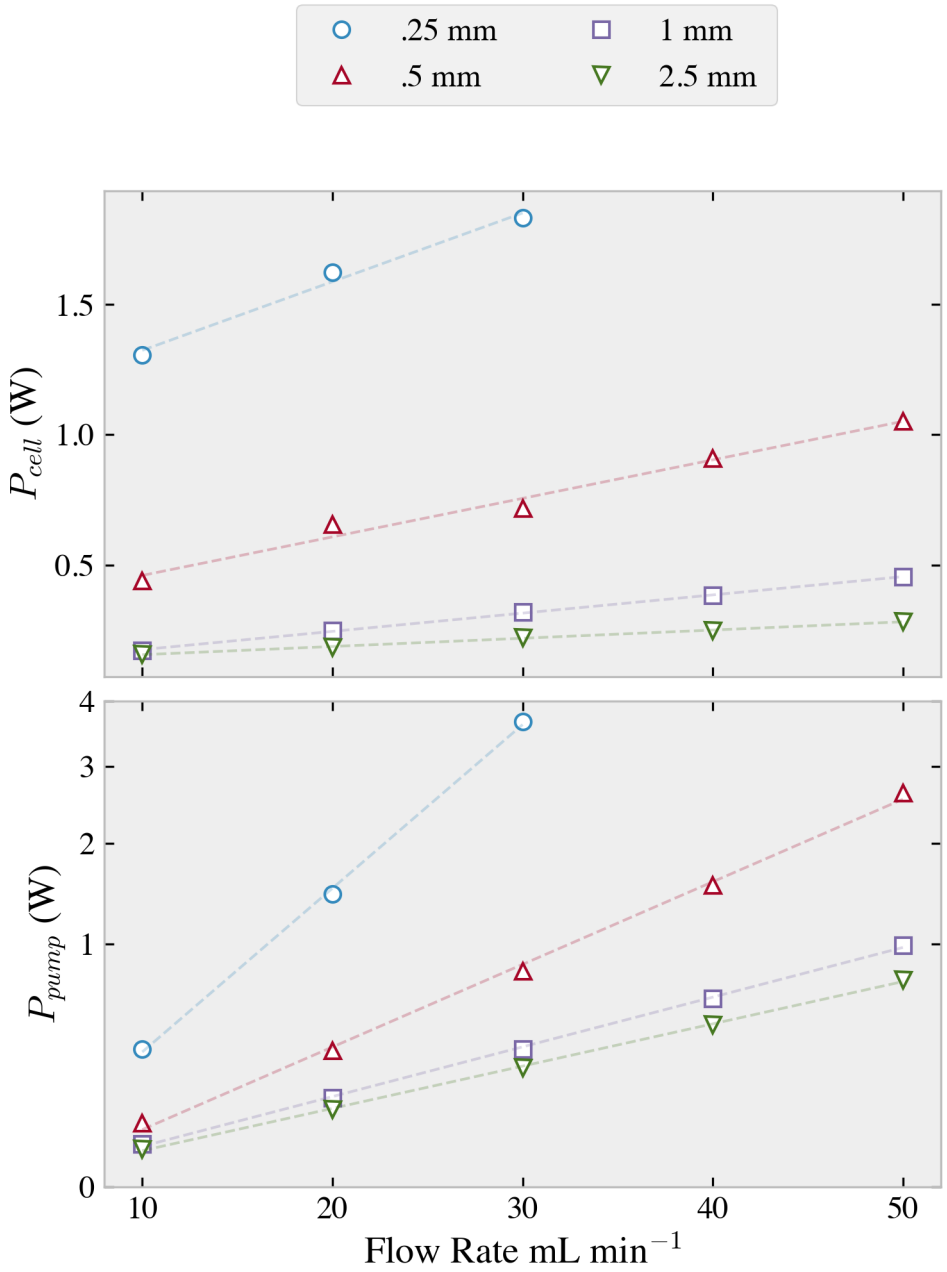

Figure 9.1: Cell power (P_{cell}) and pump power (P_{pump}) as functions of volumetric flow rate.

P_{cell} and $\sqrt{P_{pump}}$ to directly quantify the tradeoff of pumping power to cell power. Figure 9.2 shows P_{cell} plotted as a function of P_{pump} (note the nonlinear x-axis scale is square root).

The behavior observed in Figure 9.2 suggests that, for the deeper channels, the tradeoff between increasing the flow rate and mass-transfer controlled pump power is lower. For the strip-cell flow field geometry, there are no obstructions (switchbacks, dead ends, etc.) to force fluid into the electrode, which results in lower electrolyte velocity in the electrode. As the channel becomes shallower the flow becomes pressure drop increases, which forces higher velocities to occur in the porous medium (39AA, SGL Group; 280 μm nominal, uncompressed thickness). This increase results in higher mass transport controlled power. This initially results in higher mass transfer coefficients (m_o) on account of a smaller diffusion layer thickness (see Equation 9.4). The two solid markers on Figure 9.3 (solid red triangle and solid purple square) represent two operating conditions which produce the same mass transport controlled cell power. This compares the 1 mm channel depth at a volumetric flow rate of 50 mL min^{-1} (purple square) to the 0.5 mm channel depth at 10 mL min^{-1} (red triangle). Here, the tradeoff between halving the channel depth is a 14 $\times$ decrease in input power to operate the cell at the same condition. We can see that not only does the cell power increase with decreasing channel depth, we also observe that the sensitivity of the cell power to $\sqrt{P_{pump}}$ changes with channel depth. Figure 9.3 gives further insight into this balance of cell power and pump power by showing the sensitivities of the cell power (to $\sqrt{P_{pump}}$) for each channel depth.

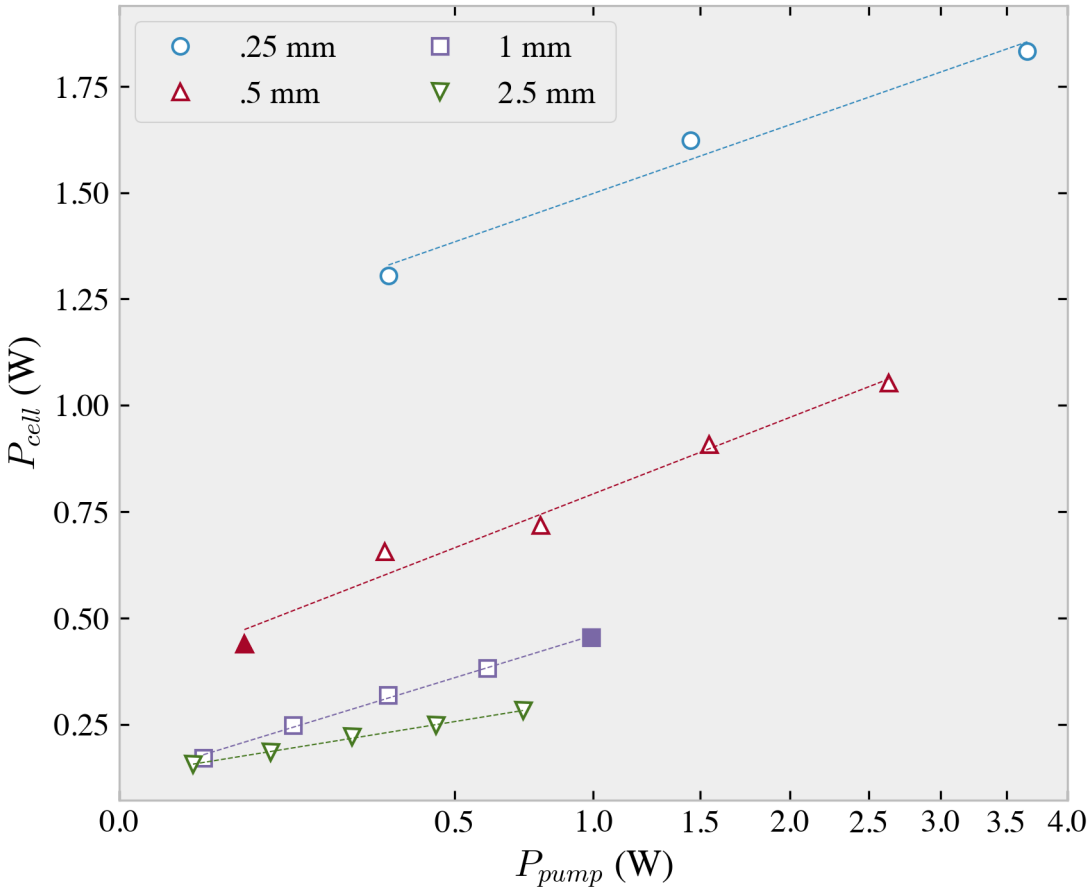

Figure 9.2: Ratio of cell power to pump power.

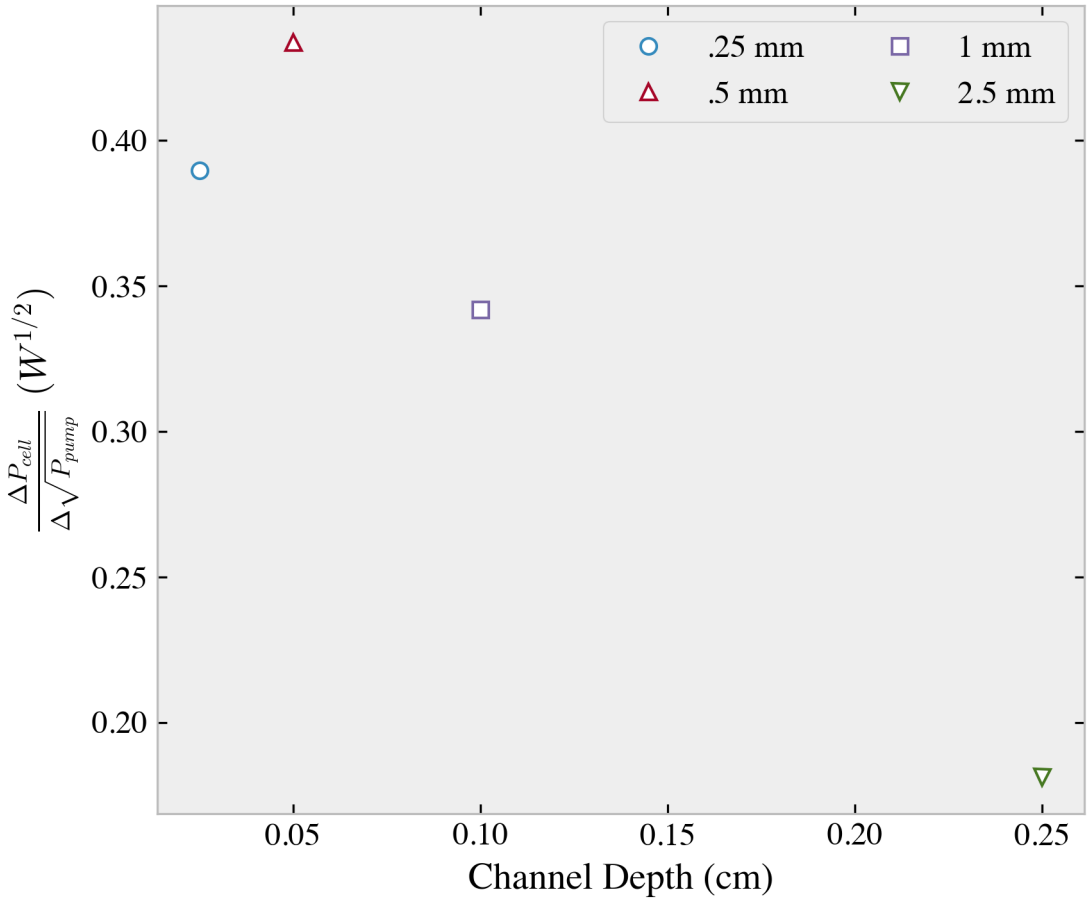

Figure 9.3: Sensitivities of P_{cell} to $\sqrt{P_{pump}}$ as a function of channel depth

We can see that, for the deepest channel, while the pumping losses are smallest, the low sensitivity indicates that the gain in cell power is minimal (low electrolyte velocity in the electrode). For the experimental conditions which were tested, the 0.5 mm depth channel showed the highest sensitivity to $\sqrt{P_{pump}}$. This does not explicitly indicate that this is the optimal channel depth (it would require ~15 $\times$ higher pump power to achieve the P_{cell} of 0.25 mm at 10 mL min^{-1}). It does, however mean that this channel depth incurs the lowest relative pumping loss (or conversely the highest relative cell power gain) per unit change in flow rate. The observation of a decrease in sensitivity going from 0.5 mm to 0.25 mm suggests that, while the cell power may still be increased by decreasing the channel further, the pumping requirements will overcome the gain in cell power. Grid-scale energy storage solutions necessitate not only high efficiency, but also operational flexibility. Having decoupled power and energy capacities is one of the primary benefits of flow batteries and the existence of a metric for this comparison has, to this author's knowledge, not been directly explored. This metric ($\Delta P_{cell} \Delta P_{pump}^{-1/2}$) together with the aforementioned efficiency metrics (Equations 9.1, 9.2, and 9.3) can be used to characterize a system's operational power flexibility.

9.4 Conclusions

The analysis of P_{cell} and P_{pump} shown in this work is a simple method to characterize and compare operating conditions for dissimilar flow fields. We have shown that the interaction between channel depth, cell output power and pump input power are nonlinear where we observed a ~14 times decrease in pump power for

halving the channel depth at equivalent cell power. It was also observed that the sensitivity of the cell power to $\sqrt{P_{pump}}$ was maximized for the 0.5 mm depth channel, indicating the maximized operational power flexibility.

Chapter 10
Conclusions and Recommendations

10.1 Conclusions

10.1.1 Electrode modifications

Several electrode treatments and modifications were performed in this work. First, Nitrogen-doped GQDs were used to improve the performance of GF electrodes The as-prepared GQDs contained ultra-high O/C (56-61%) and N/C (34-66%) atomic ratio, exhibiting a synergistic effect toward increasing the surface area thereby decreasing the faradaic impedance for the redox reactions of the V^{2+}/V^{3+} couple. The durability and voltage efficiency of GF electrodes were improved during extended cycling by 3% and 11% respectively with the GQD modification. S/N co-doped GQDs were also utilized to catalyze the surface of GF electrodes. These GQDs, having an average diameter of 6.2 nm, possessed high oxidation, amidation, and sulfonation levels (45.8 (O/C), 22.7 (N/C), and 7.8 at.% (S/C), respectively). Uniformly dispersed S/N co-doped GQDs onto the GF enabled the formation of 3D nano-structures as the high-performance electrode for VRFBs. Through the deposition of S/N co-doped GQDs, the catalytic activity, equivalent series resistance, durability, and voltage efficiency of the treated GF electrode were enhanced. The synergistic effect induced by the oxygen functionalities, lattice N atoms, and S dopants, effectively improves the surface catalytic activity and reduces charge transfer resistance for the redox reactions (V(IV)/V(V) and V(II)/V(III) couples).

Micro-channels generated by ultrafast laser ablation were utilized to enhance the porosity of GF electrodes. Laser-patterned macroscopic channels exhibited an

average width of 200 μm and a height of 1.5 mm, creating a three-dimensional carbon framework. The overpotential distribution analyzed by the EIS technique revealed that the electrode polarization involving charge transfer and ionic diffusion resistance was strongly alleviated in the presence of carbon perforation. The enhancement could be attributed to the design of L electrode that contains vast porous/ geometrical structures to render (i) high electrochemically active surface area for rapid electrochemical reactions (i.e., V(II)/V(III) at the anode) and (ii) improved transport properties for fast electron/ion/species transport. A synergistic effect between the L electrodes and the flow fields boosts the rate capability and cyclability. The channels created by ultrafast laser ablation technique enabled complete and rapid wetting of GF materials with liquid electrolyte, as formulated by the classical Washburn equation. All vanadium redox flow batteries assembled with the L electrodes demonstrated improved capacity retention upon extended cycling (84.9%). Accordingly, the design of L electrodes paves the way for micro engineering the electrode internal morphology for improved durability and cyclability in various energy storage devices (e.g. redox flow batteries)

10.1.2 Modeling

Comparison of utilizing a Randles circuit (with [RTS] and without [RFS] a low pass filter) to the macrohomogeneous porous electrode model for parameter estimation was demonstrated in this work. The ratio of the complex decay length (λ) to the characteristic length has a very strong impact on the ability for RTS to approximate the parameter values that MHPE resolves. The use of different models is most accentuated by the ability (or inability) to resolve the inductance, which the

models are most sensitive to at the maximum frequency. Because these frequencies are removed from RTS it has an enormous variance for the inductance when it is perturbed. The MHPE model is the only studied model, which can resolve high frequency content because its formulation accounts for the distributed resistance at high frequency, which also gives it the ability to resolve the inductance consistently.

Contributions from graphitic plates were quantified in the context of open circuit impedance spectra. The cathode channel electrode was shown to be dominated by mass transport at open circuit, resulting in the inability to separate any kinetics contributions from the plates. The anode, however, was shown to have a high level of interaction with the graphitic plates. It was found that using an unmodified Randles circuit yields a geometric exchange current density that differs by $\approx 36\%$ from the Tafel-estimated value. The nonlinear relationship between the addition of electrode material at open circuit was proposed to be an effect of the coupling between the double layer capacitance and rate constant of the channel with the electrode. These results indicate that when a reaction has sluggish kinetics, the decoupling of the effects from bipolar plates can be helpful in estimating kinetics parameters accurately.

A novel experimental configuration was utilized to probe the VRFB anode and cathode over a range of electrolyte compositions. The anode was investigated in greater depth than the cathode on account of constituting a much larger portion of the total cell $|\mathrm{ASR}|$. The effective surface area for all experiments was found to be higher in the high SoC range (SoC > 75%) trending downward from this point.

A (limited) novel representation of energy efficiency was derived and utilized to generalize an operating conditions over a range of SoCs and depths of discharge. It was found that the depth of discharge can be optimized for conditions with an initial SoC above 67%. While, we do not expect this behavior to be generally true of all operating conditions (charge/discharge currents), equation 6.12 can be used to profile a system when crossover is minimal, and importantly, can be determined with a single lab-scale battery (i.e not using the setup if Figure 6.1).

The analysis of the cell power and pump power shown in this work is a simple method to characterize and compare operating conditions for dissimilar flow fields. We have shown that the interaction between channel depth, cell output power and pump input power are nonlinear where we observed a ~14 times decrease in pump power for halving the channel depth at equivalent cell power. It was also observed that the sensitivity of the cell power to $\sqrt{P_{pump}}$ was maximized for the 0.5 mm depth channel, indicating the maximized operational power flexibility.

10.2 Recommendations

The scope of this work has shown the value of understanding both approaches to modifying electrode surfaces and characterizing these modifications. Balancing a rigorous approach to understanding complications that can arise when estimating parameters with practical electrode modifications, this work has pushed the state of the art in both experimental electrochemistry and modeling of electrochemical systems. However, there are still many avenues that warrant further investigation

in the space of vanadium redox flow batteries.

Understanding electrode surface properties is of interest not just to the VRFB community, but to the broader fields of electrochemistry and materials science. From this work, the ammonia heat treatment which is discussed in Chapter 2 stands apart from all other electrode modifications studied warranting further investigation. This treatment both reduces the impedance to a greater degree than all other investigated treatments, but also has been shown to have superior durability over the course of cycling experiments. Understanding the nature of these improvements can elucidate aspects of these systems from both highly applied (academic) and practical (commercial) perspectives. While the novelty of utilizing graphene quantum dots and using ultra-fast laser ablation provided interesting results, these avenues ultimately proved more academic than practical.

While trends in computing seem to point in the direction of machine learning, the physics-agnostic nature of these models presents researchers with both an extremely powerful new tool and the challenge of channeling it towards specifically academic ends. One challenge for implementation of machine learning techniques is having structured data sets as inputs/outputs (I/O) for training (e.g. neural nets). As this work has focused on understanding uncertainty and sensitivity of model parameters, it seems a daunting task to generate experimental data sets that would be well suited for training any type of machine learning network. However, the use of high fidelity models as I/O for machine learning networks has been demonstrated [22], but hardly exhausted. Indeed, there is great potential for this approach, which can render drastic computational savings making models that re-

quire the order of days to run on multiple cores a matter of matrix operations that can be solved almost instantaneously. Many system level electrochemical models are demonstrated on a narrow geometric scope [79, 203], which often proves more academic than practical. Utilizing machine learning can bring these high fidelity models into a space where they can be generalized more broadly.

Vanadium electrolyte has properties that are both highly advantageous and limiting. As discussed throughout, the use of a single electroactive species is convenient in that crossover based capacity fade is reversible. However, the cost of vanadium still proves to be a non-trivial barrier to wide-spread adoption of this technology. The pursuit of less studied chemistries is an avenue that is properly suited for a high-risk high-reward research. This includes both aqueous and non-aqueous electrolytes.

Both the novel in-situ SoC dependent configuration as well as the strip-cell power analysis can be further analyzed and extrapolated upon. Analyzing the impact of charging and discharging at different currents and using the symmetric cells to gather data over a range of operating conditions is a straightforward way to understand the impacts of depth of discharge as well as the electrolyte composition impact on the operation of a cell. Likewise, the strip cell analysis could be tested on flow fields of more complex geometries to asses the generality of the conclusions.

The aspect in the literature that is most lacking for the VRFB community in terms of durability and degradation is a standardized protocol for a 'break-in.' The transient behavior at the beginning-of-life for VRFB electrodes can lead to a great deal of uncertainty as both electroless and electrochemical processes are degrading the

electrodes and are both dependent on the composition of the electrolyte and electrochemical conditions. The standardizing of a process to stabilize the electrodes or to accelerate the process of degradation to bring the electrodes to their middle-of-life state more rapidly would be of great use to the VRFB community. This is especially of interest to lab-scale research where experimental resources that are dedicated to understanding transient processes can be freed for other uses at a higher rate. Pezeshki and co-workers developed the cell-in-series method to accelerate degradation [41], however, this method requires extra hardware and emphasizes the impact of high SoC electrolyte as opposed to an electrochemical protocol for rapidly stressing electrodes.

Bibliography

[1] S. Cai, S. Yuan, and S. Wang. Comparative study of policies on grid scale energy storage among China and other countries. In *2016 IEEE 8th International Power Electronics and Motion Control Conference, IPEMC-ECCE Asia 2016*, number Nsfc 51361135704, pages 530–535, 2016.

[2] DOE Announces $40 Million for Grid Modernization Initiative. *https://www.energy.gov/articles/doe-announces-40-million-grid-modernization-initiative*, 2019.

[3] U.S. Department of Energy. Grid Modernizaiton Multi-Year Program Plan, 2015.

[4] D. Conover, A. Crawford, V. Viswanathan, S. Ferreira, D. Rose, and D. Schoenwald. Protocol for Uniformly Measuring and Expressing the Performance of Energy Storage Systems. Technical report, 2014.

[5] U.S. Department of Energy. DOE Global Energy Storage Database, 2019.

[6] Center for Sustainable Systems. U.S. Grid Energy Storage Factsheet. *University of Michigan*, 2019.

[7] R. Kempener and d. V. Gustavo. *Renewables and Electricity Storage: A technology roadmap for REmap 2030*. 2015.

[8] D. Hart, W. Bonvillian, and N. Austin. Energy Storage for the Grid: Policy Options for Sustaining Innovation. 2018.

[9] A. A. Akhil, G. Huff, A. B. Currier, B. C. Kaun, D. M. Rastler, S. B. Chen, A. L. Cotter, D. T. Bradshaw, and W. D. Gauntlett. DOE/EPRI 2013 Electricity Storage Handbook in Collaboration with NRECA Abbas. Technical Report July, 2013.

[10] Electricity Storage Valuation Framework: Assessing system value and ensuring project viability. Technical report, 2020.

[11] S. Sabihuddin, A. E. Kiprakis, and M. Mueller. A numerical and graphical review of energy storage technologies. *Energies*, 8(1):172–216, 2015.

[12] C. Ponce de Leon, A. Frias-Ferrer, J. Gonzalez-Garcia, D. A. Szanto, and F. C. Walsh. Redox flow cells for energy conversion. *Journal of Power Sources*, 160(1):716–732, 2006.

[13] B. Chalamala, T. Soundappan, G. Fisher, M. Anstey, V. Viswanathan, and M. Perry. Redox flow batteries: An engineering perspective. *Proceedings of the IEEE*, 102(6):976–999, 2014.

[14] J. Noack, N. Roznyatovskaya, T. Herr, and P. Fischer. The Chemistry of Redox-Flow Batteries. *Angewandte Chemie - International Edition*, 54(34):9776–9809, 2015.

[15] A. Weber, M. M. Mench, J. Meyers, P. Ross, J. Gostick, and Q. Liu. Redox flow batteries: A review. *Journal of Applied Electrochemistry*, 41(10):1137–1164, 2011.

[16] M. Holland-Cunz, F. Cording, J. Friedl, and U. Stimming. Redox flow batteries — Concepts and chemistries for cost- effective energy storage. *Frontiers in Energy*, 12(1):1–27, 2018.

[17] L. F. Arenas, C. Ponce de León, and F. C. Walsh. Engineering aspects of the design, construction and performance of modular redox flow batteries for energy storage. *Journal of Energy Storage*, 11:119–153, 2017.

[18] V. Viswanathan, A. Crawford, D. Stephenson, S. Kim, W. Wang, B. Li, G. Coffey, E. Thomsen, G. Graff, P. Balducci, M. Kintner-Meyer, and V. Sprenkle. Cost and performance model for redox flow batteries. *Journal of Power Sources*, 247:1040–1051, 2012.

[19] K. Gong, X. Ma, K. Conforti, K. Kuttler, J. Grunewald, K. Yeager, M. Bazant, S. Gu, and Y. Yan. A zinc-iron redox-flow battery under $100 per kW h of system capital cost. *Energy and Environmental Science*, 8(10):2941–2945, 2015.

[20] A. Bard and L. Faulkner. *Electrochemical Methods: fundamentals and applications*. John Wiley & Sons, Inc., Hoboken, 2nd edition, 2001.

[21] D. E. Eapen, S. R. Choudhury, and R. Rengaswamy. Low grade heat recovery for power generation through electrochemical route: Vanadium Redox Flow Battery, a case study. *Applied Surface Science*, 474:262–268, 2019.

[22] J. Bao, V. Murugesan, C. J. Kamp, Y. Shao, L. Yan, and W. Wang. Machine Learning Coupled Multi-Scale Modeling for Redox Flow Batteries. *Advanced Theory and Simulations*, pages 1–13, 2019.

[23] J. Newman and K. E. Thomas-Alyea. *Electrochemical Systems*. John Wiley & Sons, third edition, 2004.

[24] Y. Gandomi, D. Aaron, J. Houser, M. Daugherty, J. Clement, A. Pezeshki, T. Ertugrul, D. Moseley, and M. Mench. Critical Review — Experimental Diagnostics and Material Characterization Techniques Used on Redox Flow Batteries. *Journal of The Electrochemical Society*, 165(5):970–1010, 2018.

[25] K. Kim, M. Park, Y. Kim, J. Kim, S. Dou, and M. Skyllas-Kazacos. A technology review of electrodes and reaction mechanisms in vanadium redox flow batteries. *Journal of Materials Chemistry A*, 3(33):16913–16933, 2015.

[26] C. Flox, J. Rubio-Garcia, R. Nafria, R. Zamani, M. Skoumal, T. Andreu, J. Arbiol, A. Cabot, and J. Morante. Active nano-CuPt3 electrocatalyst supported on graphene for enhancing reactions at the cathode in all-vanadium redox flow batteries, 2012.

[27] A. Ejigu, M. Edwards, and D. A. Walsh. Synergistic Catalyst-Support Interactions in a Graphene-Mn3O4 Electrocatalyst for Vanadium Redox Flow Batteries. *ACS Catalysis*, 5(12):7122–7130, 2015.

[28] B. Li, M. Gu, Z. Nie, X. Wei, C. Wang, V. Sprenkle, and W. Wang. Nanorod Niobium Oxide as Powerful Catalysts for an All Vanadium Redox Flow Battery. *Nano Letters*, 14(1):158–165, 2014.

[29] C. Flox, M. Skoumal, J. Rubio-Garcia, T. Andreu, and J. Morante. Strategies for enhancing electrochemical activity of carbon-based electrodes for all-vanadium redox flow batteries. *Applied Energy*, 109:344–351, 2013.

[30] M. Goulet, M. Skyllas-Kazacos, and E. Kjeang. The importance of wetting in carbon paper electrodes for vanadium redox reactions. *Carbon*, 101:390–398, 2016.

[31] X. Zhou, Y. Zeng, X. Zhu, L. Wei, and T. Zhao. A high-performance dual-scale porous electrode for vanadium redox flow batteries. *Journal of Power Sources*, 325(2016):329–336, 2016.

[32] B. Sun and M. Skyllas-Kazacos. Chemical modification of graphite electrode materials for vanadium redox flow battery application-part II. Acid treatments. *Electrochimica Acta*, 37(13):2459–2465, 1992.

[33] Z. He, L. Dai, S. Liu, L. Wang, and C. Li. Mn3 O4 anchored on carbon nanotubes as an electrode reaction catalyst of V(IV)/V(V) couple for vanadium redox flow batteries. *Electrochimica Acta*, 176:1434–1440, 2015.

[34] F. Rahman and M. Skyllas-Kazacos. Vanadium redox battery: Positive half-cell electrolyte studies. *Journal of Power Sources*, 189(2):1212–1219, 2009.

[35] J. Friedl, C. Bauer, A. Rinaldi, and U. Stimming. Electron transfer kinetics of the VO 2 + / VO 2 + - Reaction on multi-walled carbon nanotubes. *Carbon*, 63:228–239, 2013.

[36] B. Sun and M. Skyllas-Kazacos. Modification of graphite electrode materials for vanadium redox flow battery application—I. Thermal treatment. *Electrochimica Acta*, 37(7):1253–1260, 1992.

[37] H. Fink, J. Friedl, and U. Stimming. Composition of the Electrode Determines Which Half-Cell' s Rate Constant is Higher in a Vanadium Flow Battery. *The Journal of Physical Chemistry C*, 120(29):15893–15901, 2016.

[38] C. N. Sun, F. M. Delnick, D. S. Aaron, A. B. Papandrew, M. M. Mench, and T. A. Zawodzinski. Resolving Losses at the Negative Electrode in All-Vanadium Redox Flow Batteries Using Electrochemical Impedance Spectroscopy. *Journal of the Electrochemical Society*, 161(6):A981–A988, 2014.

[39] A. M. Pezeshki, R. L. Sacci, F. M. Delnick, D. S. Aaron, and M. M. Mench. Elucidating effects of cell architecture, electrode material, and solution composition on overpotentials in redox flow batteries. *Electrochimica Acta*, 229:261–270, 2017.

[40] D. Aaron, Z. Tang, J. Lawton, A. Papandrew, and T. Zawodzinski. In-situ single electrode studies of an all-vanadium redox flow battery. *ECS Transactions*, 41(23):43–51, 2012.

[41] A. M. Pezeshki, R. L. Sacci, G. M. Veith, T. A. Zawodzinski, and M. M. Mench. The Cell-in-Series Method: A Technique for Accelerated Electrode Degradation in Redox Flow Batteries. *Journal of The Electrochemical Society*, 163(1):A5202–A5210, 2016.

[42] C. Pevida, M. G. Plaza, B. Arias, J. Fermoso, F. Rubiera, and J. J. Pis. Surface modification of activated carbons for CO 2 capture. *Applied Surface Science*, 254(22):7165–7172, 2008.

[43] U. Świetlik, B. Grzyb, K. Torchała, G. Gryglewicz, and J. Machnikowski. High temperature ammonia treatment of pitch particulates and fibers for nitrogen enriched microporous carbons. *Fuel Processing Technology*, 119:211–217, 2014.

[44] H. Sun, L. Wu, W. Wei, and X. Qu. Recent advances in graphene quantum dots for sensing. *Materials Today*, 16(11):433–442, 2013.

[45] S. Gu, C. T. Hsieh, Y. Ashraf Gandomi, J. K. Chang, J. Li, J. Li, H. Zhang, Q. Guo, K. C. Lau, and R. Pandey. Microwave growth and tunable photoluminescence of nitrogen-doped graphene and carbon nitride quantum dots. *Journal of Materials Chemistry C*, 7(18):5468–5476, 2019.

[46] Z. Yang, J. Zhang, M. C. Kintner-Meyer, X. Lu, D. Choi, J. P. Lemmon, and J. Liu. Electrochemical energy storage for green grid. *Chemical Reviews*, 111(5):3577–3613, 2011.

[47] M. H. Chakrabarti, N. P. Brandon, S. A. Hajimolana, F. Tariq, V. Yufit, M. A. Hashim, M. A. Hussain, C. T. Low, and P. V. Aravind. Application of carbon materials in redox flow batteries. *Journal of Power Sources*, 253:150–166, 2014.

[48] M. Ulaganathan, V. Aravindan, Q. Yan, S. Madhavi, M. Skyllas-Kazacos, and T. Lim. Recent Advancements in All-Vanadium Redox Flow Batteries. *Advanced Materials Interfaces*, 3(1):1–22, 2016.

[49] F. Rahman and M. Skyllas-Kazacos. Solubility of vanadyl sulfate in concentrated sulfuric acid solutions. *Journal of Power Sources*, 72(2):105–110, 1998.

[50] M. Vijayakumar, W. Wang, Z. Nie, V. Sprenkle, and J. Hu. Elucidating the higher stability of vanadium(V) cations in mixed acid based redox flow battery electrolytes. *Journal of Power Sources*, 241:173–177, 2013.

[51] J. Zhang, L. Li, Z. Nie, B. Chen, M. Vijayakumar, S. Kim, W. Wang, B. Schwenzer, J. Liu, and Z. Yang. Effects of additives on the stability of electrolytes for all-vanadium redox flow batteries. *Journal of Applied Electrochemistry*, 41(10):1215–1221, 2011.

[52] S. Roe, C. Menictas, and M. Skyllas-Kazacos. A High Energy Density Vanadium Redox Flow Battery with 3 M Vanadium Electrolyte. *Journal of The Electrochemical Society*, 163(1):A5023–A5028, 2015.

[53] A. Mousa and M. Skyllas-Kazacos. Kinetics of VIII and VII Sulfate Precipitation Processes in Negative Half-Cell Electrolyte of the Vanadium Redox Flow Battery. *ChemElectroChem*, 4(1):130–142, 2017.

[54] R. G. Compton and C. E. Banks. *Understanding Voltammetry*. World Scientific (Europe), 2007.

[55] Z. Tang, R. Svoboda, J. Lawton, D. Aaron, A. Papandrew, and T. Zawodzinski. Composition and Conductivity of Membranes Equilibrated with Solutions of Sulfuric Acid and Vanadyl Sulfate. *Journal of The Electrochemical Society*, 160(9):F1040–F1047, 2013.

[56] Q. Liu, A. Shinkle, Y. Li, C. Monroe, L. Thompson, and A. Sleightholme. Non-aqueous chromium acetylacetonate electrolyte for redox flow batteries. *Electrochemistry Communications*, 12(11):1634–1637, 2010.

[57] R. Darling, K. Gallagher, J. Kowalski, S. Ha, and F. Brushett. Pathways to low-cost electrochemical energy storage: A comparison of aqueous and non-aqueous flow batteries. *Energy and Environmental Science*, 7(11):3459–3477, 2014.

[58] B. Satola, C. Kirchner, L. Komsiyska, and G. Wittstock. Chemical Stability of Graphite-Polypropylene Bipolar Plates for the Vanadium Redox Flow Battery at Resting State. *Journal of The Electrochemical Society*, 163(10):A2318–A2325, 2016.

[59] M. Park, Y. Jung, J. Ryu, and J. Cho. Material selection and optimization for highly stable composite bipolar plates in vanadium redox flow batteries. *J. Mater. Chem. A*, 2(38):15808–15815, 2014.

[60] W. Liao, Y. Zhang, X. Zhou, M. Zhuang, D. Guo, F. Jiang, and Q. Yu. Low-Carbon-Content Composite Bipolar Plates: A Novel Design and Its Performance in Vanadium Redox Flow Batteries. *ChemistrySelect*, 4(8):2421–2427, 2019.

[61] K. Kim, B. Kim, and D. Lee. Development of carbon composite bipolar plate (BP) for vanadium redox flow battery (VRFB). *Composite Structures*, 109(1):253–259, 2014.

[62] P. Qian, H. Zhang, J. Chen, Y. Wen, Q. Luo, Z. Liu, D. You, and B. Yi. A novel electrode-bipolar plate assembly for vanadium redox flow battery applications. *Journal of Power Sources*, 175(1):613–620, 2008.

[63] D. Zhang, Z. Wang, and K. Huang. Composite coatings with in situ formation for Fe-Ni-Cr alloy as bipolar plate of PEMFC. *International Journal of Hydrogen Energy*, 38(26):11379–11391, 2013.

[64] B. Satola, L. Komsiyska, and G. Wittstock. Corrosion of Graphite-Polypropylene Current Collectors during Overcharging in Negative and Positive Vanadium Redox Flow Battery Half-Cell Electrolytes. *Journal of The Electrochemical Society*, 165(5):A963–A969, 2018.

[65] Z. Liu, B. Wang, and L. Yu. Preparation and surface modification of PVDF-carbon felt composite bipolar plates for vanadium flow battery. *Journal of Energy Chemistry*, 27(5):1369–1375, 2018.

[66] A. V. Nikiforov, I. M. Petrushina, E. Christensen, A. L. Tomás-García, and N. J. Bjerrum. Corrosion behaviour of construction materials for high temperature steam electrolysers. *International Journal of Hydrogen Energy*, 36(1):111–119, 2011.

[67] A. Fattah-Alhosseini, F. R. Attarzadeh, S. Vafaeian, M. Haghshenas, and M. K. Keshavarz. Electrochemical behavior assessment of tantalum in aqueous KOH solutions. *International Journal of Refractory Metals and Hard Materials*, 64:168–175, 2017.

[68] D. Gambale. Tantalum Surface Alloys Offer New Possibilities in Energy Production. *Advanced Materials & Processes*, 171(1):26–28, 2013.

[69] A. Bhattarai, P. Ghimire, A. Whitehead, R. Schweiss, G. Scherer, N. Wai, and H. Hng. Novel Approaches for Solving the Capacity Fade Problem during Operation of a Vanadium Redox Flow Battery. *Batteries*, 4(4):48, 2018.

[70] T. Doan, T. Hoang, and P. Chen. Recent development of polymer membranes as separators for all-vanadium redox fl ow batteries. pages 72805–72815, 2015.

[71] Y. Gandomi, D. Aaron, and M. Mench. Coupled Membrane Transport Parameters for Ionic Species in All-Vanadium Redox Flow Batteries. *Electrochimica Acta*, 218:174–190, 2016.

[72] K. Schafner, M. Becker, and T. Turek. Capacity balancing for vanadium redox flow batteries through electrolyte overflow. *Journal of Applied Electrochemistry*, 48(6):639–649, 2018.

[73] S. Rudolph, U. Schröder, I. M. Bayanov, and D. Hage. Measurement, simulation and in situ regeneration of energy efficiency in vanadium redox flow battery. *Journal of Electroanalytical Chemistry*, 728:72–80, 2014.

[74] I. Derr, D. Przyrembel, J. Schweer, A. Fetyan, J. Langner, J. Melke, M. Weinelt, and C. Roth. Electroless chemical aging of carbon felt electrodes for the all-vanadium redox flow battery (VRFB) investigated by Electrochemical Impedance and X-ray Photoelectron Spectroscopy. *Electrochimica Acta*, 246:783–793, 2017.

[75] T. Tichter, D. Andrae, J. Mayer, J. Schneider, M. Gebhard, and C. Roth. Theory of cyclic voltammetry in random arrays of cylindrical microelectrodes applied to carbon felt electrodes for vanadium redox flow batteries. *Physical Chemistry Chemical Physics*, 2019.

[76] D. Dixon, D. J. Babu, J. Langner, M. Bruns, L. Pfaffmann, A. Bhaskar, J. J. Schneider, F. Scheiba, and H. Ehrenberg. Effect of oxygen plasma treatment on the electrochemical performance of the rayon and polyacrylonitrile based carbon felt for the vanadium redox flow battery application. *Journal of Power Sources*, 332:240–248, 2016.

[77] D. S. Aaron, C. N. Sun, M. Bright, A. B. Papandrew, M. M. Mench, and T. A. Zawodzinski. In Situ Kinetics Studies in All-Vanadium Redox Flow Batteries. *ECS Electrochemistry Letters*, 2(3):A29 – A31, 2013.

[78] K. W. Knehr, E. Agar, C. R. Dennison, A. R. Kalidindi, and E. C. Kumbur. A Transient Vanadium Flow Battery Model Incorporating Vanadium Crossover and Water Transport through the Membrane. *Journal of The Electrochemical Society*, 159(9):1446–1459, 2012.

[79] Y. Gandomi, D. Aaron, T. Zawodzinski, and M. Mench. In Situ Potential Distribution Measurement and Validated Model for All-Vanadium Redox Flow Battery. *Journal of The Electrochemical Society*, 163(1):A5188–A5201, 2016.

[80] A. A. Shah, M. J. Watt-Smith, and F. C. Walsh. A dynamic performance model for redox-flow batteries involving soluble species. *Electrochimica Acta*, 53(27):8087–8100, 2008.

[81] B. W. Zhang, Y. Lei, B. F. Bai, A. Xu, and T. S. Zhao. A two-dimensional mathematical model for vanadium redox flow battery stacks incorporating

nonuniform electrolyte distribution in the flow frame. *Applied Thermal Engineering*, 151(December 2018):495–505, 2019.

[82] J. Sun, M. Zheng, Z. Yang, and Z. Yu. Flow field design pathways from lab-scale toward large-scale flow batteries. *Energy*, 173:637–646, 2019.

[83] T. A. Prokop, J. S. Szmyd, and G. Brus. Developing micro-scale heterogeneous numerical simulation of a solid oxide fuel cell anode. *Journal of Physics: Conference Series*, 1101(1), 2018.

[84] J. Gostick, M. Ioannidis, M. Fowler, and M. Pritzker. Pore Network Modeling of Fibrous Gas Diffusion Layers for Polymer Electrolyte Membrane Fuel Cells. pages 1–63, 2017.

[85] W.-Q. Tao, Q. Kang, P. Zelenay, R. Mukundan, L. Chen, and Y. He. Pore-scale study of multiphase reactive transport in fibrous electrodes of vanadium redox flow batteries. *Electrochimica Acta*, 248:425–439, 2017.

[86] G. Qiu, E. Kumbur, Y. Sun, A. S. Joshi, K. Knehr, and C. Dennison. 3-D pore-scale resolved model for coupled species/charge/fluid transport in a vanadium redox flow battery. *Electrochimica Acta*, 64:46–64, 2012.

[87] E. M. Ryan and P. P. Mukherjee. Mesoscale modeling in electrochemical devices—A critical perspective. *Progress in Energy and Combustion Science*, 71:118–142, 2019.

[88] M. Sukop and D. Thorne. *Lattice Boltzmann Modeling: An Introduction for Geoscientists and Engineers*. 2007.

[89] T. Kruger, H. Kusumaatmaja, A. Kuzmin, O. Shardt, G. Silva, and E. M. Viggen. *The Lattice Boltzmann Method: Principles and Practice*. 2017.

[90] S. Girimaji. *Lattice Boltzmann Method: Fundamentals and Engineering Applications with Computer Codes*, volume 51. 2013.

[91] Q. Kang, P. C. Lichtner, and D. Zhang. An improved lattice Boltzmann model for multicomponent reactive transport in porous media at the pore scale. *Water Resources Research*, 43(12):1–12, 2007.

[92] Q. Ma, Q. Xu, Q. Chen, Z. Chen, H. Su, and W. Zhang. Lattice Boltzmann model for complex transfer behaviors in porous electrode of all copper redox flow battery with deep eutectic solvent electrolyte. *Applied Thermal Engineering*, 160(June):114015, 2019.

[93] Z. Y. Jiang, Z. G. Qu, L. Zhou, and W. Q. Tao. A microscopic investigation of ion and electron transport in lithium-ion battery porous electrodes using the lattice Boltzmann method. *Applied Energy*, 194:530–539, 2017.

[94] L. Chen, Y. L. Feng, C. X. Song, L. Chen, Y. L. He, and W. Q. Tao. Multi-scale modeling of proton exchange membrane fuel cell by coupling finite volume method and lattice Boltzmann method. *International Journal of Heat and Mass Transfer*, 63:268–283, 2013.

[95] G. Paasch, K. Micka, and P. Gersdorf. Theory of the electrochemical impedance of macrohomogeneous porous electrodes. *Electrochimica Acta*, 38(18):2653–2662, 1993.

[96] P. H. Nguyen and G. Paasch. Transfer matrix method for the electrochemical impedance of inhomogeneous porous electrodes and membranes. *Journal of Electroanalytical Chemistry*, 460(1-2):63–79, 1999.

[97] M. G. Hosseini, S. Mousavihashemi, S. Murcia-López, C. Flox, T. Andreu, and J. R. Morante. High-power positive electrode based on synergistic effect of N- and WO3 -decorated carbon felt for vanadium redox flow batteries. *Carbon*, 136:444–453, 2018.

[98] N. Yun, J. J. Park, O. O. Park, K. B. Lee, and J. H. Yang. Electrocatalytic effect of NiO nanoparticles evenly distributed on a graphite felt electrode for vanadium redox flow batteries. *Electrochimica Acta*, 278:226–235, 2018.

[99] O. Di Blasi, N. Briguglio, C. Busacca, M. Ferraro, V. Antonucci, and A. Di Blasi. Electrochemical investigation of thermically treated graphene oxides as electrode materials for vanadium redox flow battery. *Applied Energy*, 147:74–81, 2015.

[100] Z. González, C. Flox, C. Blanco, M. Granda, J. R. Morante, R. Menéndez, and R. Santamaría. Outstanding electrochemical performance of a graphene-modified graphite felt for vanadium redox flow battery application. *Journal of Power Sources*, 338:155–162, 2017.

[101] S. Wang, X. Zhao, T. Cochell, and A. Manthiram. Nitrogen-doped carbon nanotube/graphite felts as advanced electrode materials for vanadium redox flow batteries. *Journal of Physical Chemistry Letters*, 3(16):2164–2167, 2012.

[102] T. Wu, K. Huang, S. Liu, S. Zhuang, D. Fang, S. Li, D. Lu, and A. Su. Hydrothermal ammoniated treatment of PAN-graphite felt for vanadium redox flow battery. *Journal of Solid State Electrochemistry*, 16(2):579–585, 2012.

[103] K. J. Kim, Y. J. Kim, J. H. Kim, and M. S. Park. The effects of surface modification on carbon felt electrodes for use in vanadium redox flow batteries. *Materials Chemistry and Physics*, 131(1-2):547–553, 2011.

[104] E.-M. Hammer, B. Berger, and L. Komsiyska. Improvement of the Performance of Graphite Felt Electrodes for Vanadium-Redox-Flow-Batteries by Plasma Treatment. *International Journal of Renewable Energy Development (IJRED)*, 3(1), 2014.

[105] X. Wu, H. Xu, P. Xu, Y. Shen, L. Lu, J. Shi, J. Fu, and H. Zhao. Microwave-treated graphite felt as the positive electrode for all-vanadium redox flow battery. *Journal of Power Sources*, 263:104–109, 2014.

[106] K. J. Kim, S. W. Lee, T. Yim, J. G. Kim, J. W. Choi, J. H. Kim, M. S. Park, and Y. J. Kim. A new strategy for integrating abundant oxygen functional groups into carbon felt electrode for vanadium redox flow batteries. *Scientific Reports*, 4:1–6, 2014.

[107] I. Mayrhuber, C. R. Dennison, V. Kalra, and E. C. Kumbur. Laser-perforated carbon paper electrodes for improved mass-transport in high power density vanadium redox flow batteries. *Journal of Power Sources*, 260:251–258, 2014.

[108] J. R. Macdonald and D. R. Franceschetti. Precision of impedance spectroscopy estimates of bulk, reaction rate, and diffusion parameters. *Journal of Electroanalytical Chemistry*, 307(1-2):1–11, 1991.

[109] M. E. Orazem and B. Tribollet. *Electrochemical Impedance Spectroscopy*. John Wiley & Sons, New York, 2008.

[110] W. H. Wang and X. D. Wang. Investigation of Ir-modified carbon felt as the positive electrode of an all-vanadium redox flow battery. *Electrochimica Acta*, 52(24):6755–6762, 2007.

[111] A. M. Pezeshki, J. T. Clement, G. M. Veith, T. A. Zawodzinski, and M. M. Mench. High performance electrodes in vanadium redox flow batteries through oxygen-enriched thermal activation. *Journal of Power Sources*, 294:333–338, 2015.

[112] L. Yue, W. Li, F. Sun, L. Zhao, and L. Xing. Highly hydroxylated carbon fibres as electrode materials of all-vanadium redox flow battery. *Carbon*, 48(11):3079–3090, 2010.

[113] A. W. Burch. Impurity Effects in All-Vanadium Redox Flow Batteries. *MS Thesis*, 2015.

[114] M. Kubata, H. Nakaishi, and N. Tokuda. Electrolyte for Redox Flow Battery, and Redox Flow Battery. 2002.

[115] R. M. Darling and M. L. Perry. The Influence of Electrode and Channel Configurations on Flow Battery Performance. *Journal of The Electrochemical Society*, 161(9):1381–1387, 2014.

[116] R. M. Darling and M. L. Perry. Half-Cell, Steady-State Flow-Battery Experiments. *ECS Transactions*, 53(7):31–38, 2013.

[117] G. J. Brug, A. L. Van Den Eeden, M. Sluyters-Rehbach, and J. H. Sluyters. The analysis of electrode impedances complicated by the presence of a constant phase element. *Journal of Electroanalytical Chemistry*, 176(1-2):275–295, 1984.

[118] A. Lasia. *Electrochemical Impedance Spectroscopy and its Applications*. Springer, New York, 2002.

[119] T. Shibata, T. Sano, K. Yano, K. Fujikawa, S. Hayashi, K. Yamanishi, A. Inoue, K. Tada, T. Matsumoto, and E. Sasano. Demonstration project of large-scale storage battery system at Minami-Hayakita substation. In *Grand Renewable Energy 2018*, 2018.

[120] G. L. Soloveichik. Flow Batteries: Current Status and Trends. *Chemical Reviews*, 115(20):11533–11558, 2015.

[121] Z. González, A. Sánchez, C. Blanco, M. Granda, R. Menéndez, and R. Santamaría. Enhanced performance of a Bi-modified graphite felt as the positive electrode of a vanadium redox flow battery. *Electrochemistry Communications*, 13(12):1379–1382, 2011.

[122] M. Park, Y. J. Jung, J. Kim, H. I. Lee, and J. Cho. Synergistic effect of carbon nanofiber/nanotube composite catalyst on carbon felt electrode for high-performance all-vanadium redox flow battery. *Nano Letters*, 13(10):4833–4839, 2013.

[123] W. Li, J. Liu, and C. Yan. The electrochemical catalytic activity of single-walled carbon nanotubes towards VO2+/VO2+and V3+/V2+redox pairs for an all vanadium redox flow battery. *Electrochimica Acta*, 79:102–108, 2012.

[124] P. Han, H. Wang, Z. Liu, X. Chen, W. Ma, J. Yao, Y. Zhu, and G. Cui. Graphene oxide nanoplatelets as excellent electrochemical active materials for VO2+/VO2+and V2+/V3+redox couples for a vanadium redox flow battery. *Carbon*, 49(2):693–700, 2011.

[125] J. Clement, D. Aaron, and M. Mench. In Situ Localized Current Distribution Measurements in All-Vanadium Redox Flow Batteries. *Journal of The Electrochemical Society*, 163(1):A5220–A5228, 2016.

[126] V. Levich. *Physicochemical hydrodynamics*. Prentice Hall, 1962.

[127] I. Derr, M. Bruns, J. Langner, A. Fetyan, J. Melke, and C. Roth. Degradation of all-vanadium redox flow batteries (VRFB) investigated by electrochemical impedance and X-ray photoelectron spectroscopy: Part 2 electrochemical degradation. *Journal of Power Sources*, 325:351–359, 2016.

[128] P. Boškoski, A. Debenjak, and B. Mileva Boshkoska. *Fast Electrochemical Impedance Spectroscopy As a Statistical Condition Monitoring Tool*. Springer, Ljubljana, Slovenia, 1 edition, 2017.

[129] G. Kear and F. Walsh. The characteristics of a true tafel slope. *Corrosion and Materials*, 30(6):S1–S4, 2005.

[130] M. C. Daugherty, S. Gu, D. S. Aaron, R. E. Kelly, Y. Ashraf Gandomi, and C.-T. Hsieh. Graphene quantum dot-decorated carbon electrodes for energy storage in vanadium redox flow batteries. *Nanoscale*, 12(14):7834–7842, 2020.

[131] C. Koroneos, T. Spachos, and N. Moussiopoulos. Exergy analysis of renewable energy sources. *Renewable Energy*, 28(2):295–310, 2003.

[132] J. Jin, X. Fu, Q. Liu, Y. Liu, Z. Wei, K. Niu, and J. Zhang. Identifying the active site in nitrogen-doped graphene for the VO 2+/VO2+ redox reaction. *ACS Nano*, 7(6):4764–4773, 2013.

[133] B. Huskinson, M. P. Marshak, C. Suh, S. Er, M. R. Gerhardt, C. J. Galvin, X. Chen, A. Aspuru-Guzik, R. G. Gordon, and M. J. Aziz. A metal-free organic-inorganic aqueous flow battery. *Nature*, 505(7482):195–198, 2014.

[134] T. Janoschka, N. Martin, U. Martin, C. Friebe, S. Morgenstern, H. Hiller, M. D. Hager, and U. S. Schubert. An aqueous, polymer-based redox-flow battery using non-corrosive, safe, and low-cost materials. *Nature*, 527(7576):78–81, 2015.

[135] A. Orita, M. G. Verde, M. Sakai, and Y. S. Meng. A biomimetic redox flow battery based on flavin mononucleotide. *Nature Communications*, 7:1–8, 2016.

[136] J. Zhang, G. Jiang, P. Xu, A. Ghorbani Kashkooli, M. Mousavi, A. Yu, and Z. Chen. An all-aqueous redox flow battery with unprecedented energy density. *Energy and Environmental Science*, 11(8):2010–2015, 2018.

[137] P. Han, Y. Yue, Z. Liu, W. Xu, L. Zhang, H. Xu, S. Dong, and G. Cui. Graphene oxide nanosheets/multi-walled carbon nanotubes hybrid as an excellent electrocatalytic material towards VO2+/VO2+ redox couples for vanadium redox flow batteries. *Energy & Environmental Science*, 4(11):4710, 2011.

[138] K. V. Greco, A. Forner-Cuenca, A. Mularczyk, J. Eller, and F. R. Brushett. Elucidating the Nuanced Effects of Thermal Pretreatment on Carbon Paper Electrodes for Vanadium Redox Flow Batteries. *ACS Applied Materials and Interfaces*, 10(51):44430–44442, 2018.

[139] D. Aaron, S. Yeom, K. D. Kihm, Y. Ashraf Gandomi, T. Ertugrul, and M. M. Mench. Kinetic enhancement via passive deposition of carbon-based nanomaterials in vanadium redox flow batteries. *Journal of Power Sources*, 366:241–248, 2017.

[140] Z. González, C. Botas, P. Álvarez, S. Roldán, C. Blanco, R. Santamaría, M. Granda, and R. Menéndez. Thermally reduced graphite oxide as positive electrode in Vanadium Redox Flow Batteries. *Carbon*, 50(3):828–834, 2012.

[141] Y. Shao, X. Wang, M. Engelhard, C. Wang, S. Dai, J. Liu, Z. Yang, and Y. Lin. Nitrogen-doped mesoporous carbon for energy storage in vanadium redox flow batteries. *Journal of Power Sources*, 195(13):4375–4379, 2010.

[142] X. Zhai, P. Zhang, C. Liu, T. Bai, W. Li, L. Dai, and W. Liu. Highly luminescent carbon nanodots by microwave-assisted pyrolysis. *Chemical Communications*, 48(64):7955–7957, 2012.

[143] S. K. Bhunia, A. Saha, A. R. Maity, S. C. Ray, and N. R. Jana. Carbon nanoparticle-based fluorescent bioimaging probes. *Scientific Reports*, 3, 2013.

[144] P. Lu, R. Zhou, W. Guo, and X. C. Zeng. Amide functionalization of graphene and carbon nanotubes: Coverage- and pattern-dependent electronic and magnetic properties. *Journal of Physical Chemistry C*, 116(25):13722–13730, 2012.

[145] Y. Dai, H. Long, X. Wang, Y. Wang, Q. Gu, W. Jiang, Y. Wang, C. Li, T. H. Zeng, Y. Sun, and J. Zeng. Versatile graphene quantum dots with tunable nitrogen doping. *Particle and Particle Systems Characterization*, 31(5):597–604, 2014.

[146] C. Wang, Y. Zhou, L. He, T. W. Ng, G. Hong, Q. H. Wu, F. Gao, C. S. Lee, and W. Zhang. In situ nitrogen-doped graphene grown from polydimethylsiloxane by plasma enhanced chemical vapor deposition. *Nanoscale*, 5(2):600–605, 2013.

[147] I. Derr, A. Fetyan, K. Schutjajew, and C. Roth. Electrochemical analysis of the performance loss in all vanadium redox flow batteries using different cut-off voltages. *Electrochimica Acta*, 224:9–16, 2017.

[148] Q. M. Gong, Z. Li, Y. Wang, B. Wu, Z. Zhang, and J. Liang. The effect of high-temperature annealing on the structure and electrical properties of well-aligned carbon nanotubes. *Materials Research Bulletin*, 42(3):474–481, 2007.

[149] G. R. Dillip, T. V. Sreekanth, and S. W. Joo. Tailoring the bandgap of N-rich graphitic carbon nitride for enhanced photocatalytic activity. *Ceramics International*, 43(8):6437–6445, 2017.

[150] C. C. Fu, C. T. Hsieh, R. S. Juang, J. W. Yang, S. Gu, and Y. A. Gandomi. Highly efficient carbon quantum dot suspensions and membranes for sensitive/selective detection and adsorption/recovery of mercury ions from aqueous solutions. *Journal of the Taiwan Institute of Chemical Engineers*, 100:127–136, 2019.

[151] G. Wang, X. Shen, J. Yao, and J. Park. Graphene nanosheets for enhanced lithium storage in lithium ion batteries. *Carbon*, 47(8):2049–2053, 2009.

[152] C. T. Hsieh, S. M. Hsu, J. Y. Lin, and H. Teng. Electrochemical capacitors based on graphene oxide sheets using different aqueous electrolytes. *Journal of Physical Chemistry C*, 115(25):12367–12374, 2011.

[153] S. Barman and M. Sadhukhan. Facile bulk production of highly blue fluorescent graphitic carbon nitride quantum dots and their application as highly selective and sensitive sensors for the detection of mercuric and iodide ions in aqueous media. *Journal of Materials Chemistry*, 22(41):21832–21837, 2012.

[154] C. M. Chen, Q. Zhang, X. C. Zhao, B. Zhang, Q. Q. Kong, M. G. Yang, Q. H. Yang, M. Z. Wang, Y. G. Yang, R. Schlögl, and D. S. Su. Hierarchically aminated graphene honeycombs for electrochemical capacitive energy storage. *Journal of Materials Chemistry*, 22(28):14076–14084, 2012.

[155] J. Peng, W. Gao, B. K. Gupta, Z. Liu, R. Romero-Aburto, L. Ge, L. Song, L. B. Alemany, X. Zhan, G. Gao, S. A. Vithayathil, B. A. Kaipparettu, A. A. Marti, T. Hayashi, J. J. Zhu, and P. M. Ajayan. Graphene quantum dots derived from carbon fibers. *Nano Letters*, 12(2):844–849, 2012.

[156] F. Mohammadi, P. Timbrell, S. Zhong, C. Padeste, and M. Skyllas-Kazacos. Overcharge in the vanadium redox battery and changes in electrical resistivity and surface functionality of graphite-felt electrodes. *Journal of Power Sources*, 52(1):61–68, 1994.

[157] D. Qu. Studies of the activated mesocarbon microbeads used in double-layer supercapacitors. *Journal of Power Sources*, 109(2002):403–411, 2002.

[158] C. Sun, J. Chen, H. Zhang, X. Han, and Q. Luo. Investigations on transfer of water and vanadium ions across Nafion membrane in an operating vanadium redox flow battery. *Journal of Power Sources*, 195(3):890–897, 2010.

[159] G. Oriji, Y. Katayama, and T. Miura. Investigations on V(IV)/V(V) and V(II)/V(III) redox reactions by various electrochemical methods. *Journal of Power Sources*, 139(1-2):321–324, 2005.

[160] M. C. Daugherty, S. Gu, D. S. Aaron, B. Chandra Mallick, Y. A. Gandomi, and C.-T. Hsieh. Decorating sulfur and nitrogen co-doped graphene quantum dots on graphite felt as high-performance electrodes for vanadium redox flow batteries. *Journal of Power Sources*, 477:228709, 2020.

[161] B. Dunn, H. Kamath, and J. M. Tarascon. Electrical energy storage for the grid: A battery of choices. *Science*, 334(6058):928–935, 2011.

[162] H. Kaneko, K. Nozaki, Y. Wada, T. Aoki, A. Negishi, and M. Kamimoto. Vanadium redox reactions and carbon electrodes for vanadium redox flow battery. *Electrochimica Acta*, 36(7):1191–1196, 1991.

[163] J. Xi, Z. Wu, X. Qiu, and L. Chen. Nafion/SiO2 hybrid membrane for vanadium redox flow battery. *Journal of Power Sources*, 166(2):531–536, 2007.

[164] M. Rychcik and M. Skyllas-Kazacos. Characteristics of a new all-vanadium redox flow battery. *Journal of Power Sources*, 22(1):59–67, 1988.

[165] C. Ding, H. Zhang, X. Li, T. Liu, and F. Xing. Vanadium flow battery for energy storage: Prospects and challenges. *Journal of Physical Chemistry Letters*, 4(8):1281–1294, 2013.

[166] W. Li, J. Liu, and C. Yan. Reduced graphene oxide with tunable C/O ratio and its activity towards vanadium redox pairs for an all vanadium redox flow battery. *Carbon*, 55:313–320, 2013.

[167] Q. Liu, A. Turhan, T. A. Zawodzinski, and M. M. Mench. In situ potential distribution measurement in an all-vanadium flow battery. *Chemical Communications*, 49(56):6292–6294, 2013.

[168] C. H. Tseng, C. C. Wang, and C. Y. Chen. Functionalizing carbon nanotubes by plasma modification for the preparation of covalent-integrated epoxy composites. *Chemistry of Materials*, 19(2):308–315, 2007.

[169] P. Zhao, H. Zhang, H. Zhou, and B. Yi. Nickel foam and carbon felt applications for sodium polysulfide/bromine redox flow battery electrodes. *Electrochimica Acta*, 51(6):1091–1098, 2005.

[170] D. Xiong, X. Li, Z. Bai, H. Shan, L. Fan, C. Wu, D. Li, and S. Lu. Superior Cathode Performance of Nitrogen-Doped Graphene Frameworks for Lithium Ion Batteries. *ACS Applied Materials and Interfaces*, 9(12):10643–10651, 2017.

[171] G. L. Zhuang, J. Q. Bai, X. Y. Tao, J. M. Luo, X. D. Wang, Y. F. Gao, X. Zhong, X. N. Li, and J. G. Wang. Synergistic effect of S,N-co-doped mesoporous carbon materials with high performance for oxygen-reduction reaction and Li-ion batteries. *Journal of Materials Chemistry A*, 3(40):20244–20253, 2015.

[172] F. Wu, J. T. Lee, A. Magasinski, H. Kim, and G. Yushin. Solution-based processing of graphene-Li2S composite cathodes for lithium-ion and lithium-sulfur batteries. *Particle and Particle Systems Characterization*, 31(6):639–644, 2014.

[173] L. Wu, Y. Shen, L. Yu, J. Xi, and X. Qiu. Boosting vanadium flow battery performance by Nitrogen-doped carbon nanospheres electrocatalyst. *Nano Energy*, 28:19–28, 2016.

[174] M. Park, J. Ryu, Y. Kim, and J. Cho. Corn protein-derived nitrogen-doped carbon materials with oxygen-rich functional groups: A highly efficient electrocatalyst for all-vanadium redox flow batteries. *Energy and Environmental Science*, 7(11):3727–3735, 2014.

[175] Y. Zhou, L. Liu, Y. Shen, L. Wu, L. Yu, F. Liang, and J. Xi. Carbon dots promoted vanadium flow batteries for all-climate energy storage. *Chemical Communications*, 53(54):7565–7568, 2017.

[176] Y. Huang, J. Huo, S. Dou, K. Hu, and S. Wang. Graphitic C3N4 as a powerful catalyst for all-vanadium redox flow batteries. *RSC Advances*, 6(70):66368–66372, 2016.

[177] S. Gu, C. T. Hsieh, Y. Ashraf Gandomi, J. Li, X. X. Yue, and J. K. Chang. Tailoring fluorescence emissions, quantum yields, and white light emitting from nitrogen-doped graphene and carbon nitride quantum dots. *Nanoscale*, 11(35):16553–16561, 2019.

[178] S. Bian, C. Shen, H. Hua, L. Zhou, H. Zhu, F. Xi, J. Liu, and X. Dong. One-pot synthesis of sulfur-doped graphene quantum dots as a novel fluorescent probe for highly selective and sensitive detection of lead(II). *RSC Advances*, 6(74):69977–69983, 2016.

[179] S. Bian, C. Shen, Y. Qian, J. Liu, F. Xi, and X. Dong. Facile synthesis of sulfur-doped graphene quantum dots as fluorescent sensing probes for Ag+ ions detection. *Sensors and Actuators, B: Chemical*, 242:231–237, 2017.

[180] S. Li, Y. Li, J. Cao, J. Zhu, L. Fan, and X. Li. Sulfur-doped graphene quantum dots as a novel fluorescent probe for highly selective and sensitive detection of Fe3+. *Analytical Chemistry*, 86(20):10201–10207, 2014.

[181] D. Deng, X. Pan, L. Yu, Y. Cui, Y. Jiang, J. Qi, W. X. Li, Q. Fu, X. Ma, Q. Xue, G. Sun, and X. Bao. Toward N-doped graphene via solvothermal synthesis. *Chemistry of Materials*, 23(5):1188–1193, 2011.

[182] F. Cervantes-Sodi, G. Csányi, S. Piscanec, and A. C. Ferrari. Edge-functionalized and substitutionally doped graphene nanoribbons: Electronic and spin properties. *Physical Review B - Condensed Matter and Materials Physics*, 77(16):1–13, 2008.

[183] Y. Li, Z. Zhou, P. Shen, and Z. Chen. Spin gapless semiconductor-metal-half-metal properties in nitrogen-doped zigzag graphene nanoribbons. *ACS Nano*, 3(7):1952–1958, 2009.

[184] S. Gu, C. T. Hsieh, Y. Y. Tsai, Y. Ashraf Gandomi, S. Yeom, K. D. Kihm, C. C. Fu, and R. S. Juang. Sulfur and Nitrogen Co-Doped Graphene Quantum Dots as a Fluorescent Quenching Probe for Highly Sensitive Detection toward Mercury Ions. *ACS Applied Nano Materials*, 2(2):790–798, 2019.

[185] B. X. Zhang, H. Gao, and X. L. Li. Synthesis and optical properties of nitrogen and sulfur co-doped graphene quantum dots. *New Journal of Chemistry*, 38(9):4615–4621, 2014.

[186] P. R. Kharangarh, S. Umapathy, and G. Singh. Thermal Effect of Sulfur Doping for Luminescent Graphene Quantum Dots. *ECS Journal of Solid State Science and Technology*, 7(3):M29–M34, 2018.

[187] G. Sandeep Kumar, R. Roy, D. Sen, U. K. Ghorai, R. Thapa, N. Mazumder, S. Saha, and K. K. Chattopadhyay. Amino-functionalized graphene quantum dots: Origin of tunable heterogeneous photoluminescence. *Nanoscale*, 6(6):3384–3391, 2014.

[188] X. Gao, Y. Zhao, B. Liu, H. Xiang, and S. B. Zhang. Π-Bond maximization of graphene in hydrogen addition reactions. *Nanoscale*, 4(4):1171–1176, 2012.

[189] D. Qu, M. Zheng, P. Du, Y. Zhou, L. Zhang, D. Li, H. Tan, Z. Zhao, Z. Xie, and Z. Sun. Highly luminescent S, N co-doped graphene quantum dots with broad visible absorption bands for visible light photocatalysts. *Nanoscale*, 5(24):12272–12277, 2013.

[190] C. H. Choi, S. H. Park, and S. I. Woo. Heteroatom doped carbons prepared by the pyrolysis of bio-derived amino acids as highly active catalysts for oxygen electro-reduction reactions. *Green Chemistry*, 13(2):406–412, 2011.

[191] X. Li, S. P. Lau, L. Tang, R. Ji, and P. Yang. Sulphur doping: A facile approach to tune the electronic structure and optical properties of graphene quantum dots. *Nanoscale*, 6(10):5323–5328, 2014.

[192] C. T. Hsieh, Y. T. Lin, W. Y. Chen, and J. L. Wei. Parameter setting on growth of carbon nanotubes over transition metal/alumina catalysts in a fluidized bed reactor. *Powder Technology*, 192(1):16–22, 2009.

[193] K. Li, G. Ye, J. Pan, H. Zhang, and M. Pan. Self-assembled Nafion®/metal oxide nanoparticles hybrid proton exchange membranes. *Journal of Membrane Science*, 347(1-2):26–31, 2010.

[194] L. Shi, S. Liu, Z. He, and J. Shen. Nitrogen-Doped Graphene:Effects of nitrogen species on the properties of the vanadium redox flow battery. *Electrochimica Acta*, 138:93–100, 2014.

[195] H. Guo and Q. Gao. Boron and nitrogen co-doped porous carbon and its enhanced properties as supercapacitor. *Journal of Power Sources*, 186(2):551–556, 2009.

[196] A. Lherbier, X. Blase, Y. M. Niquet, F. Triozon, and S. Roche. Charge transport in chemically doped 2D graphene. *Physical Review Letters*, 101(3):2–5, 2008.

[197] J. O. Hwang, J. S. Park, D. S. Choi, J. Y. Kim, S. H. Lee, K. E. Lee, Y. H. Kim, M. H. Song, S. Yoo, and S. O. Kim. Workfunction-tunable, N-doped reduced graphene transparent electrodes for high-performance polymer light-emitting diodes. *ACS Nano*, 6(1):159–167, 2012.

[198] G. Liu, X. Li, J. W. Lee, and B. N. Popov. A review of the development of nitrogen-modified carbon-based catalysts for oxygen reduction at USC. *Catalysis Science and Technology*, 1(2):207–217, 2011.

[199] Y. Xing. Synthesis and electrochemical characterization of uniformly-dispersed high loading Pt nanoparticles on sonochemically-treated carbon nanotubes. *Journal of Physical Chemistry B*, 108(50):19255–19259, 2004.

[200] J. Houser, A. Pezeshki, J. T. Clement, D. Aaron, and M. M. Mench. Architecture for improved mass transport and system performance in redox flow batteries. *Journal of Power Sources*, 351:96–105, 2017.

[201] B. Hirschorn, M. E. Orazem, B. Tribollet, V. Vivier, I. Frateur, and M. Musiani. Determination of effective capacitance and film thickness from constant-phase-element parameters. *Electrochimica Acta*, 55(21):6218–6227, 2010.

[202] X. Zhou, R. Xue, Y. Zhong, Y. Zhang, and F. Jiang. Asymmetric porous membranes with ultra-high ion selectivity for vanadium redox flow batteries. *Journal of Membrane Science*, (August):117614, 2019.

[203] D. You, H. Zhang, and J. Chen. A simple model for the vanadium redox battery. *Electrochimica Acta*, 54(27):6827–6836, 2009.

[204] M. C. Daugherty, C. T. Hsieh, D. S. Aaron, Y. Ashraf Gandomi, J. Li, Y. Zheng, and W. Pfleging. Enabling high rate capability, low internal resistance, and excellent cyclability for vanadium redox flow batteries utilizing ultrafast laser-structured graphite felt. *Electrochimica Acta*, 344, 2020.

[205] X. W. Wu, T. Yamamura, S. Ohta, Q. X. Zhang, F. C. Lv, C. M. Liu, K. Shirasaki, I. Satoh, T. Shikama, D. Lu, and S. Q. Liu. Acceleration of the redox kinetics of VO2+/VO2+ and V3+/V2+ couples on carbon paper. *Journal of Applied Electrochemistry*, 41(10):1183–1190, 2011.

[206] H. Q. Zhu, Y. M. Zhang, L. Yue, W. S. Li, G. L. Li, D. Shu, and H. Y. Chen. Graphite-carbon nanotube composite electrodes for all vanadium redox flow battery. *Journal of Power Sources*, 184(2):637–640, 2008.

[207] G. J. Radford, J. Cox, R. G. Wills, and F. C. Walsh. Electrochemical characterisation of activated carbon particles used in redox flow battery electrodes. *Journal of Power Sources*, 185(2):1499–1504, 2008.

[208] H. Zhou, H. Zhang, P. Zhao, and B. Yi. A comparative study of carbon felt and activated carbon based electrodes for sodium polysulfide/bromine redox flow battery. *Electrochimica Acta*, 51(28):6304–6312, 2006.

[209] D. Aaron, Q. Liu, Z. Tang, G. M. Grim, A. B. Papandrew, A. Turhan, T. A. Zawodzinski, and M. M. Mench. Dramatic performance gains in vanadium redox flow batteries through modified cell architecture. *Journal of Power Sources*, 206(2010):450–453, 2012.

[210] M. Manahan, Q. Liu, M. Gross, and M. Mench. Carbon nanoporous layer for reaction location management and performance enhancement in all-vanadium redox flow batteries. *Journal of Power Sources*, 222:498–502, 2013.

[211] Q. H. Liu, G. M. Grim, a. B. Papandrew, A. Turhan, T. a. Zawodzinski, and M. M. Mench. High Performance Vanadium Redox Flow Batteries with Optimized Electrode Configuration and Membrane Selection. *Journal of the Electrochemical Society*, 159(8):A1246–A1252, 2012.

[212] X. Liu, H. Zhang, E. Mazur, R. Sanatinia, E. Mottay, and W. Pfleging. Industrial applications of ultrafast laser processing. *MRS Bulletin*, 41(12):984–992, 2016.

[213] W. Pfleging. A review of laser electrode processing for development and manufacturing of lithium-ion batteries. *Nanophotonics*, 7(3):549–573, 2017.

[214] Y. Zheng, L. Pfäffl, H. J. Seifert, and W. Pfleging. Lithium distribution in structured graphite anodes investigated by laser-induced breakdown spectroscopy. *Applied Sciences (Switzerland)*, 9(20), 2019.

[215] Y. Zheng, H. J. Seifert, H. Shi, Y. Zhang, C. Kübel, and W. Pfleging. 3D silicon/graphite composite electrodes for high-energy lithium-ion batteries. *Electrochimica Acta*, 317:502–508, 2019.

[216] T. Jansen, D. Blass, S. Hartwig, and K. Dilger. Processing of advanced battery materials—laser cutting of pure lithium metal foils. *Batteries*, 4(3), 2018.

[217] C. R. Dennison, E. Agar, B. Akuzum, and E. C. Kumbur. Enhancing Mass Transport in Redox Flow Batteries by Tailoring Flow Field and Electrode Design. *Journal of The Electrochemical Society*, 163(1):A5163–A5169, 2016.

[218] X. L. Zhou, T. S. Zhao, L. An, Y. K. Zeng, and L. Wei. Critical transport issues for improving the performance of aqueous redox flow batteries. *Journal of Power Sources*, 339:1–12, 2017.

[219] A. Bourke, M. A. Miller, R. P. Lynch, X. Gao, J. Landon, J. S. Wainright, R. F. Savinell, and D. N. Buckley. Electrode Kinetics of Vanadium Flow Batteries: Contrasting Responses of V II -V III and V IV -V V to Electrochemical Pretreatment of Carbon. *Journal of The Electrochemical Society*, 163(1):A5097–A5105, 2016.

[220] W. Pfleging and J. Pröll. A new approach for rapid electrolyte wetting in tape cast electrodes for lithium-ion batteries. *Journal of Materials Chemistry A*, 2(36):14918–14926, 2014.

[221] X. L. Zhou, T. S. Zhao, L. An, Y. K. Zeng, and X. B. Zhu. Performance of a vanadium redox flow battery with a VANADion membrane. *Applied Energy*, 180:353–359, 2016.

[222] S. Roe, C. Menictas, and M. Skyllas-Kazacos. A High Energy Density Vanadium Redox Flow Battery with 3 M Vanadium Electrolyte. *Journal of The Electrochemical Society*, 163(1):A5023–A5028, 2016.

[223] J. J. Ye, C. H. Lin, and X. J. Huang. Analyzing the anodic stripping square wave voltammetry of heavy metal ions via machine learning: Information beyond a single voltammetric peak. *Journal of Electroanalytical Chemistry*, 872:113934, 2020.

[224] K. T. Schütt, H. E. Sauceda, P. J. Kindermans, A. Tkatchenko, and K. R. Müller. SchNet - A deep learning architecture for molecules and materials. *Journal of Chemical Physics*, 148(24), 2018.

[225] G. Houchins and V. Viswanathan. An accurate machine-learning calculator for optimization of Li-ion battery cathodes. *Journal of Chemical Physics*, 153(5), 2020.

[226] S. P. Sullivan, F. M. Sani, M. L. Johns, and L. F. Gladden. Simulation of packed bed reactors using lattice Boltzmann methods. *Chemical Engineering Science*, 60(12):3405–3418, 2005.

[227] L. Chen, Q. Kang, B. A. Robinson, Y. L. He, and W. Q. Tao. Pore-scale modeling of multiphase reactive transport with phase transitions and dissolution-precipitation processes in closed systems. *Physical Review E - Statistical, Nonlinear, and Soft Matter Physics*, 87(4):1–16, 2013.

[228] R. Machado. Numerical simulations of surface reaction in porous media with lattice Boltzmann. *Chemical Engineering Science*, 69(1):628–643, 2012.

[229] T. Ertugrul, J. Clement, Y. Gandomi, D. Aaron, and M. Mench. In-situ current distribution and mass transport analysis via strip cell architecture for a vanadium redox flow battery. *Journal of Power Sources*, 437:226920, 2019.

[230] B. Akuzum, Y. C. Alparslan, N. C. Robinson, E. Agar, and E. C. Kumbur. Obstructed flow field designs for improved performance in vanadium redox flow batteries. *Journal of Applied Electrochemistry*, 49(6):551–561, 2019.

[231] T. Y. Ertugrul, M. C. Daugherty, J. R. Houser, D. S. Aaron, and M. M. Mench. Computational and Experimental Study of Convection in a Vanadium Redox Flow Battery Strip Cell Architecture. *Energies*, 13(18):4767, 2020.

[232] M. Kazacos and M. Skyllas-Kazacos. Performance Characteristics of Carbon Plastic Electrodes in the All-Vanadium Redox Cell. *Journal of The Electrochemical Society*, 136(9):2759, 1989.

[233] A. Mousa. Chemical and Electrochemical studies of V(III) and V (II) Solutions in Sulfuric Acid Solution for Vanadium Battery Applications. *PhD thesis, University of New South Wales, Australia*, (August), 2003.

[234] M. Skyllas-Kazacos, L. Cao, M. Kazacos, N. Kausar, and A. Mousa. Vanadium Electrolyte Studies for the Vanadium Redox Battery—A Review. *ChemSusChem*, 9(13):1521–1543, 2016.

[235] C. Schiller, F. Richter, E. Gülzow, and N. Wagner. Validation and evaluation of electrochemical impedance spectra of systems with states that change with time. *Physical Chemistry Chemical Physics*, 3(3):374–378, 2001.

[236] M. Skyllas-Kazacos and M. Kazacos. State of charge monitoring methods for vanadium redox flow battery control. *Journal of Power Sources*, 196(20):8822–8827, 2011.

[237] E. Barsoukov and J. R. Macdonald. *Impedance Spectroscopy:Theory, Experiment, and Applications, Second Edition*. 2005.

[238] S. M. Taylor, A. Pătru, D. Streich, M. El Kazzi, E. Fabbri, and T. J. Schmidt. Vanadium (V) reduction reaction on modified glassy carbon electrodes – Role of oxygen functionalities and microstructure. *Carbon*, 109:472–478, 2016.

[239] N. Wang, W. Zhou, and F. Zhang. L-cystine additive in the negative electrolyte of vanadium redox flow battery for improving electrochemical performance. *Ionics*, 2018.

[240] M. N. Ozisik. *Heat Conduction*. John Wiley & Sons, 2nd edition, 1993.

Appendices

Introduction Supplemental

Nernst equation as a function of SoC

To represent the Nernst equation as a function of SoC, we assume that the the concentration of V^{3+} is $C_{V^{3+}} = 1 - C_{V^{2+}}$. Likewise the concentration of $VO^{2+}$is $C_{VO^{2+}} = 1 - C_{VO_2^+}$. This allows Equation 1.2 to be written

$$E = E_0 + \frac{RT}{F} \log \left(\frac{SoC^2}{(1 - SoC)^2} \right) \tag{A.1}$$

The sensitivity coefficient (partial derivative of a the dependent variable E with respect to its parameter SoC) for the Nernst equation as a function of SoC is then:

$$\frac{\partial E}{\partial SoC} = \frac{RT(1 - SoC)^2}{FSoC^2} \left(\frac{2SoC^2}{(1 - SoC)^3} + \frac{2SoC}{(1 - SoC)^2} \right) \tag{A.2}$$

Supplement materials for chapter 2

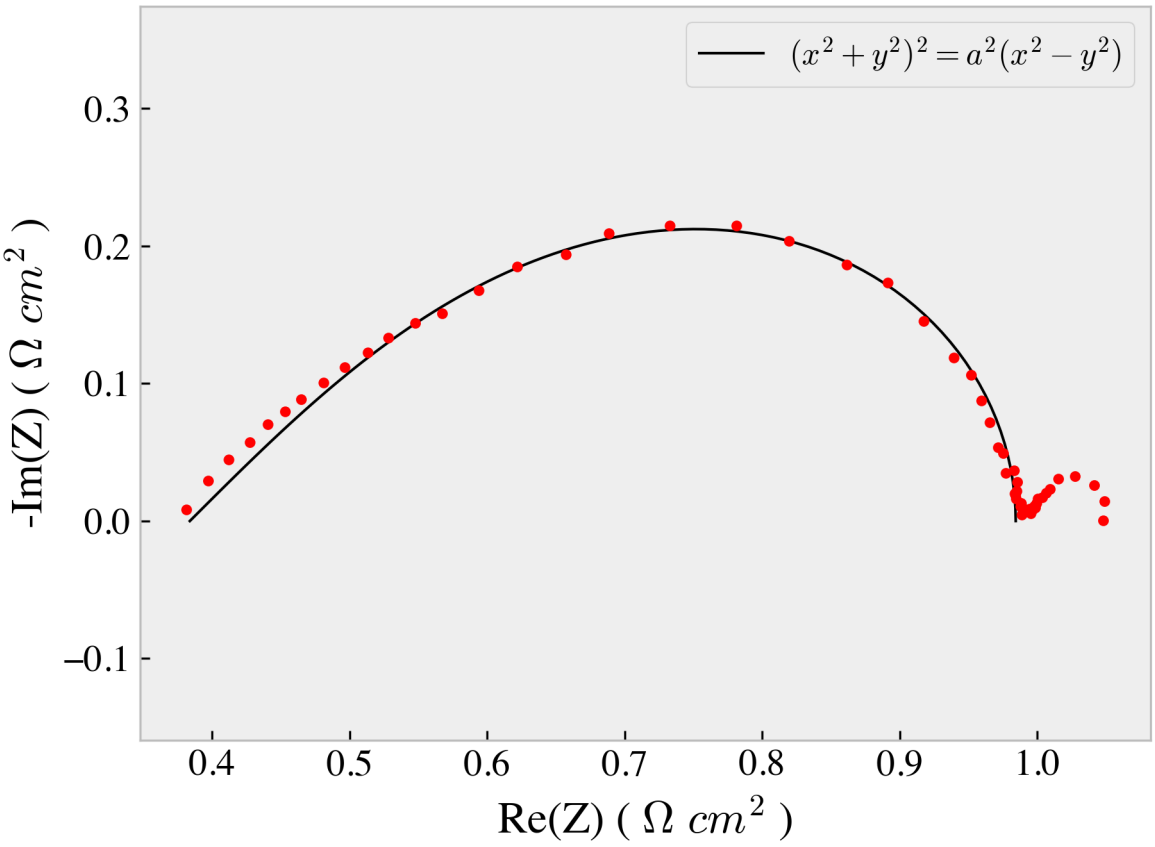

Figure A.1: Oxygen Heat Treated electrode fit to a lemniscate

Derivation of macrohomogeneous porous electrode model

The following is largely adapted from [95, 96] with added intermediate steps for clarity and some modifications. The geometric framework of the (single electrode) macrohomogeneous porous electrode is defined by the separator interface being at x = 0 and the current collector at x = b. The porous electrode exists between these two interfaces and is filled with electrolyte. The electrode and electrolyte potentials (ϕ_1 and ϕ_2 respectively) exist continuously inside of this domain. The position and time dependent polarization:

$$\tilde{E}(x,t) = \phi_1 - \phi_2 \tag{A.3}$$

The potential of the cell is then:

$$E = \tilde{E} - E_n \tag{A.4}$$

The following equation holds without regard to the solid phase conductivity (ϕ_1) [95] (conservation of energy):

$$\begin{aligned} C_1 \frac{\partial \tilde{E}}{\partial t} = -\frac{1}{r_2}\frac{\partial^2 \phi_2}{\partial x^2} \times A_t i_0 \Bigg(& \exp\left[-\frac{\alpha F}{RuT}(\tilde{E} - E_n) \right] \\ & - \exp\left[\frac{(1-\alpha)F}{RuT}(\tilde{E} - E_n) \right] \Bigg) \end{aligned} \tag{A.5}$$

Where C_1 (the double layer capacity per unit length) is calculated by:

Table A.1: MHPE Derivation Nomenclature

Symbol	Description	Units
A	Geometric surface area	cm^2
A_t	Wetted surface area	cm^2
b	Electrode thickness	cm
C_1	Double layer capacity per unit length	F cm^{-1}
C_{dl}	Area specific double layer capacitance	F cm^{-2}
E	Potential	V
$E_{+/-}$	Unknown functions of frequency	V
E_a	Complex amplitude of polarization	V
E_{el}	Potential drop over the electrode	V
E_n	Equilibrium polarization	V
$\tilde{E}(x,t)$	Potential phasor	V
F	Faraday Constant	C mol^{-1}
g_{ct}	Charge transfer admittance per unit length	S cm^{-1}
j	$\sqrt{-1}$	-
i_0	Exchange current density	mA cm^{-2}
j_a	Amplitude of current density	A
k	A characteristic frequency ($\neq \omega_1$)	rad s^{-1}
K	Field diffusion constant	cm^2 s^{-1}
r_1	Resistance per unit length of electrode	Ω cm^{-1}
r_2	Resistance per unit length of electrolyte	Ω cm^{-1}
Ru	Gas constant	J mol^{-1} K^{-1}
t	Time	s
T	Temperature	K
α	Transfer Coefficient	-
β	Solution to characteristic equation	-
ϕ_1	Solid phase potential	V
ϕ_2	Electrolyte phase potential	V
ρ_1	Electrolyte resistivity	Ω cm
ρ_2	Electrode resistivity	Ω cm
λ	Complex decay length	cm
ω	Angular frequency	rad s^{-1}
ω_1	Characteristic frequency	s^{-1}

$$C_1 = \frac{A_t}{b} C_{dl} \tag{A.6}$$

And r_2 (resistance per unit length of electrolyte) is:

$$r_2 = \frac{\rho_2}{A} \tag{A.7}$$

In the case where the polarization is sufficiently small, the exponential terms in equation A.5 can be linearized and the equation recast as:

$$C_1 \frac{\partial E}{\partial t} = -\frac{1}{r_2} \frac{\partial^2 \phi_2}{\partial x^2} - g_{ct} E \tag{A.8}$$

Where the term g_{ct}, is the charge transfer admittance per unit length of the electrolyte saturated electrode ($g_{ct} = Z_{ct}^{-1}$; Z_{ct} is defined in Equation 2 and contains 4 of the fitting parameters). This relationship only takes into account the electrolyte potential, however in cases where the solid phase resistance is also significant it becomes space-dependent. From Ohm's law together with conservation of charge the relationship between the potentials and their resistivities arises $\rho_1^{-1} \nabla^2 \phi_1 + \rho_2^{-1} \nabla^2 \phi_2 = 0$. This is used to determine the analog of A.8 the solid phase A.10:

$$\begin{aligned} \frac{\nabla^2 \phi_1}{\rho_1} + \frac{\nabla^2 \phi_2}{\rho_2} = 0 \rightarrow -\frac{\rho_2}{\rho_1} \nabla^2 \phi_1 = \nabla^2 \phi_2 \\ \frac{\nabla^2 \phi_1}{\rho_1} + \frac{\nabla^2 \phi_2}{\rho_2} = 0 \rightarrow \nabla^2 \phi_1 = -\frac{\rho_1}{\rho_2} \nabla^2 \phi_2 \end{aligned} \tag{A.9}$$

From A.8 and A.9 the space-dependent equation for the solid phase potential is now known :

$$-C_1 \frac{\partial E}{\partial t} = -\frac{1}{r_1} \frac{\partial^2 \phi_1}{\partial x^2} + g_{ct} E \tag{A.10}$$

Where r_1 is defined analogously to r_2. Letting the equilibrium polarization be 0 (E_n = 0), $\tilde{E}(x,t) = E(x,t)$, equation A.4 differentiated twice with respect to x gives:

$$\begin{aligned} \frac{\partial^2 E}{\partial x^2} = \frac{\partial^2 \phi_1}{\partial x^2} - \frac{\partial^2 \phi_2}{\partial x^2} = \frac{\partial^2 \phi_1}{\partial x^2} - (-\frac{\rho_2}{\rho_1} \frac{\partial^2 \phi_1}{\partial x^2}) \\ = \frac{\partial^2 \phi_1}{\partial x^2} + \frac{\rho_2}{\rho_1} \frac{\partial^2 \phi_1}{\partial x^2} = \frac{1}{\rho_1} \frac{\partial^2 \phi_1}{\partial x^2} + \frac{\rho_2}{\rho_1} \frac{\partial^2 \phi_1}{\partial x^2} = \frac{\partial^2 \phi_1}{\partial x^2} + \frac{\rho_2}{\rho_1} \frac{\partial^2 \phi_1}{\partial x^2} \\ = \frac{\rho_1 + \rho_2}{\rho_1} \frac{\partial^2 \phi_1}{\partial x^2} \end{aligned} \tag{A.11}$$

Likewise:

$$\frac{\partial^2 E}{\partial x^2} = -\frac{\rho_1 + \rho_2}{\rho_2} \frac{\partial^2 \phi_2}{\partial x^2} \tag{A.12}$$

Combining A.10 and with the expression shown in A.11, the PDE can be coupled and expressed solely in terms of the potential (E) instead of the respective potentials (ϕ_1 or ϕ_2) :

$$\begin{aligned} -C_1 \frac{\partial E}{\partial t} &= -\frac{A}{\rho_1 + \rho_2} \frac{\rho_1 + \rho_2}{\rho_1} \frac{\partial^2 \phi_1}{\partial x^2} + g_{ct} E \\ &= -\frac{A}{\rho_1 + \rho_2} \frac{\partial^2 E}{\partial x^2} + g_{ct} E \\ &= -\frac{1}{r_1 + r_2} \frac{\partial^2 E}{\partial x^2} + g_{ct} E \end{aligned} \tag{A.13}$$

Dividing A.13 by $-C_1$ the PDE can be expressed as:

$$\frac{\partial E}{\partial t} = \frac{1}{C_1(r_1 + r_2)} \frac{\partial^2 E}{\partial x^2} - \frac{g_{ct}}{C_1} E \tag{A.14}$$

Let K be defined by:

$$K \equiv \frac{1}{C_1(r_1 + r_2)} \tag{A.15}$$

And k be defined by:

$$k \equiv \frac{g_{ct}}{C_1} \tag{A.16}$$

Now the coupled PDE (A.14) can be expressed in terms of E, K and k:

$$\frac{\partial E}{\partial t} = K \frac{\partial^2 E}{\partial x^2} - kE \tag{A.17}$$

Solution to macrohomogeneous porous electrode PDE

The imposed current is given by:

$$I = A j_a e^{j\omega t} \tag{A.18}$$

The homogeneity and linearity of the PDE (A.17) allow us to set:

$$E(x, \omega) = E_a(x, \omega) e^{j\omega t} \tag{A.19}$$

With A.19, equation A.17 can be expressed as:

$$
\begin{aligned}
j\omega \frac{\partial}{\partial t} E_a e^{j\omega t} &= K \frac{\partial^2 E_a e^{j\omega t}}{\partial x^2} - k E_a e^{j\omega t} \\
&\rightarrow \frac{\partial^2 E_a}{\partial x^2} - \frac{j\omega + k}{K} E_a = 0
\end{aligned}
\tag{A.20}
$$

The characteristic polynomial of A.20, its roots and general solution are:

$$
\begin{aligned}
r^2 - \frac{j\omega + k}{K} &= 0 \\
r &= \pm \sqrt{\frac{j\omega + k}{K}} \\
E_a(x, \omega) &= E_+(\omega) e^{\beta x} + E_- e^{-\beta x}
\end{aligned}
\tag{A.21}
$$

Where $\beta = \sqrt{\frac{j\omega+k}{K}}$; E_+ and E_- are arbitrary functions of frequency that are solved for using the boundary conditions. The complex decay length λ is defined as:

$$
\lambda \equiv \frac{1}{Real(\beta)} \tag{A.22}
$$

The impedance response of the electrode is defined by the drop in potential over the electrode which is measured by the potential in the solid phase at x = d minus the electrolyte phase potential at x = 0:

$$
E_{el} = \phi_1(d, \omega) - \phi_2(0, \omega) = \phi_2(d, \omega) - \phi_2(0, \omega) - E_a(d, \omega) \tag{A.23}
$$

The impedance is defined as the ratio of the potential drop over the electrode to the current:

$$AZ(\omega) = \frac{E_{el}}{j_a} \tag{A.24}$$

Recall that the imposed potential across the cell is $E_a = \phi_1(x,\omega) - \phi_2(x,\omega)$.

Boundary Conditions

Ohm's Law at x = 0 for the electrolyte phase potential:

$$\left.\frac{\partial \phi_2}{\partial x}\right|_{x=0} = -\rho_2 j_a \tag{A.25}$$

Ionic current is zero at the current collector:

$$\left.\frac{\partial \phi_2}{\partial x}\right|_{x=b} = 0 \tag{A.26}$$

Electronic current is zero at the separator interface:

$$\left.\frac{\partial \phi_1}{\partial x}\right|_{x=0} = 0 \tag{A.27}$$

Ohm's Law at x = d for the electronic phase potential:

$$\left.\frac{\partial \phi_1}{\partial x}\right|_{x=b} = -\rho_1 j_a \tag{A.28}$$

(Toward solutions for E_+ and E_- from A.21) Differentiating E_a once:

$$\frac{\partial E_a}{\partial x} = \frac{\partial \phi_1}{\partial x} - \frac{\partial \phi_2}{\partial x} = \beta(E_+(\omega)e^{\beta x} - E_-(\omega)e^{-\beta x}) \tag{A.29}$$

From A.29 with the respective boundary conditions substituted corresponding to x = d and x= 0:

$$\frac{\partial E_a(d,\omega)}{\partial x} = -\rho_1 j_a - 0 = \beta(E_+(\omega)e^{\beta d} - E_-(\omega) - e^{-\beta d}) \tag{A.30}$$

$$\frac{\partial E_a(0,\omega)}{\partial x} = 0 + \rho_2 j_a = \beta(E_+(\omega) - E_-(\omega)) \tag{A.31}$$

With A.31 solving for E_+:

$$\frac{\rho_2 j_a}{\beta} + E_-(\omega) = E_+(\omega) \tag{A.32}$$

Substituting A.32 into A.30:

$$\begin{aligned} -\rho_1 j_a &= \beta\left(\left[\frac{\rho_2 j_a}{\beta} + E_-(\omega)\right]e^{\beta d} - E_-(\omega)e^{-\beta d}\right) \\ &= \rho_2 j_a e^{\beta d} + \beta E_-(\omega)e^{\beta d} - \beta E_-(\omega)e^{-\beta d} \\ &\rightarrow E_- = -j_a \frac{\rho_1 + \rho_2 e^{\beta d}}{\beta[e^{\beta d} - e^{-\beta d}]} \\ &\rightarrow E_+ = -j_a \frac{\rho_1 + \rho_2 e^{\beta d}}{\beta[e^{\beta d} - e^{-\beta d}]} + \frac{\rho_2 j_a}{\beta} \end{aligned} \tag{A.33}$$

Now that E_+ and E_- are known, they can be substituted back into the general solution of E_a (equation A.21) to get the particular solution (showing the intermediate

term reductions).

$$
\begin{aligned}
E_a(x,\omega) &= \left(-j_a \frac{\rho_1 + \rho_2 e^{\beta d}}{\beta[e^{\beta d} - e^{-\beta d}]} + \frac{\rho_2 j_a}{\beta} \right) e^{\beta x} + -j_a \frac{\rho_1 + \rho_2 e^{\beta d}}{\beta[e^{\beta d} - e^{-\beta d}]} e^{-\beta x} \\
&= -\frac{j_a(\rho_1 + \rho_2 e^{\beta d}) e^{\beta x}}{\beta[e^{\beta d} - e^{-\beta d}]} + \frac{\rho_2 j_a e^{\beta x}}{\beta} - \frac{j_a(\rho_1 + \rho_2 e^{\beta d}) e^{-\beta x}}{\beta[e^{\beta d} - e^{-\beta d}]} \\
&= -\frac{j_a(\rho_1 + \rho_2 e^{\beta d})}{\beta[e^{\beta d} - e^{-\beta d}]}(e^{\beta x} + e^{-\beta x}) + \frac{\rho_2 j_a e^{\beta x}}{\beta} \\
&= \frac{-j_a(\rho_1 + \rho_2 e^{\beta d})(e^{\beta x} + e^{-\beta x}) + \rho_2 j_a e^{\beta x}[e^{\beta d} - e^{-\beta d}}{\beta[e^{\beta d} - e^{-\beta d}]} \\
&= \frac{-j_a}{\beta[e^{\beta d} - e^{-\beta d}]}[\rho_1(e^{\beta x} e^{-\beta x}) + \rho_2(e^{\beta(d-x)} e^{-\beta(d-x)}] \\
&= \frac{-j_a}{2\beta sinh(\beta d)} 2[\rho_1 cosh(\beta x) + \rho_2 cosh(\beta(d-x))] \\
&= -j_a \frac{\rho_1 cosh(\beta x) + \rho_2 cosh(\beta(d-x))}{\beta sinh(\beta d)}
\end{aligned}
\tag{A.34}
$$

In order to solve A.17 E_a is integrated with respect to x:

$$
\begin{aligned}
\int E_a(x,\omega)dx &= -\int j_a \frac{\rho_1 cosh(\beta x) + \rho_2 cosh(\beta(d-x))}{\beta sinh(\beta d)} dx \\
&= -j_a \frac{\rho_1 sinh(\beta x) - \rho_2 sinh(\beta(d-x))}{\beta^2 sinh(\beta d)} + q(\omega)
\end{aligned}
\tag{A.35}
$$

Where the term q(ω) is an arbitrary function of frequency. Integration a second time gives:

$$\begin{aligned}\int\int E_a(x,\omega)dxdx &= -\int\int j_a\frac{\rho_1 cosh(\beta x)+\rho_2 cosh(\beta(d-x))}{\beta sinh(\beta d)}dxdx \\ &= -\int j_a\frac{\rho_1 sinh(\beta x)-\rho_2 sinh(\beta(d-x))}{\beta^2 sinh(\beta d)}+q(\omega)dx \\ &= -j_a\frac{\rho_1 cosh(\beta x)+\rho_2 cosh(\beta(d-x))}{\beta^3 sinh(\beta d)}+q(\omega)x+v(\omega) \\ &= \frac{1}{\beta^2}E_a+q(\omega)x+v(\omega)\end{aligned} \tag{A.36}$$

Where the term v(ω) is an arbitrary function of frequency. With the integrals of E_a known, A.17 can now be solved with E(x,ω) = E_a(x,ω) $e^{i\omega t}$ by direct integration:

$$\begin{aligned}\frac{\partial}{\partial t}E_a e^{j\omega t} &= K\frac{\partial^2}{\partial x^2}E_a e^{j\omega t}-kE_a e^{j\omega t} \\ \frac{\partial}{\partial t}E_a e^{j\omega t} &= j\omega E_a e^{j\omega t} \\ \frac{\partial^2}{\partial x^2}E_a e^{j\omega t} &= Ke^{j\omega t}\frac{\partial^2 E_a}{\partial x^2} \\ \rightarrow (j\omega+k)E_a &= K\frac{\partial^2 E_a}{\partial x^2}\end{aligned} \tag{A.37}$$

Recalling the definition of E, the E_a term in A.37 can be replaced by $\phi_1-\phi_2$ and simplified with A.12.

$$\begin{aligned}(j\omega+k)E_a &= K\left[\frac{\partial^2\phi_1}{\partial x^2}-\frac{\partial^2\phi_2}{\partial x_2}\right] \\ &= -\frac{\rho_1+\rho_2}{\rho_2}K\frac{\partial^2\phi_2}{\partial x^2}\end{aligned} \tag{A.38}$$

Now when A.38 is integrated with respect to x, $\int E_a(x,\omega)$ dx is known and from

the fundamental theorem of calculus, the antiderivative of $\frac{\partial^2 \phi_2}{\partial x^2}$ is $\frac{\partial \phi_2}{\partial x}$ (recall the unkonwn funciton q(ω) must be included):

$$(j\omega + k) \int E_a(x, \omega) dx = -\frac{\rho_1 + \rho_2}{\rho_2} \frac{\partial \phi_2}{\partial x} + q(\omega) \tag{A.39}$$

Using the boundary conditoin for ϕ_2 at x = b and plugging x = b into equation A.35, solve for q(ω). (recall the definition of K):

$$q(\omega) = (j\omega + k)(j_a \frac{\rho_1}{\beta^2}) + \left(\frac{\rho_1 + \rho_2}{\rho_2} K \right) \times 0 = -K j_a \rho_1 \tag{A.40}$$

Integrating A.38 a second time gives:

$$\begin{aligned} (j\omega + k) \int \int E_a(x, \omega) dx dx &= -\frac{\rho_1 + \rho_2}{\rho_2} K \phi_2 - \int K j_a \rho_1 dx + v(\omega) \\ \rightarrow (j\omega + k) \frac{1}{\beta^2} E_a(x, \omega) = K E_a &= -\frac{\rho_1 + \rho_2}{\rho_2} K \phi_2 - K j_a \rho_1 x + v(\omega) \\ \rightarrow E_a &= -\frac{\rho_1 + \rho_2}{\rho_2} \phi_2(x, \omega) - j_a \rho_1 x + \frac{v(\omega)}{K} \end{aligned} \tag{A.41}$$

The potential can be set to zero arbitrarily therefore we set v(ω) = 0 and solve for ϕ_2(x,ω).

$$\phi_2(x, \omega) = -\frac{\rho_2 E_a(x, \omega)}{\rho_1 + \rho_2} - j_a x \frac{\rho_1 \rho_2}{\rho_1 + \rho_2} \tag{A.42}$$

Now that the expressions for $E_a(x, \omega)$ (equation A.34) and $\phi_2(x, \omega)$ (equation A.42) are known, the form that has been sought (equation A.24) can be solved by plug-

ging in the respective values of x = 0 and x = d into A.23. Recall: $E_{el} = -(E_a(d,\omega) + \phi_2(d,\omega) - \phi_2(0,\omega)$:

$$\frac{E_{el}}{j_a} = \frac{\rho_2}{\rho_1+\rho_2}\frac{\rho_1+\rho_2 cosh(\beta d)}{\beta sinh(\beta d)} - \frac{\rho_1}{\rho_1+\rho_2}\frac{\rho_1 cosh(\beta d)+\rho_2}{\beta sinh(\beta d)} + b\frac{\rho_1\rho_2}{\rho_1+\rho_2} + \frac{\rho_1 cosh(\beta d)+\rho_2}{\beta sinh(\beta d)}$$
$$= \frac{\rho_1^2+\rho_2^2}{\rho_1+\rho_2}coth(\beta d) + \frac{2\rho_2\rho_1}{\rho_1+\rho_2}\frac{1}{\beta sinh(\beta d)} + b\frac{\rho_1\rho_2}{\rho_1+\rho_2} \tag{A.43}$$

The closed form expression for the impedance as a function of frequency (Z(ω) from equation A.24) is now expressed as:

$$\boldsymbol{\frac{AZ(\omega)}{b} = \frac{\rho_1^2+\rho_2^2}{\rho_1+\rho_2}\frac{\lambda}{b}coth\left(\frac{b}{\lambda}\right) + \frac{2\rho_2\rho_1}{\rho_1+\rho_2}\frac{\lambda}{b}sinh\left(\frac{b}{\lambda}\right)^{-1} + \frac{\rho_1\rho_2}{\rho_1+\rho_2}} \tag{A.44}$$

Table A.2: Chapter 2 Nomenclature

Symbol	Description	Units
a	Nernstian Diffusion layer thickness	cm
A	Geometric surface area	cm^2
A_t	Wetted surface area	cm^2
A_{eff}	Effective surface area	cm^2
ASR_x	Area Specific Resistance x	$\Omega\ cm^2$
b	Electrode thickness	cm
C_1	Double layer capacity per unit length	$F\ cm^{-1}$
C_{dl}	Area specific double layer capacitance	$F\ cm^{-2}$
C_{eff}	Effective Double Layer Capacitance	F
C_R	Concentration of reduced species	$mol\ cm^{-3}$
C_O	Concentration of oxidized species	$mol\ cm^{-3}$
D_R	Diffusivity of reduced species	$cm^2\ s^{-1}$
D_O	Diffusivity of oxidized species	$cm^2\ s^{-1}$
E	Potential	V
$E_{+/-}$	Unknown functions of frequency	V
E_a	Complex amplitude of polarization	V
E_{el}	Potential drop over the electrode	V
E_n	Equilibrium polarization	V
$\tilde{E}$(x,t)	Potential phasor	V
f	Scale factor	-
F	Faraday Constant	$C\ mol^{-1}$
g_{ct}	Charge transfer admittance per unit length	$S\ cm^{-1}$
j	$\sqrt{-1}$	-
i_0	Exchange current density	$mA\ cm^{-2}$
j_a	Amplitude of current density	A
K	Field diffusion constant	$cm^2\ s^{-1}$
L	Inductance	H
n	Number of electrons transfered	-
N(x,y)	Normal Distribution (μ = x, σ = y)	-
P	CPE exponent	-
Q	CPE parameter	F
r_1	Electrode resistivity	$\Omega\ cm^{-1}$
r_2	Electrolyte resistivity	$\Omega\ cm^{-1}$
R_x	Resistance x	Ω
Ru	Gas constant	$J\ mol^{-1}\ K^{-1}$
S	Sum of Squares	-
t	Time	s
T	Temperature	K
Z_x	Impedance x	Ω
Z'	Real component of impedance	$\Omega\ cm^2$
Z''	Imaginary component of impedance	$\Omega\ cm^2$
γ	Semi-infinite parameter	-
ϕ_1	Solid phase potential	V
ϕ_2	Electrolyte phase potential	V
ρ_1	Electrolyte resistivity	Ω cm
ρ_2	Electrode resistivity	Ω cm
λ	Complex decay length	cm
μ	Mean	-
σ	Standard deviation	-
ω	Angular frequency	$rad\ s^{-1}$
ω_1	Characteristic frequency	s^{-1}

Table A.3: Model Parameters (95% confidence intervals)

Treatment	Model	A_{eff} (cm^2)	i_0 ($\mu A\ cm^{-2}$)	a (μm)	P (x 10^{-1})	f (x 10^{-4})	L (H)
Raw	MHPE	86.8±2.3%	235.5±6.9%	20.0±7.4%	9.5±1.0%	32.6±6.6%	1.7e-07±242.5%
	RTS	85.9±3.6%	232.8±8.7%	20.1±8.2%	9.5±1.4%	32.5±7.4%	8.4e-07±497.9%
	RFS	83.9±2.7%	225.3±7.5%	20.2±7.8%	9.4±1.1%	32.1±6.8%	1.6e-08±975.4%
NAS	MHPE	99.0±0.9%	384.7±3.4%	21.0±7.7%	9.6±0.5%	122.6±6.5%	2.1e-07±75.3%
	RTS	97.4±1.3%	374.8±4.1%	21.4±9.1%	9.6±0.6%	122.9±7.5%	1.3e-27±5224.3%
	RFS	93.7±1.7%	350.2±5.4%	22.0±12.1%	9.4±0.8%	122.2±10.9%	1.4e-10±4469.4%
HtN	MHPE	157.6±1.1%	1114.3±4.9%	32.3±8.3%	9.6±0.7%	873.3±9.8%	2.2e-07±17.5%
	RTS	143.6±1.6%	1018.3±4.8%	33.2±8.8%	9.5±0.7%	874.5±8.5%	1.2e-22±2159.2%
	RFS	123.8±4.0%	677.6±14.7%	36.7±26.2%	8.8±2.1%	810.1±41.7%	2.5e-11±3826.1%
HyB	MHPE	668.1±1.4%	105.6±4.3%	32.6±11.3%	8.5±0.8%	90.3±10.8%	1.4e-07±40.2%
	RTS	629.0±2.7%	105.5±4.7%	32.8±10.7%	8.5±1.0%	92.6±10.1%	1.9e-08±3915.5%
	RFS	507.5±4.5%	74.6±12.1%	-	7.8±2.4%	-	3.9e-10±2379.3%
HyA	MHPE	1287.5±3.4%	155.0±12.3%	41.6±10.0%	8.5±2.3%	108.3±27.0%	1.4e-07±34.2%
	RTS	1181.8±11.4%	196.6±7.0%	39.9±5.1%	8.9±2.0%	122.0±13.1%	1.1e-06±1877.5%
	RFS	670.0±7.6%	89.3±22.0%	-	7.2±4.6%	-	3.8e-09±700.2%
HtO	MHPE	247.1±2.9%	1456.0±10.2%	37.6±5.8%	9.3±1.4%	646.7±10.6%	2.4e-07±14.0%
	RTS	190.4±5.4%	1595.9±10.5%	37.3±4.9%	9.2±1.6%	760.8±9.1%	1.8e-08±866.8%
	RFS	129.3±6.1%	682.2±21.5%	40.2±12.4%	8.0±3.2%	478.2±27.5%	2.5e-08±218.4%
Hyt	MHPE	335.6±5.2%	966.8±17.1%	37.6±6.9%	8.8±2.6%	353.5±16.4%	2.9e-07±18.6%
	RTS	227.3±7.5%	1104.3±18.5%	37.4±5.6%	8.8±3.1%	450.0±13.9%	4.5e-08±563.8%
	RFS	150.6±7.8%	463.7±20.9%	39.9±11.2%	7.5±3.5%	277.9±25.1%	1.2e-07±60.6%

Channel Electrode Analysis

Table A.4: Chapter 3 Nomenclature

Symbol	Description	Unit
A	Geometric surface area	cm^2
A_t	Wetted surface area	cm^2
A_{eff}	Effective surface area	cm^2
ASR_x	Area Specific Resistance x	$\Omega\ cm^2$
b	Electrode thickness	cm
C_{dl}	Area specific double layer capacitance	$F\ cm^{-2}$
C_{eff}	Effective Double Layer Capacitance	F
C_R	Concentration of reduced species	$mol\ cm^{-3}$
C_O	Concentration of oxidized species	$mol\ cm^{-3}$
d	Width of channel	cm
D_x	Diffusivity of species x	$cm^2\ s^{-1}$
F	Faraday Constant	$C\ mol^{-1}$
h	Half thickness of the electrode	cm
H	Impedance modulus	$\Omega\ cm^2$
f	Scale factor [38]	-
i_0	Exchange current density	$mA\ cm^{-2}$
j	Current density	$mA\ cm^{-2}$
J_{av}	Average diffusional flux to the electrode	$mol\ cm^{-2}$
l_e	Entry length	cm
L	Length of electrode	cm
n	Number of electrons transfered	-
p	Derivative of concentration with respect to ξ	mol
P	CPE exponent	-
Q	CPE parameter	F
R_x	Resistance x	Ω
Ru	Gas constant	$J\ mol^{-1}\ K^{-1}$
S	Sum of Squares	-
t	Time	s
T	Temperature	K
V_f	Volumetric flow rate	$cm^3\ s^{-1}$
V_O	Velocity in the center of the channel	$cm\ s^{-1}$
x	Length coordinate for channel electrode	cm
Z_x	Impedance x	Ω
Z'	Real component of impedance	$\Omega\ cm^2$
Z''	Imaginary component of impedance	$\Omega\ cm^2$
α	Transfer coefficient	-
δ_{eff}	Effective Nernstian diffusion layer thickness	cm
η_x	Overpotential associated with process x	V
γ	Semi-infinite parameter	-
Γ	Gamma function	-
λ	Complex decay length	cm
ν	Kinematic viscosity	$cm^2\ s^{-1}$
ω	Frequency	s^{-1}
ω_1	Characteristic frequency	s^{-1}

Diffusion layer thickness

From the geometric framework in which the Levich equation is solved in under limiting current conditions the length of the diffusion layer thickness as a function of distance along the channel ($\delta_d(x)$) is:

$$\delta_d(x) = \frac{\Gamma(\frac{1}{3})}{\sqrt[3]{6}}\left(\frac{xhD}{V_O}\right)^{\frac{1}{3}} \tag{A.45}$$

Integrating with respect to x and dividing by the length of the channel the average diffusion layer thickness is:

$$\begin{aligned}\delta_{mean} &= \frac{\Gamma(\frac{1}{3})}{L\sqrt[3]{6}}\left(\frac{hD}{V_O}\right)^{\frac{1}{3}}\int_0^L x^{\frac{1}{3}}dx \\ &= \frac{3\Gamma(\frac{1}{3})}{4\sqrt[3]{6}}\left(\frac{LhD}{V_O}\right)^{\frac{1}{3}}\end{aligned} \tag{A.46}$$

For a channel with a parabolic velocity profile integration across the cross sectional area of the channel yields the volumetric flow rate V_f:

$$\begin{aligned}V_f = V_O\int_0^d\int_0^{2h}\left(1-\frac{(y-h)^2}{h^2}\right)dydz \\ = \frac{4}{3}V_O hd\end{aligned} \tag{A.47}$$

From Equations A.46, 3.11 and 3.4 it is apparent that for a mass transport limiting case: $\mathbf{R_{fd}} \propto \mathbf{V_f}^{-\frac{1}{3}}$

Reynolds number and flow development

In the case of the channel electrode the Reynolds number is defined as:

$$Re = \frac{2hV_O}{\nu} \tag{A.48}$$

The entrance length is calculated by:

$$l_e = 0.1hRe \tag{A.49}$$

Table A.5 shows the values of the flow rates and the respective Reynolds numbers and entry lengths. The viscosity and density calculated by Mousa [233] and Skyllas-Kazakos [234] respectively were used (μ = 3.8 cP; ρ = 1.417 g/cm^3) to determine ν and equation 3.11 was used to approximate V_O.

We note in these instances, that because the laminar region atop the channel electrode is technically smaller for each increasing flow rate that the electrode dimensions are not identical. However, the trend is that both the electrode length is smaller and the diffusion layer thickness is smaller meaning that if the boundary layer thickness was not a function of the flow rate it would be larger for the increasing flow rates.

Kramers Kronig Analysis

Kramers-Kronig compliance was checked using the Z-HIT (Impedance Hilbert Transform) method. This method offers higher numerical stability by avoiding the need to extrapolate the impedance modulus to zero frequency and infinite fre-

Table A.5: Reynolds number and entry length for flow rates used in channel electrode experiments

Flow Rate (cm^3s^{-1})	Re	l_e (cm)
1/6	3.306	0.060
7/24	5.785	0.104
5/12	8.265	0.149
13/24	10.744	0.193
2/3	13.223	0.238

quency and instead evaluating a 'local impedance integral' [235].

$$ln|H(\omega_0)| \approx const + \frac{2}{\pi}\int_{\omega_S}^{\omega_0} \phi(\omega) dln(\omega) + \gamma \frac{d\phi(\omega_0)}{dln(\omega)} \tag{A.50}$$

Where $|H|$ is the impedance modulus, ω is angular frequency (rad s^{-1}), ω_0 is the angular frequency of interest and ω_S is the maximum angular frequency ϕ is the phase angle (rad).

Cyclic Voltammetry of N/S co-Doped GQD/GF electrode

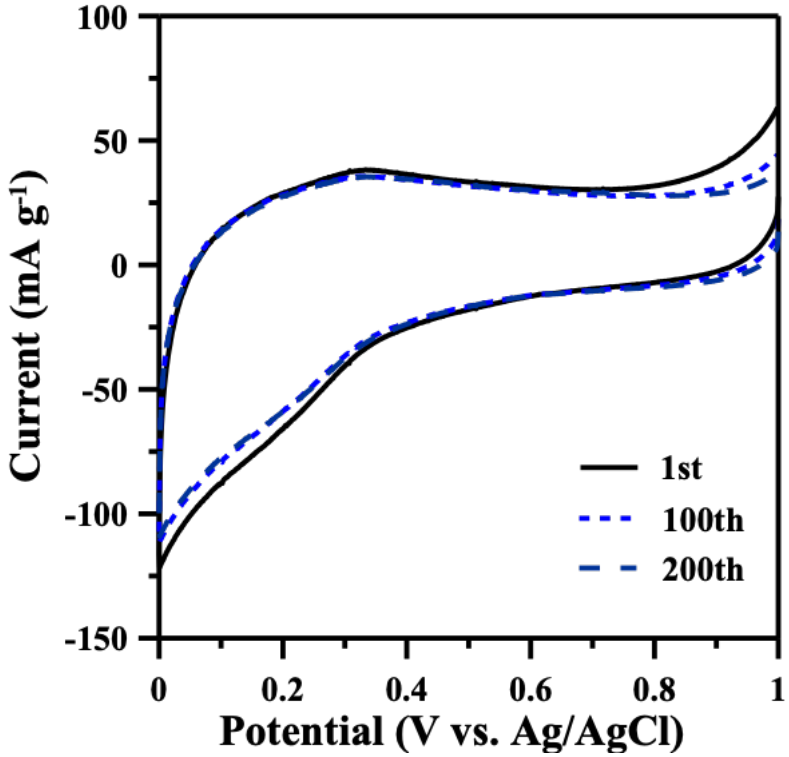

Figure A.2: CV profiles of N/S co-doped GQD/GF electrode in 1M H_2SO_4 under N_2 flow at 50 mV s^{-1}.

Acknowledgements: Financial support from the Ministry of Science and Technology of Taiwan (MOST 108-2221-E-155-036-MY3) is deeply acknowledged.

Supplemental materials for Chapter 4

Table A.6: Chapter 4 Nomenclature

Symbol	Description	Value	Unit
a	Diffusion layer thickness	*fit*	cm
A	Geometric surface area	5	cm^2
At	Total surface area of electrode	*fit*	cm^2
b	Electrode thickness (compressed)	.2	cm
C_{dl}	Specific double layer capacitance	2 x 10-5	F cm^{-2}
C_o	Concentration of oxidized species	.0005 mol	cm^{-3}
C_R	Concentration of reduced species	.0005 mol	cm^{-3}
D_O	Diffusivity of oxidized species	.57 x 10-6 [159]	cm^2 s^{-1}
D_R	Diffusivity of reduced species	1.1 x 10-6 [159]	cm^2 s^{-1}
f	Scale factor	*fit*	-
F	Faraday's constant	96,485	C mol^{-1}
i_0	Exchange current density	*fit*	A cm^{-2}
j	Imaginary unit	$\sqrt{-1}$	-
ω	Angular frequency	-	rad s^{-1}
P	Constant phase element exponent	*fit*	-
Q	CPE capacitance	A_t x C_{dl}	F
ρ_1	Specific ionic resistance	3.24 [236]	Ω cm
ρ_2	Specific electronic<tab>	.3	Ω cm
R	Gas constant	8.314	J K^{-1} mol^{-1}
T	Temperature<tab>	303.15	K
Z_p	Impedance of a single electrode	-	Ω
Z_i'	Real component of Z at frequency i	-	Ω
Z_i''	Imaginary component of Z at frequency i	-	Ω

Acknowledgements:

Financial support from the Ministry of Science and Technology of Taiwan (MOST 105-2628-E-155-002-MY3 and MOST 108-2221-E-155-036-MY3) is gratefully acknowledged.

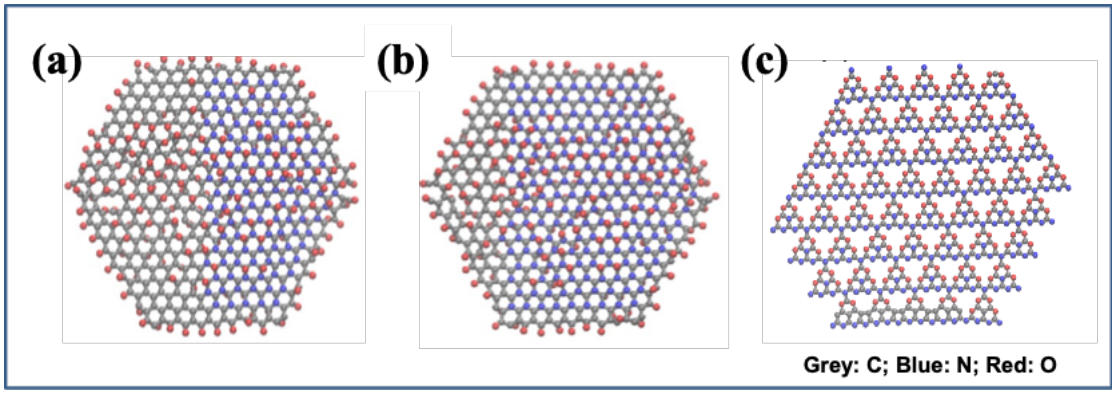

Figure A.3: The atomic configurations of (a) QD-1, (b) QD-2, and (c) QD-3 samples, simulated by LAAMPS [45].

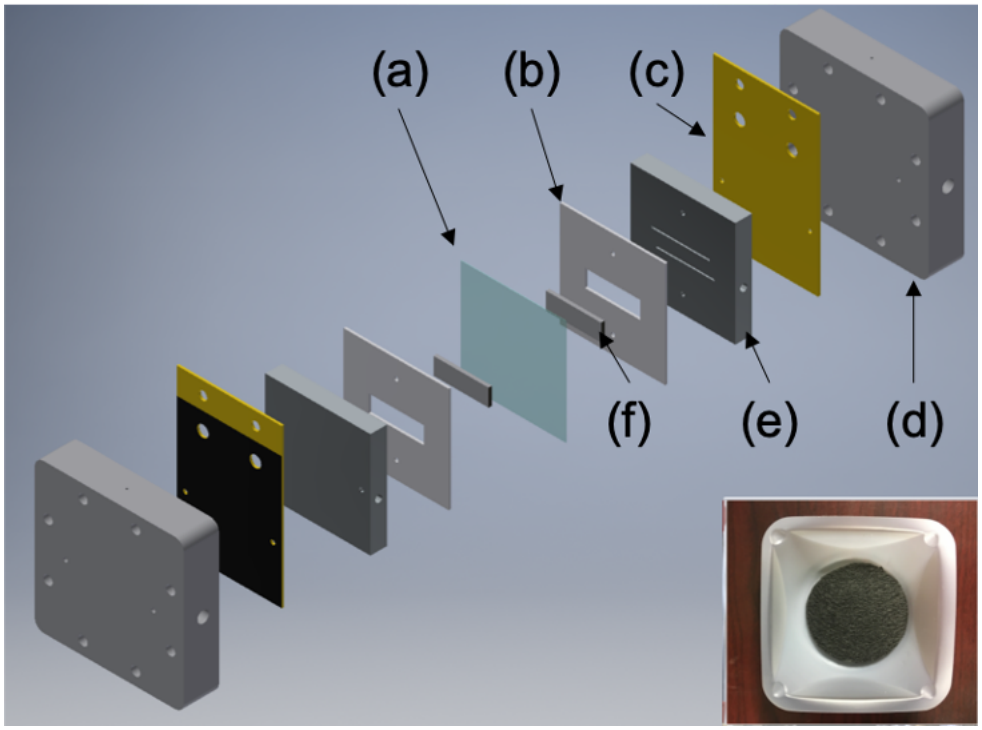

Figure A.4: Schematic of the VRFB. The components are (in clockwise order): (a) membrane, (b) gasket, (c) current collector, (d) end plate, (e) graphite plate, (f) electrode. The inset shows the GQD/GF electrode sheet.

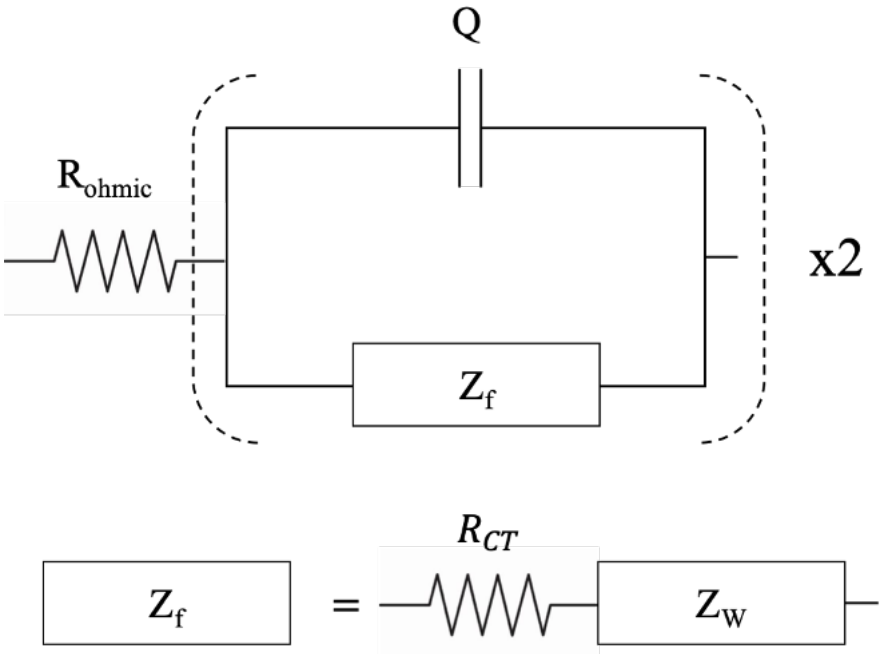

Figure A.5: Equivalent circuit proposed for describing the electrochemical impedance behavior of the symmetric cell VRFBs, where Rohmic, RCT, Zf, Zwarburg and Q components represent ohmic resistance, charge transfer resistance, faradaic impedance, Warburg impedance and constant phase element capacitance, respectively.

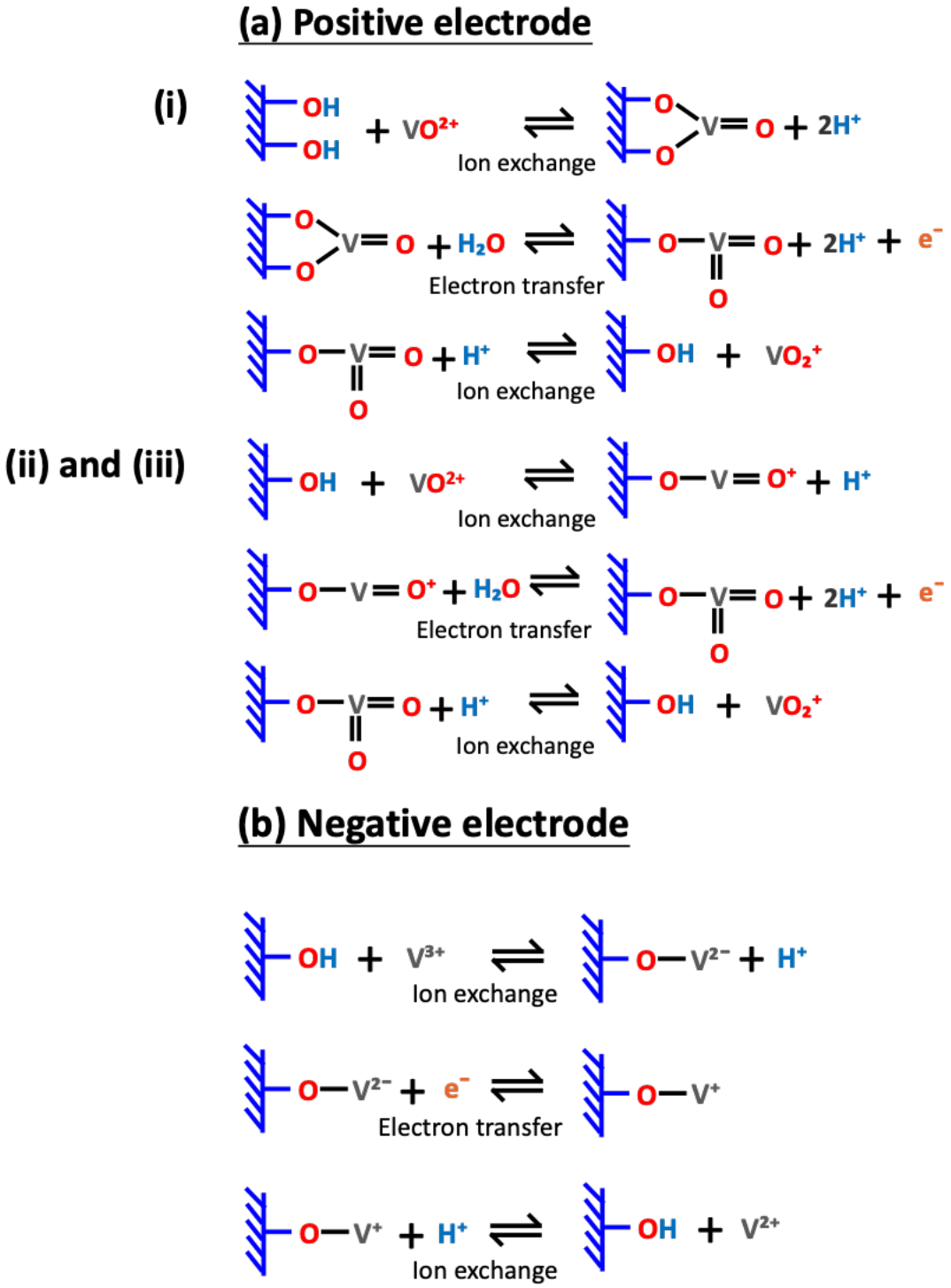

Figure A.6: Two sets of possible surface reaction steps at (a) positive and (b) negative GQD/GF electrodes of VRFBs [32,36].

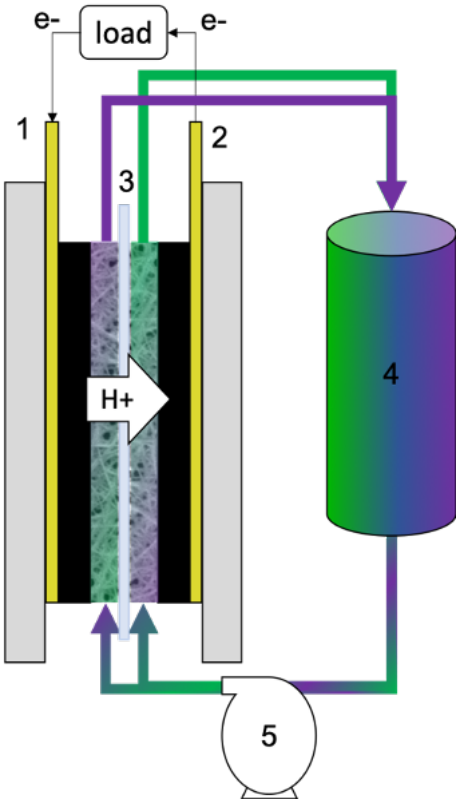

Figure A.7: Schematic of symmetric cell configuration. (1) and (2) are respectively the cathode and anode in this schematic [though these can be switched for the same operation] (3) is the point where the reference electrode contacts the cell, (4) is the electrolyte reservoir (50% SoC) and (5) is the pump.

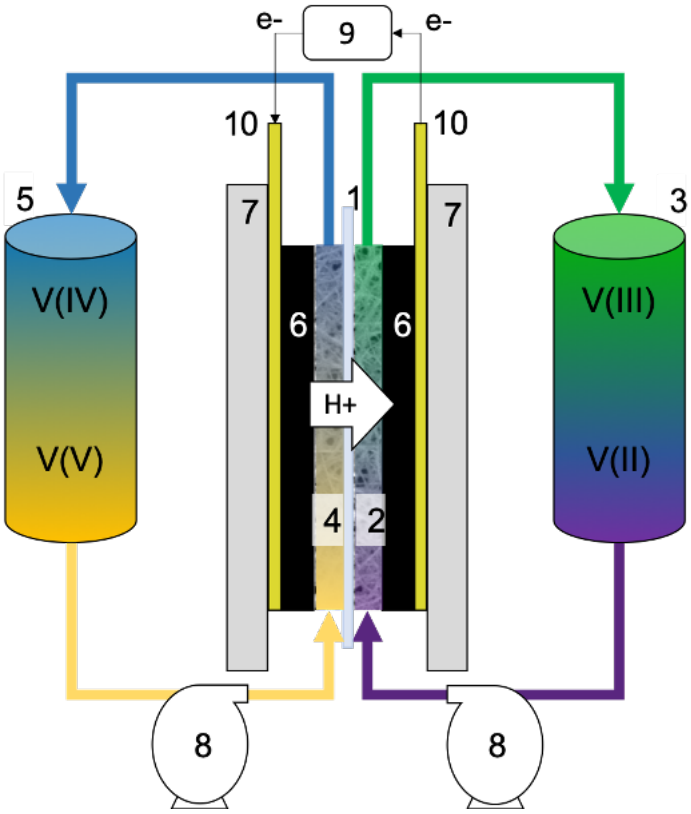

Figure A.8: Schematic of full cell configuration in discharge mode. (1) membrane/separator; (2) anode; (3) anolyte tank; (4) cathode; (5) catholyte tank; (6) graphite flow plates; (7) aluminum end plates; (8) pumps; (9) load (during discharge); (10) current collectors

Chapter 8 supplemental materials

Formulation for kang boundary on convex corner:

$$
\begin{cases}
g_{u_1,Red} - g_{kn_1,Red} + kC_{Red}^{\alpha} C_{Ox}^{1-\alpha}(exp((1-\alpha)\bar{\eta}) - exp(\alpha\bar{\eta})) = 0 \\
g_{u_2,Red} - g_{kn_2,Red} + kC_{Red}^{\alpha} C_{Ox}^{1-\alpha}(exp((1-\alpha)\bar{\eta}) - exp(\alpha\bar{\eta})) = 0 \\
g_{u_1,Ox} - g_{kn_1,Ox} - kC_{Red}^{\alpha} C_{Ox}^{1-\alpha}(exp((1-\alpha)\bar{\eta}) - exp(\alpha\bar{\eta})) = 0 \\
g_{u_2,Ox} - g_{kn_2,Ox} - kC_{Red}^{\alpha} C_{Ox}^{1-\alpha}(exp((1-\alpha)\bar{\eta}) - exp(\alpha\bar{\eta})) = 0 \\
g_{u_1,Red} + g_{kn_1,Red} + g_{u_2,Red} + g_{kn_2,Red} - (1-J_0)C_{Red} = 0 \\
g_{u_1,Ox} + g_{kn_1,Ox} + g_{u_2,Ox} + g_{kn_2,Ox} - (1-J_0)C_{Ox} = 0
\end{cases}
\tag{A.51}
$$

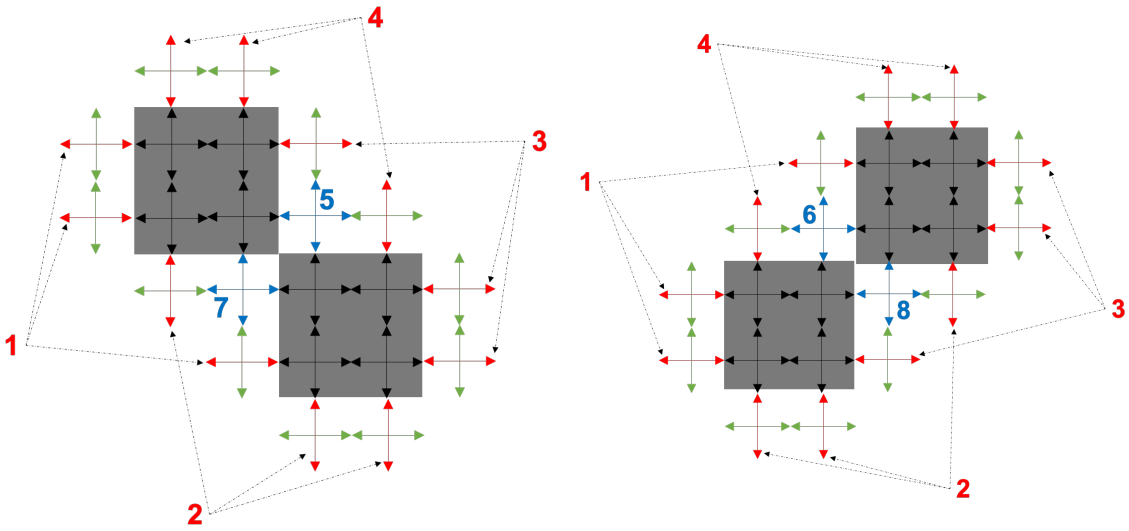

Figure A.9: Schematic of electrochemical boundary identification. Edges are shown in red, (1,2,3,4). The direction of unknown correspond with the directions from the D2Q5 lattice in Figure 8.1. Convex corners (5,6,7,8) are shown in blue.

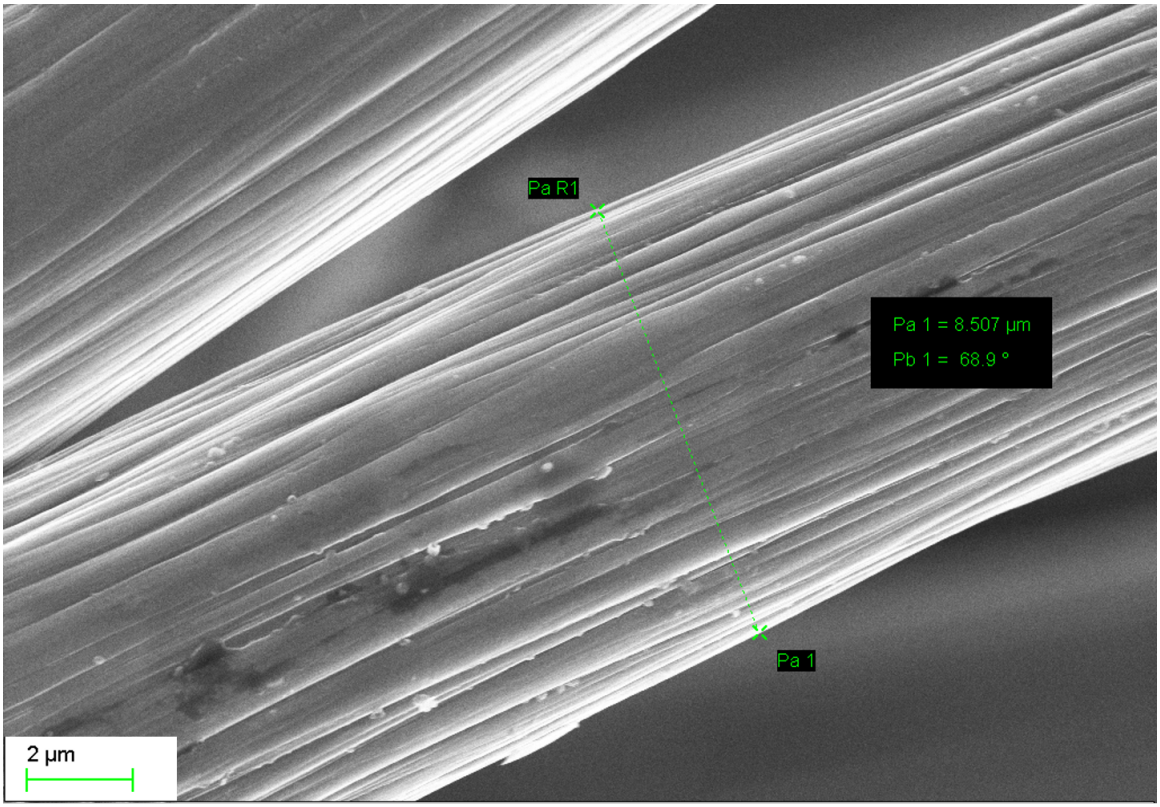

Figure A.10: SEM image of typical GFD3 fiber.

Table A.7: Parameters used for Figure 8.2

Symbol	Value	Unit
n_x	100	lattice unit
n_y	80	lattice unit
C_1	10	mol lattice unit^{-3}
C_{eq}	1	mol lattice unit^{-3}
Da	3 and 30	-
D	.5	lattice unit^2 lattice time step^{-1}

Table A.8: Parameters used for Figure 8.2

Symbol	Value	Unit
C_{in}	1	mol $\cdot$ lattice unit^{-3}
L_x	1	lattice unit
L_y	1	lattice unit
k	∞	lattice unit $\cdot$ lattice time^{-1}
n_x	320	lattice unit
n_y	320	lattice unit
u_{max}	.0086	lattice unit $\cdot$ lattice time^{-1}
τ	.5276	-

Table A.9: Chapter 8 Nomenclature

Symbol	Description	Expression/Value
$C_{Ox/Red}$	Concentration of Oxidized / Reduce species	-
$\bar{C}$	Dimensionless concentration	$\frac{C}{C_{ref}}$
D	Physical Diffusion coefficient	2.4×10^{-10} m^2s^{-1}
Da	Damkohler number	$\frac{kL}{D}$
L	Characteristic length	200 μm
Re	Reynolds number	$\frac{uL}{\nu}$
SoC	State of charge	(anode) $= \frac{C_{Red}}{C_{Red}+C_{Ox}}$
V_f	Volumetric flow rate	20 mL min^{-1}
$g_{kn_x,Red/Ox}$	Known entering stream of Reduced distribution	-
$g_{u_x,Red/Ox}$	Unknown entering stream of reduced/oxidized distribution	-
k	Rate constant	1.7×10^{-7} ms^{-1}
n_x	Lattice units in x-direction	201
n_y	Lattice units in y-direction	201
τ	Relaxation time	1.0
ν	Kinematic viscosity	4.9×10^{-6} m^2s^{-1}; [85]
α	Transfer coefficient	0.5
J_0	Rest fraction	.9
$\bar{\eta}$	Dimensionless overpotential	$\frac{F\eta}{R_uT}$
c_s	Lattice speed of sound	$3^{-1/2}$
c_i	Lattice speed in direction i	Equation 8.6
δx	Spatial step	1 lattice unit
δt	Time step	1 lattice time unit

Chapter 9 supplemental

Table A.10: Strip cell analysis data (from ref [231])

Channel Depth (mm)	Flow Rate (mL min^{-1})	Limiting Current (A cm^{-2})	Pressure drop (Pa)
2.5	10	0.1291	2433
	20	0.1528	5114
	30	0.1825	8029
	40	0.2044	11167
	50	0.2337	14510
1.0	10	0.1419	3157
	20	0.2044	6726
	30	0.2633	10693
	40	0.3161	15065
	50	0.3754	19838
0.5	10	0.3638	6992
	20	0.5424	15725
	30	0.5939	26307
	40	0.7513	38666
	50	0.8704	52679
0.25	10	1.0791	32264
	20	1.342	72569
	30	1.5150	122290

Table A.11: Chapter 9 Nomenclature

Symbol	Description	Units
A	Geometric surface area	cm^2
C	Concentration	mol cm^{-3}
D	Diffusion coefficient	cm^2 s^{-1}
F	Faraday's Constant	C mol^{-1}
V_f	Volumetric flow rate	cm^{-3} s^{-1}
V_d	Discharging Voltage	V
V_c	Charging Voltage	V
n	Number of electrons transferred	-
i_c	Charging current	A cm^{-2}
i_d	Discharging current	A cm^{-2}
i_{lim}	Limiting current	A cm^{-2}
t_c	Charging time	s
t_d	Discharging time	s
δ	Diffusion layer thickness	cm
ΔP	Pressure drop	J cm^{-3}

Chapter 6 supplemental

Error analysis

While two membranes were utilized, the Nernst equation has very low sensitivity to SoC for most of the central SoC range (< 5 mV $\%^{-1}$ from 12% - 88%). For this reason the lower concentration electrolytes experienced larger fluctuations in measured open circuit potential than the 1.5 M V necessitating error bars for the composition. The horizontal error bars for the experimental data were calculated based on normalizing the open circuit voltage to the 1.5 M V case.

$$\Delta SoC = SoC_{theoretical} - SoC_{1.5M}(OCV_{experiment}) \tag{A.52}$$

Here $SoC_{1.5M}$ represents a function that returns the cubic spline interpolation of the voltage for the 1.5 M V case across the SoC range. The 1.5 M V case had the lowest variation in its OCV and was most in-line with experimental open circuit voltages, which is why it was utilized as the base-case as opposed to the Nernst equation which differs from experimental OCVs at 50% SoC by around 90 mV. The vertical error bars were calculated by taking the difference between the two experiments.

Supplemental EIS information

The distributed ASR magnitude is determined by taking the limit of 6.1 as the frequency goes to ∞.

$$\frac{ASR_{distributed}}{A} = b\frac{\rho_1 + \rho_2}{3} + b\frac{\rho_1\rho_2}{3(\rho_1 + \rho_2)} \tag{A.53}$$

The ohmic ASR is then the sum of this resistance and the serial ohmic resistance (primarily the membrane).

$$ASR_{ohmic} = ASR_{distributed} + ASR_{series} \tag{A.54}$$

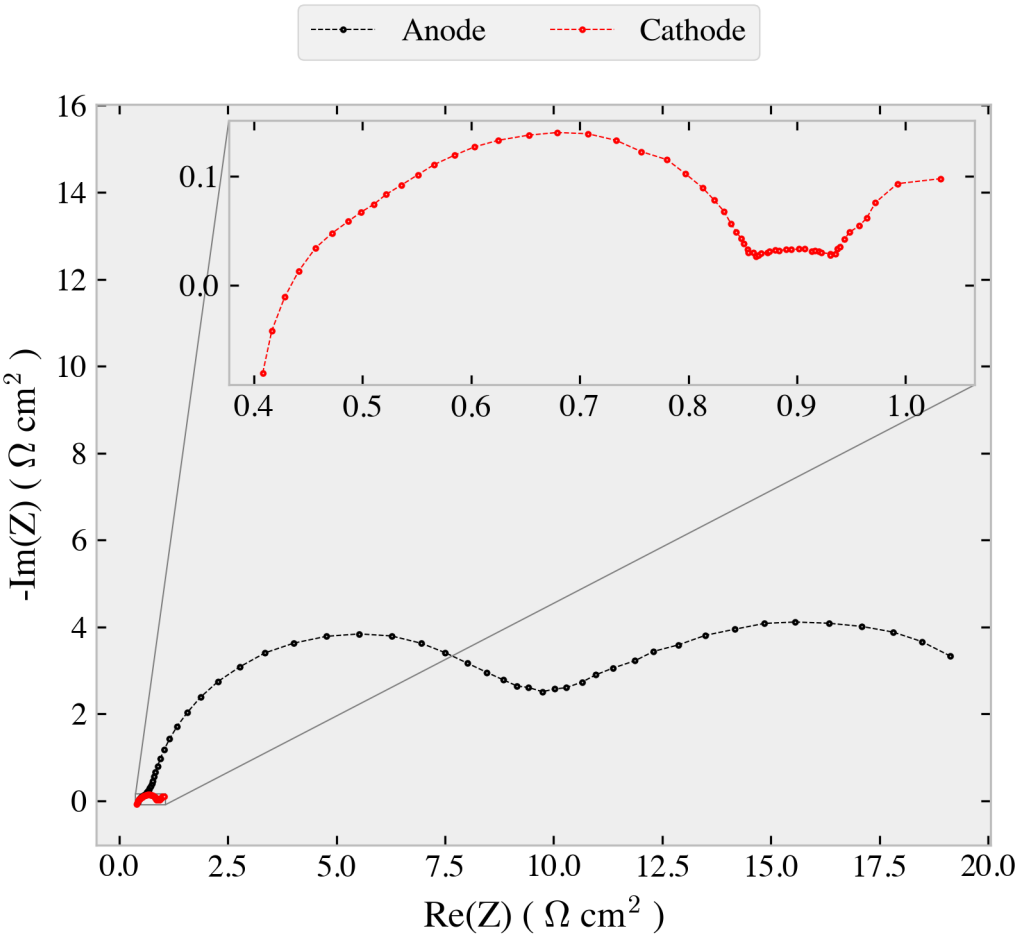

Figure A.11: Cathode and anode impedance spectra at open circuit (90% So; 0.5 M V))

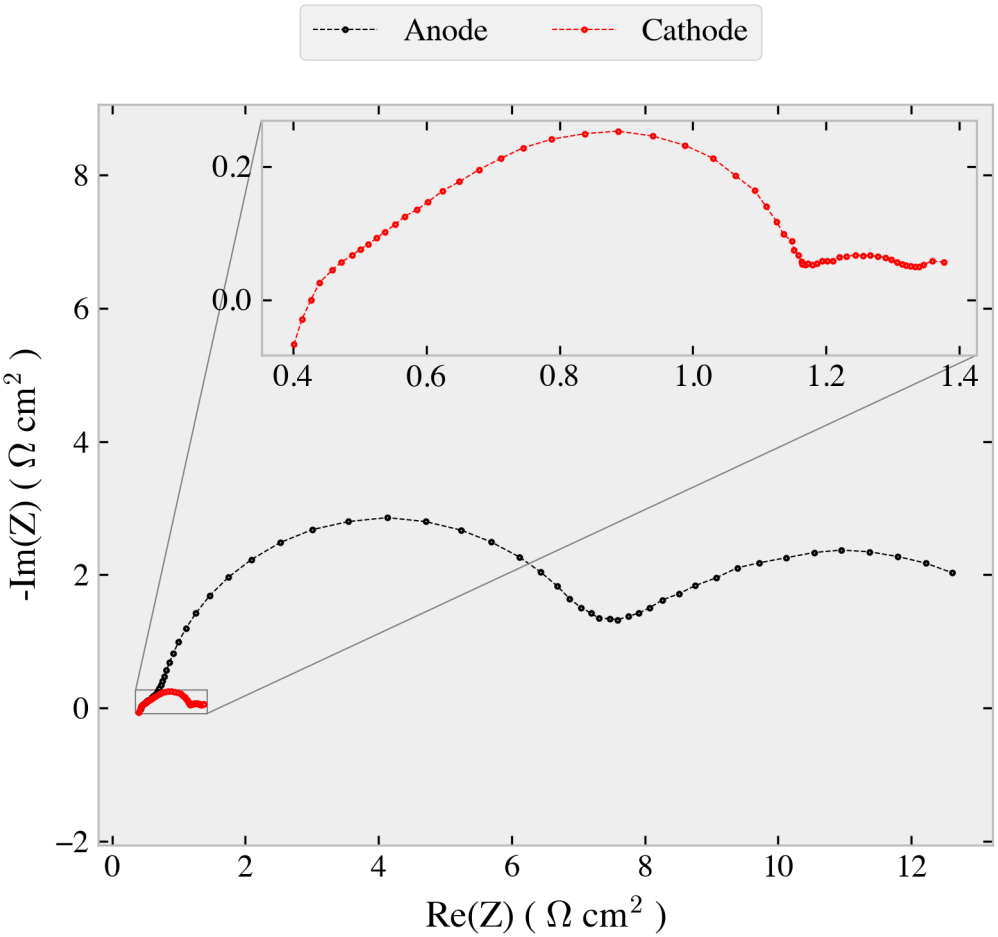

Figure A.12: Cathode and anode impedance spectra at open circuit (50% SoC; 0.5 M V)

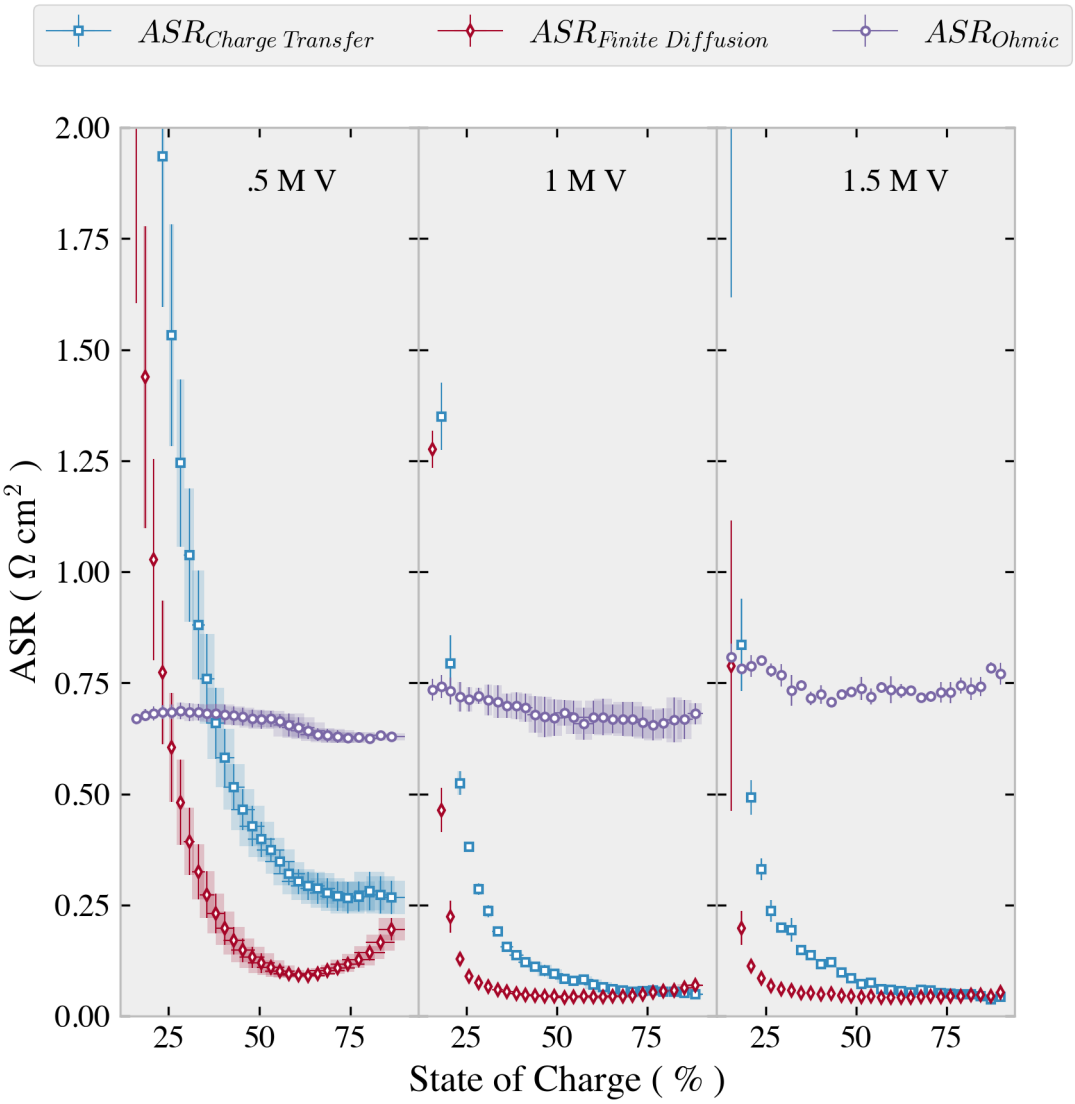

Figure A.13: ASR components for the cathode as a function of SoC.

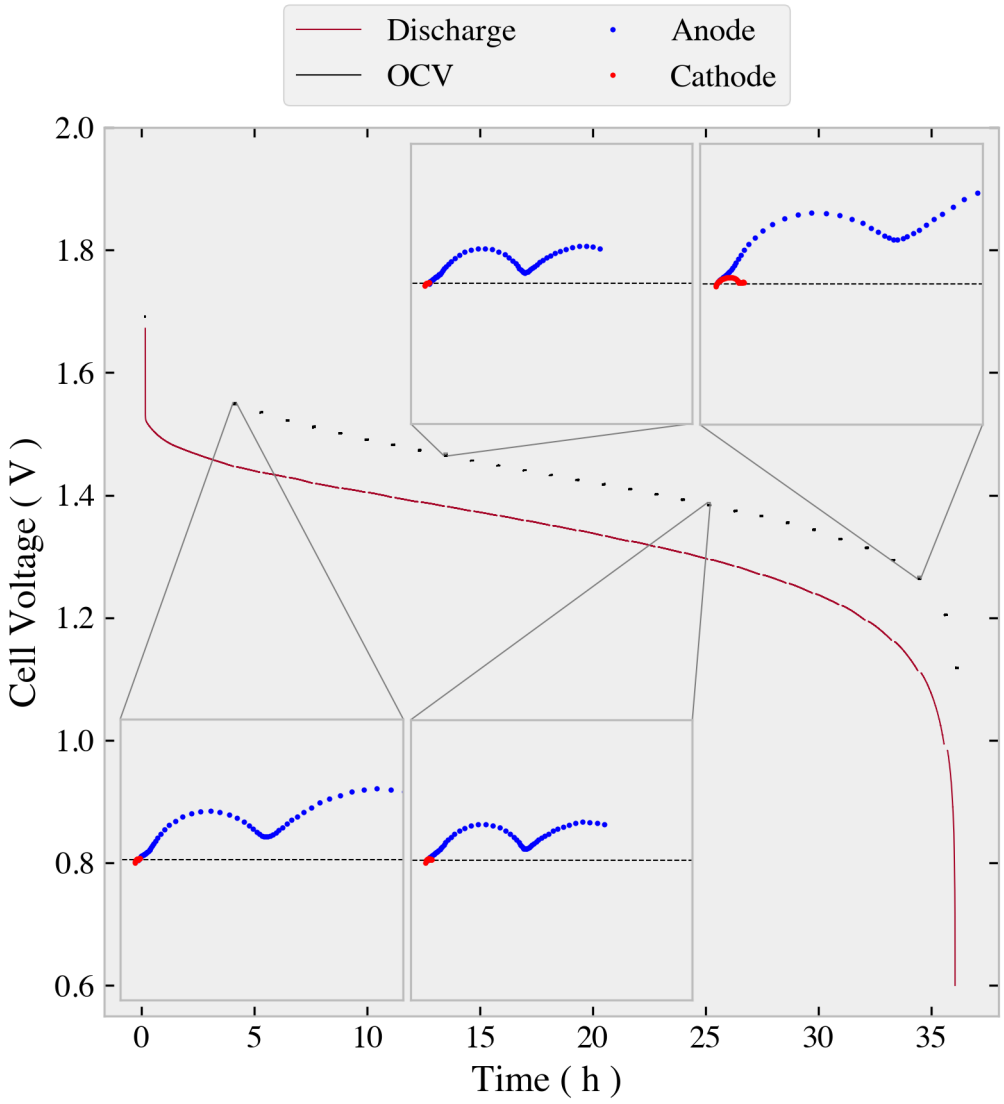

Figure A.14: Experimental profile with OCV and discharge steps labeled. Spectra shown in blue are the measured anode spectrum in the symmetric cell, while spectra in red are the cathode symmetric cell.

Chapter 7 supplemental

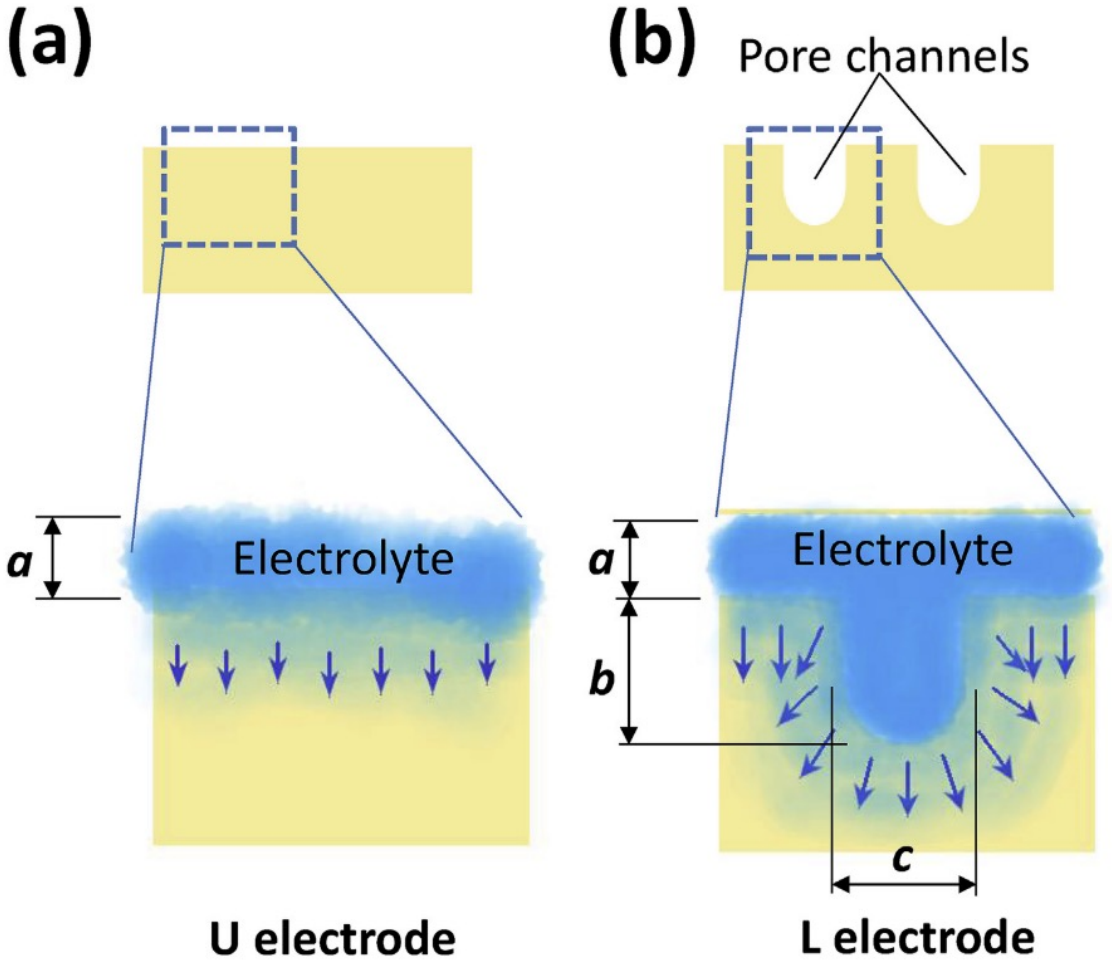

Figure A.15: Schematic diagram of electrolyte wetting on (a) U and (b) L electrodes, where a, b, and c represent original penetration depth, height, and width of pore channel, respectively. The pore channels, created by the laser treatment, allow more electrolyte diffusion, creating more reactive sites and promoting chemical reaction kinetics in VRFBs.

Sensitivity of the Randles Circuit

The complex coupling of ohmic, kinetics and mass transfer processes, which occur when electrochemical systems are polarized, Electrochemical impedance spectroscopy is one of the most common diagnostic techniques used in characterizing electrochemical systems e.g. supercapacitors, batteries, membranes, fuel cells. This is due to it being unobtrusive and providing a quantitative holistic (macro) representation of a system and the processes occurring [109, 118, 237]. Using equivalent circuit models, particularly the Randles circuit, pervades the literature of vanadium redox flow batteries e.g. [35, 98, 238, 239]; however, robust treatment of the sensitivity of parameters, which are estimated with this technique, are often discussed only qualitatively and not quantitatively. The Randles circuit is a physics-based model where the electrochemical processes are associated specifically with When this method is used strictly to estimate the magnitude of area specific resistances in a system, this is relatively unimportant, however for parameter estimation, it is nontrivial. Constant phase elements (CPE) are commonly used to model a dispersion of time constants which occur in porous media [39, 201]. This is a fitting parameter that can take values between 0 and 1 and

Sensitivity analysis gives a quantitative representation of the sensitivity of a model to each of its parameters as a function of frequency. This is helpful in elucidating what set of parameters can be fit in a least squares regression and at what frequencies a model has high or low sensitivity to each parameter.

Theory

First the terms involved in the single electrode models ($Z_{randles}$ and Z_{MHPE}) are defined, followed by their sensitivity coefficients.

Randles Circuit

The charge transfer resistance is defined as [20]:

$$R_{ct} = \frac{RT}{nFi_0} \tag{A.55}$$

The warburg element is defined as [38]:

$$Z_w = \frac{RT \tanh\left(a\sqrt{\frac{j\omega}{D_R}}\right)}{fC_R F^2 \sqrt{jD_R\omega}} + \frac{RT \tanh\left(a\sqrt{\frac{j\omega}{D_O}}\right)}{fC_O F^2 \sqrt{jD_O\omega}} \tag{A.56}$$

The charge transfer impedance (Z_f) is then the sum of the charge transfer resistance and the Warburg impedance.

$$Z_f = R_{ct} + Z_w \tag{A.57}$$

The impedance of a single electrode is then the parallel combination of a constant phase element and the charge transfer impedance:

$$Z_{Randles} = \left(C_{dl}\left(i\omega\right)^P + Z_f^{-1}\right)^{-1} \tag{A.58}$$

The macrohomogeneous porous electrode model uses the same randles circuit

(Equation A.58) in its formulation, however, it takes into account the electrolyte and electrode resistivities (ρ_1 and ρ_2). The term Q_2 (Equation A.59) has several different formulations in the literature which are all equivalent in the MHPE model. Nguyen and co. workers cast this term as the ratio of the characteristic length (b) and the complex decay length (λ) which is a measure of the length (cm) that the signal can penetrate through the electrode ($Q_2 = \frac{b}{\lambda}$) [96]. Paasch *et al.* represent this term as the product of the characteristic length (b) and the parameter β, which is the inverse of the complex decay length ($Q_2 = b\beta$). Sun *et al* use the symbol Q_2 to represent this value, which is used herein [38].

$$Q_2 = \sqrt{\frac{A_t b\left(\rho_1 + \rho_2\right)}{A Z_{Randles}}} \tag{A.59}$$

The MHPE is then [38, 39, 95, 96]:

$$Z_{MHPE} = \frac{b\rho_1\rho_2}{\rho_1 + \rho_2} + \frac{2b\rho_1\rho_2}{Q_2\left(\rho_1 + \rho_2\right)\sinh\left(Q_2\right)} + \frac{b\left(\rho_1^2 + \rho_2^2\right)\coth\left(Q_2\right)}{Q_2\left(\rho_1 + \rho_2\right)} \tag{A.60}$$

Impedance Response of the Symmetric Cell

For the symmetric cell, the response that is measured across the whole cell is then two times the response of a single electrode ($Z_{electrode} \in [Z_{Randles}, Z_{MHPE}]$)plus the membrane resistance and an inductance:

$$AZ_{cell} = \frac{2A}{At} Z_{electrode} + ASR_{mem} + AjL\omega \tag{A.61}$$

Sensitivity Coefficient

Define the sensitivity coefficient ($U(\omega; \hat{q})$) as the partial derivative of the dependent variable with respect to its parameters [240]. ω is independent and $\hat{q}$ is a model parameter ($\hat{q} \in [i_0, A_t, P, f, ASR_{mem}, a, C_O, D_O, C_R, D_R]$):

$$U(AZ_{cell}; \hat{q}) = \frac{\partial Z_{cell}}{\partial \hat{q}} \tag{A.62}$$

U represents the change of the dependent variable Z_{cell} to a change in model parameters. Note that the units of U are not $\Omega\ cm^2$, but instead $\frac{\Omega\ cm^2}{\hat{q}_{unit}}$. For this reason it is helpful to normalize U by the magnitude of $\hat{q}$ in order to compare the sensitivities in similar units. The sensitivity coefficients for the Randles circuit and MHPE models are shown in 10.2.

Sensitivity Coefficients

Randles circuit electrode model

$$U(AZ_{cell}; i_0) = -\frac{2AR_{ct}Z^2_{Randles}}{A_t Z_f^2 i_0} \tag{A.63}$$

$$U(AZ_{cell}; A_t) = -\frac{2AZ_{Randles}}{A_t^2} \tag{A.64}$$

$$U(AZ_{cell}; P) = -\frac{2AC_{dl}Z^2_{Randles}\,(j\omega)^P \log(j\omega)}{A_t} \tag{A.65}$$

$$U(AZ_{cell};f) = -\frac{2AZ^2_{Randles}\left(\frac{RT\tanh\left(a\sqrt{\frac{j\omega}{D_R}}\right)}{f^2C_RF^2\sqrt{jD_R\omega}} + \frac{RT\tanh\left(a\sqrt{\frac{j\omega}{D_O}}\right)}{f^2C_OF^2\sqrt{jD_O\omega}}\right)}{A_tZ_f^2} \tag{A.66}$$

$$U(AZ_{cell};a) = -\frac{2AZ^2_{Randles}\left(-\frac{RT\sqrt{\frac{j\omega}{D_R}}\left(-\tanh^2\left(a\sqrt{\frac{j\omega}{D_R}}\right)+1\right)}{fC_RF^2\sqrt{jD_R\omega}} - \frac{RT\sqrt{\frac{j\omega}{D_O}}\left(-\tanh^2\left(a\sqrt{\frac{j\omega}{D_O}}\right)+1\right)}{fC_OF^2\sqrt{jD_O\omega}}\right)}{A_tZ_f^2} \tag{A.67}$$

$$U(AZ_{cell}ASR_{mem}) = 1 \tag{A.68}$$

$$U(AZ_{cell};L) = Aj\omega \tag{A.69}$$

$$U(AZ_{cell};C_O) = -\frac{2ARTZ^2_{Randles}\tanh\left(a\sqrt{\frac{j\omega}{D_O}}\right)}{fA_tC_O^2F^2Z_f^2\sqrt{jD_O\omega}} \tag{A.70}$$

$$U(AZ_{cell};D_O) = -\frac{2AZ^2_{Randles}\left(\frac{0.5RTa\sqrt{\frac{j\omega}{D_O}}\left(-\tanh^2\left(a\sqrt{\frac{j\omega}{D_O}}\right)+1\right)}{fC_OD_OF^2\sqrt{jD_O\omega}} + \frac{0.5RT\tanh\left(a\sqrt{\frac{j\omega}{D_O}}\right)}{fC_OD_OF^2\sqrt{jD_O\omega}}\right)}{A_tZ_f^2} \tag{A.71}$$

Macrohomogeneous porous electrode model

Several of the sensitivity coefficients that involve the charge transfer impedance (Equation A.57) have the additional partial derivatives defined in order to simplify the representation of their expression. Equations A.72,A.74 and A.73 use the variable σ with their respective parameter subscripts to indicate the partial derivative of the warburg element with respect to that variable.

$$\sigma_a = \frac{\partial Z_f}{\partial a} = \frac{RT\sqrt{\frac{j\omega}{D_R}}\left(1-\tanh^2\left(a\sqrt{\frac{j\omega}{D_R}}\right)\right)}{fA_tC_RF^2\sqrt{jD_R\omega}} + \frac{RT\sqrt{\frac{j\omega}{D_O}}\left(1-\tanh^2\left(a\sqrt{\frac{j\omega}{D_O}}\right)\right)}{fA_tC_OF^2\sqrt{jD_O\omega}} \tag{A.72}$$

$$\sigma_{D_O} = \frac{\partial Z_f}{\partial D_O} = -\frac{RTa\sqrt{\frac{j\omega}{D_O}}\left(1-\tanh^2\left(a\sqrt{\frac{j\omega}{D_O}}\right)\right)}{2fC_OD_OF^2\sqrt{jD_O\omega}} - \frac{RT\tanh\left(a\sqrt{\frac{j\omega}{D_O}}\right)}{2fC_OD_OF^2\sqrt{jD_O\omega}} \tag{A.73}$$

$$\sigma_f = \frac{\partial Z_f}{\partial f} = -\frac{RT\tanh\left(a\sqrt{\frac{j\omega}{D_R}}\right)}{A_tf^2C_RF^2\sqrt{jD_R\omega}} - \frac{RT\tanh\left(a\sqrt{\frac{j\omega}{D_O}}\right)}{A_tf^2C_OF^2\sqrt{jD_O\omega}} \tag{A.74}$$

The sensitivity coefficients are:

$$
\begin{aligned}
U(\omega;a) = & \frac{2bk_\omega\rho_1\rho_2\cosh\left(\frac{b}{\lambda}\right)}{Z_f\left(k_\omega+(j\omega)^P\right)(\rho_1+\rho_2)\sinh^2\left(\frac{b}{\lambda}\right)}\sigma_a \\
& + \frac{bk_\omega\left(\rho_1^2+\rho_2^2\right)}{Z_f\left(k_\omega+(j\omega)^P\right)(\rho_1+\rho_2)\sinh^2\left(\frac{b}{\lambda}\right)}\sigma_a \\
& + \frac{2k_\omega\lambda\rho_1\rho_2}{Z_f\left(k_\omega+(j\omega)^P\right)(\rho_1+\rho_2)\sinh\left(\frac{b}{\lambda}\right)}\sigma_a \\
& + \frac{k_\omega\lambda\left(\rho_1^2+\rho_2^2\right)\coth\left(\frac{b}{\lambda}\right)}{Z_f\left(k_\omega+(j\omega)^P\right)(\rho_1+\rho_2)}\sigma_a
\end{aligned}
\tag{A.75}
$$

$$
U(\omega;ASR_{mem}) = 1 \tag{A.76}
$$

$$
\begin{aligned}
U(\omega;A_t) = & -\frac{4Ab^2\rho_1\rho_2\cosh\left(\frac{b}{\lambda}\right)}{2AbA_t(\rho_1+\rho_2)\sinh^2\left(\frac{b}{\lambda}\right)} \\
& - \frac{2Ab^2\left(\rho_1^2+\rho_2^2\right)}{2AbA_t(\rho_1+\rho_2)\sinh^2\left(\frac{b}{\lambda}\right)} \\
& - \frac{4Ab\lambda\rho_1\rho_2}{2AbA_t(\rho_1+\rho_2)\sinh\left(\frac{b}{\lambda}\right)} \\
& - \frac{2Ab\lambda\left(\rho_1^2+\rho_2^2\right)\coth\left(\frac{b}{\lambda}\right)}{2AbA_t(\rho_1+\rho_2)}
\end{aligned}
\tag{A.77}
$$

$$
\begin{aligned}
U(\omega;C_O) = &-\frac{2RTbk_\omega\rho_1\rho_2\cosh\left(\frac{b}{\lambda}\right)\tanh\left(a\sqrt{\frac{j\omega}{D_O}}\right)}{fA_tC_O^2F^2Z_f\sqrt{jD_O\omega}\left(k_\omega+(j\omega)^P\right)(\rho_1+\rho_2)\sinh^2\left(\frac{b}{\lambda}\right)} \\
&-\frac{RTbk_\omega\left(\rho_1^2+\rho_2^2\right)\tanh\left(a\sqrt{\frac{j\omega}{D_O}}\right)}{fA_tC_O^2F^2Z_f\sqrt{jD_O\omega}\left(k_\omega+(j\omega)^P\right)(\rho_1+\rho_2)\sinh^2\left(\frac{b}{\lambda}\right)} \\
&-\frac{2RTk_\omega\lambda\rho_1\rho_2\tanh\left(a\sqrt{\frac{j\omega}{D_O}}\right)}{fA_tC_O^2F^2Z_f\sqrt{jD_O\omega}\left(k_\omega+(j\omega)^P\right)(\rho_1+\rho_2)\sinh\left(\frac{b}{\lambda}\right)} \\
&-\frac{RTk_\omega\lambda\left(\rho_1^2+\rho_2^2\right)\tanh\left(a\sqrt{\frac{j\omega}{D_O}}\right)\coth\left(\frac{b}{\lambda}\right)}{fA_tC_O^2F^2Z_f\sqrt{jD_O\omega}\left(k_\omega+(j\omega)^P\right)(\rho_1+\rho_2)}
\end{aligned}
\tag{A.78}
$$

$$
\begin{aligned}
U(\omega;C_dl) = &-\frac{4Ab^2\rho_1\rho_2\left(\frac{A_t\left(k_\omega+(j\omega)^P\right)(\rho_1+\rho_2)}{2Ab}+\frac{G_{ct}(-\rho_1-\rho_2)}{2AC_{dl}}\right)\cosh\left(\frac{b}{\lambda}\right)}{A_tC_{dl}\left(k_\omega+(j\omega)^P\right)(\rho_1+\rho_2)^2\sinh^2\left(\frac{b}{\lambda}\right)} \\
&-\frac{2Ab^2\left(\rho_1^2+\rho_2^2\right)\left(\frac{A_t\left(k_\omega+(j\omega)^P\right)(\rho_1+\rho_2)}{2Ab}+\frac{G_{ct}(-\rho_1-\rho_2)}{2AC_{dl}}\right)}{A_tC_{dl}\left(k_\omega+(j\omega)^P\right)(\rho_1+\rho_2)^2\sinh^2\left(\frac{b}{\lambda}\right)} \\
&+\frac{4Ab\lambda\rho_1\rho_2\left(-\frac{A_t\left(k_\omega+(j\omega)^P\right)(\rho_1+\rho_2)}{2Ab}+\frac{G_{ct}(\rho_1+\rho_2)}{2AC_{dl}}\right)}{A_tC_{dl}\left(k_\omega+(j\omega)^P\right)(\rho_1+\rho_2)^2\sinh\left(\frac{b}{\lambda}\right)} \\
&+\frac{2Ab\lambda\left(\rho_1^2+\rho_2^2\right)\left(-\frac{A_t\left(k_\omega+(j\omega)^P\right)(\rho_1+\rho_2)}{2Ab}+\frac{G_{ct}(\rho_1+\rho_2)}{2AC_{dl}}\right)\coth\left(\frac{b}{\lambda}\right)}{A_tC_{dl}\left(k_\omega+(j\omega)^P\right)(\rho_1+\rho_2)^2}
\end{aligned}
\tag{A.79}
$$

$$
\begin{aligned}
U(\omega; D_O) = & \frac{2bk_\omega\rho_1\rho_2 \cosh\left(\frac{b}{\lambda}\right)}{Z_f\left(k_\omega + (j\omega)^P\right)(\rho_1+\rho_2)\sinh^2\left(\frac{b}{\lambda}\right)}\sigma_{D_O} \\
& + \frac{bk_\omega\left(\rho_1^2+\rho_2^2\right)}{Z_f\left(k_\omega + (j\omega)^P\right)(\rho_1+\rho_2)\sinh^2\left(\frac{b}{\lambda}\right)}\sigma_{D_O} \\
& + \frac{2k_\omega\lambda\rho_1\rho_2}{Z_f\left(k_\omega + (j\omega)^P\right)(\rho_1+\rho_2)\sinh\left(\frac{b}{\lambda}\right)}\sigma_{D_O} \\
& + \frac{k_\omega\lambda\left(\rho_1^2+\rho_2^2\right)\coth\left(\frac{b}{\lambda}\right)}{Z_f\left(k_\omega + (j\omega)^P\right)(\rho_1+\rho_2)}\sigma_{D_O}
\end{aligned}
\tag{A.80}
$$

$$
\begin{aligned}
U(\omega; f) = & \frac{2bk_\omega\rho_1\rho_2 \cosh\left(\frac{b}{\lambda}\right)}{Z_f\left(k_\omega + (j\omega)^P\right)(\rho_1+\rho_2)\sinh^2\left(\frac{b}{\lambda}\right)}\sigma_f \\
& + \frac{bk_\omega\left(\rho_1^2+\rho_2^2\right)}{Z_f\left(k_\omega + (j\omega)^P\right)(\rho_1+\rho_2)\sinh^2\left(\frac{b}{\lambda}\right)}\sigma_f \\
& + \frac{2k_\omega\lambda\rho_1\rho_2}{Z_f\left(k_\omega + (j\omega)^P\right)(\rho_1+\rho_2)\sinh\left(\frac{b}{\lambda}\right)}\sigma_f \\
& + \frac{k_\omega\lambda\left(\rho_1^2+\rho_2^2\right)\coth\left(\frac{b}{\lambda}\right)}{Z_f\left(k_\omega + (j\omega)^P\right)(\rho_1+\rho_2)}\sigma_f
\end{aligned}
\tag{A.81}
$$

$$
\begin{aligned}
U(\omega;i_0) = &-\frac{2R_{ct}bk_\omega\rho_1\rho_2\cosh\left(\frac{b}{\lambda}\right)}{Z_f i_0\left(k_\omega+(j\omega)^P\right)(\rho_1+\rho_2)\sinh^2\left(\frac{b}{\lambda}\right)} \\
&-\frac{R_{ct}bk_\omega\left(\rho_1^2+\rho_2^2\right)}{Z_f i_0\left(k_\omega+(j\omega)^P\right)(\rho_1+\rho_2)\sinh^2\left(\frac{b}{\lambda}\right)} \\
&-\frac{2R_{ct}k_\omega\lambda\rho_1\rho_2}{Z_f i_0\left(k_\omega+(j\omega)^P\right)(\rho_1+\rho_2)\sinh\left(\frac{b}{\lambda}\right)} \\
&-\frac{R_{ct}k_\omega\lambda\left(\rho_1^2+\rho_2^2\right)\coth\left(\frac{b}{\lambda}\right)}{Z_f i_0\left(k_\omega+(j\omega)^P\right)(\rho_1+\rho_2)}
\end{aligned}
\tag{A.82}
$$

$$
U(\omega;L) = j\omega \tag{A.83}
$$

$$
\begin{aligned}
U(\omega;P) = &-\frac{2b\rho_1\rho_2\,(j\omega)^P\log(j\omega)\cosh\left(\frac{b}{\lambda}\right)}{\left(k_\omega+(j\omega)^P\right)(\rho_1+\rho_2)\sinh^2\left(\frac{b}{\lambda}\right)} \\
&-\frac{b\,(j\omega)^P\left(\rho_1^2+\rho_2^2\right)\log(j\omega)}{\left(k_\omega+(j\omega)^P\right)(\rho_1+\rho_2)\sinh^2\left(\frac{b}{\lambda}\right)} \\
&-\frac{2\lambda\rho_1\rho_2\,(j\omega)^P\log(j\omega)}{\left(k_\omega+(j\omega)^P\right)(\rho_1+\rho_2)\sinh\left(\frac{b}{\lambda}\right)} \\
&-\frac{\lambda\,(j\omega)^P\left(\rho_1^2+\rho_2^2\right)\log(j\omega)\coth\left(\frac{b}{\lambda}\right)}{\left(k_\omega+(j\omega)^P\right)(\rho_1+\rho_2)}
\end{aligned}
\tag{A.84}
$$

$$
\begin{aligned}
U(\omega;\rho_1) = &-\frac{2b\rho_1\rho_2}{(\rho_1+\rho_2)^2} - \frac{2b\rho_1\rho_2\cosh\left(\frac{b}{\lambda}\right)}{(\rho_1+\rho_2)^2\sinh^2\left(\frac{b}{\lambda}\right)} \\
&+\frac{2b\rho_2}{\rho_1+\rho_2} - \frac{b\left(\rho_1^2+\rho_2^2\right)}{(\rho_1+\rho_2)^2\sinh^2\left(\frac{b}{\lambda}\right)} \\
&-\frac{6\lambda\rho_1\rho_2}{(\rho_1+\rho_2)^2\sinh\left(\frac{b}{\lambda}\right)} + \frac{4\lambda\rho_1\coth\left(\frac{b}{\lambda}\right)}{\rho_1+\rho_2} \\
&+\frac{4\lambda\rho_2}{(\rho_1+\rho_2)\sinh\left(\frac{b}{\lambda}\right)} - \frac{3\lambda\left(\rho_1^2+\rho_2^2\right)\coth\left(\frac{b}{\lambda}\right)}{(\rho_1+\rho_2)^2}
\end{aligned}
\tag{A.85}
$$

Vita

Michael C. Daugherty was born to in Rome, GA in 1989 moving to Oak Ridge Tennessee by 1991. He graduated from Oak Ridge High School in 2007. Michael received his Bachelor of Science in Mechanical Engineering in 2015, the same year he began his graduate studies under Dr. Matthew M. Mench. He completed his Ph.D in Mechanical Engineering in the fall of 2020.